Label-Free Analysis of Drug Delivery Systems and Cellular Interaction Studies Using Confocal Raman Microscopy

Label-Free Analysis of Drug Delivery Systems and Cellular Interaction Studies Using Confocal Raman Microscopy

Dissertation

zur Erlangung des Grades

des Doktors der Naturwissenschaften

der Naturwissenschaftlich-Technischen Fakultät III

Chemie, Pharmazie, Bio- und Werkstoffwissenschaften

der Universität des Saarlandes

von

Birthe Kann

Saarbrücken

2016

Bibliografische Information der Deutschen Nationalbibliothek
Die Deutsche Nationalbibliothek verzeichnet diese Publikation in der Deutschen Nationalbibliografie; detaillierte bibliografische Daten sind im Internet über http://dnb.d-nb.de abrufbar.
1. Aufl. - Göttingen: Cuvillier, 2016
Zugl.: Saarbrücken, Univ., Diss., 2016

Tag des Kolloquiums:	24.Juni 2016
Dekan:	Prof. Dr.-Ing. Dirk Bähre
Berichterstatter:	Prof. Dr. Claus-Michael Lehr
	Prof. Dr. Gregor Jung
Vorsitz:	Prof. Dr. Uli Kazmaier
Akademischer Mitarbeiter:	Dr. Martin Frotscher

Nonnenstieg 8, 37075 Göttingen
Telefon: 0551-54724-0
Telefax: 0551-54724-21
www.cuvillier.de

1. Auflage, 2016
Gedruckt auf umweltfreundlichem, säurefreiem Papier aus nachhaltiger Forstwirtschaft.

ISBN 978-3-7369-9321-1
eISBN 978-3-7369-8321-2

Die vorliegende Arbeit wurde von April 2011 bis März 2015 unter der Leitung von Herrn Prof. Dr. Claus-Michael Lehr und Frau Dr. Maike Windbergs am Institut für Biopharmazie und Pharmazeutische Technologie der Universität des Saarlandes angefertigt.

Table of Contents

I Summary

In pharmaceutical development many questions still remain unsolved despite the availability of many analytical techniques. Consequently, the need of novel analytical approaches is not yet satisfied. In this thesis, confocal Raman microscopy is utilized to fill the scientific gap. In fact, the benefit of this non-destructive, label-free visualization technique for profound analysis in complex pharmaceutical applications is successfully demonstrated.
The impact of drying on drug distribution is proven by localizing the drug in wet-extruded pellets with Raman imaging. Additionally to this finding, the correlation between drug distribution and release is successfully elucidated. For the first time, confocal Raman microscopy is combined with optical profilometry. Thus, the limitations of the confocal microscope are overcome and all-encompassing component visualization in complex drug delivery systems exhibiting challenging structured surfaces is realized. During development of a lipid-based drug permeation model, the successive formation of the permeation barrier during coating is finally described using Raman analysis. Investigations benefit tremendously from a combination of chemical imaging in lateral and vertical planes to depict barrier integrity and stability. Finally, human cells as well as the uptake of different nanoparticles are analyzed label-free in aqueous environment, utilizing linear and coherent Raman techniques.

II Zusammenfassung

In der pharmazeutischen Entwicklung bleiben trotz der Verfügbarkeit diverser analytischer Techniken viele Fragestellungen unbeantwortet. Daher ist die Etablierung neuer analytischer Ansätze notwendig. Diese Arbeit beschäftigt sich mit konfokaler Raman-Mikroskopie als Möglichkeit, die Lücke zu schließen. Die Eignung dieser zerstörungs- und label-frei arbeitenden Technik zur differenzierten Probenvisualisierung für diverse pharmazeutische Fragestellungen wird erfolgreich demonstriert.

Der Einfluss vom Trocknungsprozess auf die Wirkstoffverteilung im Pellet wird durch Lokalisation des Wirkstoffs mittels Raman Imaging belegt. Dadurch wird auch die Korrelation zwischen Wirkstoffverteilung und Freisetzung aufgeklärt. Erstmals wird konfokale Raman-Mikroskopie mit optischer Profilometrie kombiniert. Es werden komplexe Arzneistoffträgersysteme mit strukturierten Oberflächen detailliert dargestellt, ohne durch das konfokale Mikroskop eingeschränkt zu sein. Durch Abbildung der einzelnen Coatingschritte in chemisch selektiven Raman-Bildern in der Entwicklungsphase eines lipidbasierten Permeationsmodells wird der sukzessive Aufbau der Permeationsbarriere erstmalig nachvollzogen. Die prozessbedingte ungleiche Dicke der Barriere sowie deren Integrität werden erfolgreich durch die Aufnahme von virtuellen Querschnittsbildern abgebildet. Darüber hinaus werden humane Zellen und die Aufnahme von Nanopartikeln label-frei mit linearen und kohärenten Raman-Techniken in wässrigem Medium untersucht.

III List of Original Publications Included in this Thesis

The presented thesis contains the following publications, which are arranged in four chapters.

I S. Schrank, **B. Kann**, M. Windbergs, B. J. Glasser, A. Zimmer, J. Khinast, E. Roblegg; Microstructure of Calcium Stearate Matrix-Pellets: A Function of the Drying Process. *J. Pharm. Sci.* 2013,102:3987-3997.

II S. Schrank, **B. Kann**, E. Saurugger, H. Ehmann, O. Werzer, M. Windbergs, B. J. Glasser, A. Zimmer, J. Khinast, E. Roblegg; Impact of Drying on Solid State Modifications and Drug Distribution in Ibuprofen-Loaded Calcium Stearate Pellets. *Mol. Pharmaceutics*. 2014;11:599-609.

III S. Schrank, **B. Kann**, E. Saurugger, M. Hainschitz, M. Windbergs, B.J. Glasser, J. Khinast, E. Roblegg; The Effect of the Drying Temperature on the Properties of Wet-Extruded Calcium Stearate Pellets: Pellet Microstructure, Drug Distribution, Solid State and Drug Dissolution. *Int. J. Pharm*. 2015;478:779-787.

IV **B. Kann**, M. Windbergs; Chemical Imaging of Drug Delivery Systems with Structured Surfaces – a Combined Analytical Approach of Confocal Raman Microscopy and Optical Profilometry. *AAPS J*. 2013;15:505-510.

V C. Muehlenfeld, **B. Kann**, M. Windbergs, M. Thommes; Solid dispersions Prepared by Continuous Cogrinding in an Air Jet Mill. *J. Pharm. Sci*. 2013,102:4132-4139.

VI T. C. Beber, D. F. Andrade, **B. Kann**, M. C. Fontana, K. Coradini, M. Windbergs, R. C. R. Beck; Submicron Polymeric Particles Prepared by Vibrational Spray-Drying: Semisolid Formulation and Skin Penetration/Permeation Studies. *Eur. J. Pharm. Biopharm*. 2014;88:602-613.

VII S. P. Gantzsch*, **B. Kann***, M. Ofer-Glaessgen, P. Loos, H. Berchtold, S. Balbach, T. Eichinger, C.-M. Lehr, U. F. Schaefer, M. Windbergs; Characterization and Evaluation of a Modified PVPA Barrier in Comparison to Caco-2 Cell Monolayers for Combined Dissolution and Permeation Testing. *J. Controlled Release*. 2014;175:79-86.
***** *both authors contributed equally and are listed in alphabetical order*

VIII **B. Kann**, B. J. Teubl, E. Roblegg, M. Windbergs; Label-Free *In Vitro* Visualization of Particle Uptake into Human Oral Buccal Epithelial Cells by Confocal Raman Microscopy. *Analyst*. 2014;139:5069-5074.

IX **B. Kann**, C. Spengler, K. Coradini, L. A. Rigo, M. L. Bennink, K. Jacobs, H. L. Offerhaus, R. C. R. Beck, M. Windbergs; Intracellular Delivery of Poorly Soluble Polyphenols - Elucidating the Interplay of Self-Assembling Nanocarriers and Human Chondrocytes. *Anal. Chem.*, 2016;88:7014-7022.

IV Abbreviations

AFM	atomic force microscopy
API	active pharmaceutical ingredient
CARS	coherent anti-Stokes Raman scattering
EdU	5-ethynyl-2'-deoxyuridine
IR	infrared
MIR	mid infrared
NIR	near infrared
PAMPA	parallel artificial membrane permeation assay
PAT	process analytical technology
PCL	poly(ε-caprolactone)
PLGA	poly(lactic-co-glycolic acid)
PMMA	polymethylmethacrylate
PVPA	phospholipid vesicle-based permeation assay
SEM	scanning electron microscopy
SERS	surface enhanced Raman scattering
SRS	stimulated Raman scattering
SWCNT	single-walled carbon nanotubes
TERS	tip-enhanced Raman scattering
TiO_2	titanium dioxide

1 Introduction

Constant progress in pharmaceutical sciences regarding the improvement and new development of drug delivery systems as well as *in vitro* test systems necessitates a simultaneous advancement in analytics as well. Here, analytical techniques with high flexibility and versatility without sacrificing high-precision detection especially for visual sample examination are beneficial to be established in the pharmaceutical context. Confocal Raman microscopy represents such a highly qualified analytical technique. It combines a label-free, non-destructive working principle with chemically selective, high-resolution visualization for contactless analysis.

1.1 Basic Principles of Raman Spectroscopy

Raman spectroscopy is based on the detection of scattered light occurring upon the irradiation of a sample with monochromatic light. The majority of scattered light is generally scattered elastically. This is referred to as Rayleigh scattering and the scattered light has the same frequency as the incident light (Figure 1). However, a small portion of the light is scattered inelastically at a different frequency than the incident light. This event is called spontaneous Raman scattering or Raman effect, named after the Indian Physicist Sir C. V. Raman, who was awarded the Nobel Prize in 1930 for this discovery. [1]

If a photon strikes a molecule in its ground state, a part of its energy can be transferred to the molecule allowing it to change its excited state. Thus, the photon loses a portion of its energy and is scattered at a longer wavelength compared to the incident photon (red shift). This is called Stokes scattering (Figure 1). In contrast, light interacting with a molecule which is in an already excited vibrational state will be scattered at shorter wavelength (blue shift). This opposite event is referred to as anti-Stokes scattering.

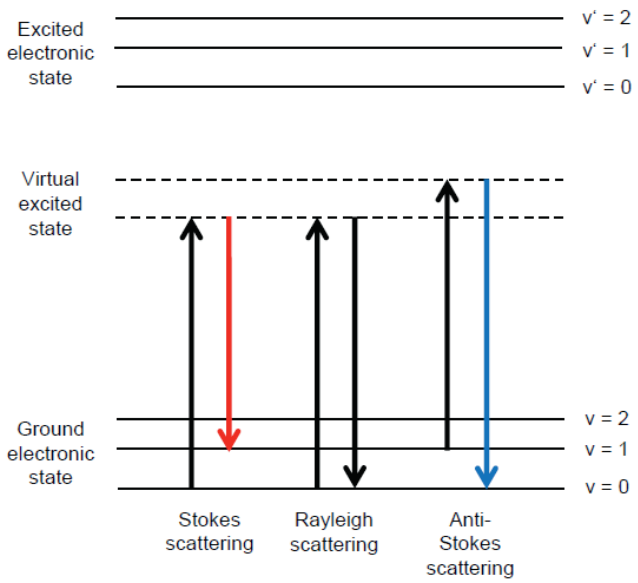

Figure 1. Energy level diagram of Rayleigh, Stokes and anti-Stokes scattering. The Raman effect comprises Stokes and anti-Stokes scattering.

The frequency shift between incident and scattered photon is equal to the frequency of the vibrational mode of the chemical moiety in the irradiated molecule. The resulting frequency difference is displayed in the Raman spectrum by plotting wavenumbers (reciprocal wavelengths) against the intensity of the scattered radiation (Figure 2). A Raman spectrum can be split into three parts. [2] Peaks at frequencies below 1800 cm^{-1} are highly specific for functional groups. Therefore, this region is referred to as the fingerprint region of the Raman spectrum. As barely any molecular bonds oscillate between 1800-2600 cm^{-1}, this spectral region is termed silent region. The high frequency region located above 2600 cm^{-1} is dominated by vibrations arising from carbon-hydrogen groups. Based on substance specific scattering, Raman spectroscopy is suited for chemically selective detection, enabling label-free compound identification.

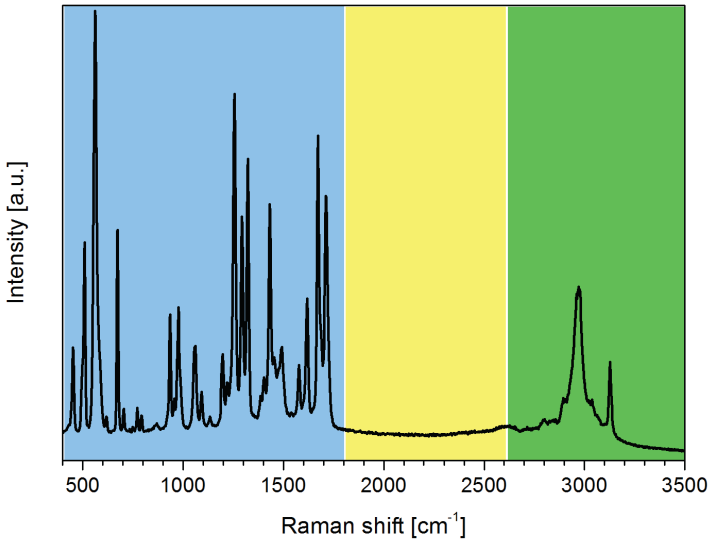

Figure 2. Exemplary Raman spectrum of a chemical compound. The fingerprint region is highlighted in blue, the silent region in yellow and the high frequency region in green.

The Raman activity of a compound is determined by its change in polarizability upon interaction with the alternating field of laser light (electromagnetic field). The more elastic the electron cloud of the molecule, the higher the Raman activity.

In spontaneous Raman spectroscopy, Stokes scattering is predominantly detected, as anti-Stokes scattering occurs rarely because the chance of striking a molecule in an excited vibrational state is low. Nevertheless, the overall probability of observing Raman scattering is by far lower than for example the observation of fluorescence. However, significant advancements in lasers and detection technology have made Raman spectroscopy an effective analytical tool.

1.2 Confocal Raman Microscopy for Chemical Imaging

The combination of Raman spectroscopy with optical microscopy is entitled Raman microscopy. Thereby, chemically selective detection is united with spatially resolved analysis.

The center piece of a Raman microscope is a conventional optical microscope as sampling device. It is equipped with a laser light source and a detection unit composed of a spectrometer and a detector. The laser light is focused onto the sample through an objective and the

scattered light is detected to record the Raman spectra. By implementing a confocal microscope, out-of-focus light is rejected by the pinhole. Thereby, lateral and more importantly depth resolution of the Raman microscope increase and background signals are effectively reduced. The spot size of the irradiated volume defines the spatial resolution of the confocal Raman microscope. As shown in the Abbe equation (Equation 1) this diffraction limited spot size (d) is determined by the excitation wavelength (λ) and the numerical aperture (focal length, NA) of the objective. [3]

$$d = \frac{\lambda}{2\,NA} \qquad (Equation\ 1)$$

Confocal Raman microscopy delivers spatially resolved chemical information of a sample by probing intrinsic properties of the molecules while irradiating the sample with monochromatic laser light. Subsequently, a color-coded distribution map of the sampled area can be generated from the recorded spectral data set to elucidate the composition of the sample. The color-code assigned to a spectral band of a component is depicted as image pixel which represents the spatial element in the false color map equal to the location from which the Raman spectrum was recorded. This is referred to as chemical imaging.

The principal procedure of creating a chemical image is schematically illustrated in Figure 3. Exemplarily, an extrudate composed of an active pharmaceutical ingredient (API) embedded in a lipid matrix is shown. The Raman spectra are recorded by stepwise rasterizing the sample with laser light. Next, a different color is assigned to the spectrum of each component. In this case, the lipid matrix spectrum is depicted in blue, whereas the API's Raman spectrum is portrayed in red. All spectral data points recorded from the sample represent one or the other compound. Thus, each spectrum is translated into an image pixel with the aforementioned color classification. Thereby, two separate false color images are constructed, each representing one compound within the extrudate cross section. By merging the two images, an overview of the component distribution within the drug delivery system is obtained.

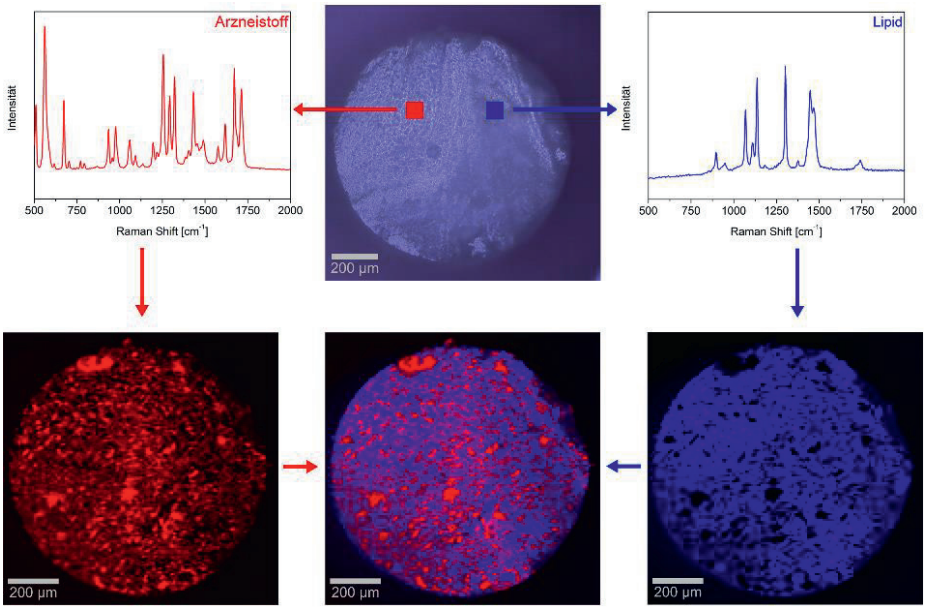

Figure 3. Schematic illustration of the sequentially performed steps to create a false color map from a Raman spectral data set. Spectra assigned to API are depicted in red, whereas Raman spectra assigned to the lipid matrix are shown in blue. This figure was first published in TechnoPharm 3, No. 3 (2013) 146-149 and is reprinted with permission. [4]

Chemical images can be acquired by point mapping, line scanning or global illumination. While the latter requires no sample transition, this is needed for point mapping and line scanning. [5] Here, the sample is moved through the focal point of the probing laser beam in a predefined raster in order to collect the spectra from the individual sample positions. Consequently, the terms ‘imaging’ (stationary sample) and ‘mapping’ (sample transition) are discussed controversially although they are generally used synonymously. [6-8]

The recorded hyperspectral data set contains manifold information about pixel coordinates where the spectra were collected, the wavelength as well as the intensity of the scattered radiation. Thus, the transformation from a spectral data set to a color-coded image necessitates the processing of the acquired raw data. The first step is often referred to as pre-processing and aims at removing spectral artefacts originating from experimental conditions. [5, 9, 10] For example, Raman peaks generated by cosmic rays are eliminated from the data set. Further, the baseline of the spectra is corrected by reducing the background noise. Additionally, the sample surface texture may lead to the detection of varying spectral intensities across the sample. To account for this, the scattering intensity may be normalized.

The pre-processed spectral data set is then further processed by chemometric tools to generate the color-coded chemical image. Univariate methods only consider one component and require therefore a component specific spectral band which is preferably rather prominent in the spectrum. More importantly, it cannot be masked or interfered by any other compound in the sample. Either the position, the intensity (height) or the area (integral) of the identified band in combination with the spatial coordinates are the basis for constructing the map. In contrast to univariate data analysis, the multivariate approach employs all spectral information from the data cube. [9, 11] The scores or parameters which are yielded for each Raman spectrum by these multivariate methods are subsequently plotted as a function of the spatial coordinates of each spectrum in the sample. [9] The most prominent algorithms comprise two complementary approaches. Cluster algorithms sort all spectra of the data set based on similarity of the spectra, whereas unmixing algorithms are sorting according to greatest dissimilarities finding the most extreme spectra. In multivariate data analysis the algorithms can work supervised or unsupervised. The latter is impossible for univariate methods, as comparison with reference data is necessary to identify the component specific spectral band. [5, 9] Especially for the analysis of low content samples, multivariate processing is needed as shown in an imaging study by Šašić et al. [12] Here, univariate methods failed to construct reliable chemical images of low alprazolam loaded tablets as the drug’s Raman signal was too weak.

Further spectroscopic techniques which are also suited for chemical imaging are infrared microscopy and fluorescence microscopy. Infrared microscopy is another vibrational spectroscopic technique. Unlike confocal Raman microscopy it is based on light absorption and not on scattering (Figure 4). When referring to IR spectroscopy, it has to be differentiated between near and mid infrared spectroscopy. While near infrared light (λ = 800 nm - 2,5 µm) excites vibrational overtones and combinations of vibrations which lead to broad and overlapping spectral bands, mid infrared light (λ = 2,5 – 50 µm) generates sharp individual bands. The most prominent example to demonstrate the difference between IR and Raman spectroscopy is the water molecule. The water molecule is a strong dipole. It shows an intense IR activity. The water absorption band covers nearly all other IR bands in the spectrum and impedes IR analysis of other molecules in aqueous surroundings. As Raman scattering depends on a change in polarizability of the molecule and not on a change in dipole, Raman microscopic investigations of wet samples or in aqueous surroundings are feasible.

Consequently, strong IR activity is often equal to weak Raman activity and vice versa. Furthermore, the resolution in confocal Raman microscopy is superior to IR microscopy due to the long excitation wavelength necessary for IR investigations. [13]

The chemical selectivity of fluorescence microscopy is based on the detection of emitted light (Figure 4) which originates in the majority of cases from a marker molecule that has been linked to the compound of interest and not from the constituent itself. However, the labeling process represents both, the up- and downside of the technique. On the one hand, it provides the great opportunity for differentiated sample visualization, which made fluorescence microscopy the state-of-art analytical technique for biological applications. On the other hand, labeling of molecules bears the risk of altering their physicochemical properties leading to data misinterpretation. Further, the fluorophore might not sufficiently bind to the target molecule and migrate within the sample. In general, the number of analytes is limited to the microscopic setup, as each analyte requires a different excitation wavelength in order to detect multiple compounds simultaneously. Moreover, many fluorescent dyes are susceptible to photo-bleaching hampering long term analysis. Nevertheless, some components fluoresce intrinsically and can be probed directly. When a sample with an autofluorescent component is investigated by spontaneous Raman microscopy, Raman bands are generally obscured, because the autofluorescence of a molecule is much stronger than its Raman scattering intensity. By increasing the excitation laser wavelength, the chance of exciting fluorescence decreases, because the energy of the incident photon is reduced. Thus, the excitation to the higher electronic energy state causing fluorescence becomes less likely. Further, photo-bleaching or quenching are alternatives to circumvent intruding fluorescence during Raman analysis.

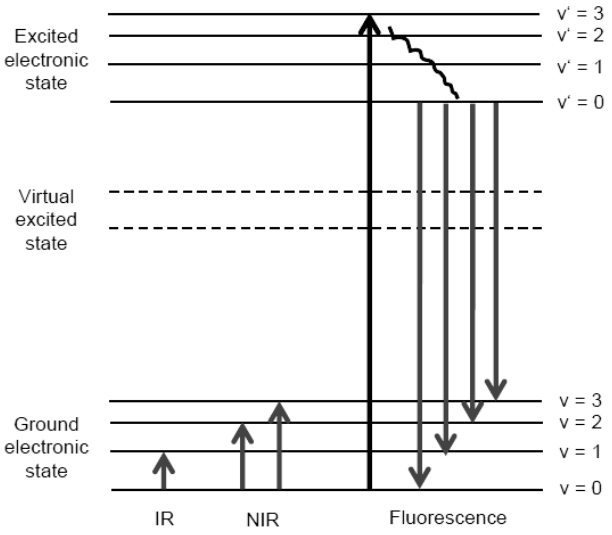

Figure 4. Energy level diagrams of IR and NIR absorption and fluorescence.

Other techniques, which are often employed to depict pharmaceutical samples, are atomic force microscopy (AFM) and scanning electron microscopy (SEM). Both of them do not offer chemically selective visualization of the complex composition of samples, but provide morphological information with extreme high resolution in the low nanometer range. However, they are restricted to the analysis of outer surfaces. Whereas AFM enables direct sample analysis on a very small scale, samples for SEM analysis generally have to be sputter-coated first. Consequently, the sample in its native state cannot be analyzed repeatedly as the applied

metal layer impairs subsequent processing steps. Both AFM and SEM have been successfully combined with Raman microscopy. The analytical AFM - Raman combination is known as tip-enhanced Raman spectroscopy (TERS), whereas only recently a correlative microscope for SEM and Raman analysis was introduced to the market.

Overall, spontaneous confocal Raman microscopy represents an advantageous and highly beneficial alternative to established analytical techniques or complements them. In contrast to staining or sputter coating processes, confocal Raman microscopy requires little if any sample preparation. It is based on a non-destructive working principle and allows repeated examination. Here, analysis in not limited to external areas, as virtual planes can be spanned through the sample depending on its opacity. Consequently, consecutive steps such as multiple processing steps can be monitored in air as well as in aqueous surroundings.

Nevertheless, the acquisition of spectral data sets using spontaneous confocal Raman spectroscopy can be time consuming due to the rare occurrence of Raman scattering. Here, non-linear Raman technologies such as stimulated Raman spectroscopy (SRS) and coherent anti-Stokes scattering (CARS) microscopy are alternatives. The linear correlation of incident light and scattering intensity in spontaneous Raman scattering is abolished, as multiple photons are involved in generating these non-linear processes. As a consequence, the probability of light scattering increases and the Raman signal is enhanced reducing the time for analysis.

In SRS, two laser beams at different frequencies (ω_{pump} and ω_{Stokes}) are irradiating the sample. The excitation of a vibrational transition is stimulated when the frequency difference corresponds to a molecular vibration of the sample. The SRS signal is detected as a loss or gain in energy of one of the incident laser beams.

In CARS microscopy the probed anti-Stokes scattering is detected. It is generated in a four photon process (Figure 5). Two laser beams irradiate the sample with photons at different frequencies (ω_{pump} and ω_{Stokes}) simultaneously. A third photon, which is usually of the same frequency as the pump photon and therefore originating from the same source, interacts with the molecule as well and the anti-Stokes photon as the fourth photon is generated. When the frequency difference between the pump photon and Stokes photon coincides with a molecular vibration of the sample, the CARS signal is resonantly enhanced. This process is coherent as all transitions are driven.

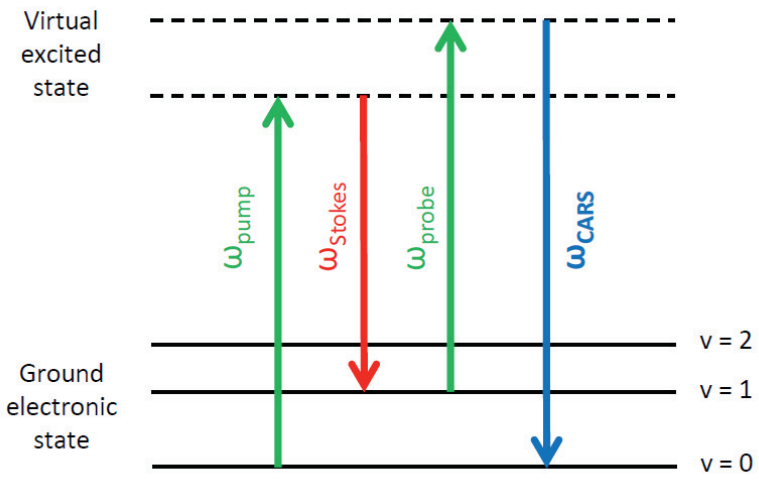

Figure 5. Energy level diagram of the CARS signal generating process.

As the frequency difference is tuned to coincide with a specifically chosen vibrational resonance, different molecules of interest can be visualized instantaneously. This is exemplarily demonstrated by CARS imaging of a transparent polymeric bead mixture composed of polystyrene and polymethylmethacrylate (PMMA) beads at different Raman shifts shown in Figure 6. The surrounding structure is revealed by a non-resonant background which accompanies the CARS signal. The spectral information is reduced in CARS imaging because only one vibrational resonance is probed at a time. In contrast to long integration times in spontaneous Raman microscopy where the full spectral information is collected, this spectral expense facilitates fast image acquisition up to video rate. Consequently, *in situ* processes in a sample can be visualized. The signal-generating process makes non-linear Raman techniques inherently confocal, and fluorescence is not interfering.

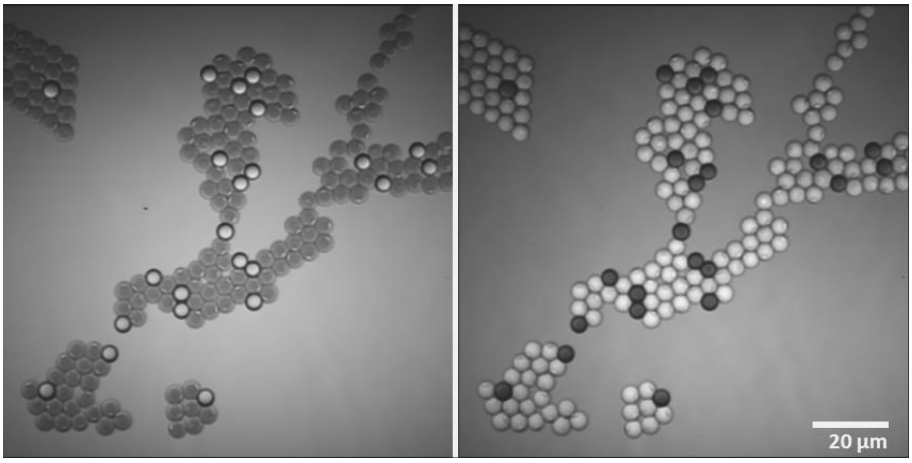

Figure 6. Chemically selective CARS images of a transparent polymeric bead mixture. Polystyrene beads (left panel) and PMMA beads (right panel) are depicted with high precision.

Depending on the sample and the focus of investigation, different variations of Raman microscopy are available for chemical imaging. Regular confocal Raman microscopes have become commercially available due to immense technical progress ever since a first self-built regular confocal Raman microspectrometer was reported in 1990. [14] Although the Raman effect was described as early as 1928 [1], non-linear Raman techniques such as CARS and SRS were first reported as early as 1982 and 2007, respectively. [13, 15] These microscopes are still predominantly reserved to specialized laboratories, which limits their availability to the general research community. However, the techniques are on the verge of being marketed commercially besides their linear counterpart.

1.3 Pharmaceutical Applications of Confocal Raman Microscopy

The variety of pharmaceutical samples is large. It reaches from classic oral solid dosage forms like tablets to modern drug delivery systems on the nanometer-sized scale. Cell culture based and artificial *in vitro* test systems are comprised as well as drug coated medical products. As a versatile analytical technique, confocal Raman microscopy is generally suited to cover this manifold sample spectrum. However, its application only started to emerge in the pharmaceutical community over the last decades. This is mainly due to the immense progress in laser technology and the development of sensitive detection units, which led to the commercial availability of confocal Raman microscopes and therefore to a greater access to

Raman analysis. Despite the longtime utilization of Raman spectroscopy, confocal Raman microscopy has not yet become a standard analytical technique.

One crucial parameter hampering a broad use is the challenging interpretation of the spectra. For confocal Raman microscopy, the recorded hyperspectral data set requires explicit knowledge about spectral processing methods to generate reliable false color images.

As the majority of employed raw materials (both excipients and active pharmaceutical ingredients) for manufacturing drug delivery systems is simply white, visual component discrimination in the final delivery system becomes impossible due to the uniform appearance. Similarly, biological systems show the same difficulty. While drug delivery systems, especially the classic solid ones, are opaque, biological samples rather show a gradual transparency. Consequently, color-coded chemical images of pharmaceutical samples are highly desirable to gain an in-depth understanding of the often complex structures and to elucidate fabrication and interaction processes. Such visualization approaches can add valuable information to an ongoing study because of clarifying the context of puzzling analytical results.

The drug distribution in a delivery system impacts the drugs dissolution rate and consequently its bioavailability. In this context, chemical imaging is of great value to evaluate changes in drug distribution before and after dissolution experiments to understand the release mechanism in order to design delivery systems with tailor-made release profiles. Matrix systems are often utilized when sustained release is requested. The effect of adding a pore former in an extruded solid lipid matrix system on drug dissolution was observed by Raman mapping. [16, 17] Pores started to form immediately in the water insoluble lipid matrix upon contact with the dissolution medium as visualized in comparative false color maps of the drug delivery system before and after dissolution testing. Consequently, the contact area for the dissolution medium with the API increased and the drug was released significantly faster than from extrudates which were lacking the pore former. Here, Raman images barely showed any difference in component localization after dissolution.

Solution-mediated solid-state transformations have been observed spectroscopically *in situ* during dissolution. As these processes occur at the interface of delivery system and dissolution medium, they can be visualized by Raman microscopy. However, spontaneous Raman microscopy is too slow to image these rapid transformations. Here, coherent anti-Stokes Raman scattering microscopy has been successfully employed to monitor the transformation of the model drug into its monohydrate. [18-20] Due to the generation of a coherent signal, events can be followed with video rate.

Active coatings are not only applied to oral solid dosage forms but also to biomedical implants to deliver drugs to specific body regions. One popular example are stents, which are covered with drug-eluting coatings to locally prevent restenosis. [21] Here, the analytical strength of confocal Raman microscopy becomes evident as it facilitates the non-destructive visualization of the polymeric coat and the embedded drug throughout the entire thickness of the film coating in virtual cross section images. [22] Thus, API diffusion during stent elution was characterized without laborious sample preparation, and segregation of drug enriched regions inside the coating was detected. Another study by Dong et al. [23] depicted the distribution of rapamycin in another therapeutic coating by exploiting all axes of the Raman microscope for chemical imaging. Lateral images showed a homogenous distribution of rapamycin domains in the polymer, whereas cross section images portrayed the formation of drug columns spanning vertically through the coating. The acquisition of lateral scans at different distances from the water coating interface depicted a clear drug migration towards this interface during elution.

The recording of spectral data sets was performed with a water immersion objective to capture drug diffusion during the actual elution process. Due to the aqueous surroundings, IR investigations of the coating are impossible. To gain deeper insight in the effects of drug elution on surface properties of drug-eluting stents, confocal Raman microscopy analysis was correlated with atomic force microscopy studies. [24] Whereas Raman imaging facilitates the surface and subsurface characterization of chemical distribution, AFM complements surface analysis by high resolution profiling. Thereby, the drug elution dependent change of voids in the coating is visualized. Three dimensional drug redistribution during its release from polymers used for stent coatings was visualized *in situ* by depth resolved CARS imaging. [25]

These studies on stents nicely demonstrate the potential and versatility of Raman microscopy for non-destructive analysis along all three axes of the microscope, which facilitates access to internal sample structures. As the polymer used for coating is gradually transparent, virtual planes can be spanned within the coating. Thus, the laser light penetrates through the material and Raman signals are recorded from within the sample without destroying it. Thereby, internal structures of the sample as well as e. g. changes upon drug elution were successfully characterized.

Although especially the field of classic drug delivery system is predestined for the analysis with linear as well as non-linear Raman techniques as the molecules are generally strong Raman scatterers, the number of studies employing Raman imaging is low. This is mainly due to the fact that IR microscopy is a long established technique in this area of pharmaceutics and samples are rather large, which often does not necessitate the use of analytical techniques with higher resolution. However, the few studies employing both vibrational techniques demonstrate the potential benefit of adapting confocal Raman microscopy in this field on a larger scale.

A comparative chemical imaging study of a tablet with five components showed the superiority of Raman microscopy over NIR microscopy. All five components were retrieved by multivariate data analysis of the Raman spectral data set, whereas a maximum of three compounds was identified in the NIR spectral data set. [26] Furthermore, the distribution of an API with a content of less than 1% was shown by Raman mapping. [12] Model tablets containing polymeric beads of defined sizes demonstrated the accuracy of Raman chemical imaging to evaluate API particle sizes within tablets. [27] The domain size of API in a chemically selective map of a tablet with an API concentration of 0,5 % w/w was shown to be dependent on the size distribution of raw API material. [28] Even polymorphic impurities were still detectable from the Raman spectral data set. Due to broad overtone bands, NIR spectroscopy is not accurate enough for polymorph detection. This is however possible in MIR spectra, but the low dose API causes detectability problems as signals from excipients are competing with API bands if not even shadowing them. Consequently, confocal Raman microscopy is a suited alternative technique showing high precision. Besides, the detectability of amorphous compounds in multi-component solid mixtures by Raman as well as NIR spectroscopy was shown in several studies. [29-31]

NIR and Raman spectroscopy are also competing as process analytical technology (PAT) tools. Its goal is to gain fundamental understanding of fabrication processes, which are often a black box up to today. Here, vibrational molecular spectroscopy can contribute significant insight into fabrication processes as fiber-optic probe instruments for NIR and Raman spectroscopy can be implemented into process streams of various unit operations for continuous real-time monitoring in a non-destructive manner.

Especially probing in aqueous surroundings pointed at the different analytical focus of the two techniques. While NIR spectroscopy is sensitive to different water states, Raman spectroscopy solely probes the molecular vibrations of the analyte. Thus, the stepwise dehydration of theophylline monohydrate during fluid-bed drying was monitored on line by following the free water content as well as lattice-bound water. [32] On the contrary, Raman spectroscopy was shown to be superior to NIR spectroscopy during wet granulation. [33] The broad water band in the NIR spectra covered the peak which indicated the hydrate formation of theophylline (1686 cm^{-1}). The sensitivity of Raman spectroscopy for structural changes of drug molecules in water rich environments was also demonstrated in a solution-mediated crystallization study of carbamazepine. [34]

Besides the investigation of solid states, Raman spectroscopy as a PAT tool was applied to observe other parameters of pharmaceutical production processes. Blend homogeneity was determined in powder mixtures as well as in aqueous suspension. [33, 35-37] Furthermore, coating processes of tablets were spectroscopically analyzed by correlating Raman spectra to coating time representing the weight gain of the tablet. [38-40] Active coating processes were also successfully evaluated. [41, 42] The endpoint of coating was determined by detecting the API quantity applied with the coating. [41] Raman spectroscopy was also feasible to monitor the active coating of a two layer tablet which contributes different spectral bands to the signal depending on the side facing the laser beam. [42] By implementing Raman probes in the extruder barrel during hot melt extrusion, profound process understanding regarding the influence of different settings and formulations on the solid state of polymer and drug was gained and in-line drug quantification was possible. [43-46] The development of protein drug delivery systems, which are often manufactured by lyophilization, is steadily increasing. The therapeutic performance of such protein formulations is highly dependent on the protein's physical stability. Here, Raman spectroscopy was used *in situ* to investigate the degree of protein denaturation and thus inactivation, based on process parameters during freeze drying and stabilization strategies using trehalose. [47, 48] Further, the suitability of Raman spectroscopy as sensitive PAT technology was shown by determining the secondary structure of fourteen model proteins during freezing, thawing as well as during frozen storage. [49]

Although the variety of investigated samples indicates the potential of confocal Raman microscopy, the field is still wide open. Besides its application for the characterization of classic solid drug delivery systems and for quality assessment, another rapidly evolving field are biological systems.

In this regard, rapidly evolving therapeutic concepts for curing diseases on the subcellular level have resulted in developing novel, small so-called modern carrier systems for adequate intracellular drug delivery. As IR microscopy suffers from poor spatial resolution of several micrometers and as water shows an interfering strong IR absorption, its application is limited for biological investigations. The analysis of cell culture models and their interaction with the micro- to nanometer sized drug carriers as well as potential internalization is predominantly performed by fluorescence microscopy as state-of-the-art technique in the biomedical field. However, recently investigations including single cell imaging as well as drug carrier uptake visualization with Raman microscopy emerged. In fact, Puppels et al. [14] introduced confocal Raman spectroscopy for the analysis of single living cells and chromosomes already in 1990. Cell cycle phases were spectroscopically determined *in situ* as well as apoptotic changes. [50, 51] Further, various cell types and their subcellular structures were imaged solely based on molecular vibrations of chemical moieties inside the cell. [52-57] The investigations were not limited to any specific cell type and included human embryonic stem cells as well as diverse

epithelia cell lines and sperm cells. Even chemical imaging of the cellular nucleus and subcellular RNA clusters were reported as an approach to evaluate chemotherapeutic drug effects on cancer cells, which often express large nucleoli owed to rapid proliferation. [58, 59] Comparative studies of confocal Raman and fluorescence microscopy demonstrated the sensitivity of vibrational spectroscopy, as mitochondria were effectively detected solely based on two peaks arising from lipid molecules in their complex membrane structures. [56] Subsequent staining of mitochondria in the same cells with the fluorescent dye Mitotracker showed congruent mitochondria-rich areas in pseudo color maps for both techniques. Consequently, confocal Raman microscopy delivers equivalent analytical results. Its label-free principle due to probing molecular vibrations is advantageous in comparison to fluorescence microscopy. The introduction of dyes, which is often time consuming and laborious, can be omitted. Furthermore, the risk of altering physicochemical properties of the sample, the migration of the labeling molecule and its attachment to wrong chemical entities is abolished. Hence, the chance of obtaining falsified analytic results is minimalized. Moreover, the number of analytes is not limited to the number of available excitation wavelength of the microscope. The sample can be investigated multiple times as photobleaching is not an issue. It was reported that a living lymphocyte was repeatedly imaged for 10-15 times in series by confocal Raman microscopy before it showed physical damage. [60]

The feasibility of studying single cells and their interaction with nanocarriers for intracellular drug delivery with confocal Raman microscopy is evident in literature. Interaction and uptake studies are important to evaluate the therapeutic intention of these small systems as well as the cytotoxic potential on cells. Nanotoxicity is an important aspect not only for nanosized delivery systems, but mainly with regard to non-biodegradable engineered nanoparticles coming from the field of material sciences.

Poly(lactic-*co*-glycolic acid) (PLGA) and poly(ε-caprolactone) (PCL) are biocompatible and biodegradable polymers which are often used for nanoparticle preparation. [61] Internalization and intracellular degradation of PLGA and PCL nanoparticles were monitored spectroscopically following changes in the carbonyl stretching vibrations of the ester bond in both polymers. [62, 63] Further, vesicular inclusion of particles was concluded from increasing lipid signals with incubation time. [63] Intracellularly delivered β-carotene from low-loaded PLGA nanoparticles could be determined by confocal Raman imaging due to the resonance Raman effect of β-carotene molecules upon irradiation at an excitation wavelength of 785 nm. [64]

As compounds used to fabricate drug delivery systems intended for cellular application are often similar to the biological molecules of cells, their respective Raman spectra are consequently alike and often indistinguishable. Here, isotopes like deuterium (^{2}H) or ^{13}C are used to trace the sample molecules spectroscopically. Isotopes comprise similar chemical properties as their natural counterparts. They lead to a band shift in the Raman spectrum often to the silent region of the spectrum, which makes molecules comprising isotopes distinguishable. This effect was exploited to study the uptake of liposomes composed of deuterated phospholipids and the impact of different surface modifications on uptake kinetics. [65, 66] A study by Ye et al. [67] showed that cell penetrating peptides, which can be used for intracellular delivery of carrier systems, can be traced even to the nucleus when natural carbon atoms are exchanged for ^{13}C. Similarly, the uptake of nutrition such as amino acids and lipid metabolism of cells have been investigated. [68, 69] Alkyne groups are small, exogenous molecules barely existing naturally in cells. They are considered bioorthogonal and do thus, not react with endogenous biomolecules. [70, 71] Click chemistry has come up with alkyne

modified molecules for bioorthogonal labeling allowing the introduction of a fluorescent dye after sample fixation. However, alkyne moieties feature Raman peaks in the silent region of the spectrum (1800 cm^{-1}-2600 cm^{-1}). Thus, the alkyne tagged thymidine analog 5-ethynyl-2'-deoxyuridine (EdU) for example was used to measure *de novo* DNA synthesis in HeLa cells by Raman imaging as EdU was incorporated into cellular DNA during replication. [72] The concept of alkyne-tag Raman imaging has been transferred to non-linear Raman techniques as well. [70] Drug molecules like erlotinib (chemotherapeutic drug) and terbinafine (antifungal drug) comprise an internal alkyne moiety and therefore, drug molecules applied in solution to cultured cells can be traced non-invasively. [71, 73] Wei et al. [71] presented a broad study of tracing molecules with alkyne moieties in cells with stimulated Raman spectroscopy including analogues of thymidine, uridine, and methionine to overcome time-consuming spectra acquisition by spontaneous Raman microscopy.

Overall, performed studies on cell carrier and drug interactions are limited to a few examples, which, however, demonstrate the potential of confocal Raman microscopy as a valuable analytical technique in this field. It is also discussed as a suitable alternative to fluorescence microscopy in stem cell research. Here, commonly the stem cells are genetically modified to express luciferase and fluorescent proteins in order to track them. [74-76] Mao et al. [77] continuously mapped marrow-derived mesenchymal stem cells cultured over 14 days. The original culture was incubated with collagen coated single-walled carbon nanotubes (SWCNT) detectable by the outstanding G-band of carbon. Proceeding cell culture images showed a decrease of SWCNT per cell as a result of SWCNT dilution due to continuous cell division. Metal complexes with therapeutic activity have raised attention in medical organic chemistry. Unfortunately, the biodistribution as well as properties of ruthenium-bipyridyl complexes were altered by fluorescence labeling. [78] As this problem might transfer to other metal complexes, Meister et al. [79] proved confocal Raman microscopy as a suitable alternative to study the internalization of these complexes. The number of studies here is sparse; although fluorescence microscopy does not present an analytical possibility, researchers barely looked out for suitable alternatives. Moreover, the field of nanomaterials representing body invading, non-active compounds is almost neglected by chemical mapping. As these materials often have unique scattering attributes, they are most likely to be ideal candidates to be characterized by vibrational microscopy including their cellular interaction. Cellular uptake of these nanoparticles represents a clear indication for further inspections on the subcellular structure regarding genotoxic aspects among others.

Further, Raman imaging plays an important role for cellular investigations such as cell visualization. The engulfment and localization of drug delivery systems are of high interest and allow insight into interaction correlations. In contrast, Raman spectroscopic investigations became more of recent interest when the technique was introduced as an efficient tool for the identification, differentiation and characterization of bacteria. [80] Further, high-speed image generation made non-linear Raman techniques more popular in the biomedical field, especially for tissue investigation and cancer research.

Due to the low Raman scattering activity in samples of biological origin, surface enhanced Raman scattering (SERS) can be exploited to amplify the scattering intensity of the analyte. So-called SERS probes are noble metal nanostructures often made out of gold. [81-83] They come in different geometries such as spheres, rods, flowers or stars. [84-91] However, graphene oxide has also been used for cellular investigations. [92, 93] When these metallic nanostructures are irradiated with monochromatic laser light, an additional electric field arises resulting in a dipolar localized surface plasmon resonance at the surface of the nanostructure.

[64, 67, 94-98] An analyte in close proximity of this electric field can interact with it, thereby the extent of the induced dipole of the analyte increases, consequently increasing its Raman scattering signal. [99] Two approaches are feasible to introduce SERS probes to a cellular sample. It is either linked to the designated sample molecule similar to a fluorophore or the SERS substrate is applied passively prior to analysis in order to sense it. The SERS probe itself represents the pitfall of this special Raman application as it potentially alters cell properties, and the Raman signal enhancement strongly depends on the position of the plasmon resonance. [100] Although SERS microscopy is still maturing, it has successfully been applied for cellular investigations such as the identification of cells based on expressed receptors. [89, 91, 93, 101, 102] But also drug diffusion through the cell membrane was successfully monitored. [103] To reach an even higher resolution, tip enhanced Raman scattering (TERS) microscopy was introduced combining SERS with AFM.

All in all, the diverse applicability of confocal Raman microscopy in pharmaceutical sciences is indicated by the performed investigations covering a great sample variety from classic solid drug delivery systems to biological systems. Nevertheless, the overall number of studies is low as confocal Raman microscopy is still an upcoming analytical technique. Sometimes even only the spectroscopic part as for PAT is used. Most often studies only apply confocal Raman microscopy as a single analytical technique neglecting the potential of incorporating it into a versatile analytical context. Yet, inherent advantages of Raman microscopy regarding its non-destructive, label-free working principle and high resolution constantly promotes its application. Furthermore, steady instrumental progress and research lead to a growing selection of Raman techniques available for analysis with high spatial as well as temporal resolution. Overall, it completes the spectrum of state-of-the-art analytical visualization techniques in pharmaceutical sciences and provides an adequate alternative when other spectroscopic techniques reach their limitation.

2 Aims of the Thesis

The main goal of this thesis is to apply confocal Raman microscopy to the analysis of classic solid drug delivery systems up to studies of cultured human cells. This analysis will be performed entirely label-free without sample destruction to realize chemically selective, spatially resolved sample visualization. The intention of implementing this approach in the pharmaceutical context is to gain novel insight into complex studies and to advance the application of confocal Raman microscopy as a beneficial analytical technique in this scientific field.

More specific the aims of this thesis are:

- To elucidate the impact of fabrication processes on drug distribution in the respective delivery systems and to identify correlations between drug distribution and release.

- To accomplish all-encompassing visualization of drug delivery systems exhibiting structured surfaces without sample alterations despite the limitations of the confocal setup of the Raman microscope.

- To understand the barrier formation process during fabrication of a lipid-based drug permeation model.

- To realize single cell Raman imaging on the subcellular level and to visualize the uptake of nano-sized drug delivery systems by cultured human cells.

3 Results and Discussion

3.1 Elucidating the Impact of Drying on Drug Distribution and Release in Wet-Extruded Pellets by Raman Imaging

Drying is a standard unit operation during the fabrication of solid oral dosage forms. Various types of equipment such as fluid-bed dryers, freeze dryers, or ovens are available for this manufacturing step. Drying, however, does not only remove any remaining solvent, it can also severely affect the API distribution within a dosage form.

In the presented studies, drying is performed to remove the solvent which has been applied during the fabrication of ibuprofen loaded calcium stearate pellets by wet extrusion and subsequent spheronization. Migration of dissolved API molecules is prone to occur as they follow the granulation liquid until recrystallizing when the granulation liquid evaporates. This intragranular migration can significantly influence the *in vitro* dissolution profile of the API, which represents a very critical parameter as only a stable and reproducible API release from the delivery system enables a safe and effective drug therapy. Here, the effect of different drying methods, diverse drying temperatures and varying API incorporation strategies on intragranular drug distribution patterns were investigated by chemical imaging to elucidate the correlation between drug distribution patterns and the obtained drug release profiles.

The most plausible option to study drug distribution is to visualize the drug within its delivery system. Unfortunately, the pharmaceutical compounds ibuprofen (API) and calcium stearate (matrix forming excipient) are white, thus visually indistinguishable. Thus, an analytical technique is needed which enables component discrimination and depiction within the pellet based on a unique feature such as the molecular structure. These analytical requirements are precisely fulfilled by confocal Raman microscopy. Both ibuprofen and calcium stearate show a unique peak pattern in their Raman spectra and are consequently distinguishable in chemical maps.

Lyophilization, fluid-bed drying and desiccation were employed drying techniques. Although they represent different drying speeds and consequently different chances for API migration, Raman microscopy investigations showed a random API distribution within the pellet. No location pattern could be linked to a specific drying technique. Contrarily, *in vitro* dissolution profiles showed a clear correlation between drying technique and API release rate in decreasing order from lyophilization to desiccation. Thus, it was not the drug location but the internal structure of the pellet determining the drug release rate here. The so-called microstructure of the pellet was previously depicted in electron microscopy images showing a less pronounced internal porous structure for lyophilisation, fluid bed drying and desiccation. Nevertheless, without localizing the API within the pellet matrix an impact of drug distribution on the dissolution rate cannot be excluded as different drying speeds potentially entail varying API migration. Whereas electron microscopy images show the pore distribution, it lacks the capability to discriminate between API and excipient. Here, analysis can highly benefit from confocal Raman microscopy as the technique fills the analytical gap of differentiating the white compound in the delivery system. Finally, based on Raman images, it can be concluded that the *in vitro* dissolution profile is not determined by the drug location but is only determined by the microstructure as the latter is a strong function of the drying process itself.

The effect of different drying temperatures (20 – 60 °C) on ibuprofen release and spatial distribution in tray dried calcium stearate pellets were quite contrarily to observations of

different drying techniques. Pellets dried at 20 °C show the highest ibuprofen release rate. All other drying temperatures led to a dramatic decrease in API dissolution rates (Figure 7). Opposite to Raman investigations in the first study, here a unique distribution pattern of ibuprofen for each drying temperature was captured. The most extreme difference was observed for the two opposing drying temperatures. At 20 °C an API corona covering the pellet surface was observed, whereas fast drying at 60 °C resulted in a homogeneous API distribution throughout the pellet cross section (Figure 7). In between drying temperatures entailed a gradual change in API distribution showing an intermittent lamellar formation. In any case, the API was detected with chemical selectivity irrespective of the distribution pattern and was precisely differentiated from the spectral pattern of calcium stearate. Thus, due to valuable results from Raman analysis the correlation of API dissolution and its intragranular distribution

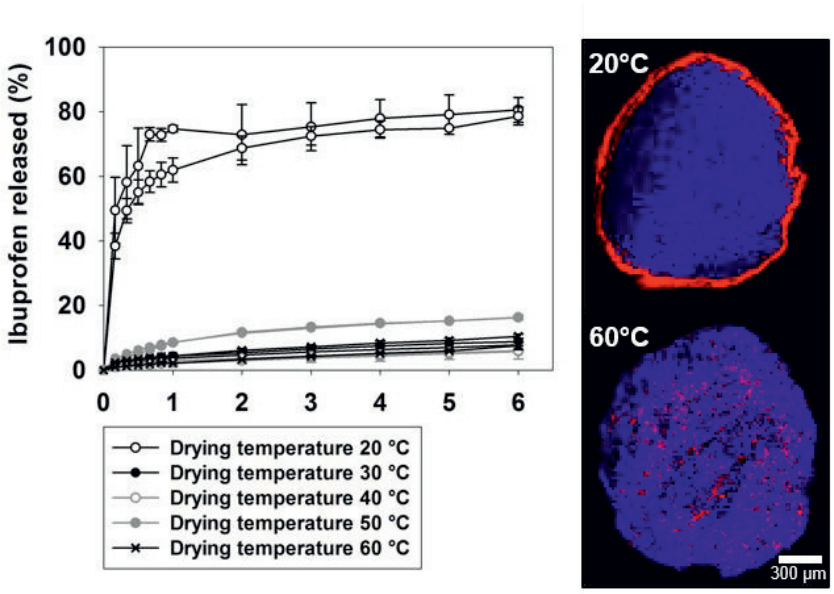

Figure 7. Correlation between different API release rates and drying temperature dependent drug localization within the delivery system.
Reprinted from International Journal of Pharmaceutics, 478, S. Schrank, B. Kann, E. M. Saurugger, M. Hainschitz, M. Windbergs, B.J. Glasser, J. G. Khinast, E. Roblegg, The Effect of the Drying Temperature on the Properties of Wet-Extruded Calcium Stearate Pellets: Pellet Microstructure, Drug Distribution, Solid State and Drug Dissolution, 779-787, Copyright (2014), with permission from Elsevier. [104]

was proven to be a function of the drying temperature. Results from Raman investigation of drug distribution were similar when API was either dry blended with the excipient or dissolved in the granulation liquid during manufacturing and the pellet was subsequently dried at different temperatures. Yet, dissolving the API in the granulation liquid led to an API depleted center which was not found for pellets with API included in the dry blend when low drying temperatures were applied. Further, high drying temperatures resulted in a more homogeneous API distribution throughout the pellet. However, a few agglomerates were observed. Agglomerates in pellets manufactured by incorporating API as powder were larger than in the counterpart formulation.

Overall, confocal Raman microscopy filled the analytical gap to exclude or prove the dependency of *in vitro* dissolution rates on API distribution. Thereby, the influence of drying on

final pellet properties was successfully elucidated. The technique substantially helps to meet quality criteria of solid dosage forms by gaining a deeper understanding of how standard fabrication processes impact final drug product properties. Further, it shows great potential to be implemented for the rational design of tailor made dosage forms.

This chapter refers to the following publications:

S. Schrank, **B. Kann**, M. Windbergs, B. J. Glasser, A. Zimmer, J. Khinast, E. Roblegg; Microstructure of Calcium Stearate Matrix-Pellets: A Function of the Drying Process. *J. Pharm. Sci.* 2013,102:3987-3997.

S. Schrank, **B. Kann**, E. Saurugger, H. Ehmann, O. Werzer, M. Windbergs, B. J. Glasser, A. Zimmer, J. Khinast, E. Roblegg; Impact of Drying on Solid State Modifications and Drug Distribution in Ibuprofen-Loaded Calcium Stearate Pellets. *Mol. Pharmaceutics*. 2014;11:599-609.

S. Schrank, **B. Kann**, E. Saurugger, M. Hainschitz, M. Windbergs, B.J. Glasser, J. Khinast, E. Roblegg; The Effect of the Drying Temperature on the Properties of Wet-Extruded Calcium Stearate Pellets: Pellet Microstructure, Drug Distribution, Solid State and Drug Dissolution. *Int. J. Pharm*. 2015;478:779-787.

3.2 Investigating Drug Delivery Systems with Structured Surfaces – Overcoming the Pitfalls of a Confocal Setup

The majority of pharmaceutical samples does not express smooth but rather structured surface areas, which either represent the exterior sample surface or an artificial cross section. Here, analysis with confocal Raman microscopy is hindered as spectra can only be recorded from one focal plane. Consequently, sample analysis will be incomplete, as a structured surface cuts through many focal planes. Therefore, samples are often altered by invasive methods such a polishing to create a smooth and even sample surface for valuable analysis. This manipulation potentially changes the original composition and falsifies analytical results due to smearing effects. Nevertheless, surface analysis can provide important information about fabrication processes among others. Process parameters potentially have a high impact on sample characteristics such as differing component distribution ratios between outer surface and the sample's interior. In this context, it would be highly desirable to establish an analytical approach benefitting from label-free and contactless confocal Raman analysis without changing the surface conditions of the sample. Here, a novel approach in the pharmaceutical context is realized for the first time by combining confocal Raman microscopy with a technique termed optical profilometry to overcome these limitations of a confocal setup.

Optical profilometry is based on irradiating the sample with white light and collecting the reflected light through a sensor probe. Within this probe is a hyperchromatic lens assembly. All lenses have a distinct chromatic error. White light is composed of different colors (different wavelength), and each color has a unique focal distance. When the reflected light passes through the pinhole in the probe, only the color in focus is detected (Figure 8A). This color represents the distance between the probe and the sample surface and can be translated into topographic height differences creating a surface map (Figure 8B). With this background information, Raman spectra of the same area can be subsequently recorded and the microscope focus is automatically positioned at the sample surface facilitating all-encompassing analysis. Generally, the resulting false color Raman image is a two dimensional depiction of the sample. However, when superimposing the topographic profile with the false color Raman image, an image which is spatially resolved in three dimensions is obtained (Figure 8C).
This straightforward approach bears great analytical potential for the investigation of today's complex pharmaceutical samples expressing various surface geometries. Their fabrication process can lead to numerous modifications within the delivery systems, which potentially affect the therapeutic efficiency. As changes of a compound itself often go along with a change in the respective Raman spectrum, Raman microscopic investigations are favorable as changes within a sample, which are not based on spectroscopic changes such as component redistributions, can be observed simultaneously. By generating topographic profiles of the sample prior to Raman analysis, surface structures would not limit the applicability of confocal Raman microscopy any longer. From the available broad spectrum of pharmaceutical dosage forms four different carrier systems namely extrudate, compacted solid dispersion, lyophilisate and spray dried particles have been exemplarily investigated using the introduced approach. Moreover, besides solely challenging the practicability of the approach it was even implemented into complex study designs.

Extrudates, an opaque solid oral dosage form, are often also intermediate products in pharmaceutical production which are mainly processed into pellets. Thus, a thorough understanding of the initial solid dosage form is of vital importance for the evaluation of subsequent processing steps like spheronization. However, due to the cylindrical morphology

of the extrudate, confocal Raman microscopy analysis has so far been restricted to the investigation of cross sections as analysis of the exterior surface has been impaired by the curvature. Nevertheless, the interior component distribution does not necessarily reflect the exterior ratio due to the manufacturing procedure. Here, analytics can benefit from the introduced combinatorial approach. The curvature and smoothness of the extrudate's exterior were captured in a topography profile showing a symmetric gradient of the color scale, which demonstrates the precise functioning of the sensor probe. Raman mapping of the curved surface was successfully performed in a subsequent analytical step. Furthermore, the interior of the extrudate represented in a cross section was portrayed in a color-coded chemical image as well. By comparing the Raman maps depicting the exterior and interior component distribution no differences were observed for the API embedded in the lipid matrix of the extrudate. Therefore, the fabrication process yields a homogeneous ratio of API and matrix former in this particular case. Nevertheless, the combined analytical approach is suited to detect such inconsistencies and the visual presentation of analytical results enables immediate discussion with researchers which are newly introduced to the technique.

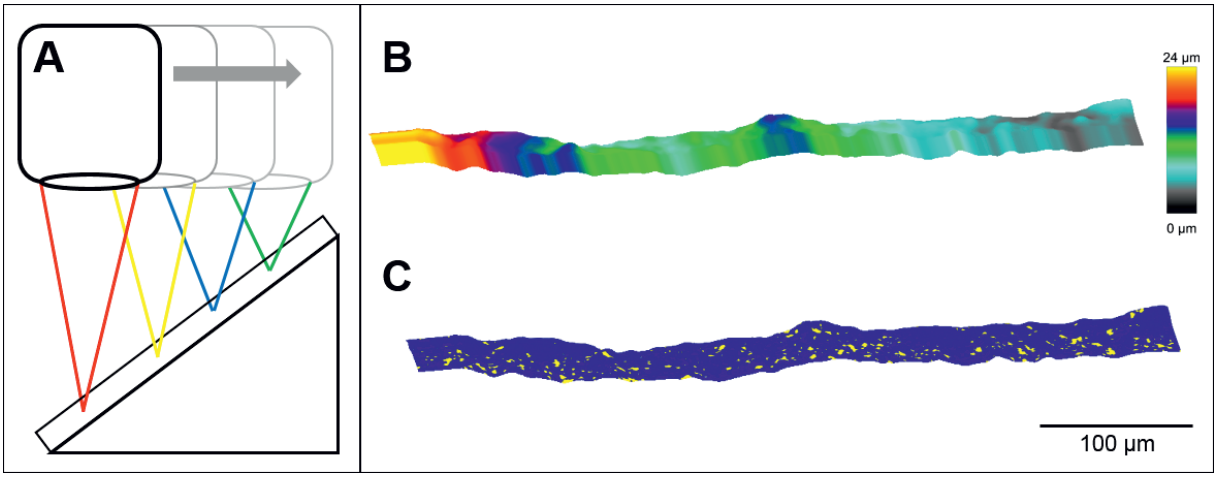

Figure 8. Sketch of the working principle of the chromatic sensor and combination with results from Raman analysis. A) An incline is scanned by the sensor and at each position a different distance based on the wavelength of the reflected light is detected. B) Topography profile of a bisected compact. C) Overlay of topography profile with respective false color Raman image depicting high degree of drug dispersity (yellow) due to cogrinding.

Besides smooth but curved surfaces exhibited by extrudates, pellets, capsules or tablets as a result of the fabrication process, another frequent surface geometry is an extremely irregular, highly structured area displayed by lyophilisates, powder beds or manually bisected dosage forms to access the sample's interior. This surface structure is even more challenging for the combination of optical topography and confocal Raman microscopy.

In order to verify if the combined analytical approach can cope with such a fragile, highly irregular structure a lyophilisate with a protein in its active and inactive form was fabricated. Lyophilisation is a widely used technique to stabilize proteins which gain more and more impact in drug therapy. Their pharmacological activity however highly depends on the secondary structure conformation, which is prone to undergo changes easily. This conformational change can be spectroscopically detected by a shift in the so-called amide I band [105, 106], which is located at 1500-1800 cm^{-1} arising due to C=O vibrations of the amide groups in the backbone of the peptide. [105-109] Unfortunately, the stabilizing process itself induces stress to the

system and can still lead to structural changes in the proteins secondary structure. Consequently, this step has to be closely monitored. However, the precise detection of this single marginal spectral shift to identify the protein conformation represents an additional analytical challenge. By rasterizing the identical grid of a predefined surface area of the lyophilisate, a spatially resolved location map of native and thermally denatured protein has successfully been portrayed in a merged topography and Raman image. Consequently, the novel technical combination is neither limited to challenging irregular surface structures nor to valid component discrimination by using marginal spectral differences for chemical imaging.

Improving drug solubility and bioavailability is of significant interest in pharmaceutical sciences, as the incidence of new drug candidates showing poor water solubility is increasing. A possible strategy to enhance the drug dissolution rate is to fabricate a solid dispersion by cogrinding, where a poorly water-soluble drug is embedded in a hydrophilic carrier.
Here, a solid dispersion of griseofulvin (10%) and mannitol, a hydrophilic sugar alcohol, was fabricated by continuous cogrinding. To elucidate the mechanism for enhanced dissolution of the drug, four different physical mixtures of the same components in different grinding states were analyzed in parallel. Comparing the dissolution profiles of the five formulations the lowest dissolution rate was observed for the physical mixture comprising both components unground, and a 10fold higher rate for the coground formulation. Here, the dissolution rate was even higher when compared to the physical mixture containing both components ground. It was excluded that the observed accelerated dissolution rate is related to any modification of the physical form (crystalline structure) of drug or excipient. However, enhanced dissolution was linked to drug particle size, raised surface free energy as well as increased bulk dispersity of the drug. Especially, the latter finding was solely driven by Raman analysis as both components were optically indistinguishable white powders. Characteristic Raman peaks for griseofulvin (1710 cm^{-1}) and mannitol (881 cm^{-1}) were identified for spectroscopic discrimination of the two compounds. The drug dispersity on the exterior was mapped without complication, as the compacts exhibited a smooth surface. To access the interior, the compacts were manually broken resembling a highly structured cross-section surface necessitating the acquisition of a topography profile prior to Raman analysis (Figure 8B). The superimposed images visualize the interior drug dispersity in an artificial but unaltered surface of the compacts (Figure 8C). Overall, the exterior and interior drug dispersity for each compact was the same. However, the comparison of the coground formulation and the four physical mixtures shows qualitative differences in drug dispersity. Whereas griseofulvin is rather homogeneously distributed in the coground formulation, the drug particles tend to agglomerate in the physical mixtures. When ground griseofulvin was used the tendency was lower than for unground drug. This observation was confirmed by image analysis.
Overall different factors affecting the enhanced dissolution of griseofulvin from a solid dispersion were investigated and discussed in this study. Especially, investigations of the drug's bulk dispersity played a key role in elucidating aspects of the underlying mechanism of dissolution enhancement. As these conditions can only be evaluated upon visualizing the drug in the excipient matrix with high resolution, investigations benefitted tremendously from the analytical capabilities of confocal Raman microscopy in this case.

Spray drying has become a widely esteemed technique for the fabrication of nano- and micrometer sized particles for drug delivery. Due to the small size of the particles, the optical limitations of a confocal Raman microscope may impede analysis of individual particles. However, to gain a deeper understanding of the spray drying process in terms of component distribution in the particle bed the technique is still favorable. Here, the influence of the polymer poly-(ε-caprolactone) on drug distribution during particle preparation via spray drying was

investigated. Therefore, submicron particles composed of dexamethasone (API) and sodium deoxicholate were fabricated in the presence and absence of the polymer. The three compounds can be discriminated by distinct peaks in the respective Raman spectra. The rough surface of the particle powder was virtually corrected by recording topography profiles prior to Raman analysis of the same sample area. In both cases the homogenous distribution of the drug dexamethasone is portrayed within the respective particle bed thus, the use of poly-(ε-caprolactone) during the spray drying process does not affect the dexamethasone distribution. As all components are detectable in every recorded Raman spectrum, the overlay of the individual false color Raman images result in a mixed color image.

In summary, various samples have been successfully visualized with the novel analytical approach of combining confocal Raman microscopy with optical profilometry. After successful investigations of designed pharmaceutical samples, the combinatorial approach was implemented in studies to elucidate drug release mechanisms and drug distribution. Neither, different morphologies with a smooth surfaces or highly irregular, fragile structures were a hindrance nor did the sample composition of different chemical compounds or molecular conformations impede precise analysis. Thus, the complementary techniques can cope with diverse sample specifications. Consequently, the straightforward approach is valid for a wide use in pharmaceutical research.

This chapter refers to the following publications:

B. Kann, M. Windbergs; Chemical Imaging of Drug Delivery Systems with Structured Surfaces – a Combined Analytical Approach of Confocal Raman Microscopy and Optical Profilometry. *AAPS J.* 2013;15:505-510.

C. Muehlenfeld, **B. Kann**, M. Windbergs, M. Thommes; Solid dispersions Prepared by Continuous Cogrinding in an Air Jet Mill. *J. Pharm. Sci.* 2013,102:4132-4139.

T. C. Beber, D. F. Andrade, **B. Kann**, M. C. Fontana, K. Coradini, M. Windbergs, R. C. R. Beck; Submicron Polymeric Particles Prepared by Vibrational Spray-Drying: Semisolid Formulation and Skin Penetration/Permeation Studies*. Eur. J. Pharm. Biopharm.* 2014;88:602-613.

3.3 Novel Insight into the Development Process of a Lipid-Based Drug Permeation Assay by Raman Imaging

The oral route is still predominant for drug application into the human body as it is convenient and widely accepted by patients and thus, yields sufficient therapeutic compliance. As the drug needs to permeate across the intestinal mucosa to enter the human body, satisfactory biopharmaceutical properties are mandatory to reach therapeutic concentrations. For the evaluation of drug permeability during development of novel oral therapeutics different cellular and non-cellular based *in vitro* assays are available.

The prevalent cell culture-based model for permeability studies is the Caco-2 cell monolayer. [110] These epithelial colon cells generally show good barrier properties and structural and biological characteristics of the intestinal epithelia are reflected quite well. [111, 112] However, due to their biological nature, these models are affiliated with variations in stability, properties and reproducibility of analytical results. [113] Furthermore, significant costs and long cultivation times damp the attractiveness of cellular models for high throughput screenings.
However, during drug discovery permeability characteristics of new chemical entities are frequently tested on a large scale to select and optimize lead candidate drug molecules. Here, models based on artificial membranes offer a suitable alternative as they are relatively cheap and provide a comparatively high throughput capacity. Nevertheless, in contrast to their cellular-based counterparts these artificial models are only valid for passive diffusion. The first artificial assay termed parallel artificial membrane permeability assay (PAMPA) was developed by Kansy et al. [114] It comprises a hydrophobic filter saturated with a mixture of lecithin and organic solvent and is available in numerous variations today. [115-119]
More recently another assay called phospholipid vesicle-based permeation assay (PVPA) was developed to study passive permeability of drugs. [120, 121] Here, the use of organic solvents was omitted as they potentially interact with the filter substrate. Liposomes were deposited on a porous filter accumulating inside the pores and on top of the filter. The phospholipid barrier was stabilized by solvent evaporation and a subsequent freeze-thaw cycle.
Inspired by this non-cellular based assay with a non-fluid barrier, an artificial membrane assay termed modified PVPA barrier was developed. The fabrication involves a complex sequence of coating steps to cover a porous membrane with lipid. The modified PVPA model is supposed to present a suitable alternative to cell culture models used in combined dissolution and permeation devices. These systems have been created to investigate correlations and possible dependencies of drug dissolution and subsequent permeation through a cellular barrier. [122-125]

To monitor the fabrication process as well as stability against medium the analytical technique should be capable to differentiate between compounds. However, the sample should not be altered or destroyed to enable the observation of subsequent development stages in the same sample to gain a thorough understanding of the overall fabrication process.
During the development of the original PVPA Flaten et al. [120] chose confocal fluorescence microscopy to characterize the phospholipid barrier formation. Therefore, a dye was incorporated into the liposomes, whereas the filter was labeled by bathing it in a dye solution. This approach is feasible as it is non-destructive and detects the labelled components chemically selective. Nevertheless, only a small fraction of the entire filter area was investigated and the repetitive investigation of the same sample might be challenging. Especially the dye labeling the membrane is prone to migrate during subsequent fabrication steps, therefore in repeated analysis of a successive step entailing false interpretation. Further,

due to the susceptibility to photobleaching, fluorescence microscopy images of consecutive steps might potentially not show compounds from the previous steps as the fluorescent dye loses part of its activity due to laser irradiation. Confocal fluorescence microscopy is generally suited, however not ideal for the visual examination of the development process of a lipid-based membrane model for drug permeation testing.
Here, confocal Raman microscopy takes the analytical possibilities one step further. Like confocal fluorescence microscopy it is chemically selective, thus the lipid component and the filter can be spectrally discriminated, as a visual differentiation due to similar optical properties is impossible. Yet, unlike fluorescence microscopy labeling is not required, as the technique is based on the detection of scattered light from the sample itself. The scattering ability is ultimately associated with the molecular structure of each compound and will not change due to continuous fabrication and analysis.

In previous chapters, chemical imaging was introduced for the investigation of external surfaces and artificially created surfaces by sample bisection of opaque solid dosage forms. For the development of the modified PVPA barrier the analytical demand differs. Here, the stepwise assembly of the permeation barrier is of interest. As the application of lipid not only changes the lateral coverage of the filter membrane but also the coating thickness, investigations in different planes namely lateral (Figure 9A) and vertical (Figure 9B) are requested. Further, observations of the membrane pores as they represent the major permeation route for drug molecules are important. As the pores are tiny in comparison to the entire membrane, the sample scale varies (Figure 9C). Finally, the stability of the lipid-based barrier against medium in the permeation apparatus has to be screened.

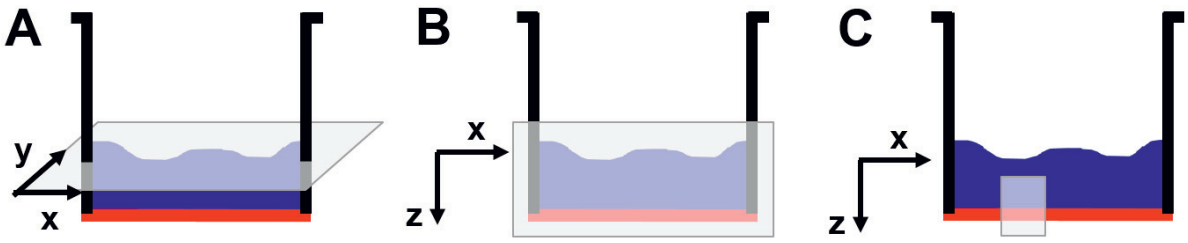

Figure 9. Schematic overview of the optical planes in lateral (A) and vertical (B, C) direction to monitor the development process of the modified PVPA barrier.

Here again, the concerned components are visually indistinguishable. However, lipid and filter membrane are not opaque but semitransparent. This allows the laser light to penetrate into and through the sample, thereby scattered light from below the sample surface can be collected. Consequently, the concept of chemical imaging can be extended as the non-destructive acquisition of virtual cross section images becomes feasible (Figure 9B, 9C).
Color-coded images based on Raman analysis of the permeation barrier formation depict the continuous lipid coverage of the membrane with each coating step for the first time. After applying the first lipid coat, a lipid-free ring remained between the center and the rim of the membrane. Two further coating steps were necessary until the membrane was fully covered with lipid and the permeation barrier was thus integer. Two additional coating layers serve to stabilize the coating. The formation of the coating led to a patterned lipid surface necessitating a virtual correction by optical topography prior to Raman analysis. Raman images of vertical cross sections proved a varying coating thickness across the diameter of the membrane which was hypothesized based on results from the coating formation. The coating formed a

prominent wavelike pattern on the supporting membrane. Furthermore, close-up Raman images of the membrane pores from three dimensional analysis depict an alike morphology with distinct boundaries for all investigated pores. They were all filled with lipid after coating without any detectable changes to their morphology.
Finally, coating stability was investigated by chemical imaging in virtual cross sections when exposed to liquid medium as the barrier integrity is a decisive factor during the validation of permeation experiments. The coating remained integer for at least 18 hours, as no lipid-depleted areas of the membrane were observed.

Altogether, confocal Raman microscopy is feasible for the analysis of all critical development steps of the modified PVPA barrier. The development and fabrication processes benefit remarkably from confocal Raman analysis as their first time visualization gave significant insight. Overall, the concept of chemical imaging is transferred from surface analysis to the acquisition of depth scans in vertical cross sections in this chapter, enlarging the analytical capabilities of the confocal Raman microscopy to all three axes.

This chapter refers to the following publication:

S. P. Gantzsch*, **B. Kann***, M. Ofer-Glaessgen, P. Loos, H. Berchtold, S. Balbach, T. Eichinger, C.-M. Lehr, U. F. Schaefer, M. Windbergs; Characterization and Evaluation of a Modified PVPA Barrier in Comparison to Caco-2 Cell Monolayers for Combined Dissolution and Permeation Testing. *J. Controlled Release*. 2014;175:79-86.
***** *both authors contributed equally and are listed in alphabetical order*

3.4 Non-Invasive Visualization of Nanoparticle Uptake in Human Cells

Not only the rapid development of modern drug carrier systems but also frequent use of nanosized particles in daily consumer products as well as their fabrication have raised intensive interest about their fate in the human body. Consequently, research focuses on their interaction with and potential uptake by cells. This is primarily due to an emerging knowledge about complex relations of diseases as well as to potential toxicological effects on the subcellular level. In this context, appropriate analytical investigations are of high importance to gain sufficient knowledge about cells, carrier systems or pure particles and the extent of their interaction.

Light microscopy is routinely employed in any cell culture lab for a quick evaluation of confluence levels and morphology of cultured cells. However, it is not suited to gain detailed structural information of cells nor of particulate systems on the nanometer scale. In this regard, the combination with a spectroscopic technique presents a valuable analytical approach for investigations on the subcellular level. Fluorescence microscopy is still the state-of-the-art technique for cell visualization and multiple fluorescent marker molecules have been introduced making chemically selective visualization of cellular structures as well as carrier systems and other particles feasible. Nevertheless, among other drawbacks, the introduction of marker molecules potentially impacts any possible interaction behavior. Here, vibrational spectroscopic techniques are an interesting alternative as complications arising with the introduction of a label become irrelevant.

Prior to any interaction studies, a profound visual characterization of the concerned cell line is inevitable. Here, Raman analysis faces another challenge. First, cells are too small to be seen with the naked eye. Thus, a light microscopy is needed for a first evaluation of the sample (Figure 10A). More important, cells are biological samples. Consequently, their Raman scattering activity is inherently weak in comparison to chemical compounds. Nevertheless, the technique is sensitive enough to detect spectral differences for the differentiation of subcellular compartments. False color Raman images of epithelial cells originating from the oral buccal mucosa utilized in the following publication picture the nucleus very distinct in the cytosol (Figure 10 B-D). The discrimination of the compartments in the Raman data is based on spectral differences between cell nucleus and body which mainly arise from the phosphate groups and the ring breathing modes of pyrimidine bases of the DNA backbone. As discussed in previous chapters, the optical properties of the sample determine the penetration behavior of the irradiating laser light and therefore, the location of the imaging planes in the sample. Cell layers generally represent transparent optical properties. Hence, the laser beam can penetrate through the entire cell body and virtual cross section images of the cell body can be acquired as well (Figure 10E). Equivalent analytical results to fluorescence microscopy investigations using the dyes Hoechst 33342 and Calcein AM (both Invitrogen, Austria) were obtained and are discussed in detail in the publication. Similarly, the feasibility of Raman microscopy to be equal to fluorescence microscopy depiction of cellular compartments is discussed in literature for other compartments as well. [56] The combination of optical properties and a weak Raman scattering activity of cells requires a thorough understanding of the sample preparation. Individual cells without a substrate cannot be placed on the microscopic stage. The substrate is generally a plastic dish and shows a scattering activity overruling any signal from the cell due to its optical properties. Here, other substrates such as calcium fluoride glass proved itself to be superior to standard dishes as their Raman bands to not interfere with signals originating from the sample and can easily be subtracted from the data set.

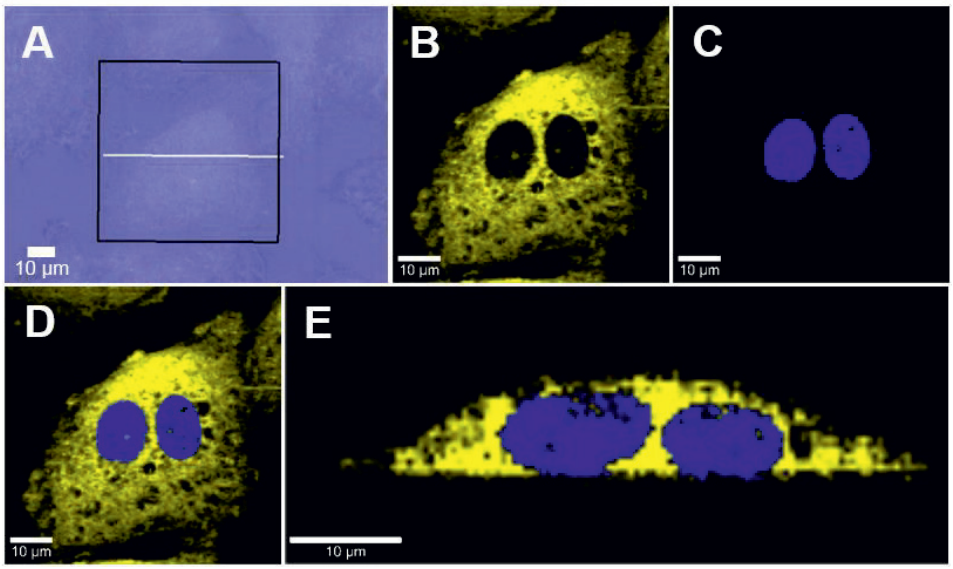

Figure 10. Depiction of an oral buccal mucosa cell in different perspectives. A) Light microscope image showing the area of Raman analysis in lateral (black) and vertical direction (white). False color Raman images of cytosol (B), nuclei (C), and combined images of lateral (D) and vertical cross section (E) investigation.

The depiction of the cell nucleus is beneficial to gain a first impression if potentially genotoxic substances such as titanium dioxide (TiO_2) an inorganic, white pigment enter the cell nucleus. As TiO_2 shows Raman bands only below 700 cm^{-1} the material can be easily distinguished from the cellular environment. Moreover, the polymorphic form of the utilized TiO_2 is simply verified by spectral bands of the material without the necessity of further analysis. After incubating cells with TiO_2 particles, they can be localized in lateral Raman images. However, it cannot be differentiated between internalized particles and particles settled on top of the cells. Thus, virtual cross section images were acquired to distinguish these two possibilities. In fact, Raman images depict both situations where internalized TiO_2 particles were even found in the nucleus of the oral buccal mucosa cells. This concept of analytical differentiation is not only beneficial when the interaction of engineered particles with cells is in focus but also of particular interest for investigations of cells interacting with drug delivery systems. Here, depicting the location and fate of the carrier will contribute valuable insight into the successful drug delivery to the intracellular target structure.

Nevertheless, recording of Raman spectral data sets with high resolution is often time consuming, as long integration times have to be taken into account due to the low scattering intensity of biological samples. Upon the investigation of endpoints concerning particle uptake for example, time is not a critical parameter. This changes when various time points are of interest and temporal resolution for *in situ* experiments is needed. Here, anti-Stokes Raman scattering (CARS) microscopy is a suitable alternative. As only one specific frequency is probed at a time, images are acquired within seconds. Hence, consecutive image acquisition at shifting frequencies facilitates a versatile depiction of different molecular structures in the sample. In general, the best contrast in CARS images is generated in the high frequency region where the CH-stretch vibrations are arising in the Raman spectrum.

Lipid-core nanocapsules are a well-characterized drug delivery system suited for intracellular delivery of poorly water soluble drug molecules. [126, 127] They are composed of a polymeric shell encapsulating a lipid core. This core-shell structure makes the delivery systems well

suited for CARS analysis as the concentrated lipid in the core can be visualized with high contrast against the cellular surrounding (Figure 11). Images at the two frequencies of interest namely 2928 cm^{-1} for proteins (Figure 11A) and 2845 cm^{-1} for lipids (Figure 11B) are first acquired using the CARS microscope. In order to solely depict the lipid-core nanocapsules, the non-resonant background in the lipid image has to be eliminated. Therefore, the signals from an image acquired at a different frequency than the lipids representing the non-resonant signals are subtracted from the lipid image. As are result the lipid-core nanocapsules can be depicted in false color here the red channel (Figure 11C). Cells naturally contain lipids themselves, however, due to the concentration of lipids in the nanocapsule core a by far more intense CARS signal is generated overtopping the natural cell lipids which are only visible as a light hue. At last, the red over white image can be merged with the image depicting the cell body to visualize the lipid-core nanocapsule locations within the cell (Figure 11D).

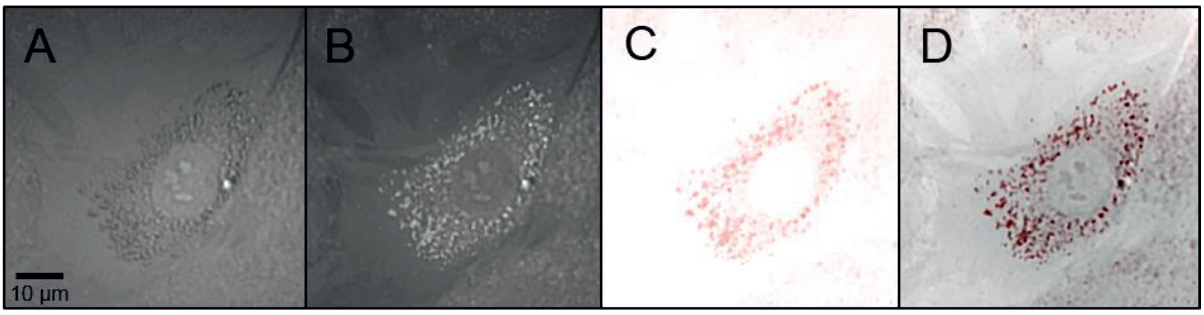

Figure 11. Exemplary process of visualizing lipid-core nanocapsules within the cell body of a chondrocyte in a false color image using CARS microscopy data. Cell imaged by probing proteins at a frequency of 2928 cm^{-1} (A) and lipids at a frequency of 2845 cm^{-1} (B). C) Background free image of the lipids depicted in the red channel. D) Overlay image depicting the merge of lipids in false color within the cell body.

The analytical focus regarding the application of CARS microscopy in this study was to investigate if lipid-core nanocapsules are engulfed over time by chondrocytes while they were kept under standard cell culture conditions. Chondrocytes play an important role during the emergence of osteoarthritis. Lately, resveratrol and curcumin, two natural substances with anti-inflammatory and anti-oxidant activity, were shown to be effective for treatment of this disease. Due to their poor water solubility and their intracellular target, lipid-core nanocapsules represent a promising choice as delivery system here. By effectively tracing the strong anti-Stokes scattering signal of the lipid core during exposition of chondrocytes with nanocapsules, cellular uptake was successfully monitored. The natural cell lipids were not interfering as the signal contrast of the nanocapsules was significantly higher. Besides investigating the general uptake and location in the cell body, the influence of uptake inhibitors on engulfment behavior was monitored as well in order to gain more detailed insight in the underlying cellular uptake mechanism. The analytical concept was transferred to another study, where the skin application of the discussed drug delivery system was centered. [128] Here, additionally to investigating the penetration depth into different skin layers, the chance of nanocapsule uptake by skin cells was questioned to find out if drug molecules potentially reach intracellular targets or if they are released intercellular. Again, CARS microscopy data visualized the intracellular accumulation of lipid-core nanocapsules.

In this section, it is shown that confocal Raman microscopy is also well suited for the analysis of cell culture samples. Equal analytical performance is demonstrated in comparison to

confocal fluorescence microscopy. Further, while investigating interactions between cells and particles, data regarding physical characterization of the particles can be retrieved. Thus, analytical characterization by Raman microscopy is straightforward without necessitating other techniques. Additionally, utilization of non-linear variations add to the analytical portfolio as time consuming investigations can be omitted while maintaining chemically selective analysis with high resolution.

This chapter refers to the following publications:

B. Kann, B. J. Teubl, E. Roblegg, M. Windbergs; Label-Free *In Vitro* Visualization of Particle Uptake into Human Oral Buccal Epithelial Cells by Confocal Raman Microscopy. *Analyst*. 2014;139:5069-5074.

B. Kann, C. Spengler, K. Coradini, L. A. Rigo, M. L. Bennink, K. Jacobs, H. L. Offerhaus, R. C. R. Beck, M. Windbergs; Intracellular Delivery of Poorly Soluble Polyphenols - Elucidating the Interplay of Self-Assembling Nanocarriers and Human Chondrocytes. *Anal. Chem.*, 2016;88:7014-7022.

4 Conclusions and Outlook

This thesis demonstrates the successful implementation of confocal Raman microscopy in pharmaceutical sciences as a key technique for label-free analysis of classic solid dosage forms up to cellular interactions with nanoparticles.

The first chapter focused on the application and analytical importance of chemical imaging in studies investigating the effect of drying on final properties of ibuprofen loaded calcium stearate pellets. The varying drug release profiles as a result of different drying techniques and temperatures during fabrication were finally elucidated, because the drug was localized within the pellet using confocal Raman microscopy as the key analytical technique. Differing drug distribution patterns were depicted in false color chemical maps of pellet cross sections. They strongly depend on the drying temperature, but not on the drying technique. Based on Raman analysis, it was found that drug release profiles only correlate to drug distribution determined by drying temperature.

In the second chapter a novel analytical approach was pursued to overcome the limitation of confocal Raman microscopy analysis, which is impeded by structured surfaces. By combining the technique with optical profilometry, an at first generated topography profile of the sample surface serves as a default setting for the focal point during subsequent acquisition of the Raman spectral data set. Subsequently, the topography profile can be overlaid with the color-coded Raman image to construct a three dimensional image. Alternatively, the Raman image can simply be displayed in two dimensions. The analytical potential of this combinatorial approach was evaluated and challenged in this first time application during the analysis of diverse pharmaceutical samples exhibiting different surface geometries. Thereby, the analytical accuracy and benefit was nicely demonstrated. At last, this combinatorial approach was successfully implemented as a key technique in complex studies with a focus on solid carrier development and drug release mechanisms.

The subsequent chapter introduced Raman analysis to be performed in virtual cross section planes and depth scans in addition to the lateral plane during the investigation of the development process of a lipid-based drug permeation assay. By performing a combination of lateral and cross section Raman scans, the stepwise lipid deposition on the supportive membrane and the resulting successive formation of the permeation barrier was explained for the first time. Further, Raman investigations showed that the barrier is only integer after three coating steps and that the coating itself displays a prominent pattern. The lipid barrier remains stable against liquid medium during permeation testing as proven visually in Raman images, which depict an integer coating. Consequently, Raman analysis is not only a valid tool during development steps but also for the quality control of such systems.

Similarly, the advantage of acquiring Raman spectra along x, y, and z axis of the microscope was demonstrated for cellular investigations. False color images generated in the horizontal plane give a very good overview of cellular structures in oral buccal cells such as nucleus and cytosol. Further, externally applied TiO_2 particles were located. To distinguish between settled and internalized particles, the cell was analyzed in vertical planes. Raman images pictured settled and engulfed TiO_2 particles with some invading the cell nucleus. Consequently, results from Raman analysis serve as intermediate results triggering further investigations on the molecular level with a focus on genotoxic effects of inorganic particles. Despite the low scattering intensities of the cells, label-free analysis was pursued effectively without sacrificing

high precision chemical selective detection as comparative fluorescence microscopy studies proved.

The subsequent study focused on the uptake of lipid-core nanocapsules in human chondrocytes by CARS microscopy for instantaneous visualization. As the lipid in the core of the nanocapsules generates a strong CARS signal, the carrier was successfully traced inside the cell. This is promising for the application of the carrier for intracellular drug delivery. Furthermore, monitoring the effect of uptake inhibitors on the chondrocytes exposed to the carrier by CARS imaging gave insight in the underlying cellular uptake mechanism.

Although confocal Raman microscopy is available as an analytical technique, its application is challenging. Nevertheless, chemically selective sample visualization often provides significant insight, especially when integrated into a complex study design. Here, chemical imaging of drug distribution in a pellet formulation was needed to finally understand the obtained drug release profiles. Or in case of the lipid-based drug permeation model, the formation of the drug permeation barrier was successfully elucidated during development. Consequently, Raman analysis can contribute significantly to the design and fabrication of tailor-made carrier systems or permeation assays. Furthermore, the obstacle of applying confocal Raman microscopy to the analysis of structured sample surface was solved. Here, the combination with optical topography was elementary. The concept was transferred to encompassing investigations. Finally, the long time frame required to analyzing biological samples due to their low Raman scattering intensity was overcome by using a non-linear coherent Raman technique.

Overall, all presented studies benefitted tremendously from chemical imaging, as confocal Raman microscopy provided important analytical results. The introduced concept of chemical imaging was extended continuously from lateral mapping to mapping of structured surfaces and virtual cross section imaging. It concluded in imaging with temporal resolution. The benefit of integrating the technique rather than its sole use as a stand-alone technique was demonstrated. As shown in this thesis, confocal Raman microscopy is well-suited for profound analysis of pharmaceutical samples. It represents a promising and versatile analytical technique, and although confocal Raman microscopy has not become a state-of-the-art technique yet, a continuously growing application in pharmaceutical sciences can be expected.

5 Original Publications

5.1 Microstructure of Calcium Stearate Matrix-Pellets: A Function of the Drying Process

Microstructure of Calcium Stearate Matrix-Pellets: A Function of the Drying Process

S. Schrank, B. Kann, M. Windbergs, B. J. Glasser, A. Zimmer, J. Khinast, E. Roblegg

J. Pharm. Sci. **2013**, 102:3987-3997.

DOI: 10.1002/jps.23707

RESEARCH ARTICLE – *Pharmaceutics, Drug Delivery and Pharmaceutical Technology*

Microstructure of Calcium Stearate Matrix Pellets: A Function of the Drying Process

SIMONE SCHRANK,[1,2,3] BIRTHE KANN,[4] MAIKE WINDBERGS,[4,5] BENJAMIN J. GLASSER,[6] ANDREAS ZIMMER,[3] JOHANNES KHINAST,[1,2] EVA ROBLEGG[2,3]

[1]Institute for Process and Particle Engineering, Graz University of Technology, Graz, Austria
[2]Research Center Pharmaceutical Engineering GmbH, Graz, Austria
[3]Institute of Pharmaceutical Sciences, Department of Pharmaceutical Technology, University of Graz, Graz, Austria
[4]Department of Biopharmaceutics and Pharmaceutical Technology, Saarland University, Saarbruecken, Germany
[5]Department of Drug Delivery (DDEL), Helmholtz-Institute for Pharmaceutical Research Saarland (HIPS), Helmholtz Centre for Infection Research (HZI), Saarbruecken, Germany
[6]Department of Chemical and Biochemical Engineering, Rutgers University, New Jersey

Received 14 May 2013; revised 25 July 2013; accepted 31 July 2013

Published online in Wiley Online Library (wileyonlinelibrary.com). DOI 10.1002/jps.23707

ABSTRACT: Drying is a common pharmaceutical process, whose potential to modify the final drug and/or dosage form properties is often underestimated. In the present study, pellets consisting of the matrix former calcium stearate (CaSt) incorporating the active pharmaceutical ingredient ibuprofen were prepared via wet extrusion and spheronization. Subsequent drying was performed by either desiccation, fluid-bed drying, or lyophilization, and the final pellets were compared with respect to their microstructure. To minimize the effect of solute ibuprofen molecules on the shrinking behavior of the CaSt, low ibuprofen loadings were used, as ibuprofen is soluble in the granulation liquid. Pellet porosity and specific surface area increased during desiccation, fluid-bed drying, and lyophilization. The inlet-air temperature during fluid-bed drying affected the specific surface area, which increased at lower inlet-air temperatures rather than the pellet porosity. The *in vitro* dissolution profiles were found to be a nonlinear function of the specific surface area. Overall, the microstructure, including porosity, pore size, and specific surface area, of CaSt pellets was a strong function of the drying conditions. © 2013 Wiley Periodicals, Inc. and the American Pharmacists Association J Pharm Sci

Keywords: drying; extrusion; dissolution; fluid-bed; lyophilization

INTRODUCTION

Drying is a standard unit operation in pharmaceutical processing with the goal to remove solvents (most often water) from wet materials providing sufficient product stability and enabling further processing. For example, pellets, manufactured by wet extrusion followed by spheronization, still contain a certain amount of liquid after fabrication, and thus require a final drying step. Similarly, the product of high-shear granulation, that is, pharmaceutical granules, is dried in a subsequent step. In literature, it is described that drying of pellets can be performed in various types of equipment, including fluid-bed dryers,[1–20] freeze dryers,[4,10,11,14,16–19,21–28] ovens,[2,4,7,17–19,21,23,26–33] microwave dryers,[7,23] filter-bed dryers, and other individually designed dryers.[34] In the pharmaceutical industry, the fluid-bed drying process is of greatest relevance, as it provides high drying rates, thereby ensuring short drying times and reduced process costs. However, fluid-bed drying may not always yield in desired final dosage form properties. It is well known to the pharmaceutical practitioner that the drying step may considerably alter the pellet's final properties, thus affecting both the excipient structure and the release rate of the active pharmaceutical ingredient (API). As such, the bioavailability of the API in the human body is affected. Nevertheless, only few systematic studies of this unit operation have been published in literature[10,14,21–23,26,27,35,36], and a mechanistic understanding of the impact of drying on pellet properties is still a field of active research.

Excipients swelling in the granulation medium (and thereby taking up liquid) are frequently used for wet extrusion/spheronization, as they ensure suitable rheological properties of the wet mass and the resulting extrudates. The opposite behavior (i.e., shrinkage) occurs upon solvent removal. For example, it was reported that several extrusion/spheronization excipients, including microcrystalline cellulose,[4,7,10,11,14,20–23,36,37] cellulose,[38] pectinic acid,[8] calcium stearate (CaSt),[16] and κ-carrageenan,[12] can swell upon contact with liquid and tend to shrink (to a certain extent) during drying. Moreover, it was observed that the final porosity and the structure of the porous matrix strongly depend on the drying technique and/or drying conditions.[4,10,14,16,17,19,22,23,26,27,34]

With regard to the drying rate, drying processes have two main periods: the constant rate period (CRP) and the falling rate period (FRP). The CRP is characterized by liquid evaporation from the surface facilitated by sufficient liquid transport toward the surface, which in porous media occurs because of capillary pressure gradients with a flow rate following a modified Darcy's law.[39,40] In this period, the surface is still wet, yet the moisture levels are decreasing. Once the liquid recedes into the pores, a drying front develops and liquid evaporation takes place mostly inside the pores. This condition is called the FRP. Subsequently, the vapor is transported through the pores toward the surface via diffusion and convection. In general, the FRP, where the outer shell of the particle is dry, is only observed

Correspondence to: Eva Roblegg (Telephone: +43-316-380-8888; Fax: +43-316-380-910; E-mail: eva.roblegg@uni-graz.at)

Journal of Pharmaceutical Sciences

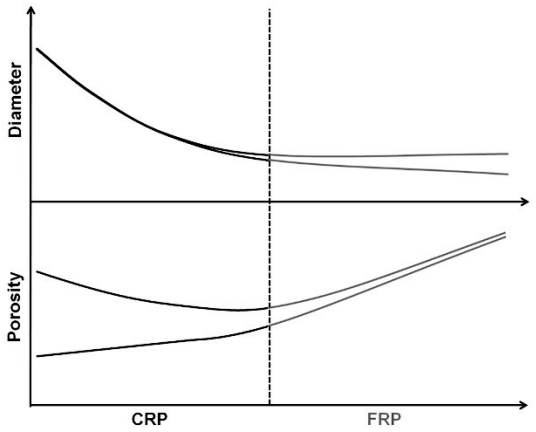

Figure 1. Pellet diameter (upper graph) and pellet porosity (lower graph) as a function of the drying process.

under fast drying conditions. For mild drying conditions, liquid transport to the surface is usually sufficient to keep the surface wet. One further effect is the impact on the temperature: as long as the material is wet the temperature maintains the (low) "wet-bulb" temperature, because of endothermic evaporation. Once the material is dry, it approaches the (higher) temperature of the drying medium (and may soften if the temperature is sufficiently high).

Shrinkage occurs during reduction of the liquid content of a material, as mentioned above. Thus, shrinkage takes place in many materials upon solvent removal, that is, during drying. During the CRP, this shrinkage occurs throughout the entire pellet as the whole pellet is wet, yet the moisture level is decreasing. Even though stress is involved in this process, this effect may be considered small as long as the whole pellet uniformly deforms (shrinks). Once the material is dry, it does not shrink anymore. Hence, as soon as the FRP starts, the outer (dry) region of the pellet resists deformation. If the internal stress overcomes the yield stress of the outer dry shell, the particle still shrinks or deforms irregularly, as often observed in many materials (e.g., organic materials[41]). If the outer shell resists stress, the outer diameter of the pellet remains constant. Then, shrinkage occurs only inside the pellet, associated with an increase of internal porosity. Thus, it was conjectured that the main size reduction of pellets occurs during the CRP, and the internal porosity increases during the FRP. These effects are schematically illustrated in Figure 1. Clearly, the extent of shrinkage determines the pellet's microstructure and in turn the dissolution[17,18,26,27] and compaction behavior.[10,19,27,28,34]

In addition to impacting the microstructure, drying may cause a migration of API molecules that are dissolved in the granulation liquid, leading to nonuniform final API distribution profiles within the pellet.[2] In the literature, it was shown that the API distribution profile can significantly influence the *in vitro* dissolution behavior.[42,43] In nonspherical pharmaceutical granules, API migration was found to be induced by the drying technique.[44] However, different drying conditions (i.e., drying temperature) for the same drying technique do not necessarily affect API migration, most probably because the drying regime does not change.[45] It was even suggested that the burst effect, which is frequently observed during dissolution testing of some delivery forms, derives from API migration during drying and the resulting API accumulation close to the surface.[46] Physicochemical properties, including the API solubility,[47,48] viscosity of the granulation liquid,[47,49] and the excipient's properties[50,51] have an additional impact on the extent of API migration.

The present study addresses the effect of the drying process on the shrinking behavior (and consequently on the microstructure) of the pellet matrix (CaSt in the present case). Pellets were prepared via wet extrusion and spheronization with subsequent drying using three techniques: desiccation, fluid-bed drying (under different process conditions) and lyophilization. As it was assumed that drug migration may influence the shrinking behavior because of osmotic pressure (generated by a concentration gradient after the API moved toward outer regions), a low ibuprofen loading (i.e., 3.5%) was used to prevent interactions. Consequently, the studied model formulation mimics the behavior of swellable extrusion/spheronization matrix excipients during drying, whereas any interactions between matrix shrinkage and API migration are not accounted for.

MATERIALS AND METHODS

Pellet Preparation

The formulation and process parameters were adapted from our previous studies.[16,32] A two-component system based on vegetable CaSt (Werba-Chem GmbH, Vienna, Austria) and ibuprofen (GL Pharma, Lannach, Austria) was used. The drug loading was 3.5% (w/w). CaSt and ibuprofen were dry blended in a TURBULA® T2F mixer (Willy A Bachofen AG Maschinenfabrik, Muttenz, Switzerland) at 50 rpm for 20 min. The blending parameters were optimized in prestudies to ensure drug content deviation of below 5% from the theoretical ibuprofen loading (data not shown).

As it is described in literature that extrusion/spheronization parameters, including the spheronization time,[52] may impact the pellet microstructure, all process parameters throughout wetting, extrusion, and spheronization were kept constant. Thereby, drying-induced changes in the final pellet microstructure could be elucidated. One hundred gram of the powder mixture was manually wetted with 50 g of 50% (w/w) ethanol. Ethanol (50%, w/w) was previously shown to result in favorable pellet properties.[16,32] The extrusion/spheronization process was performed using the same equipment and parameters as previously described.[16] The optimum spheronization time, which provides a narrow size distribution and appropriate sphericity (i.e., above 0.8), was 6 min.

Drying Procedures

After spheronization, three drying techniques were applied:

- desiccation (D) over silica gel at ambient temperature and pressure,
- fluid-bed drying (FB) at two different inlet-air temperatures (20°C and 50°C), and
- lyophilization (L) under vacuum (pressure below 6 mbar) and ambient temperature.

For each drying method, two batches were prepared, and drying was continued until the final moisture content was below 1%. Additionally, the shrinking behavior, that is, reduction

 DOI 10.1002/jps.23707

in pellet outer volume (envelope volume), was determined by measuring the bulk (nonconsolidated) volume of 50 g pellets before and after drying.

For desiccation, pellets were transferred into a flat-bottom bowl with a bed diameter of 17 cm and a height of 0.8 cm. The moisture content was determined as a function of time by measuring the pellets' weight after certain time intervals. The moisture content drop over time was calculated based on the dry pellets' mass.

Fluid-bed drying was performed in a Mycrolab apparatus (Oystar Hüttlin, Schopfheim, Germany) equipped with a compressor to provide a constant inlet airflow of 40 m^3/h. To evaluate the drying profile, samples of 1 g were manually taken every 5 min from the container opening, and the moisture content was determined offline with a moisture halogen analyzer. To exclude any possible physical and chemical interactions between CaSt and ibuprofen at the elevated inlet-air temperature of 50°C, differential scanning calorimetry (DSC) measurements were performed with a DSC 204 F1 Phoenix (Netzsch, Selb, Germany) under nitrogen atmosphere. CaSt and ibuprofen were mixed at a ratio of 1:1 to increase the possibility of interactions. Samples were placed into aluminum pans closed with pierced lids.

Drying via lyophilization was performed in a LYOVAC GT 2 (Steris, Köln, Germany). The pellets were transferred into flat, kidney-shaped bowls, immersed into liquid nitrogen (−196°C) for 15 min prior to drying and were then lyophilized for 24 h.

Pellet Characterization

Pellet-size distributions were evaluated via sieve analyses according to Ph. Eur. 6.0 2.9.38. For further characterization studies, the yield fraction (defined between 1.4 and 1.8 mm) was divided into representative samples with a rotary cone divider. The shapes and sizes of at least 500 pellets were analyzed using the dynamic image processing system QicPic (Sympatec GmbH, Clausthal-Zellerfeld, Germany) operated with the dry dispersing unit Rhodos/L. Size (Ferret's diameter) and shape (aspect ratio, AR) distributions (Q_3) were determined. Each batch was analyzed in triplicate.

The pellet microstructure was characterized in terms of pellet density, specific pellet inner-surface area, and pellet porosity. Pellet density and porosity were determined via helium pycnometry and mercury porosimetry, as described in our previous work.[16] The specific surface area was evaluated via Brunauer Emmett Teller (BET) adsorption method using the ASAP 2000 (Micromeritics, Norcross, Georgia) system and nitrogen as analytical gas. Prior to measurements, samples were degassed under vacuum. Nitrogen adsorption occurred at −196°C (temperature of liquid nitrogen), and the volume of nitrogen adsorbed was recorded over a range of relative pressure between ≈0.05 and ≈0.2.

A scanning electron microscope (Zeiss Ultra 55; Carl Zeiss NTS GmbH, Oberkochen, Germany) was used to evaluate the morphology of the pellet surface and the pellet cross-section. For that purpose, pellets were manually cut with a scalpel. Prior to scanning electron microscopy, all samples were sputter-coated with chromium.

The mechanical properties of the pellets were investigated with respect to the crushing strength. Here, a rheometer (MCR 301; Anton Paar, Graz, Austria) equipped with a parallel plate measuring system was used in the nonrotational mode. The details of the method were previously published.[53] For each batch, 50 individual pellets were evaluated.

To determine the ibuprofen distribution throughout the pellets, Raman spectroscopy was performed with a confocal Raman microscope WITec alpha 300R^+ (WITec GmbH, Ulm, Germany) using an implemented Zeiss objective with a 10-fold magnification (numerical aperture 0.25). Samples were manually cut in half with razor blades and fixed on glass slides. Raman spectra were acquired every 5 μm along the x- and y-axes at an excitation wavelength of 532 nm (Nd:YAG laser, operated at 10 mW) and an integration time of 0.3 s. Subsequently, the spectral data sets were processed and converted into false-color images by cluster analysis using the software WITec Project Plus showing ibuprofen in red, whereas CaSt is represented in blue color.

in vitro dissolution studies were carried out in a United States Pharmacopoeia (USP) apparatus I (Pharma Test Type PTWS III C; Pharma Test Apparatebau AG, Hainburg, Germany). According to the USP XXVIII monograph for ibuprofen tablets, 900 mL of pH 7.2 monopotassium phosphate buffer was used as dissolution medium. In order to ensure sink conditions throughout the experiment, a sample mass of 500 mg was selected. The temperature was 37 ± 0.5°C and the stirring speed was set to 100 rpm. Samples of 1 mL were withdrawn from the dissolution media at specific time intervals and analyzed via reversed-phase high-performance liquid chromatography (HPLC). The HPLC method's details are described elsewhere.[53] Each batch was analyzed at least three times.

RESULTS AND DISCUSSION

Pellet Preparation

Pellets were prepared via wet extrusion/spheronization. During the wetting step, two processes occur simultaneously: swelling of CaSt in the granulation liquid (i.e., 50% ethanolic solution) and/or ibuprofen dissolution in the granulation liquid. It was previously reported by our group that at ambient temperature and pressure, CaSt swells in ethanol by a factor of 3.96 (volume based) at equilibrium, that is, the volume increases almost fourfold.[16] As in each experiment 100 g of the powder mixture (3.5% API) was used, CaSt weight was 96.5 g, which corresponds to 482.5 mL (poured bulk density of 200 g/L, data provided by the supplier). Fifty gram of 50% ethanol solution was used as granulation liquid, which approximately corresponds to 55 mL of 50% ethanol solution. Taking into account that CaSt powder can absorb a volumetric ethanol amount matching three times the powder volume, it can be assumed that in our experiments CaSt did not swell to a maximum.

From solubility experiments, it was determined that the ibuprofen equilibrium solubility was 48 g/L.[16] Each powder mixture contained 3.5 g ibuprofen. Thus, if the whole granulation liquid was available for dissolution, 75% of ibuprofen, corresponding to 2.64 g, could be dissolved in the 55 mL of the solvent. However, as a significant part of the solvent was absorbed by CaSt (i.e., inducing swelling), only a small fraction of ibuprofen was dissolved. It can be assumed that the major part of ibuprofen was present in the solid state. The moisture content, which was around 32% after wetting, dropped during the entire preparation process to 19% as a result of liquid evaporation (because of the open operating system). Consequently, after spheronization the amount of dissolved ibuprofen was likely to be even further decreased.

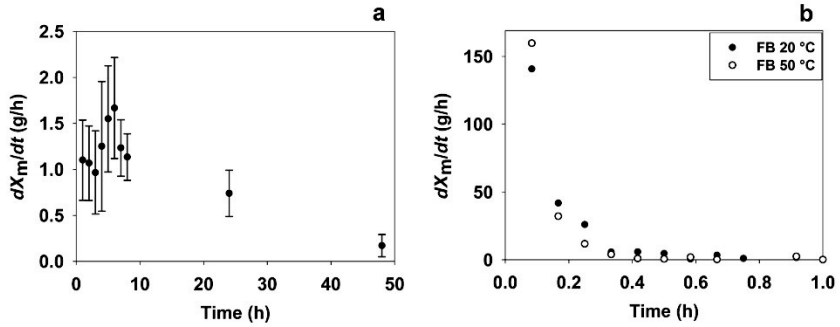

Figure 2. Drying process (water contents and drying rates) of the pellets dried via (a) desiccation and (b) in the fluid-bed apparatus at different inlet-air temperatures.

Dying Procedures

Drying curves (weight based) and drying rates for desiccation and fluid-bed drying are shown in Figure 2. As expected, the graph indicates a much slower drying in the dessicator. During desiccation, the rate of evaporation (i.e., dX_m/dt) was nearly constant for 8 h (Fig. 2a). After these 8 h, drying was somewhat faster, yet decreased again to the initial level. Given the large standard deviation of the data at intermediate times, it can be concluded that the drying rate was rather constant over the whole process, indicating that internal transport was not rate limiting. Thus, drying occurred in the CRP throughout the process,[54] and the pellets fairly dried uniformly over the entire diameter.

During the fluid-bed drying processes, a CRP (Fig. 2b) was not observed. This is typical for high drying rates, where the internal transport of liquid rather rapidly limits the transport of liquid to the surface.[55] The drying rate dropped promptly, indicating that the total drying process only took place in the FRP regime. (However, it is possible that a very short initial CRP occurred, shorter than the sampling time). The inlet-air temperatures (20°C and 50°C) had no significant influence on the drying rate (Fig. 2b), as the mass transfer coefficients in the fluid-bed are very high, resulting in fast mass transfer and drying.

From the above theoretical discussion, it can be concluded that the different drying conditions should have a different impact on the shrinkage behavior and thus on the pellet volume. Material drying in the CRP should have a stronger reduction in pellet diameter and the corresponding volume. Indeed, this was observed during our studies (Table 1): the pellet bulk volume was measured prior and after desiccation and it was found that pellets shrunk by 20.3 ± 2.40%. In contrast, during fluid-bed drying, the volume shrunk by 16.3 ± 1.91% and 15.7 ± 0.743% for an inlet-air temperature of 20°C and 50°C, respectively, which is significantly less than the shrinkage observed during desiccation. (Shrinking during fluid-bed drying is also in accordance with studies reporting that pellets do shrink during fluid-bed drying [4,7,8,11,12,14,25]).

Table 1. Results of Shrinkage Studies (Shrinkage Refers to Reduction in Pellet Bulk Volume)

Drying Method	Shrinkage (%) (SD)
Desiccation	20.3 (2.40)
Fluid-bed drying at 20°C	16.3 (1.91)
Fluid-bed drying at 50°C	15.7 (0.743)
Lyophilization	3.77 (0.693)

Lyophilization caused only little shrinkage, that is, reduction in pellet volume by 3.77 ± 0.693% (Table 1). In general, lyophilization can be subdivided into three stages: freezing of the sample, primary drying, and secondary drying.[56] During primary drying, which constitutes the largest part of the lyophilization process, the granulation liquid is removed via sublimation. During secondary drying, solvent that did not freeze is removed by desorption from the solute phase.

As the pellets were frozen rapidly in liquid nitrogen (cooling rate of approximately 250 K/min),[57] pellet shrinkage was minor. This is supported by Balaxi et al.[22] and Gómez-Carracedo et al.[26], who found that final pellet diameters increased with decreasing freezing temperature.

Differential Scanning Calorimetry

Figure 3a depicts DSC thermograms of the individual powders, as well as the physical powder mixture (ibuprofen and CaSt at a ratio of 1:1) in the dry state and wetted with ethanol (i.e., part of the granulation liquid). The DSC measurements were reproducible; for each sample, one representative thermogram is shown. The characteristic peaks of ibuprofen and CaSt (Fig. 3a, curves 1 and 2) are in accordance with literature; for detailed description, the reader is referred to elsewhere.[58,59] The mixture of ibuprofen and CaSt (Fig. 3a, thermogram 3) showed a lowering of the melting temperature of ibuprofen (endothermic peak in Fig. 3a, thermogram 1) from 75.3°C onset temperature to 55.5°C onset temperature. This indicates the formation of a eutectic mixture between ibuprofen and CaSt and is in accordance with previous findings.[60] The addition of ethanol (Fig. 2a, thermogram 4) caused a broadening of the endothermic peak because of simultaneous evaporation of ethanol during the first heating cycle. As the evaporation of ethanol superimposed the endothermic melting peak, determination of the peak onset temperature was not possible. However, it seems that the endothermic peak was shifted toward the melting temperature of ibuprofen again. During the second heating cycle (Fig. 3a, thermogram 5), where ethanol had already been removed because of evaporation and subsequent vapor removal through the pierced lid, the endothermic peak was shifted toward lower values (i.e., below the melting temperature of pure ibuprofen).

DOI 10.1002/jps.23707

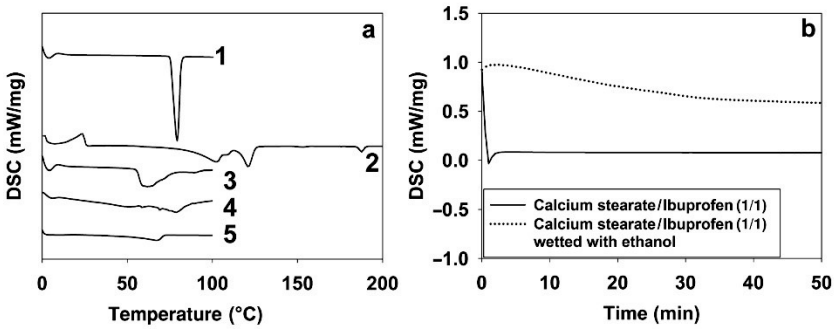

Figure 3. Differential scanning calorimetry curves: (a) DSC curves in dependence upon temperature of ibuprofen (1), CaSt (2), ibuprofen/CaSt mixture 1/1 (3), first (4), and second (5) heating cycle of ibuprofen/CaSt mixture 1/1 wetted with ethanol. No ethanol was present anymore in the second cycle because of ethanol evaporation during the first heating cycle. (b) DSC curves of ibuprofen/CaSt mixture 1/1 and ibuprofen/CaSt mixture 1/1 kept isotherm at 50°C over 50 min.

Additionally, the dry and wet powder mixtures were kept constant at 50°C and DSC thermograms were recorded (Fig. 3b). Here, neither exothermic nor endothermic peaks were observed, suggesting that no interactions occurred at 50°C. The DSC signal of the wetted powder mixture declined because of ethanol evaporation. Nevertheless, ethanol did not impact the physiochemical properties of ibuprofen and CaSt.

Pellet Characterization

The final pellet size distribution (PSDs) varied for the different drying techniques (data not shown). However, the amounts of pellets in the yield fraction (i.e., between 1.4 and 1.8 mm) were similar for all batches. The desiccated pellets showed higher amounts in the fractions below 1.4 mm in comparison to the other drying procedures, which correlates to the highest extent of shrinkage for desiccation (i.e., the pellet volume reduction by 20.3 ± 2.4%). Lyophilization yielded a significant fraction of pellets above 1.8 mm because of the low extent of shrinkage during lyophilzation. Interestingly, the inlet-air temperature during the fluid-bed process had no impact on the PSDs, which correlated to the equal extent of volume reduction in the fluid-bed apparatus (i.e., by 16.3 ± 1.9% and 15.7 ± 0.7% for FB 20°C and FB 50°C, respectively). Furthermore, the particle size distribution suggested that the fluid-bed process did not cause significant pellet abrasion. The amount of pellets with a diameter below 0.5 μm was not significantly increased as compared with the pellets dried via lyophilization.

The median pellet diameter of the pellets produced via the three drying methods ranged between 1610 and 1656 μm (Table 2). Similar values were expected as only the yield fraction was subjected to image analysis. The AR was well above 0.8 (Table 2) and was identical for all batches. Evidently, the drying procedure influenced the PSD but not the pellet shape.

The parameters describing the pellet microstructure are listed in Table 2. The apparent pellet density (obtained from helium pycnometry measurements) was similar for all batches (Table 2) and did not deviate from the apparent density of the powder mixture used for pellet preparation, that is, 1.0571 ± 0.0012 g/cm^3. This indicates the absence of closed pores independent upon the drying procedure. The presence of closed pores would have yielded a decreased density.

Because of shrinkage, not only the pellet diameter and the corresponding size distributions but also the porosities were affected. As shrinkage was minor during lyophilization, the initially present solvent-filled pore space was largely conserved. Thus, it is assumed that the final porosity was similar to the initial one (about 33%, see Table 2). Shrinkage during desiccation and fluid-bed drying, however, significantly reduced the internal porosity. As expected, the largest shrinkage in case of desiccation led to the smallest final porosity at around 16.5%. Fluid-bed drying also led to a porosity reduction of about 28% (Table 2). Finally, the pellet's crushing strength (Table 2) was inversely proportional to the porosity and decreased in the order D > FB > L.

The mercury intrusion/extursion curves showed the presence of ink-bottle-shaped pores (i.e., hysteresis; data not shown). Pore size data obtained from mercury porosimetry are reported in Table 2 in terms of median and modal pore diameter. All pore diameters ranged between 0.02 and 1 μm. At higher pressures, corresponding to lower pore sizes, samples deformed and pores collapsed. Thus, data evaluation was performed between 0.02 and 1 μm. Median pore diameters were similar after desiccation, after fluid-bed drying at 50°C, and after lyophilization. Median pore diameters of fluid-bed-dried pellets at 20°C slightly decreased compared with other batches. The modal pore diameters were similar after desiccation and fluid-bed drying at 20°C, but slightly decreased after fluid-bed drying at 50°C and significantly increased after lyophilization.

Although the porosity was not significantly affected by the inlet-air temperature during fluid-bed drying, the inlet-air temperature affected the pore size distributions. At 50°C, the median (0.23 μm for both) and modal pore diameters (0.23 and 0.24 μm) were equal, whereas for FB 20°C, modal diameters were increased (0.27 μm for both) and median diameters were decreased (0.19 and 0.18 μm), implying a broadened pore size distributions for FB 20°C in comparison to FB 50°C. Hence, drying conditions did not excessively impact the extent of shrinkage, but rather the mechanism of shrinkage: obviously, fluid-bed drying at 50°C favored the collapse of smaller pores (possibly because of softening of the material, leading to pore collapse upon impact, see *Differential Scanning Calorimetry* section above), whereas at 20°C, smaller pores shrunk but still remained intact after drying.

Determination of the total pore surface area was not possible with mercury porosimetry, as the samples tended to deform at higher pressures. This yielded in excessively high surface

Table 2. Results of Pellet Characterization

Batch Abbreviation	Median Pellet Diameter[a] (μm) (SD)	AR[b] (–) (SD)	Density (g/cm^3) (SD)	Porosity (%)	Median Pore Diameter[c] (μm)	Modal Pore Diameter[c] (μm)	Specific Surface Area[d] (m^2/g)	Crushing Strength (MPa) (SD)
D1	1611.10 (5.70)	0.9338 (0.0017)	1.0509 (0.0007)	16.0	0.24	0.27	1.7175	0.262 (0.0828)
D2	1621.71 (2.68)	0.9346 (0.0023)	1.0689 (0.0031)	16.7	0.21	0.25	2.1286	0.305 (0.0773)
FB 20°C 1	1639.27 (17.43)	0.9417 (0.0056)	1.0517 (0.0005)	28.3	0.19	0.27	5.3528	0.208 (0.0594)
FB 20°C 2	1624.46 (9.21)	0.9414 (0.0016)	1.0511 (0.0005)	28.6	0.18	0.27	5.4754	0.210 (0.0547)
FB 50°C 1	1629.97 (17.91)	0.9401 (0.0018)	1.0562 (0.0008)	27.7	0.23	0.23	2.7747	0.217 (0.0676)
FB 50°C 2	1643.38 (17.18)	0.9367 (0.0016)	1.0558 (0.0011)	28.1	0.23	0.24	2.8995	0.222 (0.0649)
L1	1656.00 (20.27)	0.9339 (0.0037)	1.0549 (0.0009)	32.7	0.24	0.38	10.5819	0.157 (0.0653)
L2	1610.31 (6.97)	0.9353 (0.0019)	1.0571 (0.0016)	32.8	0.21	0.35	11.3989	0.160 (0.193)

[a]The values were obtained from the number-based PSD.
[b]Aspect ratio is defined as the ratio between the minimum and the maximum Ferret's diameter. Ferret's diameters represent the median of the cumulative number distribution.
[c]The values were obtained from the volume-based pore size distribution.
[d]The values were obtained from nitrogen absorption measurements following the BET procedure.

areas. However, BET gas adsorption measurements were used to determine the specific surface area. The specific surface area was strongly influenced by the drying method and correlated with the porosity and the median pore diameter. In case of fluid-bed drying, the specific surface area was influenced by the inlet-air temperature (Table 2) and was significantly higher for 20°C than for 50°C. As the values for the median pore diameter were obtained from the volume-based size distribution, it was assumed that for similar pore sizes the total number of pores increased for FB 20°C, which is in accordance with the increased specific surface area for FB 20°C (Table 2). The effects of inlet-air temperature on the pore size distributions may be attributed to temperature-dependent mechanical properties of the matrix,[61] as described above. The DSC graphs (Fig. 2) reveal that CaSt lowers the melting temperature onset from 75°C to 55°C. Although the higher fluid-bed drying temperature was "only" 50°C, a certain local softening of the material may have occurred. Consequently, the mechanical properties and in turn the shrinkage behavior of the pellets were altered.

Scanning electron microscopy images did not reveal particular differences in the pellet surface structure (Fig. 4a) with respect to the different drying techniques. Magnifications (Fig. 4b) showed a distinct porous system for all drying methods, which is supported by the porosity determinations. When the pellets were manually cut with a scalpel to investigate the pellet cross-section, the center broke off, that is, fragmented, as can be seen in Figure 4c. Although Figure 4 only shows a single pellet per batch, more than one pellet was investigated, and fragmentation was generally observed during cutting, most notably for the pellets dried via lyophilization and desiccation. This characteristic was not that pronounced for FB-dried pellets as during FB drying the pellets experienced mechanical loading because of collisions. According to the true densities (Table 2), no air pockets (i.e., closed pores) were formed because of collisions. Instead, collisions caused densification. Magnification of the pellet cross-sections (Figure 4d) illustrates qualitative variations in the pellet structure. After desiccation, comparatively few pores were detected, which corresponds to the low porosity (i.e., 16.0% and 16.7% for D1 and D2). Lyophilization seemed to create numerous small pores throughout the pellet cross-section. This was attributed to the fast freezing of pellets upon immersion into liquid nitrogen. Because of the high freezing rate, a high number of ice/solid ethanol nuclei,[62] which condition the final pore size, were formed. Consequently, for fast freezing, more but smaller pores are formed than for slow freezing.[22,26] The microstructure of the lyophilized pellet surface differed from that of the cross-section. In contrast, after fluid-bed drying, the surface and cross-section microstructures appeared similar regardless of the drying temperature.

Raman images in Figure 5 display the spatial ibuprofen distribution throughout the pellet cross-sections. As images were reproducible, one representative image of one batch for each drying method is shown. No preferred position of randomly distributed API within the pellet was found for any of the drying procedures. This may be related to the drying procedure: during fluid-bed drying, ibuprofen was not transported toward the external surface as no CRP was present (Fig. 3b). Moreover, at 50°C, inlet-air temperature ibuprofen was likely to cause phase separation of 50% ethanol solution.[63] Hence, ibuprofen spontaneously recrystallized in the aqueous phase[64] and was no longer available for redistribution. As during desiccation a long CRP occurred (Fig. 3a), ibuprofen migration toward the outer

DOI 10.1002/jps.23707

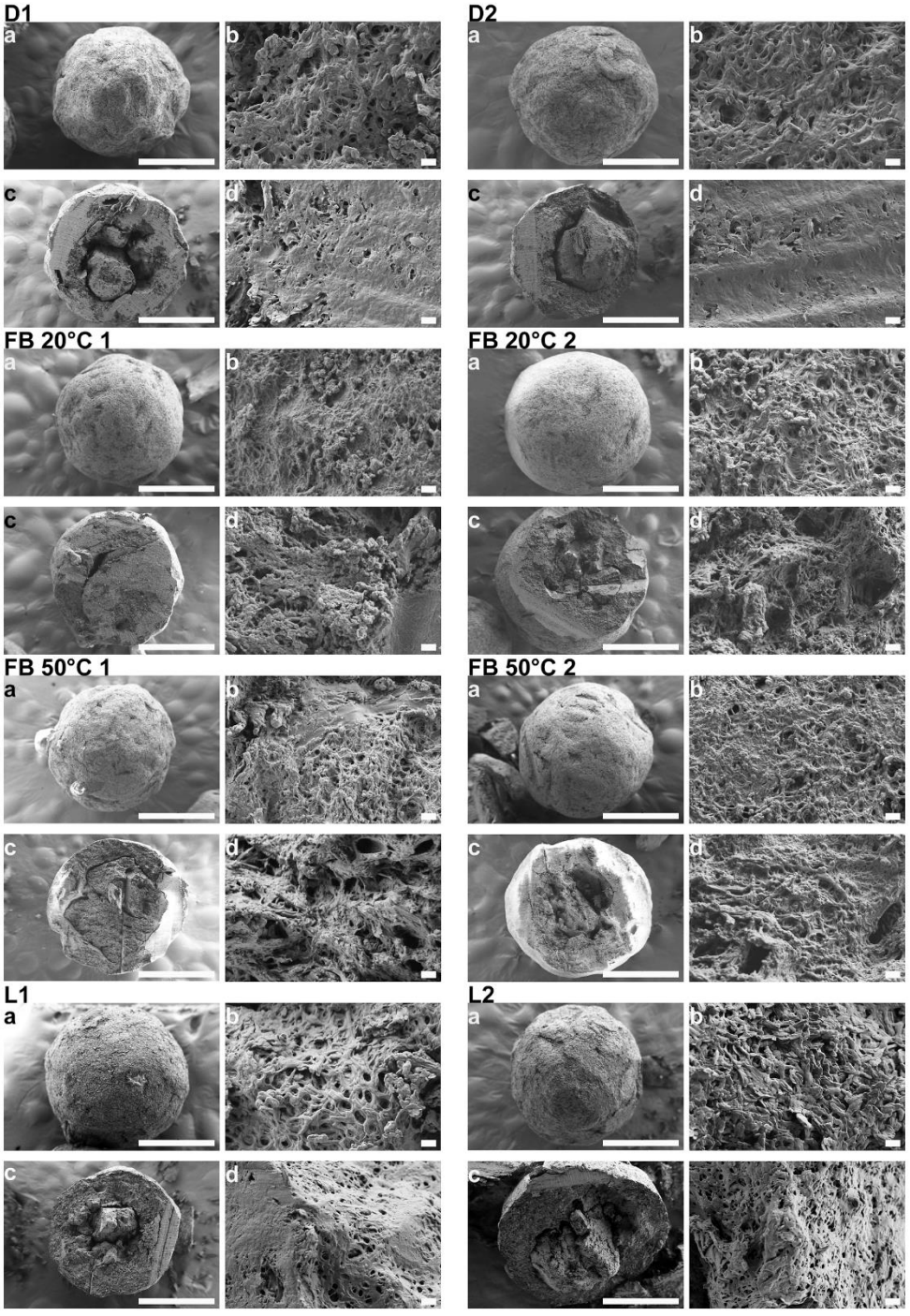

Figure 4. Scanning electron microscopy images of the pellets dried via different techniques. (a) Entire pellet (bar size 100 μm); (b) magnification of the external surface (bar size 1 μm); (c) pellet cross-section (bar size 100 μm); and (d) magnification of the pellet cross-section (bar size 1 mm).

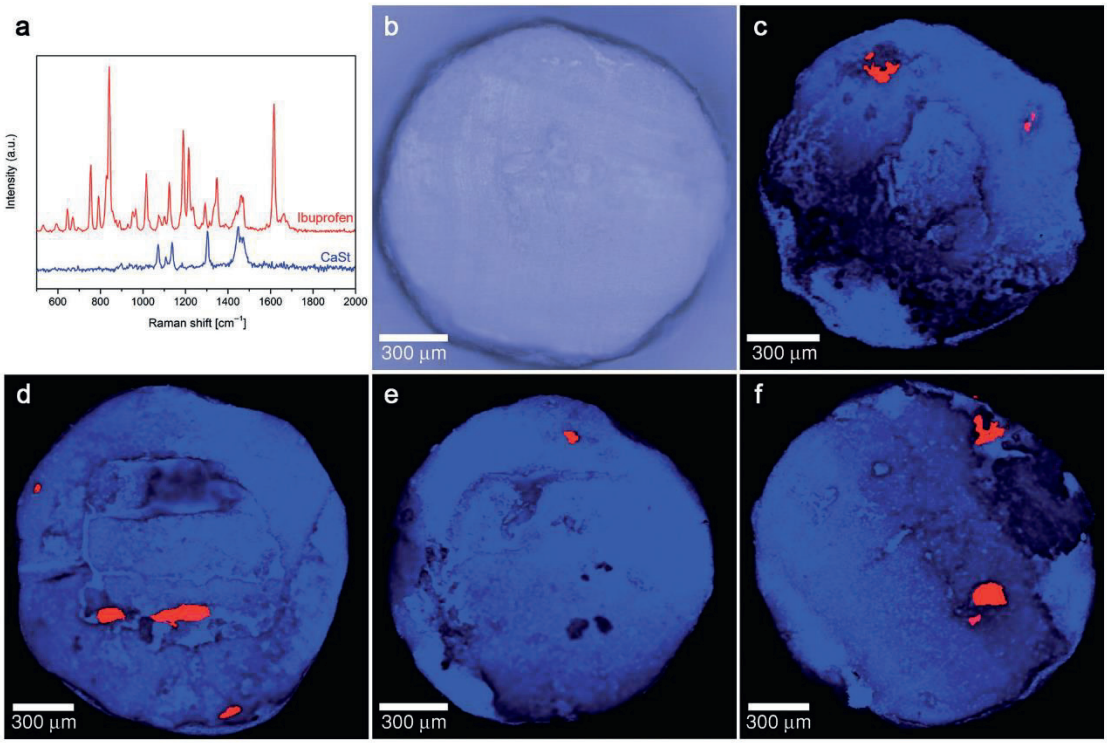

Figure 5. Results of Raman spectroscopy analysis. (a) Single spectrum of the individual powders; (b) exemplary microscopic image of a pellet cross-section prepared for Raman measurements; (c) Raman image of D1; (d) Raman image of FB 20°C 1; (e) Raman image of FB 50°C 2; and (f) Raman image of L1. Ibuprofen is represented in red, whereas CaSt is shown in blue color.

surface could have occurred. However, the conditions during desiccation prevented ibuprofen from accumulating in specific regions of the final pellets because of the strength of back-diffusion relative to convection toward the pellet surface for these mild drying conditions.

Therefore, as expected, the impact of the drying procedure on the ibuprofen profile was minor: although ibuprofen is highly soluble in the granulation liquid and has a high dissolution rate, the granulation liquid did not dissolve much of the ibuprofen but was rather absorbed by CaSt. Thus, only low fractions of ibuprofen might have been dissolved, being subject to migration. This is supported by the fact that the ibuprofen clusters observed in the Raman images were in the size range of the primary ibuprofen particles (i.e., median Feret's diameter 104.67 µm, Fig. 5).

The *in vitro* dissolution profiles are depicted in Figure 6. As expected, ibuprofen release was found to be incomplete for all batches after 6 h. This was caused by the low ibuprofen loading (3.5%), which was below the percolation threshold. Below the percolation threshold, it can be assumed that accessibility of many ibuprofen particles to the dissolution medium is limited because of complete "encapsulation" of ibuprofen particles in the insoluble CaSt matrix (the so-called finite clusters). Hence, all dissolution data did not fit the Higuchi model,[65] although it is known from previous studies that the CaSt matrix remains intact during dissolution testing, providing controlled ibuprofen release.[16,32]

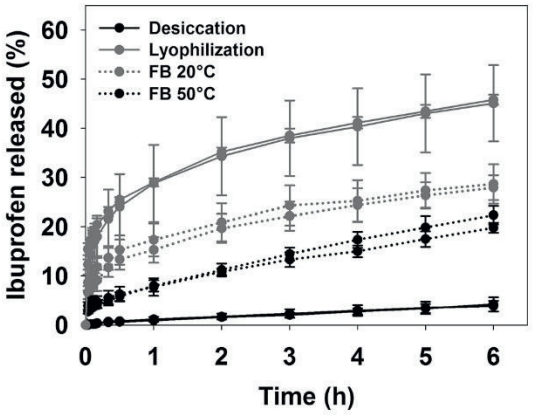

Figure 6. *in vitro* dissolution profiles generated in USP phosphate buffer pH 7.2.

The *in vitro* dissolution profiles over 6 h varied significantly ($p < 0.05$) as a function of the drying conditions (Fig. 6). The rate of ibuprofen release decreased in the order L, FB 20°C, FB 50°C, and D. After 6 h, around 45% of ibuprofen was released from the pellets dried via lyophilization, whereas only around 4% was released from those dried via desiccation.

DOI 10.1002/jps.23707

During fluid-bed drying at 20°C and 50°C, a decrease in the inlet-air temperature yielded in an increased dissolution rate.

As the Raman images revealed random ibuprofen distribution regardless of the drying procedure (Fig. 5), a biased ibuprofen distribution in the pellets clearly does not contribute to the overall dissolution behavior. However, the pellet microstructure (porosity, pore size, and surface area, see Table 2) correlates with the drug release rate. The rate of ibuprofen release tends to increase with the increasing porosity and modal pore diameter. It was reported in the literature that drug release from pellets increased with increasing porosity.[66] Moreover, Costa et al.[67] previously reported that drug release from pellets increased with the increasing mean pore diameter. This was also the case in our study with respect to the different drying techniques. After fluid-bed drying, FB 20°C and FB 50°C showed different release behavior despite similar porosities and modal pore diameters. However, the pore size distribution was impacted by the drying temperature as pointed out above, which can clearly be seen in the different BET surface areas for FB 20°C and FB 50°C (Table 2), respectively. FB 20°C has a significantly higher specific surface area and thus also showed higher release rates.

As already mentioned, during dissolution studies, the pellets remained intact because of the poor water solubility of CaSt. Hence, ibuprofen release occurred by dissolution through capillaries composed of the pore network and interconnecting drug particle clusters.[68] Ibuprofen release occurred when the drug came into contact with the dissolution medium, subsequently dissolved and diffused through the porous system. Higher specific surface areas, thus, provide a higher chance for the drug to come into contact with the dissolution medium, resulting in higher dissolution rates.

The pore shape, represented by the tortuosity, is another microstructure-related parameter that was shown to account for drug release characteristics.[69] For the presented pellets, it was not possible to generate reliable values of the tortusosity: the calculation of the tortousity requires the surface area obtained from mercury porosimetry,[70] which was difficult to determine, because the CaSt matrix tends to deform upon higher pressures.

Nevertheless, the results of the dissolution tests clearly indicate that the microstructure (porosity, pore size, and corresponding pore size distribution) of CaSt matrix pellets governs the dissolution profiles. The microstructure can systematically be tailored by the drying step, the drying technique, and the applied drying process parameters. As many pellet properties (including dissolution characteristics) are frequently related to the microstructure, the drying process plays a crucial role in achieving desired pellet properties. This is especially true for pellets containing a swellable matrix, which is most often the case for formulations processed via wet extrusion/spheronization.

CONCLUSIONS

Although the microstructure of low ibuprofen-loaded CaSt pellets changed depending on the drying procedure, the ibuprofen distribution throughout the pellets was not altered by the drying conditions, as apparently only a minor portion of ibuprofen was dissolved during wetting. During desiccation at ambient conditions, shrinkage (in terms of diameter and resulting volume reduction) of the CaSt matrix occurred. As drying took place mainly in the CRP, pellet porosity and specific surface area were decreased, leading to very low drug release rates. Also, during fluid-bed drying, particle shrinkage occurred to a lesser extent, which was possibly because of the absence of an overall CRP. Although different inlet-air temperatures during fluid-bed drying did not alter the pellet microstructure with respect to porosity, the specific surface area decreased at higher temperatures. Thus, drug release was accelerated for pellets dried at lower temperatures. The least shrinkage and consequently the highest specific surface area were observed for lyophilization, leading to the highest drug release rates.

Summarizing the impact of the drying procedure on the CaSt matrix pellets, it was found that:

- porosity decreased in the order lyophilization, fluid-bed drying (independent upon the drying temperature), and desiccation. This is because of the different shrinking mechanisms discussed above for the different drying modes;
- for fluid-bed drying, the median pore diameter was a function of the drying temperature, where lower temperatures yielded in smaller diameters;
- the specific surface area was a function of porosity and pore size distribution and thus decreased in the order lyophilization, fluid-bed drying at 20°C, fluid-bed drying at 50°C, and desiccation; and
- the *in vitro* dissolution profiles were a function of the pellets' specific surface area.

These findings suggest that the pellet microstructure is a strong function of the drying process. Pellet properties related to their microstructure can selectively be modified by adjusting the drying procedure.

In summary, this study highlighted the impact of the drying process on the pellet matrix. Future work will cover the impact of the drying process on the API that is incorporated into matrix pellets. Thereby, the drying process can be applied for a rational design of pellet characteristics accounting for the impact of the drying process on both the matrix and the API.

ACKNOWLEDGMENTS

The authors thank GL Pharma (Lannach, Austria) for providing ibuprofen, Mario Hainschitz (RCPE GmbH, Graz. Austria) for his help with the BET measurements, and Bettina Bauer (University of Graz, Austria) for her assistance with the HPLC measurements. Moreover, Julia Paller (University of Graz, Austria) is acknowledged for her assistance during pellet preparation.

REFERENCES

1. Kleinebudde P. 1993. Application of low substituted hydroxypropylcellulose (L-HPC) in the production of pellets using extrusion/spheronization. Int J Pharm 96(1–3):119–128.
2. Dyer AM, Khan KA, Aulton ME. 1994. Effect of the drying method on the mechanical and drug release properties of pellets prepared by extrusion-spheronization. Drug Dev Ind Pharm 20(20):3045–3068.
3. Lindner H, Kleinebudde P. 1994. Use of powdered cellulose for the production of pellets by extrusion/spheronization. J Pharm Pharmacol 46(1):2–7.

4. Kleinebudde P. 1994. Shrinking and swelling properties of pellets containing microcrystalline cellulose and low substituted hydroxypropylcellulose: I. Shrinking properties. Int J Pharm 109(3):209–219.
5. Kleinebudde P, Schröder M, Schultz P, Müller BW, Waaler T, Nymo L. 1999. Importance of the fraction of microcrystalline cellulose and spheronization speed on the properties of extruded pellets made from binary mixtures. Pharm Dev Technol 4(3):397–404.
6. Basit AW, Newton JM, Lacey LF. 1999. Formulation of ranitidine pellets by extrusion-spheronization with little or no microcrystalline cellulose. Pharm Dev Technol 4(4):499–505.
7. Pérez JP, Rabisková M. 2002. Influence of the drying technique on theophylline pellets prepared by extrusion-spheronization. Int J Pharm 242(1–2):349–351.
8. Tho I, Sande SA, Kleinebudde P. 2002. Pectinic acid, a novel excipient for production of pellets by extrusion/spheronisation: Preliminary studies. Eur J Pharm Biopharm 54(1):95–99.
9. Steckel H, Mindermann-Nogly F. 2004. Production of chitosan pellets by extrusion/spheronization. Eur J Pharm Biopharm 57(1):107–114.
10. Bashaiwoldu AB, Podczeck F, Newton JM. 2004. A study on the effect of drying techniques on the mechanical properties of pellets and compacted pellets. Eur J Pharm Biopharm 21(2–3):119–129.
11. Chatchawalsaisin J, Podczeck F, Newton JM. 2005. The preparation by extrusion/spheronization and the properties of pellets containing drugs, microcrystalline cellulose and glyceryl monostearate. Eur J Pharm Sci 24(1):35–48.
12. Thommes M, Kleinebudde P. 2006. Use of k-carrageenan as alternative pelletisation aid to microcrystalline cellulose in extrusion/spheronisation. I. Influence of type and fraction of filler. Eur J Pharm Biopharm 63(1):59–67.
13. Thommes M, Kleinebudde P. 2008. The behavior of different carrageenans in pelletization by extrusion/spheronization. Pharm Dev Technol 13(1):27–35.
14. Balaxi M, Nikolakakis I, Kachrimanis K, Malamataris S. 2009. Combined effects of wetting, drying, and microcrystalline cellulose type on the mechanical strength and disintegration of pellets. J Pharm Sci 98(2):676–689.
15. Ghanam D, Kleinebudde P. 2011. Suitability of k-carrageenan pellets for the formulation of multiparticulate tablets with modified release. Int J Pharm 409(1–2):9–18.
16. Schrank S, Hodzic A, Zimmer A, Glasser B, Khinast J, Roblegg E. 2012. Ibuprofen-loaded calcium stearate pellets: Drying-induced variations in dosage form properties. AAPS PharmSciTech 13(2):686–698.
17. Sousa JJ, Sousa A, Podczeck F, Newton JM. 1996. Influence of process conditions on drug release from pellets. Int J Pharm 144(2):159–169.
18. Lutchman D, Dangor CM, Perumal D. 2005. Formulation of rate-modulating pellets for the release of ibuprofen: An extrusion/spheronization process. J Microencapsul 22(6):643–659.
19. Bashaiwoldu AB, Podczeck F, Newton JM. 2004. The application of non-contact laser profilometry to the determination of permanent structural change induced by compaction of pellets: II. Pellets dried by different techniques. Eur J Pharm Biopharm 22(1):55–61.
20. Schmidt C, Kleinebudde P. 1999. Influence of the granulation step on pellets prepared by extrusion/spheronization. Chem Pharm Bull 47(3):405–412.
21. Song B, Rough SL, Wilson DI. 2007. Effects of drying technique on extrusion-spheronisation granules and tablet properties. Int J Pharm 332(1–2):38–44.
22. Balaxi M, Nikolakakis I, Malamataris S. 2009. Preparation of porous microcrystalline cellulose pellets by freeze-drying: Effects of wetting liquid and initial freezing conditions. J Pharm Sci 99(4):2104–2113.
23. Wlosnewski JC, Kumpugdee-Vollrath M, Sriamornsak P. 2010. Effect of drying technique and disintegrant on physical properties and drug release behavior of microcrystalline cellulose-based pellets prepared by extrusion/spheronization. Chem Eng Res Des 88(1):100–108.
24. Habib YS, Augsburger LL, Shangraw RF. 2002. Production of inert cushioning beads: Effect of excipients on the physicomechanical properties of freeze-dried beads containing microcrystalline cellulose produced by extrusion-spheronization. Int J Pharm 233(1–2):67–83.
25. Tho I, Arne Sande S, Kleinebudde P. 2003. Disintegrating pellets from a water-insoluble pectin derivative produced by extrusion/spheronisation. Eur J Pharm Biopharm 56(3):371–380.
26. Gómez-Carracedo A, Souto C, Martínez-Pacheco R, Concheiro A, Gómez-Amoza JL. 2007. Microstructural and drug release properties of oven-dried and of slowly or fast frozen freeze-dried MCC-Carbopol® pellets. Eur J Pharm Biopharm 67(1):236–245.
27. Gómez-Carracedo A, Souto C, Martinez-Pacheco R, Concheiro A, Gómez-Amoza JL. 2008. Incidence of drying on microstructure and drug release profiles from tablets of MCC-lactose-Carbopol® and MCC-dicalcium phosphate-Carbopol® pellets. Eur J Pharm Biopharm 69(2):675–685.
28. Murray T, Rough SL, Wilson DI. 2007. The effect of drying technique on tablets formed from extrusion-spheronization granules. Chem Eng Res Des 85(7):996–1004.
29. Krogars K, Heinämäki J, Vesalahti J, Marvola M, Antikainen O, Yliruusi J. 2000. Extrusion/spheronization of pH-sensitive polymeric matrix pellets for possible colonic drug delivery. Int J Pharm 199(2):187–194.
30. Almeida Prieto S, Blanco Mandez J, Otero Espinar FJ. 2005. Starch-dextrin mixtures as base excipients for extrusion-spheronization pellets. Eur J Pharm Biopharm 59(3):511–521.
31. Sinha VR, Agrawal MK, Kumria R. 2005. Influence of formulation and excipient variables on the pellet properties prepared by extrusion spheronization. Curr Drug Deliv 2(1):1–8.
32. Roblegg E, Ulbing S, Zeissmann S, Zimmer A. 2010. Development of lipophilic calcium stearate pellets using ibuprofen as model drug. Eur J Pharm Biopharm 75(1):56–62.
33. Alvarez L, Concheiro A, Gomez-Amoza JL, Souto C, Martinez-Pacheco Rn. 2003. Powdered cellulose as excipient for extrusion-spheronization pellets of a cohesive hydrophobic drug. Eur J Pharm Biopharm 55(3):291–295.
34. Berggren J, Alderborn G. 2001. Effect of drying rate on porosity and tabletting behaviour of cellulose pellets. Int J Pharm 227(1–2):81–96.
35. Bika DG, Gentzler M, Michaels JN. 2001. Mechanical properties of agglomerates. Powder Technol 117(1–2):98–112.
36. Berggren J, Alderborn G. 2001. Drying behaviour of two sets of microcrystalline cellulose pellets. Int J Pharm 219(1–2):113–126.
37. Kleinebudde P, SoLvberg AJ, Lindner H. 1994. The power-consumption-controlled extruder: A tool for pellet production. J Pharm Pharmacol 46(7):542–546.
38. Kleinebudde P, Jumaa M, El Saleh F. 2000. Influence of degree of polymerization on behavior of cellulose during homogenization and extrusion/spheronization. AAPS J 2(3):18–27.
39. Kowalski SJ. 2000. Toward a thermodynamics and mechanics of drying processes. Chem Eng Sci 55(7):1289–1304.
40. Scherer GW. 1990. Theory of drying. J Am Ceram Soc 73(1):3–14.
41. Yang H, Sakai N, Watanabe M. 2001. Drying model with non-isotropic shrinkage deformation undergoing simultaneous heat and mass transfer. Drying Technol 19(7):1441.
42. Ansari MA, Stepanek F. 2006. Design of granule structure: Computational methods and experimental realization. AlChE J 52(11):3762–3774.
43. Ansari MA, Stepanek F. 2008. The evolution of microstructure in three-component granulation and its effect on dissolution. Part Sci Technol 26:55–66.
44. Poutiainen S, Honkanen M, Becker J, Nachtweide D, Järvinen K, Ketolainen J. 2012. X-ray microtomography analysis of intragranular drug migration during fluidized bed and oven tray drying. J Pharm Sci 101(4):1587–1598.
45. Kiekens F, Zelko R, Remon JP. 2000. Influence of drying temperature and granulation liquid viscosity on the inter- and intragranular drug migration in tray-dried granules and compacts. Pharm Dev Technol 5(1):131–137.

 DOI 10.1002/jps.23707

46. Huang X, Brazel CS. 2001. On the importance and mechanisms of burst release in matrix-controlled drug delivery systems. J Control Release 73(2–3):121–136.
47. Kapsidou T, Nikolakakis I, Malamataris S. 2001. Agglomeration state and migration of drugs in wet granulations during drying. Int J Pharm 227(1–2):97–112.
48. Kiekens F, Zelko R, Remon JP. 1999. A comparison of the inter- and intragranular drug migration in tray- and freeze-dried granules and compacts. Pharm Dev Technol 4(3):415–420.
49. Warren JW, Price JC. 1977. Drug migration during drying of tablet granulations II: Effect of binder solution viscosity and drying temperature. J Pharm Sci 66(10):1409–1412.
50. Warren JW, Price JC. 1977. Drug migration during drying of tablet granulations I: Effect of particle size of major diluent. J Pharm Sci 66(10):1406–1409.
51. Chaudry IA, King RE. 1972. Migration of potent drugs in wet granulations. J Pharm Sci 61(7):1121–1125.
52. Mehta KA, Kislalioglu MS, Phuapradit W, Malick AW, Shah NH. 2000. Effect of formulation and process variables on porosity parameters and release rates from a multi unit erosion matrix of a poorly soluble drug. J Control Release 63(1–2):201–211.
53. Roblegg E, Schrank S, Griesbacher M, Radl S, Zimmer A, Khinast J. 2011. Use of the direct compression aid Ludiflash® for the preparation of pellets via wet extrusion/spheronization. Drug Dev Ind Pharm 37(10):1231–1243.
54. Moore F. 1961. The mechanism of moisture movement in clays with particular reference to drying—A concise review. Trans Br Ceram Soc 60:517–539.
55. Prakash S, Jha SK, Datta N. 2004. Performance evaluation of blanched carrots dried by three different driers. J Food Eng 62(3):305–313.
56. Tang X, Pikal M. 2004. Design of freeze-drying processes for pharmaceuticals: Practical advice. Pharm Res 21(2):191–200.
57. Hottot A, Vessot S, Andrieu J. 2004. A direct characterization method of the ice morphology. Relationship between mean crystals size and primary drying times of freeze-drying processes. Drying Technol 22(8):2009–2021.
58. Roblegg E, Jäger E, Hodzic A, Koscher G, Mohr S, Zimmer A, Khinast J. 2011. Development of sustained-release lipophilic calcium stearate pellets via hot melt extrusion. Eur J Pharm Biopharm 79(3):635–645.
59. Lerdkanchanaporn S, Dollimore D, Evans SJ. 2001. Phase diagram for the mixtures of ibuprofen and stearic acid. Thermochim Acta 367–368(0):1–8.
60. Gordon RE, VanKoevering CL, Reits DJ. 1984. Utilization of differential scanning calorimetry in the compatibility screening of ibuprofen with the stearate lubricants and construction of phase diagrams. Int J Pharm 21(1):99–105.
61. Ratti C. 1994. Shrinkage during drying of foodstuffs. J Food Eng 23(1):91–105.
62. Bentejac R. 1998. Freeze-drying. In Powder technology and pharmaceutical processes; Chulia D, Deleuil M, Pourcelot Y, Eds. 7th ed. Amsterdam, The Netherlands: Elsevier, pp 257–271.
63. Manrique J, Martinez F. 2007. Solubility of ibuprofen in some ethanol + water cosolvent mixtures at several temperatures. Latin Am J Pharm 26(3):344–354.
64. Jbilou M, Ettabia A, Guyot-Hermann A-M, Guyot J-C. 1999. Ibuprofen agglomerates preparation by phase separation. Drug Dev Ind Pharm 25(3):297–305.
65. Zhang F, McGinity JW. 2000. Properties of hot-melt extruded theophylline tablets containing poly(vinyl acetate). Drug Dev Ind Pharm 26(9):931–942.
66. Chopra R, Alderborn G, Podczeck F, Newton JM. 2002. The influence of pellet shape and surface properties on the drug release from uncoated and coated pellets. Int J Pharm 239(1–2):171–178.
67. Costa FO, Pais AACC, Sousa JJS. 2004. Analysis of formulation effects in the dissolution of ibuprofen pellets. Int J Pharm 270(1–2):9–19.
68. Holman LE, Leuenberger H. 1988. The relationship between solid fraction and mechanical properties of compacts—The percolation theory model approach. Int J Pharm 46(1–2):35–44.
69. Crowley MM, Schroeder B, Fredersdorf A, Obara S, Talarico M, Kucera S, McGinity JW. 2004. Physicochemical properties and mechanism of drug release from ethyl cellulose matrix tablets prepared by direct compression and hot-melt extrusion. Int J Pharm 269(2):509–522.
70. León y León CA. 1998. New perspectives in mercury porosimetry. Adv Colloid Interface Sci 76–77(0):341–372.

5.2 Impact of Drying on Solid State Modifications and Drug Distribution in Ibuprofen-Loaded Calcium Stearate Pellets

Impact of Drying on Solid State Modifications and Drug Distribution in Ibuprofen-Loaded Calcium Stearate Pellets

S. Schrank, B. Kann, E. Saurugger, H. M. Ehmann, O. Werzer, M. Windbergs, B. Glasser, A. Zimmer, J. Khinast, E. Roblegg

Mol. Pharmaceutics. **2014**;11:599-609.

DOI: 10.1021/mp4005782

molecular pharmaceutics

Article

pubs.acs.org/molecularpharmaceutics

Impact of Drying on Solid State Modifications and Drug Distribution in Ibuprofen-Loaded Calcium Stearate Pellets

S. Schrank,[†,‡,§] B. Kann,[∥] E. Saurugger,[‡] H. Ehmann,[⊥] O. Werzer,[§] M. Windbergs,[∥,#] B. J. Glasser,[¶] A. Zimmer,[§] J. Khinast,[†,‡] and E. Roblegg*[,‡,§]

[†]Institute for Process and Particle Engineering, Graz University of Technology, Inffeldgasse 13/3, 8010 Graz, Austria

[‡]Research Center Pharmaceutical Engineering GmbH, Inffeldgasse 13/2, 8010 Graz, Austria

[§]Institute of Pharmaceutical Sciences, Department of Pharmaceutical Technology, University of Graz, Humboldtstraß4 46/1, 8010 Graz, Austria

[∥]Department of Biopharmaceutics and Pharmaceutical Technology, Saarland University, Campus A4 1, Saarbruecken, Germany

[⊥]Institute of Chemistry, Department of Physical and Theoretical Chemistry, University of Graz, Heinrichstraße 28/4, 8010 Graz, Austria

[#]Department of Drug Delivery (DDEL), Helmholtz-Institute for Pharmaceutical Research Saarland (HIPS), Helmholtz Centre for Infection Research (HZI), Campus A4.1, Saarbruecken, Germany

[¶]Department of Chemical and Biochemical Engineering, Rutgers University, Busch Campus 98 Brett Road, Piscataway New Jersey, United States

ABSTRACT: Drying is a common pharmaceutical process, whose potential to alter the final drug properties—even at relatively low temperatures—is often neglected. The present study addresses the impact of drying at 20 and 50 °C on wet-extruded calcium stearate (CaSt) pellets. Drying at 20 °C caused the majority of ibuprofen to accumulate at the pellet surface due to a strong convective flow from the pellet's center to the surface. In contrast, pellets dried at 50 °C still contained ibuprofen in the pellet's interior due to the higher drying rate and the associated film breakage during drying. Moreover, the higher drying temperature caused CaSt to form a second lamellar phase and ibuprofen to convert (partly) into its amorphous state. Overall, the drying process affected the solid state and the spatial ibuprofen distribution within the pellet. Knowledge of these effects can aid in tailoring advanced multipellet formulations.

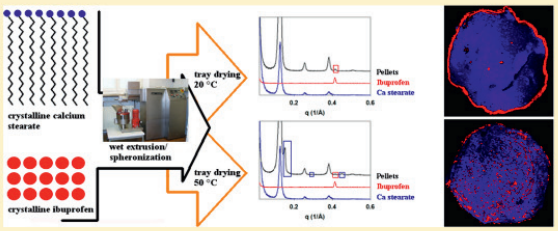

KEYWORDS: *extrusion/spheronization, drying, pellets, Raman mapping, small- and wide-angle X-ray scattering, differential scanning calorimetry*

■ INTRODUCTION

Drying is one of the standard unit operations during manufacturing of solid dosage forms. In products prepared by wet granulation and wet extrusion, drying is a key process, as it allows the formation of permanent bonds (so-called solid bridges) between primary particles.[1] However, drying not only removes the liquid from wet granules/pellets but also may impact the physicochemical properties of both the active pharmaceutical ingredient (API)[2−7] and the excipient(s).[8,9] Thereby, the performance of the dried pellets may be modified with respect to their in vitro dissolution characteristics[10−13] and compaction behavior.[8,10,14−16] Physicochemical properties are likely to change where there are interactions between the API, excipient(s), and granulation liquid.[17] In general, interactions with the granulation liquid include swelling and dissolution of excipient and/or API particles in the granulation liquid. Wet extrusion processes often use excipients that swell in the granulation liquid due to their large liquid absorption and retention capacity.[18] As the granulation liquid is removed upon drying, the excipient matrix is likely to shrink. Consequently, different drying conditions may result in variations of the pellet microstructure. In previous studies[19,20] we showed that the microstructure of pellets that contain calcium stearate (CaSt) is a strong function of the drying technique and the drying process parameters. CaSt swells in ethanol (i.e., part of the granulation liquid) and is prone to shrinkage upon drying. The extent and the mechanism of shrinkage are governed by the drying process conditions.

Apart from changes in the microstructure (associated with modifications of the excipient), drying is also expected to modify the final API properties and the API distribution within

Received: September 30, 2013
Revised: January 7, 2014
Accepted: January 8, 2014
Published: January 8, 2014

the pellet. A certain number of API particles get dissolved in the granulation liquid during wetting as a function of the drug solubility. During drying, the dissolved API is prone to intragranular migration, i.e., migration within a pellet.

Initially, during the constant rate period (CRP) the pellets contain sufficient liquid to keep the surface (nearly) saturated. The liquid evaporates from the surface, which is kept wet by liquid transport from the interior due to convective flow according to a modified Darcy's law.[21,22] Dissolved API can migrate toward the outer pellet regions as it is transported with the convective liquid flow. Due to liquid evaporation from the pellet surface, a higher drug concentration is generated close to the surface. Liquid containing the dissolved API flows from the interior toward the pellet's surface, gradually increasing the concentration gradient by depleting the pellet's interior. However, due to the concentration gradient, back-diffusion may occur, transporting the drug back toward the pellet's interior. The relative strength of the two phenomena, i.e., convective liquid transport toward the surface and back-diffusion, is a function of the drying rate and determines the final API concentration profile in the pellet (i.e., the API distribution in the dried pellet). Diffusion is dominant at low drying rates, which are common during CRPs with low (gentle) drying temperatures and during the falling rate period (FRP). Thereby, the final API profiles are uniform or API even accumulates in central regions of the pellets. In contrast, for harsh drying conditions, typical of CRPs with elevated temperatures, convection dominates, leading to API accumulation close to the pellet's surface.

In addition to liquid convection[23] and diffusion of the API in the liquid,[23] there are several other mechanisms that impact API migration: (i) adsorption of the API on the carrier (i.e., matrix excipient),[23] (ii) film breakage,[24] and (iii) recrystallization.[25] Adsorption is a spontaneous process that takes place if the free energy of adsorption becomes negative. Energies that contribute to the free energy of adsorption can be grouped into electrostatic and non-electrostatic energies. Electrostatic energies refer to Coulombic interactions that appear in cases where the adsorptive (i.e., the API) is dissociated or protonated. Non-electrostatic interactions include van der Waals forces, hydrophobic interactions, and hydrogen bonding. For strong API adsorption the amount of API adsorbed on the matrix may exceed the amount of freely dissolved API. Hence, drying influences the final API profile only to a minor extent.[24]

Film breakage inside the pores was found to occur at high drying rates (corresponding to high temperatures)[26] and/or the late stage of drying, i.e., in the FRP.[27] Film breakage results in the formation of isolated liquid domains. Then, solute API migration can only occur within these domains, and the API profile of the pellet is only changed to a minor extent.

Recrystallization occurs as soon as a supersaturated solution has been created due to liquid evaporation. The combination of granulation liquid and drying conditions may provide a suitable environment for the conversion of the API to a different polymorphic form, most often associated with hydrate formation.[28,29] This might be an obstacle to meet in vitro dissolution requirements,[30−32] and thus, bioavailability is lowered. In contrast, Yano et al.[33] reported that partial polymorphic transition of indomethacin (i.e., conversion from the crystalline γ-form into the amorphous state) during wet extrusion/spheronization significantly increased the in vitro dissolution (yielding dissolution profiles similar to those of extrudates prepared by melt extrusion). Consequently, the oral bioavailability was expected to be improved.

The present study addresses the impact of the drying process following extrusion/spheronization on wet extruded CaSt pellets focusing the physicochemical properties of the API, including (i) recrystallization and adsorption characteristics during drying and (ii) the solid state and the spatial distribution of the API after drying. A simple three-component system was used, comprising ibuprofen as model API, CaSt as matrix carrier, and ethanol as granulation liquid. In a first approach (i.e., the conventional approach), the API was dry blended with the excipient and the blend was wetted prior to extrusion/spheronization. In a second approach, the model API was dissolved in the granulation liquid and the excipient was wetted with the solution. Thereby, it was ensured that the majority of the API was present in the dissolved state during pellet preparation and was, thus, likely to be modified by the drying process to a maximum extent.

■ EXPERIMENTAL SECTION

Chemicals. Vegetable calcium stearate (CaSt; Werba-Chem GmbH, Vienna, Austria) was used as matrix for pellet preparation. Ibuprofen (G.L. Pharma, Lannach, Austria) served as model drug, and 96 vol % ethanol (Merck, Darmstadt, Germany) was used as granulation liquid.

Granulation Liquid Characterization. Since during the second approach ibuprofen was incorporated into the pellets by wetting CaSt with an ethanolic ibuprofen solution, the impact of solute ibuprofen molecules on the physicochemical properties of ethanol was investigated.

First, the contact angle was evaluated as it is the key parameter for the wetting step. The ibuprofen concentration was adjusted in the granulation liquid to achieve 38 wt %. To elucidate concentration dependent variations, solutions containing 29 and 44 wt % were tested as well. CaSt was compacted into disks and contact angles were determined with the EasyDrop System (Krüss, Hamburg, Germany) equipped with a CCD camera. The contact angles were calculated using the H/W method. Each experiment was performed at 20 °C and in triplicate.

Second, the viscosities of the ethanolic ibuprofen solutions were determined. An MCR 301 (Anton Paar, Graz, Austria) equipped with a cone plate measuring system (CP 50-1) in the rotational mode was used. The shear rate varied logarithmically from 10 to 100 s^{-1}, and flow curves were recorded. All measurements were conducted at 20 °C and were repeated three times.

Crystallization Studies. As ibuprofen was either dissolved during the wetting step in the first approach or was predissolved in the granulation liquid in the second approach, and pellet drying causes ibuprofen recrystallization, the recrystallization behavior was investigated as a function of the drying temperature and initial ibuprofen concentration. For this, 10 μL of ethanolic ibuprofen solutions (i.e., 29, 38, and 44 wt %) were dripped onto microscope slides and covered with glass coverslips. The samples were dried following the drying procedure of the pellets, that is, at a temperature of either 20 or 50 °C, while the relative air humidity was kept constant between 26 and 31%. After certain time intervals samples were analyzed via polarization optical microscopy (Axiiovert 40 CFL, Carl Zeiss NTS GmbH, Oberkochen, Germany).

Quartz Crystal Microbalance with Dissipation (QCM-D). QCM measurements were performed in order to account

for ibuprofen adsorption onto CaSt. Measurements were carried out with a QCM-D E4 (Q Sense, Gothenburg, Sweden) and QCM Au coated crystals (GSX301, from Q-Sense, Gothenburg, Sweden) with a resonance frequency of 5 MHz. The substrate was modified by dripping 10 μL of a CaSt solution (2 wt % in hot pyridine) onto the crystals under ambient conditions. The modified crystals were mounted into the QCM chambers, and the system was equilibrated with ethanol. After five minutes of equilibration, ethanolic ibuprofen test solutions (0.1, 0.5, and 1 wt %) were pumped through the chamber with a flow rate of 0.3 mL/min. Each experiment was performed in duplicate. The temperature was held constant, at 20.0 ± 0.1 or 50 °C ± 0.1 °C, resembling the drying temperatures. Changes in the third overtone were recorded, and dissipation was calculated applying the Sauerbrey equation:

$$\Delta m = -\frac{C\Delta f}{n}$$

where Δm is the change in crystal mass, C is the Sauerbrey constant, Δf is the observed frequency shift, and n is the overtone number. For detailed description of QCM measurements the reader is referred to elsewhere.[34]

Pellet Preparation and Drying Procedures. Pellets were prepared via the wet extrusion/spheronization technique, where the equipment and process parameters were adapted from previous works.[19,20,35] Each batch was produced in duplicate for reproducibility testing. Two different methods were used for ibuprofen incorporation. In a first approach ibuprofen was applied as a powder. Here, CaSt and ibuprofen were dry blended at a mass ratio of 5.67 to 1 (corresponding to 15 wt % drug loading) using a TURBULA T2F mixer (Willy A Bachofen AG Maschinenfabrik, Muttenz, Switzerland). Subsequently, 100 g of the powder mixture (further referred as P) was manually wetted by dripping the granulation liquid, i.e., 25 g of ethanol, onto the powder bed during mixing in a planetary mixer. In a second approach, ibuprofen was applied as an ethanolic solution (further referred as S) with a concentration of 38 wt % (prepared by dissolving 15 g of ibuprofen in 25 g of ethanol). 85 g of CaSt was manually wetted with 40 g of the ibuprofen solution; again yielding a final drug loading of 15 wt %.

The wet mass was extruded through a 1.5 mm multihole die plate, and the extrudates were spheronized at 600 rpm for three minutes. Lastly, the pellets were tray dried at either 20 or 50 °C at a relative air humidity ranging between 26 and 31%. The number in the batch abbreviation corresponds to the drying temperature (for details, see Table 1). Pellets were placed into round, flat-bottom bowls with a diameter of 17 cm, which equals a bed surface area of 227 cm^2. The pellet bed height was 8 mm, which means that approximately 6 pellet layers were on top of each other. Drying at 50 °C was performed in an oven (Heraeus, Vienna, Austria). In order to dry the pellets at 20 °C, they were placed into an air-conditioned laboratory that provided the drying conditions mentioned above. Drying was carried out until a final moisture content below 1% was reached.

Table 1. Pellet Formulation Details

abbreviation	ibuprofen applied as	drying temp (°C)
P20	powder	20
S20	solution	20
P50	powder	50
S50	solution	50

The drying profiles were generated by weighing the pellets after certain time intervals. The moisture content drop over time was calculated based on the dry pellets' mass and plotted against time.

Pellet Characterization. Prior to pellet characterization the batches were sieved according to Ph. Eu. 7.0 2.9.38 and the fraction between 1.4 and 1.8 mm was used for characterization studies.

Differential Scanning Calorimetry (DSC). DSC measurements were performed using a DSC 204 F1 Phoenix (Netzsch, Selb, Germany). Pellets (sample weight 5−9 mg) were gently crushed with a spatula and transferred into aluminum pans, which were subsequently closed with a pierced lid. The samples were heated from 20 to 100 °C at 5 °C/min, and after the samples were kept at 100 °C for 5 min, they were cooled to 20 °C at −5 °C/min. Nitrogen was applied as analytical gas (volume flow of 20 mL/min). Three samples were collected and analyzed from each batch.

Attenuated Total Reflectance Fourier Transform Infrared Spectroscopy (ATR-FTIR). Pellets were gently crushed with a spatula, and IR spectra were recorded on a Bruker VERTEX 70 (Bruker, Rheinstetten, Germany) apparatus using a DLaTGS detector and an ATR unit (MVP Pro Star, Diamond crystal). A total of 64 scans were done at wavelengths ranging from 4000 to 600 cm^{-1} with a resolution of 4 cm^{-1}. Three samples were collected from each batch and subjected to IR measurements.

Small- and Wide-Angle X-ray Scattering (SWAXS). A high-flux laboratory small- and wide-angle X-ray scattering camera S3-Micro (Hecus X-ray Systems, Graz, Austria) equipped with a high-brilliance microbeam delivery system was used. Samples were gently crushed with the help of a spatula and packed into glass capillaries (inner diameter 2 mm), sealed with wax, and placed into the SpinCap (i.e., sample holder). The refracted intensities were recorded with a 1D-detector (PSD-50, Hecus X-ray Systems, Graz, Austria) with the following settings: wavelength, 1.54 Å; angular range, 0.02−8°; exposure time, 800 s; beam size, 200 μm. The data were calculated to reciprocal space vectors by

$$q = \frac{4\pi \sin\theta}{\lambda}$$

where q is the reciprocal space vector, θ is the scattering angle, and λ is the wavelength.

All measurements were carried out at ambient temperature, and for each batch three samples were investigated.

Raman Mapping. In order to determine the ibuprofen distribution throughout the pellets after drying, samples were bisected using a razorblade and fixed on glass slides. Confocal Raman microscopy (WITec alpha 300R+, WITec GmbH, Ulm, Germany) was performed at an excitation wavelength of 532 nm (Nd:YAG laser, operated at 10 mW) using an implemented Zeiss objective with a 10-fold magnification (N.A. 0.25). Raman spectra were acquired with an integration time of 0.2 s every 10 μm along the x- and y-axes. Subsequently, the spectral data sets were processed and converted into false-color images using the software WITec Project Plus. Image pixels assigned to ibuprofen spectra are depicted as red, whereas pixels assigned to CaSt are depicted as blue.

dx.doi.org/10.1021/mp4005782 | Mol. Pharmaceutics 2014, 11, 599−609

RESULTS

Granulation Liquid Characterization. The results of the granulation liquid characterization are summarized in Table 2.

Table 2. Contact Angles of Calcium Stearate with Ethanolic Solutions of Ibuprofen

solution	contact angle with CaSt (deg) (RSD)[a]	viscosity (mPa s) (RSD)[a]
ethanol	25.6 (3.13)	1.082[b]
29 wt % ibuprofen in ethanol	31.9 (5.71)	2.71 (2.16)
38 wt % ibuprofen in ethanol	34.3 (7.14)	3.39 (1.40)
44 wt % ibuprofen in ethanol	33.3 (2.32)	4.27 (0.17)

[a]Values were determined at 20 °C. [b]Values are taken from the literature.[57]

The addition of ibuprofen slightly increased the contact angles (from 25° to approximately 33°) independent of ibuprofen concentrations between 29 and 44%. Although this indicates that dissolved ibuprofen molecules lower the wettability, the CaSt particles were expected to get perfectly wetted as the contact angles were still well below 90°.

The viscosity increased with increasing ibuprofen concentration (Table 2) and was a linear function of the weight based ibuprofen concentration in the range between 29 and 44% ibuprofen. Note that values presented in Table 2 were obtained at 20 °C.

Measurements were not reproducible at 50 °C, since the ethanol evaporated quickly at this temperature, inducing ibuprofen crystallization during measurements. Therefore, results at 50 °C are not presented.

Crystallization Studies. During the crystallization studies, we focused on the impact of the initial ibuprofen concentration and the drying temperature on the recrystallization behavior of ibuprofen from ethanol. This gives an idea of the way ibuprofen recrystallizes from the granulation liquid during pellet drying. It should be noted that experiments were carried out on smooth glass slides and, thus, any interactions between CaSt and ibuprofen were neglected. Moreover, the drying kinetics may differ from those present in the pellets due to different geometries. Figure 1 shows microscopic images of ibuprofen that recrystallized from ethanol at either 20 °C (a; left column) or 50 °C (b; right column). These images were recorded after 48 h of drying; thereafter no changes in crystal shape and size were observed. It was found that crystals grown at 20 °C (Figures 1a2 and 1a3) were larger in comparison to crystals grown at 50 °C (Figures 1b2 and 1b3) for initial ibuprofen concentrations of 38 and 44 wt %, respectively. Regarding recrystallization from a 29% solution (Figures 1a1 and 1b1), the effects of drying temperature on crystal size were not as pronounced.

Upon considering crystal morphology, it was clearly observed that the initial ibuprofen concentration and drying temperature impacted the final crystal shape, and the arrangement of the crystals on the glass slides. The initial ibuprofen concentration influenced the final crystal shape at 20 °C: crystals that were grown from a 29 wt % solution formed dendritic structures as they were branching (Figure 1a1). At higher concentrations the crystals initially formed ropelike structures (Figures 1a2 and 1a3), from which large, cubic crystals emanated. Moreover, crystals formed agglomerates, covering comparatively large fractions of the glass slides independent of the initial concentration (Figure 1a).

In contrast, at 50 °C, the initial ibuprofen concentration did not appear to mediate crystal shape. The crystals formed ropelike structures, with attached needle-shaped crystals (Figure 1b). Domains were found that were surrounded by crystal ropes (Figure 1b).

DSC thermograms of all recrystallized ibuprofen samples revealed that ibuprofen did not change its polymorphic form upon recrystallization from ethanol (data not shown), which is in accordance with the literature.[36]

Quartz Crystal Microbalance with Dissipation (QCM-D). QCM measurements provide insight into the adsorption behavior of solute ibuprofen molecules onto solid CaSt. CaSt films were prepared by recrystallizing CaSt from pyridine. DSC

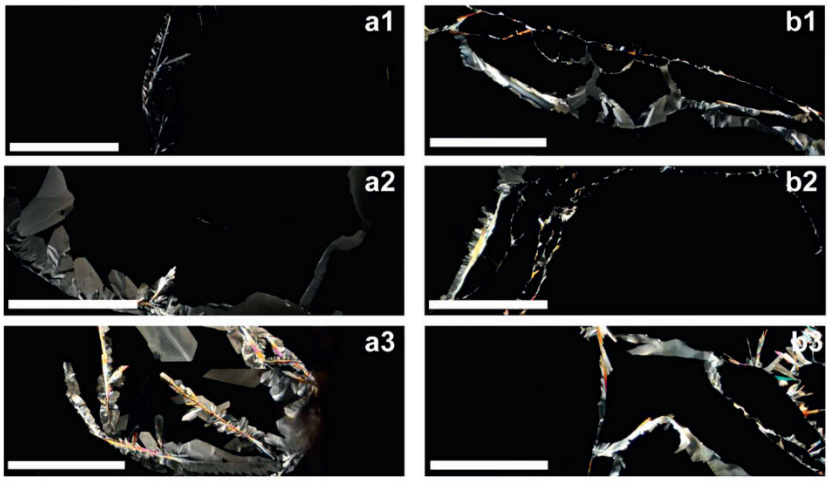

Figure 1. Microscopic images of ibuprofen after recrystallization from ethanol: (a) drying at 20 °C; (b) drying at 50 °C; (1) 29 wt % ibuprofen in ethanol; (2) 38 wt % ibuprofen in ethanol; (3) 44 wt % ibuprofen in ethanol. Scale bar: 3 mm.

thermograms of recrystallized CaSt did not indicate changes in the ibuprofen solid state (data not shown).

Figure 2 shows the results of the QCM-D measurements at 20 °C. First, the chamber was flushed with 0.1 wt % ibuprofen

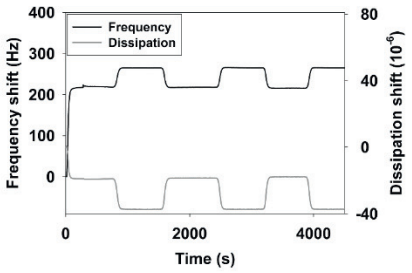

Figure 2. Frequency (third overtone) and dissipation curves from QCM measurements testing CaSt and ethanolic ibuprofen solutions at 20 °C.

solution. As ibuprofen was adsorbed onto the CaSt layer, the frequency was shifted toward lower values. Second, the chamber was flushed with ethanol and the initial frequency (i.e., the frequency of the crystal with the CaSt layer) was immediately reached, meaning ibuprofen desorbed. Similar observations were made when the chamber was flushed with solutions of higher ibuprofen concentrations (i.e., 0.5 and 1.0 wt %). The observed dissipation shifts were comparatively high when the sample was flushed with ibuprofen solutions and were not a function of the ibuprofen concentration. After the chamber was flushed with an ibuprofen solution, it was flushed with ethanol again, and the initial dissipation was instantly reached. As the dissipation was independent of the ibuprofen concentration, it follows that the same total amount of ibuprofen was adsorbed for every concentration.

Pellet Preparation and Drying Procedures. Both ways of ibuprofen incorporation, i.e., as powder (blended with CaSt) and as granulation solution (dissolved in ethanol), led to the formation of smooth extrudates and spherical pellets. The moisture content of the wet mass was around 20% for all batches and dropped to 10% during extrusion/spheronization due to ethanol evaporation in the open system.

Upon considering the drying process (Figure 3), pellets dried at 50 °C initially showed a drying rate (change of mass per unit time) that was nearly 2-fold the drying rate at 20 °C (Figure 3a). However, the drying profiles showed a steeper slope (i.e., a faster decay) at 50 °C. After 60 min, the drying rates approached zero and were similar at 20 and at 50 °C.

Pellet Characterization. *Differential Scanning Calorimetry (DSC).* Figure 4 comprises the results of the DSC measurements. For every preparation method only one curve is shown, as the thermograms did not deviate within multiple measurements of one batch or between different batches.

Figure 4a shows the DSC thermograms recorded during the first heating cycles of the pellets. The thermograms of ibuprofen powder (thermogram 1) and CaSt powder (thermogram 2) are shown for comparison reasons. For better reading the sharp endothermic peak of ibuprofen powder occurring during heating (thermogram 1) is not entirely shown. This peak showing an onset of 75.3 °C reflects the melting process and is in accordance with previously measured values.[37] The decline of the CaSt curve (thermogram 2) indicates water loss. For a detailed description of the CaSt thermogram the reader is

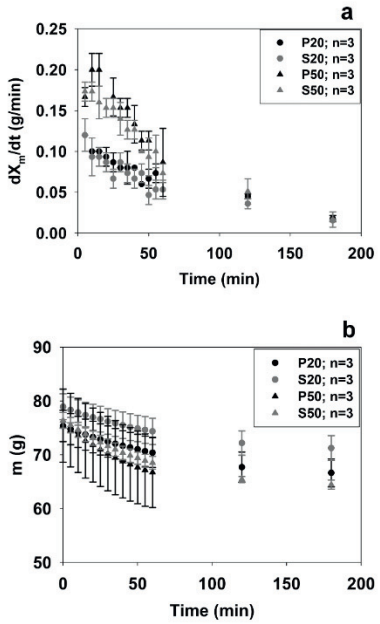

Figure 3. Drying profiles of tray dried pellets: (a) change of pellet mass per time unit as a function of time; (b) pellet mass as a function of time.

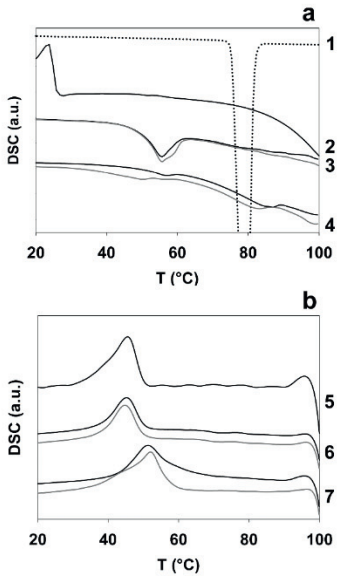

Figure 4. DSC thermograms of pellets and primary powders/powder mixture: (a) first heating cycle; (b) first cooling cycle. (1) Ibuprofen primary powder. (2) CaSt primary powder. (3, 6) Pellets dried at 20 °C: (black line) ibuprofen was applied as powder; (gray line) ibuprofen was applied as solution. (4, 7) Pellets dried at 50 °C: (black line) ibuprofen was applied as powder; (gray line) ibuprofen was applied as solution. (5) Physical mixture of CaSt and ibuprofen (mass ratio 1:1).

referred to a recent publication by Roblegg et al.[38] The thermograms of pellets dried at 20 °C, i.e., P20 (thermogram 3,

dx.doi.org/10.1021/mp4005782 | *Mol. Pharmaceutics* 2014, 11, 599−609

black line) and S20 (thermogram 3, gray line), show the characteristic endothermic ibuprofen peak, which was, however, shifted toward lower temperatures, yielding a peak onset around 50 °C. Pellets dried at 50 °C, i.e., P50 (spectrum 4, black line) and S50 (spectrum 4, gray line), showed different thermal behavior upon heating: Again, the characteristic ibuprofen peak was lowered to a peak maximum around 55 °C. However, compared to the thermograms of P20 and S20, this peak appeared small in height and was fairly broad. Additionally, a glass transition occurred at around 86 °C onset temperature. The thermograms of pellets prepared from ibuprofen powder (thermograms 3 and 4, black line) do not differ markedly from the thermograms of pellets prepared from ibuprofen solution (thermograms 3 and 4, gray line).

Considering the first cooling cycle of the pellets (Figure 4b), again, the method of ibuprofen incorporation, i.e., as powder (thermograms 6 and 7, black line) or as solution (thermograms 6 and 7, gray line), did not markedly affect the thermograms. Thermograms generated from the physical mixture of CaSt and ibuprofen (mass ratio 1 to 1) that was investigated in a previous study[20] are shown for comparison reasons (thermogram 5). Pellets dried at 20 °C, i.e., P20 (thermogram 6, black line) and S20 (thermogram 6, gray line), showed an exothermic peak upon cooling identical to the exothermic peak of the physical mixture. The cooling curves of pellets dried at 50 °C, i.e., P50 (thermogram 7, black line) and S50 (thermogram 7, gray line), however, are different. An exothermic peak was observed, but its onset was shifted toward higher temperatures.

Attenuated Total Reflectance Fourier Transform Infrared Spectroscopy (ATR-FTIR). ATR-FTIR investigations were performed to elucidate any interactions between ibuprofen and CaSt. Again, the results did not deviate within multiple measurements of one batch or within different batches for one preparation method. The spectrum of CaSt (Figure 5, spectrum

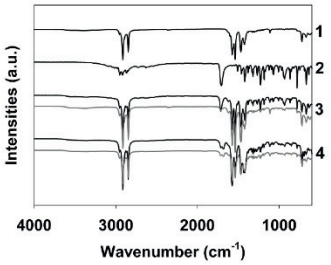

Figure 5. IR spectra of pellets and primary powders. (1) CaSt primary powder. (2) Ibuprofen primary powder. (3) Pellets dried at 20 °C: (black line) ibuprofen was applied as powder; (gray line) ibuprofen was applied as solution. (4) Pellets dried at 50 °C: (black line) ibuprofen was applied as powder; (gray line) ibuprofen was applied as solution.

1) includes bands between 2956 and 2848 cm^{-1} assignable to CH stretching vibrations. Furthermore, the spectrum contains a doublet at 1575 and 1540 cm^{-1}, which derives from asymmetric COO stretching vibrations.[39] The IR spectrum of ibuprofen (Figure 5, spectrum 2) shows a characteristic carbonyl band at 1707 cm^{-1}. The bands between 2954 and 2850 cm^{-1} were caused by CH stretching vibrations.

Spectra of pellets dried at 20 °C, i.e., P20 (Figure 5, spectrum 3, black line) and S20 (Figure 5, spectrum 3, gray line), showed both the characteristic COO stretching of CaSt and the carbonyl band of ibuprofen. In contrast, drying at 50 °C modified the pellets' IR spectra (Figure 5, spectra 4): Instead of the characteristic carbonyl band of ibuprofen at 1707 cm^{-1}, a doublet was found at 1707 and 1680 cm^{-1}.

Whether ibuprofen was applied as powder (Figure 5, spectrum 3, black line) or as solution (Figure 5, spectrum 3, gray line) did not modify any of the spectra markedly.

Small and Wide Angle X-ray Scattering (SWAXS). Since both primary powders were crystalline, some Bragg peaks[40] may have overlapped, especially in the molecular WAXS angular range. Consequently, data analysis was performed by applying the SAXS angular range, which depicts the internal order.[41] The SAXS spectra of the primary powders and the pellets are summarized in Figure 6. CaSt primary powder

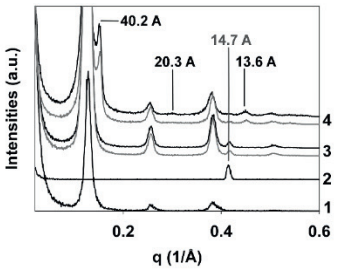

Figure 6. SAXS spectra of pellets and primary powders. (1) CaSt primary powder. (2) Ibuprofen primary powder. (3) Pellets dried at 20 °C: (black line) ibuprofen was applied as powder; (gray line) ibuprofen was applied as solution. (4) Pellets dried at 50 °C: (black line) ibuprofen was applied as powder; (gray line): ibuprofen was applied as solution.

(Figure 6, spectrum 1) shows lamellar phase morphology,[42] which was evident as the Bragg SAXS scattering peaks (i.e., q^* of 0.132 and q of 0.262 and 0.392 1/Å; where q^* refers to the scattering vector of the first order peak) possess ratios (q/q^*) of 1:2:3. Crystalline ibuprofen (i.e., primary powder) exhibits a characteristic peak at 14.7 Å (Figure 6, spectrum 2), which was clearly detected in the spectra of pellets dried at 20 °C, i.e., P20 (Figure 6, spectrum 3, black line) and S20 (Figure 6, spectrum 3, gray line). Likewise, in these spectra the three CaSt Bragg peaks were observed.

After drying at 50 °C, however, the pellets' SAXS spectra contained three additional peaks at 40.2, 20.3, and 13.7 Å (Figure 6, spectra 4). Moreover, the characteristic ibuprofen Bragg peak at 14.7 Å was not clearly observed. Pellets that were produced from ibuprofen powder (Figure 6, spectra 3 and 4, black lines) and pellets that were prepared from ibuprofen solution (Figure 6, spectra 3 and 4, gray lines) yielded identical SAXS spectra.

Raman Mapping. Raman mapping was performed to investigate the final ibuprofen distribution throughout the pellets. The results are shown in Figure 7. Larger fractions of ibuprofen were located at the pellet surface after drying at 20 °C (Figures 7c and 7d) than after drying at 50 °C (Figures 7e and 7f). Whether ibuprofen was applied as powder or as solution affected the final ibuprofen profiles: P20 (Figure 7c) still showed some ibuprofen in inner regions, whereas for S20 the pellet's interior was nearly depleted of ibuprofen (Figure 7d). For both P50 and S50 ibuprofen was found in the pellet's interior. However, the ibuprofen agglomerates were larger for P50 in comparison to S50.

dx.doi.org/10.1021/mp4005782 | *Mol. Pharmaceutics* 2014, 11, 599−609

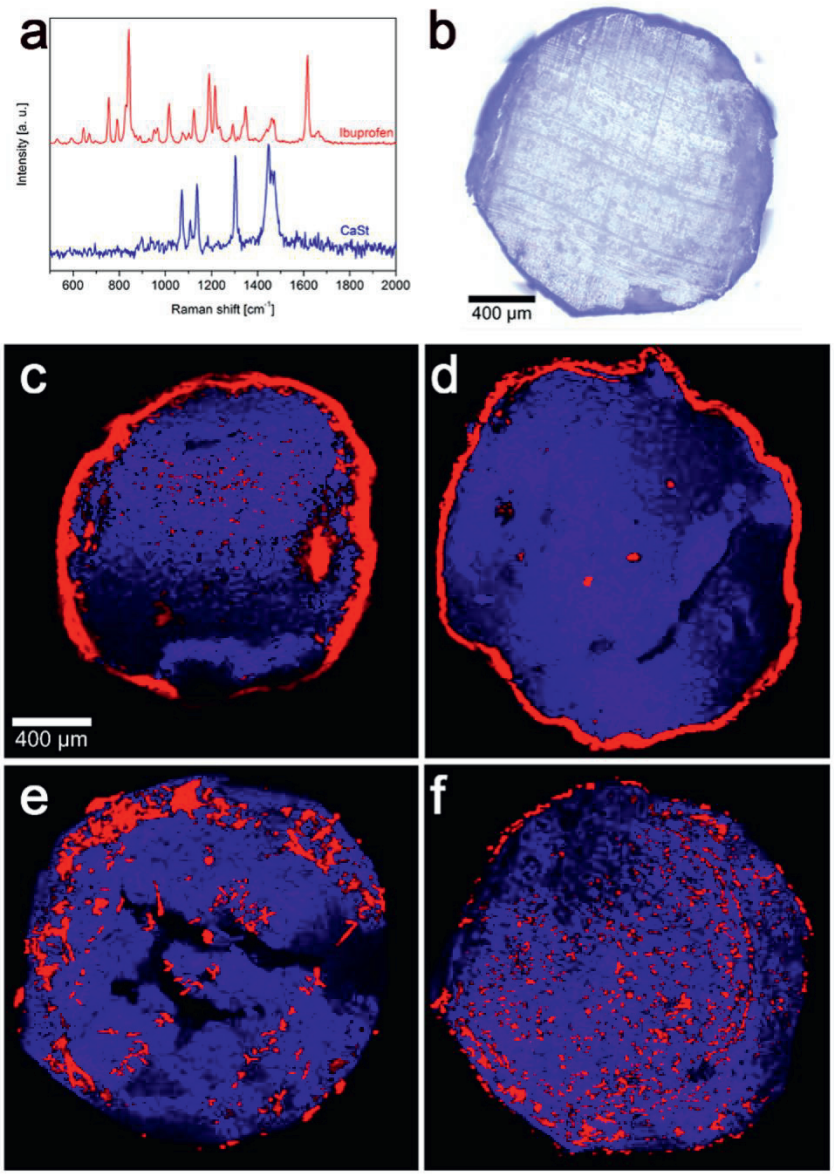

Figure 7. Results of Raman microscopy analysis: (a) single Raman spectra of primary powders; (b) exemplary light microscopic image of a pellet cross section prepared for Raman analysis; (c) Raman image of P20; (d) Raman image of S20; (e) Raman image of P50; (f) Raman image of S50. Ibuprofen is depicted in red, whereas CaSt is shown in blue color.

■ DISCUSSION

CaSt pellets comprising 15% ibuprofen were prepared via a wet extrusion/spheronization process followed by drying. As clearly illustrated by Raman mapping, the drying conditions indeed strongly impacted the ibuprofen distribution and the solid state of ibuprofen in the pellets. As all process steps prior to drying (i.e., blending, wetting, extrusion, and spheronization) were carried out under identical conditions, influences of these process steps were not evident.

Since we applied ibuprofen as an ethanolic solution (i.e., the granulation liquid) in parts of the experiments, the impact of dissolved ibuprofen on the physicochemical properties of ethanol that may affect the overall process performance were evaluated. The contact angles, which are a measure of the wettability and are crucial during the wetting step, were not a function of the ibuprofen concentration in the tested range (Table 2). CaSt particles were expected to get perfectly wetted during the wetting step as the contact angles are all well below 90°. Overall, both ways of ibuprofen incorporation, i.e., as powder (blended with CaSt) and as solution (dissolved in ethanol), led to the formation of extrudates with smooth surfaces and spherical pellets after spheronization.

dx.doi.org/10.1021/mp4005782 | *Mol. Pharmaceutics* 2014, 11, 599−609

During the drying process, a clear CRP was not observed for any of the batches, regardless of the drying temperature (Figure 3). This implies that the internal transport of liquid rapidly limited the transport of liquid toward the pellet surface.[43] Thereby, only falling rate periods (FRPs) were observed. Frequently, the solute concentration impacts the drying rate, since the vapor pressure decreases (according to Raoult's law) and the solution viscosity increases with higher solute concentrations (see Table 2). Hence, drying rates are increased for lower solute concentrations.[27] In the present study the drying profiles were similar for identical temperatures, i.e., P20 and S20 have a similar profile as well as P50 and S50. This indicates that the drying process was not impacted by the way ibuprofen was incorporated. Thus, it can be assumed that either a large fraction of ibuprofen powder was dissolved during the wetting step (yielding ibuprofen concentrations comparable to that of the ibuprofen solution) and/or the ibuprofen induced changes in liquid viscosity were below the threshold to considerably impact the drying rate.

During drying API migration may occur in cases where the API is not strongly adsorbed onto the carrier[23] and liquid viscosity is sufficiently low.[44−47] The viscosity of ethanol at 20 °C increases with increasing ibuprofen concentration (Table 2) and is a linear function of the weight based ibuprofen concentration. Nevertheless, viscosities were far below values at which drug migration is impacted, i.e., above 90 mPa s.[44] Hence, it is very unlikely that the solution viscosity affected drug migration during the drying experiments at 20 °C. Furthermore, liquid viscosities tend to decrease with increasing temperature, obeying an exponential decay proposed by Reynolds. This implies that drug migration was not influenced by the solution viscosity during drying at 50 °C, either.

Ibuprofen was found to only weakly adsorb onto CaSt during the QCM measurements (Figure 2). Generally, weak adsorption is caused by weak electrostatic and non-electrostatic interactions, including van der Waals interactions, hydrophilic interactions, and hydrogen bonding. As ethanol was used as solvent, the majority of the ibuprofen molecules were not dissociated and, thus, electrostatic interactions were negligible. From a molecular point of view, the weak hydrogen bonding between CaSt and ibuprofen may be explained by alignment of CaSt molecules: They build a bilayered structure, where the carboxyl groups (being attached to Ca cations) face each other.[48] Thereby, interactions (hydrogen bonding) of the CaSt carboxyl group with the ibuprofen carboxyl group are sterically hindered. Obviously, van der Waals interactions and hydrophobic interactions are not strong enough to provide constant adsorption.

Clearly, adsorption is a function of temperature as the adsorption constant varies with temperature.[49] However, in the present study QCM experiments at 50 °C failed. Consequently, it can be only proposed that most of the ibuprofen molecules (in dissolved state) did not adsorb onto the CaSt particles at 20 °C and were, thus, prone to migration during drying.

Solute API migration within a pellet during drying impacts the final API profile, which was elucidated via Raman mapping (Figure 7). The final ibuprofen profiles were a function of the drying temperature. More ibuprofen was located at the pellet surface after drying at 20 °C (Figure 7c,d) than after drying at 50 °C (Figure 7e,f). The impact of the drying temperature on the migration of solute molecules has been frequently described in literature with respect to impregnated catalysts. However, experimental findings are contradictory. Studies report that solute migration toward outer regions increased with increasing temperature,[50] while other studies found that solute migration was favored at lower temperatures.[51]

As the drying rate was rather constant at 20 °C (Figure 3), we can assume that convective liquid transport was sufficient to transport most of the solute ibuprofen molecules toward the surface, where they finally recrystallized, leaving an ibuprofen-enriched outer shell. This may be problematic for further pellet processing, as potential surface abrasion would lead to considerably lowered final API contents. Moreover, an ibuprofen-enriched outer shell can be expected to change the pellet compaction behavior. Concerning the in vitro dissolution behavior, the ibuprofen-enriched outer shell dramatically increases the dissolution rate, since most of the ibuprofen molecules are immediately available to the dissolution medium. Hence, the dissolution behavior is a function of the ibuprofen solubility only. In contrast, for homogeneous ibuprofen distributions the in vitro dissolution behavior was shown to be a function of the CaSt microstructure.[19,20]

Drying rates dropped fairly fast at 50 °C, and the CRP was comparatively short or even missing (Figure 3). Hence, lower fractions of solute ibuprofen were transported toward the pellet surface, resulting in a less ibuprofen-enriched pellet surface (Figure 7e,f). Instead, liquid evaporated inside the pores at early stages of the drying process, leaving a supersaturated ibuprofen solution, from which ibuprofen recrystallized. Additionally, film breakage might have occurred due to the comparatively high drying temperature.[26,27] Thereby, isolated liquid domains were formed and ibuprofen migration was limited to these domains. Furthermore, it is not clear if ibuprofen is (more strongly) adsorbed onto the CaSt matrix at 50 °C and was, thus, partly hindered from migration.

Whether ibuprofen was applied as powder or as solution affected the final API profiles. P20 (Figure 7c) still showed some ibuprofen in inner regions, whereas for S20 the pellet's interior was nearly depleted of ibuprofen (Figure 7d). This indicates incomplete ibuprofen powder dissolution during wetting, resulting in lower fractions of ibuprofen that were prone to redistribution.

Different observations were made for P50 (Figure 7e) and S50 (Figure 7f). For both pellet samples ibuprofen was found in the pellet's interior. However, the ibuprofen agglomerates were larger for P50 in comparison to S50. This may be again attributed to incomplete ibuprofen dissolution during wetting. In addition film breakage, leaving isolated liquid domains, was more pronounced at 50 °C, compared to 20 °C, and hence, ibuprofen migration was limited to the domains. During drying the solid ibuprofen particles were likely to act as crystal seeds. Dissolved ibuprofen particles preferably recrystallized on the seeds, since transport toward the pellet surface was impeded. Thereby, larger agglomerates were generated in comparison to P20.

In order to get a deeper understanding on the ibuprofen recrystallization under the applied drying conditions and, consequently, on the observed ibuprofen profiles, recrystallization studies were performed on glass slides. The drying temperatures modified the crystal morphology (in terms of shape and arrangement on the slides), which were attributed to different degrees of saturation as a function of temperature. Due to its temperature dependent solubility[52] the degree of ibuprofen saturation was dramatically decreased at 50 °C for identical initial concentrations. Differences in the crystal arrangement were due to film breakage phenomena. It is

assumed that the formation of domains was due to film breakage, which is favored early in the drying process for higher temperatures (due to increased drying rates)[24] and results in the formation of isolated liquid domains. Consequently, drug recrystallization can only occur within these domains resulting in smaller crystal agglomerates after evaporation at 50 °C. These findings are in accordance with the final ibuprofen distributions throughout the pellets after drying at 50 °C.

Besides the final API distribution, the drying conditions also modified the solid state of the API. The DSC thermograms of P20 and S20 show that the characteristic endothermic ibuprofen peak was shifted toward lower temperatures, i.e., peak onset around 50 °C (Figure 4a, thermograms 3). This indicates that a eutectic between ibuprofen and CaSt was formed[53] during heating of the pellets in the DSC apparatus. It is not believed that the eutectic was formed during drying for two reasons: First, drying was performed at 20 °C, which is far below the eutectic temperature (i.e., peak temperature of 55 °C[53]). Second, in a previous study we observed the lowered melting point during heating in the DSC for the physical mixture of ibuprofen and calcium stearate (mass ratio 1 to 1), as well.[20] In addition, IR spectra of P20 and S20 (Figure 5, spectra 3) showed both the characteristic COO stretching of CaSt and the carbonyl band of ibuprofen. Hence, it can be assumed that drying at 20 °C did not lead to any interactions between ibuprofen and CaSt. These findings are further supported by the results of the SAXS measurements. The characteristic ibuprofen peak at 14.7 Å (Figure 6, spectrum 2) was detected in spectra of pellets dried at 20 °C (Figure 6, spectra 3). Likewise, the three CaSt Bragg peaks were observed indicating that CaSt did not change its solid state upon drying, either. Overall, we conjuncture that drying at 20 °C did neither affect the solid state of ibuprofen nor induce interactions between ibuprofen and CaSt.

P50 and S50, however, showed different thermal behavior upon heating in the DSC apparatus (Figure 4a, thermograms 4). Specifically, the characteristic ibuprofen peak was lowered to a peak maximum around 55 °C corresponding to the eutectic. Additionally, a glass transition occurred at around 86 °C onset temperature. From these data we conclude that drying at 50 °C may have mediated the physicochemical properties of ibuprofen in two ways: (i) the formation of a eutectic between ibuprofen and CaSt and (ii) the transformation of the initial crystalline ibuprofen into an amorphous state. During drying, the temperature was likely to rise above 50 °C as soon as the pellets were locally dried. Thereby, the partial formation of a eutectic between ibuprofen and CaSt was favored. Nevertheless, the eutectic could again have been formed during heating in the DSC. In contrast, the glass transition was not observed in the thermograms of P20 and S20, which implies that the glass transition of P50 and S50 was attributed not to the measurement procedure but rather to the drying process.

Moreover, the cooling curves of P50 and S50 (Figure 4b, thermograms 7) were different from the cooling curves of P20 and S20 (Figure 4b, thermograms 6) and the physical mixture (Figure 4b, thermograms 5). An exothermic peak indicating recrystallization was observed, but its onset was shifted toward higher temperatures. This further indicates changes in the solid state of ibuprofen after drying at 50 °C.

Likewise, modifications in the pellets' IR spectra (Figure 5, spectra 4) were found: Instead of the characteristic carbonyl band of ibuprofen at 1707 cm^{-1}, a doublet was found at 1707 and 1680 cm^{-1}. The doublet indicates that drying at 50 °C induced interactions between ibuprofen and CaSt resulting in partial shifting of the characteristic ibuprofen band toward lower wavenumbers. The doublet suggests hydrogen bonding between ibuprofen and CaSt.[54] The pellets' SAXS spectra after drying at 50 °C again indicated changes in the solid state. The spectra contained three additional peaks at 40.2, 20.3, and 13.7 Å (Figure 6, spectra 4). These Bragg SAXS scattering peaks (i.e., q^* of 0.156 and q of 0.308 and 0.463 1/Å) exhibit ratios (q/q^*) of 1:2:3, which are indicative for the presence of a well ordered lamellar phase morphology. Hence, it seems likely that CaSt partially changed its internal structure upon drying at 50 °C. Thereafter, CaSt was present in two lamellar phases. In addition to drying induced structural changes of CaSt, modifications in the ibuprofen solid state were observed: The characteristic ibuprofen Bragg peak at 14.7 Å was not clearly observed, which implies that ibuprofen had transformed in its amorphous state, which is in accordance with the DSC measurements (Figure 4). Considering the DSC thermograms and the IR and the SAXS spectra (Figure 5), we propose that a certain fraction of ibuprofen interacted with the second lamellar phase (formed during drying) on a molecular level. Thereby, a solid dispersion, which comprises amorphous ibuprofen, was created. The transformation of ibuprofen, a poorly water-soluble API, into its amorphous state may be desirable as it benefits the in vitro dissolution characteristics of ibuprofen.[55,56]

■ CONCLUSIONS

The impact of drying on ibuprofen that was incorporated into pellets via wet extrusion/spheronization was 2-fold, i.e., modifications in the solid state and in the final spatial ibuprofen distribution. Elevated temperatures that are commonly applied during drying of pellets were sufficient to modify the solid state of both ibuprofen and CaSt. Drying at 50 °C caused the formation of a second lamellar CaSt phase, which interacted with (parts of) ibuprofen on a molecular level via hydrogen bonding. Thereby, a solid dispersion containing amorphous ibuprofen was formed. Modifications in the solid state were not observed after drying at 20 °C.

The final ibuprofen distribution throughout the pellets was a function of the drying temperature and the dissolved ibuprofen fraction. As the adsorption tendency of solute ibuprofen molecules onto solid CaSt was rather low, the majority of dissolved ibuprofen molecules were prone to redistribution upon drying. For drying at 20 °C, ibuprofen was accumulated at the pellet surface due to strong convective liquid flow toward the surface. Higher amounts of ibuprofen were found in the pellet's interior when ibuprofen was applied as powder, indicating incomplete ibuprofen dissolution during wetting. For drying at 50 °C, the ibuprofen concentration in the pellet's interior was increased due to the absence of a constant rate period and an increased potential of film breakage to occur. Larger ibuprofen agglomerates were found in the pellet's interior when ibuprofen was applied as powder due to the combined effects of incomplete ibuprofen dissolution during wetting and favored film breakage during drying.

This study demonstrated that the drying conditions may significantly modify the API's physicochemical properties for certain pellet formulations. Likewise, final dosage form properties that are related to the solid state of the API and its distribution throughout the pellets, such as dissolution characteristics, are expected to be a strong function of the drying process parameters.

AUTHOR INFORMATION

Corresponding Author

*Karl Franzens University of Graz, Institute of Pharmaceutical Sciences/Pharmaceutical Technology, Humboldtstrasse 46, 8010 Graz, Austria. E-mail: eva.roblegg@uni-graz.at. Phone: +43 316 380-8888. Fax: +43 316 380-910.

Notes

The authors declare no competing financial interest.

ACKNOWLEDGMENTS

The authors would like to thank G.L. Pharma (Lannach, Austria) for the kind donation of ibuprofen. Christoph Neubauer (Institute for Process and Particle Engineering, Graz University of Technology) is acknowledged for his assistance with the granulation liquid characterization.

REFERENCES

(1) Farber, L.; Tardos, G. I.; Michaels, J. N. Evolution and structure of drying material bridges of pharmaceutical excipients: studies on a microscope slide. *Chem. Eng. Sci.* **2003**, *58* (19), 4515−4525.

(2) Airaksinen, S.; Karjalainen, M.; Räsänen, E.; Rantanen, J.; Yliruusi, J. Comparison of the effects of two drying methods on polymorphism of theophylline. *Int. J. Pharm.* **2004**, *276* (1−2), 129−141.

(3) Davis, T.; Peck, G.; Stowell, J.; Morris, K.; Byrn, S. Modeling and Monitoring of Polymorphic Transformations During the Drying Phase of Wet Granulation. *Pharm. Res.* **2004**, *21* (5), 860−866.

(4) Tantry, J. S.; Tank, J.; Suryanarayanan, R. Processing-induced phase transitions of theophylline—implications on the dissolution of theophylline tablets. *J. Pharm. Sci.* **2007**, *96* (5), 1434−1444.

(5) Di Martino, P.; Malaj, L.; Censi, R.; Martelli, S. Physico-chemical and technological properties of sodium naproxen granules prepared in a high-shear mixer-granulator. *J. Pharm. Sci.* **2008**, *97* (12), 5263−5273.

(6) Burggraeve, A.; Sandler, N.; Heinämäki, J.; Räikkönen, H.; Remon, J. P.; Vervaet, C.; De Beer, T.; Yliruusi, J. Real-time image-based investigation of spheronization and drying phenomena using different pellet formulations. *Eur. J. Pharm. Sci.* **2011**, *44* (5), 635−642.

(7) Airaksinen, S.; Karjalainen, M.; Kivikero, N.; Westermarck, S.; Shevchenko, A.; Rantanen, J.; Yliruusi, J. Excipient selection can significantly affect solid-state phase transformation in formulation during wet granulation. *AAPS PharmSciTech* **2005**, *6* (2), E311−E322.

(8) Berggren, J.; Alderborn, G. Effect of drying rate on porosity and tabletting behaviour of cellulose pellets. *Int. J. Pharm.* **2001**, *227* (1−2), 81−96.

(9) Wlosnewski, J. C.; Kumpugdee-Vollrath, M.; Sriamornsak, P. Effect of drying technique and disintegrant on physical properties and drug release behavior of microcrystalline cellulose-based pellets prepared by extrusion/spheronization. *Chem. Eng. Res. Des.* **2010**, *88* (1), 100−108.

(10) Gómez-Carracedo, A.; Souto, C.; Martinez-Pacheco, R.; Concheiro, A.; Gómez-Amoza, J. L. Incidence of drying on microstructure and drug release profiles from tablets of MCC-lactose-Carbopol® and MCC-dicalcium phosphate-Carbopol® pellets. *Eur. J. Pharm. Biopharm.* **2008**, *69* (2), 675−685.

(11) Gómez-Carracedo, A.; Souto, C.; Martínez-Pacheco, R.; Concheiro, A.; Gómez-Amoza, J. L. Microstructural and drug release properties of oven-dried and of slowly or fast frozen freeze-dried MCC-Carbopol® pellets. *Eur. J. Pharm. Biopharm.* **2007**, *67* (1), 236−245.

(12) Sousa, J. J.; Sousa, A.; Podczeck, F.; Newton, J. M. Influence of process conditions on drug release from pellets. *Int. J. Pharm.* **1996**, *144* (2), 159−169.

(13) Dyer, A. M.; Khan, K. A.; Aulton, M. E. Effect of the Drying Method on the Mechanical and Drug Release Properties of Pellets Prepared by Extrusion-Spheronization. *Drug Dev. Ind. Pharm.* **1994**, *20* (20), 3045−3068.

(14) Bashaiwoldu, A. B.; Podczeck, F.; Newton, J. M. A study on the effect of drying techniques on the mechanical properties of pellets and compacted pellets. *Eur. J. Pharm. Biopharm.* **2004**, *21* (2−3), 119−129.

(15) Murray, T.; Rough, S. L.; Wilson, D. I. The Effect of Drying Technique on Tablets Formed from Extrusion-spheronization Granules. *Chem. Eng. Res. Des.* **2007**, *85* (7), 996−1004.

(16) Bashaiwoldu, A. B.; Podczeck, F.; Newton, J. M. The application of non-contact laser profilometry to the determination of permanent structural change induced by compaction of pellets: II. Pellets dried by different techniques. *Eur. J. Pharm. Biopharm.* **2004**, *22* (1), 55−61.

(17) Serajuddin, A. T. M.; Thakur, A. B.; Ghoshal, R. N.; Fakes, M. G.; Ranadive, S. A.; Morris, K. R.; Varia, S. A. Selection of solid dosage form composition through drug−excipient compatibility testing. *J. Pharm. Sci.* **1999**, *88* (7), 696−704.

(18) Liew, C.; Gu, L.; Soh, J. P.; Heng, P. S. Functionality of Cross-Linked Polyvinylpyrrolidone as a Spheronization Aid: A Promising Alternative to Microcrystalline Cellulose. *Pharm. Res.* **2005**, *22* (8), 1387−1388.

(19) Schrank, S.; Hodzic, A.; Zimmer, A.; Glasser, B.; Khinast, J.; Roblegg, E. Ibuprofen-Loaded Calcium Stearate Pellets: Drying-Induced Variations in Dosage Form Properties. *AAPS PharmSciTech* **2012**, *13* (2), 686−698.

(20) Schrank, S.; Kann, B.; Windbergs, M.; Glasser, B. J.; Zimmer, A.; Khinast, J.; Roblegg, E. Microstructure of Calcium Stearate Matrix Pellets: A Function of the Drying Process. *J. Pharm. Sci.* **2013**, *102* (11), 3987−3997.

(21) Kowalski, S. J. Toward a thermodynamics and mechanics of drying processes. *Chem. Eng. Sci.* **2000**, *55* (7), 1289−1304.

(22) Scherer, G. W. Theory of Drying. *J. Am. Ceram. Soc.* **1990**, *73* (1), 3−14.

(23) Lekhal, A.; Glasser, B. J.; Khinast, J. G. Impact of drying on the catalyst profile in supported impregnation catalysts. *Chem. Eng. Sci.* **2001**, *56* (15), 4473−4487.

(24) Liu, X.; Khinast, J. G.; Glasser, B. J. Drying of Supported Catalysts: A Comparison of Model Predictions and Experimental Measurements of Metal Profiles. *Ind. Eng. Chem. Res.* **2010**, *49* (6), 2649−2657.

(25) Liu, X.; Khinast, J. G.; Glasser, B. J. A parametric investigation of impregnation and drying of supported catalysts. *Chem. Eng. Sci.* **2008**, *63* (18), 4517−4530.

(26) Komiyama, M.; Merrill, R. P.; Harnsberger, H. F. Concentration profiles in impregnation of porous catalysts: Nickel on alumina. *J. Catal.* **1980**, *63* (1), 35−52.

(27) Liu, X.; Khinast, J. G.; Glasser, B. J. Drying of supported catalysts for low melting point precursors: Impact of metal loading and drying methods on the metal distribution. *Chem. Eng. Sci.* **2012**, *79* (0), 187−199.

(28) Wong, M. W. Y.; Mitchell, A. G. Physicochemical characterization of a phase change produced during the wet granulation of chlorpromazine hydrochloride and its effects on tableting. *Int. J. Pharm.* **1992**, *88* (1−3), 261−273.

(29) Otuska, M.; Hasegawa, H.; Matsuda, Y. Effect of Polymorphic Forms of Bulk Powders on Pharmaceutical Properties of Carbamazepine Granules. *Chem. Pharm. Bull.* **1999**, *47* (6), 852−856.

(30) Phadnis, N. V.; Suryanarayanan, R. Polymorphism in anhydrous theophylline—implications on the dissolution rate of theophylline tablets. *J. Pharm. Sci.* **1997**, *86* (11), 1256−1263.

(31) Debnath, S.; Suryanarayanan, R. Influence of processing-induced phase transformations on the dissolution of theophylline tablets. *AAPS PharmSciTech* **2004**, *5* (1), 39−49.

(32) Herman, J.; Remon, J. P.; Visavarungroj, N.; Schwartz, J. B.; Klinger, G. H. Formation of theophylline monohydrate during the pelletisation of microcrystalline cellulose-anhydrous theophylline blends. *Int. J. Pharm.* **1988**, *42* (1−3), 15−18.

(33) Yano, H.; Kleinebudde, P. Improvement of Dissolution Behavior for Poorly Water-Soluble Drug by Application of Cyclodextrin in Extrusion Process: Comparison between Melt Extrusion and Wet Extrusion. *AAPS PharmSciTech* **2010**, *11* (2), 885−893.

(34) Rodahl, M.; Hook, F.; Krozer, A.; Brzezinski, P.; Kasemo, B. Quartz crystal microbalance setup for frequency and Q-factor measurements in gaseous and liquid environments. *Rev. Sci. Instrum.* **1995**, *66* (7), 3924−3930.
(35) Roblegg, E.; Ulbing, S.; Zeissmann, S.; Zimmer, A. Development of lipophilic calcium stearate pellets using ibuprofen as model drug. *Eur. J. Pharm. Biopharm.* **2010**, *75* (1), 56−62.
(36) Garekani, H. A.; Sadeghi, F.; Badiee, A.; Mostafa, S. A.; Rajabi-Siahboomi, A. R. Crystal Habit Modifications of Ibuprofen and Their Physicomechanical Characteristics. *Drug Dev. Ind. Pharm.* **2001**, *27* (8), 803−809.
(37) Lerdkanchanaporn, S.; Dollimore, D.; Evans, S. J. Phase diagram for the mixtures of ibuprofen and stearic acid. *Thermochim. Acta* **2001**, *367*−*368* (0), 1−8.
(38) Roblegg, E.; Jäger, E.; Hodzic, A.; Koscher, G.; Mohr, S.; Zimmer, A.; Khinast, J. Development of sustained-release lipophilic calcium stearate pellets via hot melt extrusion. *Eur. J. Pharm. Biopharm.* **2011**, *79* (3), 635−645.
(39) Kimura, F.; Umemura, J.; Takenaka, T. FTIR-ATR Studies on Langmuir-Blodgett Films of Stearic Acid with 1−9 Monolayers. *Langmuir* **1985**, *2*, 96−102.
(40) Bragg, W. L. The diffraction of short electromagnetic waves by a crystal. *Proc. Cambridge Philos. Soc.* **1913**, *17*, 43−57.
(41) Glatter, O.; Kratky, O. *Small angle x-ray scattering*; Academic Press: New York, 1982.
(42) Deamer, D. W.; Leonard, R.; Tardieu, A.; Branton, D. Lamellar and hexagonal lipid phases visualized by freeze-etching. *Biochim. Biophys. Acta, Biomembr.* **1970**, *219* (1), 47−60.
(43) Prakash, S.; Jha, S. K.; Datta, N. Performance evaluation of blanched carrots dried by three different driers. *J. Food Eng.* **2004**, *62* (3), 305−313.
(44) Warren, J. W.; Price, J. C. Drug migration during drying of tablet granulations II: Effect of binder solution viscosity and drying temperature. *J. Pharm. Sci.* **1977**, *66* (10), 1409−1412.
(45) Kapsidou, T.; Nikolakakis, I.; Malamataris, S. Agglomeration state and migration of drugs in wet granulations during drying. *Int. J. Pharm.* **2001**, *227* (1−2), 97−112.
(46) Kiekens, F.; Zelko, R.; Remon, J. P. Influence of Drying Temperature and Granulation Liquid Viscosity on the Inter- and Intragranular Drug Migration in Tray-Dried Granules and Compacts. *Pharm. Dev. Technol.* **2000**, *5* (1), 131−137.
(47) Kiekens, F.; Zelko, R.; Remon, J. P. A Comparison of the Inter- and Intragranular Drug Migration in Tray- and Freeze-Dried Granules and Compacts. *Pharm. Dev. Technol.* **1999**, *4* (3), 415−420.
(48) Garnier, P.; Gregoire, P.; Montmitonnet, P.; Delamare, F. Polymorphism of crystalline phases of calcium stearate. *J. Mater. Sci.* **1988**, *23* (9), 3225−3231.
(49) Liu, Y. Some consideration on the Langmuir isotherm equation. *Colloids Surf., A* **2006**, *274* (1−3), 34−36.
(50) Van Den Berg, G. H.; Rijnten, H. T. The Impregnation and Drying Step in Catalyst Manufacturing. *Stud. Surf. Sci. Catal.* **1979**, *3*, 265−277.
(51) Komiyama, M. Design and Preparation of Impregnated Catalysts. *Catal. Rev.* **1985**, *27* (2), 341−372.
(52) Manrique, J.; Martinez, F. Solubility of Ibuprofen in Some Ethanol + Water Cosolvent Mixtures at Several Temperatures. *Lat. Am. J. Pharm.* **2007**, *26* (3), 344−354.
(53) Gordon, R. E.; VanKoevering, C. L.; Reits, D. J. Utilization of differential scanning calorimetry in the compatibility screening of ibuprofen with the stearate lubricants and construction of phase diagrams. *Int. J. Pharm.* **1984**, *21* (1), 99−105.
(54) Stott, P. W.; Williams, A. C.; Barry, B. W. Transdermal delivery from eutectic systems: enhanced permeation of a model drug, ibuprofen. *J. Controlled Release* **1998**, *50* (1−3), 297−308.
(55) Shen, S.-C.; Ng, W. K.; Chia, L.; Dong, Y.-C.; Tan, R. B. H. Stabilized amorphous state of ibuprofen by co-spray drying with mesoporous SBA-15 to enhance dissolution properties. *J. Pharm. Sci.* **2010**, *99* (4), 1997−2007.
(56) Mallick, S.; Pattnaik, S.; Swain, K.; De, P. K.; Saha, A.; Ghoshal, G.; Mondal, A. Formation of physically stable amorphous phase of ibuprofen by solid state milling with kaolin. *Eur. J. Pharm. Biopharm.* **2008**, *68* (2), 346−351.
(57) Nikam, P. S.; Shirsat, L. N.; Hasan, M. Density and Viscosity Studies of Binary Mixtures of Acetonitrile with Methanol, Ethanol, Propan-1-ol, Propan-2-ol, Butan-1-ol, 2-Methylpropan-1-ol, and 2-Methylpropan-2-ol at (298.15, 303.15, 308.15, and 313.15) K. *J. Chem. Eng. Data* **1998**, *43* (5), 732−737.

5.3 The Effect of the Drying Temperature on the Properties of Wet-Extruded Calcium Stearate Pellets: Pellet Microstructure, Drug Distribution, Solid State and Drug Dissolution

The Effect of the Drying Temperature on the Properties of Wet-Extruded Calcium Stearate Pellets: Pellet Microstructure, Drug Distribution, Solid State and Drug Dissolution

S. Schrank, B. Kann, E. M. Saurugger, M. Hainschitz, M. Windbergs, B.J. Glasser, J. G. Khinast, E. Roblegg

Int. J. Pharm. **2015**;478:779-787.

DOI: 10.1016/j.ijpharm.2014.12.030

International Journal of Pharmaceutics 478 (2015) 779–787

Contents lists available at ScienceDirect

International Journal of Pharmaceutics

journal homepage: www.elsevier.com/locate/ijpharm

The effect of the drying temperature on the properties of wet-extruded calcium stearate pellets: Pellet microstructure, drug distribution, solid state and drug dissolution

S. Schrank [a,b,c], B. Kann [d], E. Saurugger [b], M. Hainschitz [b], M. Windbergs [d,e], B.J. Glasser [f], J. Khinast [a,b], E. Roblegg [b,c,*]

[a] Institute for Process and Particle Engineering, Graz University of Technology, Austria
[b] Research Center Pharmaceutical Engineering GmbH, Graz, Austria
[c] Institute of Pharmaceutical Sciences, Department of Pharmaceutical Technology, University of Graz, Austria
[d] Department of Biopharmaceutics and Pharmaceutical Technology, Saarland University, Saarbruecken, Germany
[e] Helmholtz Centre for Infection Research (HZI) and Helmholtz-Institute for Pharmaceutical Research Saarland (HIPS), Department of Drug Delivery (DDEL), Saarbruecken, Germany
[f] Department of Chemical and Biochemical Engineering, Rutgers University, Piscataway, NJ, USA

ARTICLE INFO

Article history:
Received 31 October 2014
Received in revised form 12 December 2014
Accepted 13 December 2014
Available online 16 December 2014

Keywords:
Extrusion/spheronization
Ibuprofen
Differential scanning calorimetry
Infrared spectroscopy
Small and wide angle X-ray scattering
Raman imaging

ABSTRACT

Although drying is widely applied during the manufacturing of solid dosage forms, its potential effect on the product's (key) properties is often underestimated. Hence, the present study addresses drying related modifications of wet-extruded pellets comprising calcium stearate (CaSt, matrix former) and ibuprofen (model drug). After spheronization, the pellets were tray dried at different temperatures. The dried pellets were evaluated regarding their microstructure, the ibuprofen distribution, solid state modifications and the resulting in-vitro dissolution profiles. The ibuprofen distribution profiles along the pellets' cross-sections varied for the different drying conditions. The profiles turned from inhomogeneous to uniform with increasing drying temperature. Temperatures above 20 °C yielded solid state modifications, including ibuprofen transition into the amorphous state and the formation of eutectic compositions. As none of the batches exhibited a high specific surface area associated with an open, well-interconnected pore system, the dissolution profiles were a function of the ibuprofen distribution. Differences in the solid state did not contribute to the dissolution behavior, since the CaSt matrix did not swell or dissolve in the dissolution medium. These findings show that drying may considerably affect the final product properties even for moderate drying conditions.

1. Introduction

Drying operations are often encountered during the manufacturing of solid pharmaceutical products. Frequently, its purpose is to remove any liquid, which was added for processing reasons. For example, during wet granulation processes, the formation of micro-particulate systems is only possible due to the addition of liquid. This liquid needs to be removed in a final processing step. Thereby, permanent solid bridges between the primary particles are formed (Farber et al., 2003), segregation and stability issues of the product are avoided and further processing is facilitated.

The wet extrusion/spheronization process is another technique to manufacture micro-particles. Similar to other wet granulation techniques, the liquid is finally removed during drying. However, drying does not only remove the liquid, but may modify the micro-particles', so-called pellets', properties. First, drying potentially affects the microstructure of the pellets (Baert et al., 1993; Balaxi et al., 2009; Bashaiwoldu et al., 2004b; Berggren and Alderborn, 2001b; Gómez-Carracedo et al., 2007), as materials that swell in the granulation liquid and shrink to a certain extent upon drying are frequently used as matrix materials (Berggren and Alderborn, 2001a; Fielden et al., 1992; Kleinebudde, 1994; Schrank et al., 2012, 2013). Hence, characteristics associated with the pellet micro-structure, including the in-vitro dissolution characteristics (Dyer et al., 1994; Gómez-Carracedo et al., 2007, 2008; Lutchman et al.,

* Corresponding author at: Karl Franzens University of Graz, Institute of Pharmaceutical Sciences/Pharmaceutical Technology, Universitätsplatz 1, 8010 Graz, Austria. Tel.: +43 316 380 8888; fax: +43 316 380 910.
E-mail address: eva.roblegg@uni-graz.at (E. Roblegg).

http://dx.doi.org/10.1016/j.ijpharm.2014.12.030
0378-5173/

2005; Schrank et al., 2012, 2013; Sousa et al., 1996; Wlosnewski et al., 2010), the compaction behavior (Bashaiwoldu et al., 2004a,b, b; Berggren and Alderborn, 2001b; Gómez-Carracedo et al., 2008; Murray et al., 2007) and the mechanical strength (Schrank et al., 2012; Wlosnewski et al., 2010) were shown to be a function of the drying process conditions. Second, drying alters the physicochemical properties of the active pharmaceutical ingredient (API) after it is dissolved in the granulation liquid. Drying induced modifications of the API were reported with respect to solid state transitions (Herman et al., 1989; Sandler et al., 2005; Schrank et al., 2014; Yano and Kleinebudde, 2010) after re-crystallization and API re-distribution throughout the pellets (i.e., the API profile) due to intra-particular migration (Schrank et al., 2014). Polymorphic transitions affect the in-vitro dissolution behavior (Debnath and Suryanarayanan, 2004; Phadnis and Suryanarayanan, 1997; Yano and Kleinebudde, 2010). API accumulation at certain pellet regions was observed to alter the pellet's mechanical properties (Poutiainen et al., 2012) and the in-vitro dissolution characteristics (Huang and Brazel, 2001).

In general, a drying process can be subdivided into three stages according to the observed drying rate: (i) the pre-heating period, (ii) the constant-rate period (CRP) and (iii) the falling-rate period (FRP). During the pre-heating period the wet pellet surface temperature steadily increases yielding gradually increasing evaporation rates. During the CRP the pellet surface temperature is constant (i.e., the wet bulb temperature), since the energy loss due to evaporation and the heating rate are in equilibrium. The rate of evaporation does not change as long as the pellet surface is kept saturated due to capillary liquid flow from the pellet's interior toward the surface. At a certain point, however, the moisture content inside the pellet drops below a critical value indicating the start of the FRP, where the surface is not saturated anymore. The liquid recedes into the pellet, yielding a steady reduction of the drying rate. The liquid evaporates inside the pores and the rate of evaporation is governed by the vapor removal through the porous system via diffusion. Dry patches appear at or close to the pellet surface, at which the temperature gradually approaches the temperature of the surrounding drying medium (most often air).

The CRP is associated with uniform pellet shrinkage, leaving decreased pellet diameters and/or modified pore structures. The FRP does not induce changes with respect to the pellet diameter. Still, the inner pore structure may be changed in terms of pore size distributions (Schrank et al., 2013).

During the CRP dissolved API is transported with the convective liquid flow toward the pellets surface. The convective flow is more pronounced for a high permeability (Lekhal et al., 2001), which is governed by the microstructure, i.e., the pore size distribution, pore shape, pore connectivity and pore tortuosity (Liu et al., 2008). Once a supersaturated solution is created due to liquid evaporation, the API re-crystallizes at the pellet surface. API enriched shells are formed, while the pellet's interior is depleted of API. Alternatively, dissolved API may be transported back toward the center by diffusion driven by the concentration gradient that was formed over the pellet's cross-section. As a consequence, the API profile becomes uniform again or the API may even accumulate at the pellet's center. The final concentration profile is determined by the complex interplay of convection, diffusion, re-crystallization thermodynamics and the heat and mass transfer in the film around the pellet.

Migration of the API toward the pellet surface is prevented during the FRP. Instead, back-diffusion may become dominant and the API can accumulate in the pellet's center. For very harsh drying conditions (typically no CPR is observed) drug migration is even impeded. Here, convective flow toward the surface is suppressed and hence, no concentration gradient causing diffusion is formed. Moreover, film breakage occurs (Komiyama et al., 1980) (i.e., disruption of the formerly continuous liquid phase). Thereby, isolated liquid domains are formed suppressing API migration.

The present study investigates tray drying of pellets produced using wet extrusion/spheronization. In our previous work pellets were dried at 20 and 50 °C and the ibuprofen distribution profiles and solid state modifications were evaluated (Schrank et al., 2014). In the present study pellets were dried at different temperatures (i.e., 30, 40 and 60 °C) and the ibuprofen distribution and its solid state were investigated. Additionally, the pellet microstructure and the in-vitro dissolution profiles were determined for all drying temperatures (i.e., 20, 30, 40, 50 and 60 °C). Thereby, we aimed at generating a deep understanding of the effect of the drying temperature on: (i) the pellet microstructure, (ii) the spatial ibuprofen distribution, (iii) the solid state of ibuprofen and (iv) the corresponding in-vitro dissolution performance.

2. Materials and methods

2.1. Materials

Vegetable calcium stearate (CaSt) was purchased from Werba-Chem GmbH, Vienna, Austria. Ibuprofen (G.L. Pharma, Lannach, Austria) served as a model API and 96 v% ethanol (Merck, Darmstadt, Germany) was used as granulation liquid. Monopotassium phosphate and sodium hydroxide (both Merck, Darmstadt, Germany) served for dissolution medium preparation. Milli-Q water (ultrapure water according to ISO 3696), triethylamine, orthophosphoric acid 85%, and acetonitrile (all Merck, Darmstadt, Germany) were used as mobile phase during the HPLC measurements.

2.2. Pellet preparation and drying

Pellets containing 15 w% ibuprofen and CaSt as matrix material were prepared via wet extrusion/spheronization according to Schrank et al. (2014). In contrast to conventional extrusion processes, where the API is added as powder, ibuprofen was dissolved in the granulation liquid, i.e., ethanol. Thereby, a large fraction of ibuprofen stayed in the dissolved state throughout the entire preparation process and the impact of drying on the API's physicochemical properties could readily be studied. In the previous study tray drying was performed at 20 and 50 °C (Schrank et al., 2014). During the present study pellets were dried at 30, 40, and 60 °C and at a relative humidity ranging between 25 and 35%. Immediately after spheronization, the pellets were transferred into round, flat-bottom bowls with a diameter of 17 cm equaling a pellet bed surface are of 227 cm^2. The bed height was 8 mm, which results in approximately 6 pellets lying on top of each other. Drying was carried out until a constant weight was reached.

The drying curves were determined by weighing the pellets after certain time intervals and the moisture content was calculated as a function of time. For each drying temperature three batches were prepared.

2.3. Pellet characterization

The pellets were sieved according to Ph. Eu. 7.0 2.9.38 and the fraction between 1.4 and 1.8 mm was used for characterization studies.

2.3.1. Differential scanning calorimetry (DSC)

DSC measurements were conducted using a DSC 204 F1 Phoenix (Netzsch, Selb, Germany). Pellets (sample weight 5–10 mg) were gently crushed with a spatula and transferred into aluminum pans that were closed with a pierced lid via cold welding. Samples were heated from 20 to 100 °C with a heating rate of 5 K/min. The

samples were kept at 100 °C for 5 min and cooled to 20 °C with a cooling rate of −5 K/min. Nitrogen (20 ml/min) was used as analytical gas. From each batch three samples were taken for investigations.

2.3.2. Attenuated total reflectance Fourier transform infrared spectroscopy (ATR-FTIR)

Pellets were gently crushed with a spatula and subjected to IR measurements using a Bruker VERTEX 70 (Bruker, Rheinstetten, Germany) equipped with a DLaTGS detector and an ATR unit (MVP Pro Star, Diamond crystal). A total of 64 scans were performed within a wavelength range between 4000 and 600 cm^{-1}. From each batch three samples were collected and investigated via IR spectroscopy.

2.3.3. Small- and wide-angle X-ray scattering (SWAXS)

Pellet samples were packed into glass capillaries (inner diameter 2 mm), which were sealed with wax. SWAXS spectra were recorded with a high-flux laboratory small- and wide-angle X-ray scattering camera S3-Micro (Hecus X-ray Systems, Graz, Austria) equipped with a high-brilliance microbeam delivery system. A 1D-detector (PSD-50, Hecus X-ray Systems, Graz, Austria) was used at the following settings: wave length: 1.54 Å; angular range: 0.02–8°; exposure time: 800 s; beam size: 200 μm. The obtained data were calculated to reciprocal space vectors by:

$$q = \frac{4\pi \sin\theta}{\lambda} \quad (1)$$

where q is the reciprocal space vector, θ is the scattering angle and λ is the wavelength.

2.3.4. Raman mapping

The pellets were bisected with a razor blade and confocal Raman spectroscopy (WITec alpha 300R+, WITec GmbH, Ulm Germany) was performed. The excitation wavelength was 532 nm (Nd:YAG laser, operated at 10 mW) and an implemented Zeiss objective with a 10-fold magnification (N.A. 0.25) was applied. Raman spectra were acquired every 10 μm along the pellet cross section (i.e., along the x- and y-axis) with an integration time of 0.2 s. Finally, the spectral data sets were converted into false-color images using the software WITec Project Plus, where image pixels assigned to ibuprofen are depicted in red and pixels assigned to CaSt are depicted in blue. For every batch five pellets were investigated.

2.3.5. Brunauer–Emmet–Teller (BET) measurements

The specific surface area was determined on an ASAP 2000 system (Micromeritics, Norcross, Georgia) using nitrogen as analytical gas and on a Tristar II 3020 (Micromeritics, Norcross, Georgia) using krypton. Prior to the measurements, representative samples were degassed under vacuum at ambient temperature. Subsequently, they were frozen in liquid nitrogen (−196 °C) and the volume of nitrogen adsorption was recorded over a relative pressure range between 0.05 and 0.2. Additionally, pellets dried at 20 and at 50 °C (Schrank et al., 2014) were investigated.

2.3.6. In-vitro dissolution characteristics

The in-vitro dissolution studies were performed in a United States Pharmacopoeia (USP) apparatus I (Pharma Test Type PTWS III C, Pharma Test Apparatebau AG, Hainburg, Germany) at a rotational speed of 100 rpm and a constant temperature of 37 ± 0.5 °C. 900 ml of monopotassium phosphate buffer pH 7.2 served as dissolution medium according to the USP XXVIII monograph for ibuprofen tablets. The sample mass was 500 mg as this yielded perfect sink conditions throughout the entire experiment (Schrank et al., 2012). Samples (sample volume 1 ml) were withdrawn at certain time intervals over 6 h. The amount of ibuprofen in the dissolution medium was quantified via reversed-phase high performance chromatography (RP-HPLC). For details of the HPLC method, the reader is referred elsewhere (Roblegg et al., 2011b). In addition to pellets prepared during this study, pellets dried at 20 and at 50 °C (Schrank et al., 2014) were evaluated regarding their release characteristics.

The underlying release kinetics were investigated by fitting dissolution data to existing mathematical approaches, including the zero order release model, the Korsemeyer–Peppas model (i.e., the power law) and the Higuchi model (for the formulae see (Costa et al., 2003)). In addition, a specific form of the Higuchi model was applied (Dubernet et al., 1990), which allows the estimation of the diffusion coefficients (Eq. (2)).

$$3 - 2A_t - 3(1 - A_t)^{2/3} = 6D\frac{\varepsilon C_S}{\tau A a_0^2}t, \quad (2)$$

with A_t: fractional cumulative amount of API dissolved at time t,D: diffusion coefficient, ε: porosity of the matrix, C_S: saturation concentration of ibuprofen in phosphate buffer pH 7.4 (i.e., 0.013 g/cm^3 (Dubernet et al., 1990)), τ: tortuosity, A: initial concentration of the drug in the matrix and a_0: initial radius of the matrix (i.e., 1.6 mm). When plotting the left hand side term of Eq. (2) against time, the effective diffusion coefficient D_{eff} (i.e., diffusion through a porous system) can be determined from the slope. Additionally, this procedure allows the estimation of the tortuosity based on dissolution data.

3. Results

3.1. Pellet preparation and drying

The wet extrusion/spheronization process yielded smooth extrudates and spherical pellets as previously shown for CaSt pellets comprising ibuprofen (Roblegg et al., 2010; Schrank et al., 2012, 2013). The drying profiles differed qualitatively and quantitatively depending on the drying temperature (Fig. 1). Different drying temperatures were previously shown to modify the CaSt shrinking behavior (Schrank et al., 2013), thereby affecting the heat and mass exchange area during drying. As expected, the drying rates increased with increasing temperature. Moreover, the temperature modified the shape of the drying profiles (mostly during the initial stage of drying). For moderate temperatures, i.e., 30 and 40 °C, the drying rate was rather constant initially (Fig. 1b), suggesting the initial presence of a CRP. During drying at 60 °C an increasing drying rate was observed during the initial 15 min representing the pre-heating period. Thereafter, the drying rate continuously decreased with a comparatively large decay (Fig. 1b). Consequently, a CRP was missing and instead, only an FRP was observed.Nevertheless, the drying rate was similar for all batches after 60 min (Fig. 1b). The drying times necessary to reach a constant weight decreased from 8 to 6 h when increasing the drying temperature from 30 to 60 °C. After that time the residual moisture content, which was determined via a moisture halogen analyzer, was below 1% for all batches.

3.2. Pellet characterization

3.2.1. Differential scanning calorimetry (DSC)

For each drying temperature one thermogram is shown, since the curves did not deviate within multiple measurements of one batch ($n = 3$) or between different batches. Ibuprofen shows a sharp endothermic peak at 75.3 °C upon heating (Fig. 2) resembling the melting event (Lerdkanchanaporn et al., 2001). The decline of the CaSt curve is due to water loss (Fig. 2). For a detailed description of

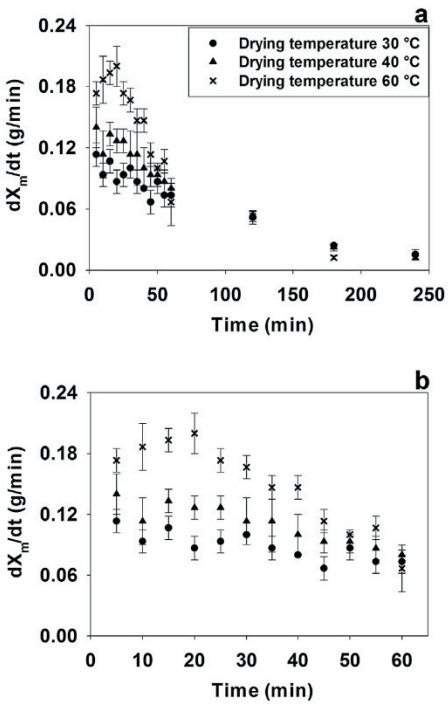

Fig. 1. Drying profiles for different drying temperatures. (a) Change of pellet mass per time unit as a function of time for the entire drying process and (b) magnification of the first 60 min. Values represent the means of three batches.

the CaSt thermogram the reader is referred to elsewhere (Roblegg et al., 2011a). After drying at 30, 40 and 60 °C the endothermic peak was shifted to an onset temperature of around 50 °C. The shift in the onset temperature was attributed to the formation of a eutectic between CaSt and ibuprofen during preparation and/or during heating in the DSC apparatus (Gordon et al., 1984). Drying at 60 °C yielded a double peak, where the onset was further shifted toward lower temperatures, i.e., 45 °C. Additionally, a glass transition was observed at 86 °C onset temperature for all drying temperatures.

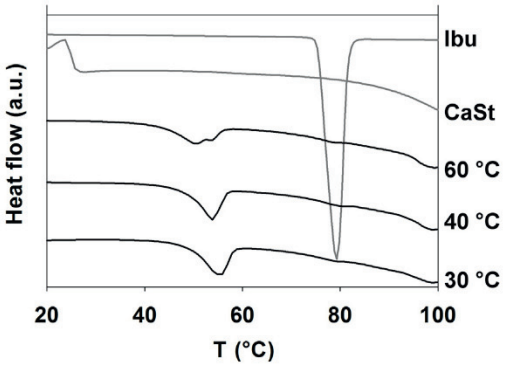

Fig. 2. DSC thermograms: thermal behavior during heating of pellets dried at different temperatures. The thermal behavior of the primary powders (gray lines) is shown for comparison reasons. Exothermic events are upwards.

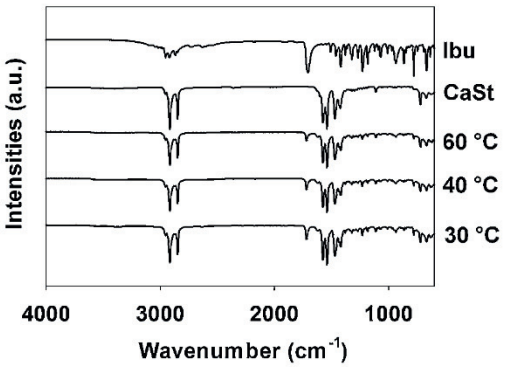

Fig. 3. FTIR spectra of pellets dried at different temperatures. The spectra of the raw powders are shown for comparison reasons.

3.2.2. Attenuated total reflectance Fourier transform infrared spectroscopy (ATR-FTIR)

Again, the IR spectra did neither vary within multiple measurements of one batch ($n = 3$) nor between batches. Hence, for every drying temperature one spectrum is shown in Fig. 3. The spectra of CaSt and ibuprofen show bands between 2956 and 2848 cm^{-1} and between 2954 and 2850 cm^{-1}, respectively, which are assigned to CH stretching vibrations. Moreover, CaSt shows a doublet at 1570 and 1540 cm^{-1} that is due to asymmetric COO stretching vibrations (Kimura et al., 1985). Ibuprofen exhibits a

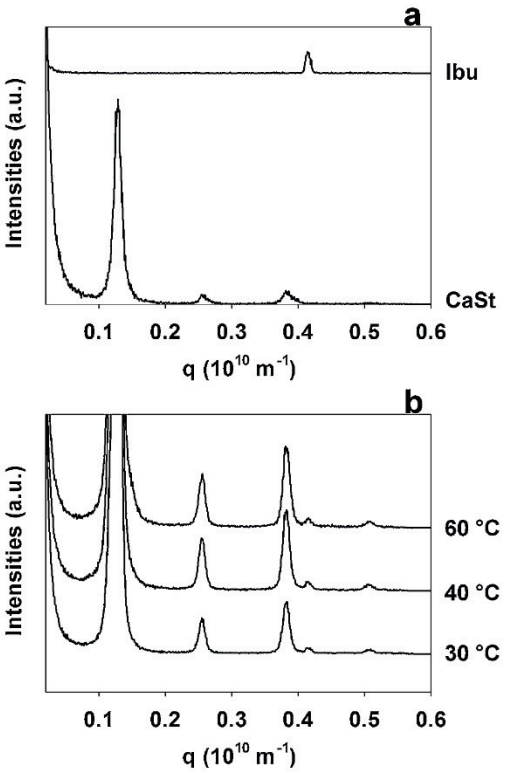

Fig. 4. (a) SAXS spectra of primary powders and (b) pellets dried at different temperatures.

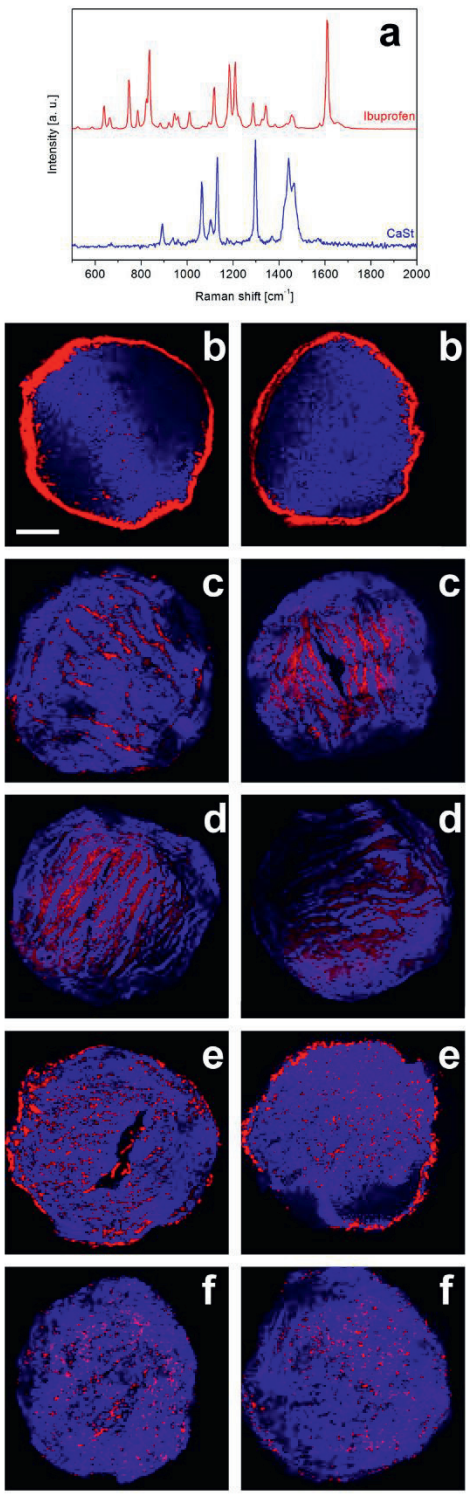

Fig. 5. Results of Raman microscopy analysis. (a) Raman spectra of single compounds. (b–f) False color Raman images of pellets dried at (b) 20 °C, (c) 30 °C, (d) 40 °C, (e) 50 °C and (f) 60 °C. Ibuprofen is represented in red color, whereas CaSt is shown in blue. Scale bars are sized to 400 μm. (For interpretation of the references to color in this figure legend, the reader is referred to the web version of this article.)

carbonyl band at 1707 cm^{-1} (Bondesson et al., 2007). All pellet spectra contained this carbonyl band and reflect all the peaks deriving from CaSt regardless of the drying temperature. This indicates that no solid state transitions occurred during drying.

3.2.3. Small- and wide-angle X-ray scattering (SWAXS)

Since both, ibuprofen and CaSt are crystalline, Bragg peak overlapping was evident especially in the WAXS angular region. Hence, data analysis was performed in the SAXS region, which shows the internal order (Glatter and Kratky, 1982). For every preparation method one curve is shown as the spectra did neither deviate within multiple measurements of one batch ($n = 3$) nor between different batches. Crystalline ibuprofen shows a clear peak at $0.427 \times 10^{10}\ m^{-1}$ (Fig. 4a). CaSt yields three peaks (q^* of 0.132×10^{10} and q of 0.262×10^{10} and $0.392 \times 10^{10}\ m^{-1}$) providing a ratio q^*/q of 1:2:3 (Fig. 4a), which is characteristic for lamellar structures (Deamer et al., 1970). The characteristic ibuprofen peak at $0.427 \times 10^{10}\ m^{-1}$ was found in the spectra of all pellets regardless of the drying technique (Fig. 4b). The spectra of pellets dried at 60 °C contained an additional peak at $0.463 \times 10^{10}\ m^{-1}$, which derived from solid state modifications of CaSt (Schrank et al., 2014).

3.2.4. Raman mapping

Raman spectra of single compounds prove chemically selective discrimination of CaSt and ibuprofen (Fig. 5a). For every drying temperature two Raman images are shown. Additionally, Raman images of pellets dried at 20 and 50 °C are included. The spatial ibuprofen distribution within the pellets varied with different drying techniques. After drying at 20 °C, the major fraction of API was located at the pellet surface (Fig. 5b) as previously shown (Schrank et al., 2014). In contrast pellets dried at 30, 40, 50 and 60 °C yielded overall homogeneous ibuprofen profiles (Fig. 5c–f). When the pellets were dried at 30 and 40 °C, the ibuprofen distribution showed some pattern, where ibuprofen was aligned in elongated assemblies (Fig. 5c and d). Drying at 50 °C yielded a higher fraction of ibuprofen located at the pellet surface (Fig. 5e, (Schrank et al., 2014)) compared to pellets dried at 60 °C, in which ibuprofen was homogeneously dispersed (Fig. 5f).

3.2.5. Brunauer–Emmet–Teller (BET) measurements

The specific surface area couldnot be determined using neither nitrogen nor krypton as analytical gas. According to the manufacturer, absolute areas that can be captured with nitrogen are of a minimum 10 m^2 and 1 m^2 with krypton. Due to the sample holder geometry and the pellet characteristics a maximum mass of around 5 g pellets can be investigated. Thus, it can be concluded that the free specific surface area; i.e., the BET surface area, was below 0.2 m^2/g for all batches. The low BET surface area suggests that the pellets had a low internal surface area, meaning they did not exhibit a pronounced, inter-connected porous system. For a mean pellet diameter of 1.6 mm the outer surface area is 8.04 mm^2 (assuming a perfect sphere). Consequently, an absolute surface area of 1 m^2 equals 124,340 pellets or 357 g pellets (mean pellet weight of 2.87 mg) assuming that the pellets did not exhibit an internal surface accessible to the BET measurements.

3.2.6. In-vitro dissolution characteristics

The release profiles of pellets dried at 20 °C showed a pronounced burst effect (Fig. 6). Around 60% of the API was

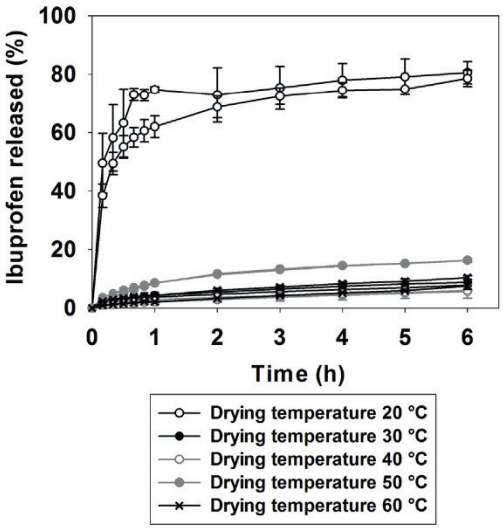

Fig. 6. In-vitro dissolution profiles generated in USP buffer pH 7.2 over 6 h. For every preparation method two batches are shown. The values represent mean values of three samples.

released within 1 h. Subsequently, the release rate slowed and finally a plateau (80% drug release) was reached. In contrast, for all other drying temperatures the ibuprofen release was markedly decreased. Pellets dried at 30, 40 and 60 °C released only 6–8% ibuprofen within 6 h. The profiles of pellets dried at 50 °C were shifted slightly toward higher values. After 6 h 15% of the incorporated API was detected in the dissolution medium.

The profiles of pellets dried at 20 °C followed zero order kinetics in the first 40 min ($R^2 > 0.98$). The release kinetics of all other batches were diffusion controlled as they obeyed the Higuchi model rather well ($R^2 > 0.97$). This was supported by the release exponent n derived from the Korsmeyer–Peppas model, which was between 0.37 and 0.44 ($R^2 > 0.97$). Release exponents of 0.43 are indicative for diffusion controlled release from spheres (Siepmann and Peppas, 2001). The values for D_{eff} and τ that were calculated from the Higuchi model are listed in Table 1.

4. Discussion

CaSt matrix-pellets containing ibuprofen (15% drug loading) were prepared via wet extrusion/spheronization using ethanol as granulation liquid. In a final step the granulation liquid was removed by tray drying at different temperatures. At the beginning of drying, where the ethanol content was comparatively high, the pellets contained CaSt in a swollen state as it is highly swellable in ethanol (Schrank et al., 2012). The swollen state resembles a coherent CaSt structure, which is interpenetrated by ethanol. At early drying stages (i.e., during the CRP) ethanol evaporation occurred from the pellet surface and the pellet deformed uniformly, meaning shrinkage occurred throughout the entire pellet. Thereby, the pellets' diameter and correspondingly, the total porosity were reduced. CaSt matrix-pellets were previously shown to shrink upon drying by a factor of 3.7–20% (in terms of pellet diameter reduction) as a function of the drying process parameters and the drug loading (Schrank et al., 2012, 2013). At later drying stages (i.e., during the FRP), during which evaporation took place inside the pellets, shrinkage was non-uniform and modifications of the internal microstructure – that are modifications of the total porosity, the BET surface area, the pore size and shape – occurred. Note that during the aforementioned studies a water/ethanol mixture (50/50 by weight) was used as granulation liquid. Water aided to maintain the pore structure of the swollen state throughout drying yielding final porosities ranging between 16 and 33%. In the present study, during which ethanol was applied as granulation liquid, all drying temperatures yielded very dense systems with low BET surface areas (i.e., below 0.2 m^2/g). The low BET surface areas suggest the absence of a pronounced, inter-connected porous system. As drying lasted rather long for all temperatures (i.e., 6–8 h), pellet shrinkage occurred to a high extent (Bashaiwoldu et al., 2004b).

Note that the pellet microstructure, which is related to the BET surface are, the total porosity, the pore size distributions and the pore shape, continuously changed throughout the drying procedure. Consequently, parameters that are affected by the pellet micro-structure also changed throughout the entire drying procedure. Specifically, the diffusion coefficients, which directly impacts API migration are affected by this phenomenon. At initial drying stages a pore system filled with ethanol was present. However, as drying continued, the pellets gradually shrunk thereby, reducing the porosity and finally leaving behind a dense system.

Drying highly affected the spatial ibuprofen distribution in the pellets (Fig. 5). Drying at 20 °C yielded an initial CRP (Schrank et al., 2014), during which the liquid was transported by capillary flow due to the pressure gradient (described by a modified Darcy's law (Kowalski, 2000; Scherer, 1990)). The major fraction of ibuprofen was transported toward the pellet surface by the convective liquid flow, where re-crystallization was dominant and back-diffusion toward the center (due to a developing concentration gradient) was largely suppressed. Thereby, after drying the surface was ibuprofen enriched, whereas the pellet's interior was nearly depleted from the API (Fig. 5b, (Schrank et al., 2014)).

Although drying at 20 °C (Schrank et al., 2014), 30 °C and 40 °C (Fig. 1) initially yielded similar (low) drying rates, the ibuprofen distribution profiles differed markedly. Drying at 30 and 40 °C yielded overall more uniform ibuprofen distribution profiles, where the API was present in elongated assemblies (Fig. 5c and d). In contrast, studies evaluating the migration behavior in wet granules report that low drying rates yielded surface enriched API distribution profiles independent upon the drying temperature (Kiekens et al., 2000; Poutiainen et al., 2012; Warren and Price, 1977). Obviously, the API migration behavior is different in spherical wet-extruded granules (i.e., pellets) comprising a gradually shrinking excipient.

Generally, the reason for the formation of uniform profiles can be two-fold (Lekhal et al., 2003). For high drying rates, which do not yield a CRP, no capillary flow is present and the liquid evaporates inside the porous structure. Hence, API migration toward the surface is suppressed; the API re-crystallizes inside the pores and thus, the profiles remain uniform. In contrast, for low drying rates a CRP is observed, during which capillary flow is dominant. Consequently, dissolved API may be transported with the convective liquid flow toward outer pellet regions. Thereafter,

Table 1
Values for D_{eff} and τ estimated from the Higuchi model described by Eq. (2).

Drying temperature (°C)	Batch #	D_{eff} ($cm^2\,s^{-1}$)	τ
30	1	4.58×10^{-11}	4.54×10^{3}
30	2	6.17×10^{-11}	3.37×10^{3}
40	1	2.65×10^{-11}	7.84×10^{3}
40	2	2.65×10^{-11}	7.83×10^{3}
50	1	2.26×10^{-10}	9.21×10^{2}
50	2	2.36×10^{-10}	8.80×10^{2}
60	1	3.10×10^{-11}	5.92×10^{3}
60	2	8.60×10^{-11}	2.42×10^{3}

during later drying stages back-diffusion may become dominant resulting in uniform final API distributions.

Although the drying profiles generated at 30 and 40 °C did not reflect a distinct CRP (Fig. 1), initially a (short) CRP was likely to be present. For shrinking materials, such as CaSt (Schrank et al., 2013), the CRP is often difficult to identify due to the gradually changing mass and heat exchange surface area (Berggren and Alderborn, 2001a). Nevertheless, we assume that some of the dissolved ibuprofen migrated toward the pellet surface at early drying stages. Ibuprofen did not re-crystallize at the pellet surface but back-diffusion became dominant due to the increased solubility of ibuprofen in ethanol at 30 and 40 °C compared to 20 °C (Manrique and Martinez, 2007). The observed ibuprofen patterns may be attributed to the gradually changing microstructure (i.e., decrease in porosity and modification of pore size and shape), which caused ibuprofen to accumulate in elongated assemblies.

After drying at 50 °C, ibuprofen was rather finely dispersed throughout the pellet's cross-section. Additionally, some of the API was accumulated at the pellet's surface (Fig. 5e (Schrank et al., 2014)). Again, it is assumed that a certain fraction of the dissolved ibuprofen was transported toward the surface. However, back-diffusion was not as dominant as during drying at 30 and 40 °C. Instead, some of the API precipitated at the pellet surface at early drying stages. Back-diffusion may be hindered by the gradually changing pellet microstructure and/or by liquid film breakage. Liquid film breakage was likely to occur at rather early drying stages (i.e., during the CRP) due to a comparatively high drying rate (Komiyama et al., 1980). Thereby, isolated liquid domains were formed, which limited API migration and ibuprofen back-diffusion toward the pellet center.

Drying at 60 °C yielded perfectly homogeneous distribution profiles, where ibuprofen was neither accumulated at the pellet's surface, nor in assemblies in internal pellet regions (Fig. 5f). As the drying profiles did not include a CRP, but a steeply declining FRP (Fig. 1), ibuprofen transport toward the pellet surface was largely suppressed. The prevailing FRP favored liquid film breakage (Liu et al., 2012), which limits ibuprofen migration. Thus, homogeneous ibuprofen distributions were observed after ibuprofen re-crystallization.

Re-crystallization may induce polymorphic transitions of the API, which may be crucial to the product quality. Hence, the solid state of ibuprofen after drying was evaluated. We previously showed that drying at 20 °C did not yield any solid state modifications, whereas drying at 50 °C caused ibuprofen to largely transform into its amorphous state and CaSt to form a second lamellar phase (Schrank et al., 2014). Drying at 30 and 40 °C did not cause solid state modifications according to the IR (Fig. 3) and SAXS (Fig. 4) spectra. However, the DSC thermograms (Fig. 2) showed a decrease of the endothermic ibuprofen peak attributed to the formation of a eutectic (Gordon et al., 1984). Most probably, the eutectic was formed during the heating procedure in the DSC apparatus. It is rather unlikely that the eutectic temperature (55 °C (Gordon et al., 1984)) was reached during drying at 30 and 40 °C. Additionally, the thermograms contained a glass transition with an onset around 86 °C. This suggests that ibuprofen partly transformed into its amorphous state (Shen et al., 2010). The formation of amorphous ibuprofen may be favored by pore sizes that are too small to allow for crystallization (Charnay et al., 2004). As the pores sizes decreased throughout the drying procedure due to CaSt shrinkage, ibuprofen re-crystallization might have been partially impeded.

The DSC thermograms of pellets dried at 60 °C comprised the endothermic peak corresponding to the eutectic (Fig. 2). Considering the eutectic temperature of 55 °C, it was likely that the eutectic was formed during the drying procedure (or after drying when the pellets were cooled to ambient temperature). Again, the DSC thermograms showed the glass transition indicative for amorphous ibuprofen (Fig. 2). The IR spectrum (Fig. 3) did not indicate interactions between CaSt and ibuprofen as the carbonyl band attributed to ibuprofen (1707 cm^{-1}) was clearly detected. This suggests that there is no mutual miscibility between CaSt and ibuprofen, which is typical of two components forming a eutectic but no solid solution (Benessam et al., 2013). The SAXS spectrum contained the characteristic crystalline ibuprofen peak at 0.427×10^{10} m^{-1} and a small additional peak at 0.463×10^{10} m^{-1}, deriving from CaSt transformations (Schrank et al., 2014). Summarizing, drying at 60 °C favored the formation of the eutectic. Additionally, a certain fraction of ibuprofen transformed into its amorphous state.

Overall, drying affected: (i) the pellet microstructure, (ii) the ibuprofen distribution profiles and (iii) the ibuprofen solid state of the pellet formulation under investigation. All those factors are known to impact the in-vitro dissolution characteristics, e.g., (Gómez-Carracedo et al., 2007; Huang and Brazel, 2001; Yano and Kleinebudde, 2010). During the dissolution studies CaSt did neither swell nor dissolve in the dissolution medium (Roblegg et al., 2010). Theoretically, the dissolution medium needs to enter the pellet pores first, dissolve the API accessible to the pores and subsequently, the API needs to diffuse through the porous system prior to entering the bulk dissolution medium (Schrank et al., 2012). However, the presented pellets do not comprise a distinct porous system and hence, ibuprofen located at the pellet surface gets dissolved first. The dissolved ibuprofen leaves behind pores, through which the dissolution medium can enter more internal pellet regions.

The ibuprofen release rate was highest after drying at 20 °C (Fig. 6), since most of the API was located at the pellet's surface. Ibuprofen release was mainly a function of the ibuprofen solubility, which is reflected by the fact that the initial release followed zero order kinetics. However, after 6 h the released API fraction was 80%, which suggests that some of the ibuprofen was located in interior pellet regions. Obviously, the dissolved ibuprofen did not leave behind a well interconnected pore system and the internally located ibuprofen was enclosed by the CaSt matrix.

For pellets dried at temperatures higher than 20 °C, the dissolution rates were dramatically decreased and only a minor fraction of ibuprofen, i.e., less than 15%, was released during 6 h (Fig. 6). The release was diffusion controlled as all batches obeyed the Higuchi law and the release exponents of the Korsmeyer–Peppas approach ranged between 0.37 and 0.44. Incomplete ibuprofen release was observed as the dissolved ibuprofen did not provide a well interconnected pore system due to the comparatively low ibuprofen loading of 15%.

The diffusion coefficients determined via the Higuchi model were 10^{-11} cm^2/s for pellets dried at 30, 40 and 60 °C (Table 1). These values are far lower than values reported for the diffusion of small molecules (e.g., ibuprofen) in aqueous system, which are 10^{-5} cm^2/s (Lustig and Peppas, 1985). This supports the observation that diffusion was impeded due to the absence of a well-interconnected pore system. As such, high values for the tortuosity calculated from the dissolution data were obtained, i.e., 10^3 (Table 1), which is indicative of very narrow and tortuous or a missing pore system. The average value for tortuosity of a porous system is 3 (Higuchi, 1963).

One would expect that the eutectic prevalently formed during drying at 60 °C improves the release rate. Eutectics are known to improve solubility and consequently, the release rates due to size reduction (Leuner and Dressman, 2000). If the carrier is rapidly dissolved, it leaves very fine API crystals that show improved solubility. However, as CaSt did not dissolve during dissolution testing, the effect of the eutectic was not observed.

The diffusion coefficients (i.e., 10^{-10} cm^2/s; Table 1) and the tortuosity (i.e., 10^2; Table 1) calculated from the dissolution data of

pellets dried at 50 °C were higher compared to pellets dried at 30, 40 and 60 °C. As most of the ibuprofen was present in its amorphous state interacting with CaSt (Schrank et al., 2014), it should be noted that the diffusion coefficients also reflect the diffusion of the API through the CaSt matrix. Obviously, diffusion of ibuprofen through the CaSt matrix was very slow as CaSt did not swell in the dissolution medium. The increased amounts of ibuprofen released (Fig. 6) were due to the slightly ibuprofen enriched pellet surface (Fig. 5e).

Overall, it can be concluded that the in-vitro dissolution characteristics were dominated by the ibuprofen distribution profiles. As drying did not leave a well-interconnected pore system for all drying temperatures, the pellet microstructure did not contribute to the ibuprofen release. Solid state modifications; i.e., formation of amorphous ibuprofen and formation of a eutectic; did not improve the ibuprofen release rates compared to crystalline ibuprofen as ibuprofen was entrapped in internal pellet regions by the CaSt matrix.

5. Conclusions

The drying temperature during tray drying highly affected the final properties of wet-extruded pellets comprising CaSt as matrix former and ibuprofen as model API. As previously shown, drying at 20 °C resulted in ibuprofen enriched surfaces. Drying at 30 and 40 °C yielded overall homogeneous ibuprofen distribution profiles. However; ibuprofen was located in elongated assemblies, which were formed during back-diffusion of ibuprofen. Pellets dried at 60 °C showed perfectly homogeneous ibuprofen distributions as ibuprofen migration was largely suppressed due to the prevailing FRP associated with liquid film breakage.

All drying conditions (i.e., drying temperatures of 30, 40 and 60 °C) yielded solid state modifications. Ibuprofen partially transformed into its amorphous state. Drying at 60 °C prevalently contained ibuprofen in its crystalline state but favored the formation of a eutectic between ibuprofen and CaSt.

As no open inter-connected pore system was formed during drying, the in-vitro dissolution profiles were a function of the spatial ibuprofen distribution. The solid state modifications did not significantly contribute to the ibuprofen release profiles, since CaSt did neither swell (which would favor diffusion of amorphous ibuprofen through the matrix) nor dissolve in the dissolution medium (which would increase the dissolution rates for eutectics).

Overall, this study demonstrated that small variations in the drying temperature highly impact the final pellet properties of certain systems, including the spatial API distribution and the solid state. Likewise, the in-vitro dissolution characteristics, which were a function of the API distribution and frequently play a key role in meeting quality criteria of the final dosage form, were strongly affected.

Acknowledgements

G.L. Pharma (Lannach, Austria) is acknowledged for the kind donation of ibuprofen. Bianca Seidl (Department of Pharmaceutical Technology, University of Graz) is acknowledged for her help with the in-vitro dissolution studies.

References

Baert, L., Vermeersch, H., Remon, J.P., Smeyers-Verbeke, J., Massart, D.L., 1993. Study of parameters important in the spheronisation process. Int. J. Pharm. 96, 225–229.
Balaxi, M., Nikolakakis, I., Malamataris, S., 2009. Preparation of porous microcrystalline cellulose pellets by freeze-drying: effects of wetting liquid and initial freezing conditions. J. Pharm. Sci. 99, 2104–2113.
Bashaiwoldu, A.B., Podczeck, F., Newton, J.M., 2004a. The application of non-contact laser profilometry to the determination of permanent structural change induced by compaction of pellets: II. Pellets dried by different techniques. Eur. J. Pharm. Biopharm. 22, 55–61.
Bashaiwoldu, A.B., Podczeck, F., Newton, J.M., 2004b. A study on the effect of drying techniques on the mechanical properties of pellets and compacted pellets. Eur. J. Pharm. Biopharm. 21, 119–129.
Benessam, S., Khimeche, K., Djellouli, F., Benziane, M., Dahmani, A., 2013. Phase diagram of ibuprofen with fatty acids. J. Therm. Anal. Calorim. 112, 317–320.
Berggren, J., Alderborn, G., 2001a. Drying behaviour of two sets of microcrystalline cellulose pellets. Int. J. Pharm. 219, 113–126.
Berggren, J., Alderborn, G., 2001b. Effect of drying rate on porosity and tabletting behaviour of cellulose pellets. Int. J. Pharm. 227, 81–96.
Bondesson, L., Mikkelsen, K.V., Luo, Y., Garberg, P., Ågren, H., 2007. Hydrogen bonding effects on infrared and Raman spectra of drug molecules. Spectrochim. Acta Part A: Mol. Biomol. Spectrosc. 66, 213–224.
Charnay, C., Bégu, S., Tourné-Péteilh, C., Nicole, L., Lerner, D.A., Devoisselle, J.M., 2004. Inclusion of ibuprofen in mesoporous templated silica: drug loading and release property. Eur. J. Pharm. Biopharm. 57, 533–540.
Costa, F.O., Sousa, J.J.S., Pais, A.A.C.C., Formosinho, S.J., 2003. Comparison of dissolution profiles of ibuprofen pellets. J. Controlled Release 89, 199–212.
Deamer, D.W., Leonard, R., Tardieu, A., Branton, D., 1970. Lamellar and hexagonal lipid phases visualized by freeze-etching. Biochim. Biophys. Acta Biomembr. 219, 47–60.
Debnath, S., Suryanarayanan, R., 2004. Influence of processing-induced phase transformations on the dissolution of theophylline tablets. AAPS PharmSciTech 5, 39–49.
Dubernet, C., Benoit, J.P., Peppas, N.A., Puisieux, F., 1990. Ibuprofen-loaded ethylcellulose microspheres: release studies and analysis of the matrix structure through the Higuchi model. J. Microencapsulation 7, 555–565.
Dyer, A.M., Khan, K.A., Aulton, M.E., 1994. Effect of the drying method on the mechanical and drug release properties of pellets prepared by extrusion-spheronization. Drug Dev. Ind. Pharm. 20, 3045–3068.
Farber, L., Tardos, G.I., Michaels, J.N., 2003. Evolution and structure of drying material bridges of pharmaceutical excipients: studies on a microscope slide. Chem. Eng. Sci. 58, 4515–4525.
Fielden, K.E., Newton, J.M., Rowe, R.C., 1992. Movement of liquids through powder beds. Int. J. Pharm. 79, 47–60.
Gómez-Carracedo, A., Souto, C., Martínez-Pacheco, R., Concheiro, A., Gómez-Amoza, J.L., 2007. Microstructural and drug release properties of oven-dried and of slowly or fast frozen freeze-dried MCC-Carbopol® pellets. Eur. J. Pharm. Biopharm. 67, 236–245.
Gómez-Carracedo, A., Souto, C., Martinez-Pacheco, R., Concheiro, A., Gómez-Amoza, J.L., 2008. Incidence of drying on microstructure and drug release profiles from tablets of MCC-lactose-Carbopol® and MCC-dicalcium phosphate-Carbopol® pellets. Eur. J. Pharm. Biopharm. 69, 675–685.
Glatter, O., Kratky, O., 1982. Small Angle X-Ray Scattering. Academic Press, New York.
Gordon, R.E., VanKoevering, C.L., Reits, D.J., 1984. Utilization of differential scanning calorimetry in the compatibility screening of ibuprofen with the stearate lubricants and construction of phase diagrams. Int. J. Pharm. 21, 99–105.
Herman, J., Visavarungroj, N., Remon, J.P., 1989. Instability of drug release from anhydrous theophylline-imcrocrystalline cellulose formulations. Int. J. Pharm. 55, 143–146.
Higuchi, T., 1963. Mechanism of sustained-action medication: theoretical analysis of rate of release of solid drugs dispersed in solid matrices. J. Pharm. Sci. 52, 1145–1149.
Huang, X., Brazel, C.S., 2001. On the importance and mechanisms of burst release in matrix-controlled drug delivery systems. J. Controlled Release 73, 121–136.
Kiekens, F., Zelko, R., Remon, J.P., 2000. Influence of drying temperature and granulation liquid viscosity on the inter- and intragranular drug migration in tray-dried granules and compacts. Pharm. Dev. Technol. 5, 131–137.
Kimura, F., Umemura, J., Takenaka, T., 1985. FTIR-ATR studies on Langmuir–Blodgett films of stearic acid with 1–9 monolayers. Langmuir 2, 96–102.
Kleinebudde, P., 1994. Shrinking and swelling properties of pellets containing microcrystalline cellulose and low substituted hydroxypropylcellulose: I. Shrinking properties. Int. J. Pharm. 109, 209–219.
Komiyama, M., Merrill, R.P., Harnsberger, H.F., 1980. Concentration profiles in impregnation of porous catalysts: nickel on alumina. J. Catal. 63, 35–52.
Kowalski, S.J., 2000. Toward a thermodynamics and mechanics of drying processes. Chem. Eng. Sci. 55, 1289–1304.
Lekhal, A., Glasser, B.J., Khinast, J.G., 2001. Impact of drying on the catalyst profile in supported impregnation catalysts. Chem. Eng. Sci. 56, 4473–4487.
Lekhal, A., Girard, K.P., Brown, M.A., Kiang, S., Glasser, B.J., Khinast, J.G., 2003. Impact of agitated drying on crystal morphology KCl-water system. Powder Technol. 132, 119–130.
Lerdkanchanaporn, S., Dollimore, D., Evans, S.J., 2001. Phase diagram for the mixtures of ibuprofen and stearic acid. Thermochim. Acta 367–368, 1–8.
Leuner, C., Dressman, J., 2000. Improving drug solubility for oral delivery using solid dispersions. Eur. J. Pharm. Biopharm. 50, 47–60.
Liu, X., Khinast, J.G., Glasser, B.J., 2008. A parametric investigation of impregnation and drying of supported catalysts. Chem. Eng. Sci. 63, 4517–4530.
Liu, X., Khinast, J.G., Glasser, B.J., 2012. Drying of supported catalysts for low melting point precursors: impact of metal loading and drying methods on the metal distribution. Chem. Eng. Sci. 79, 187–199.

Lustig, S.R., Peppas, N.A., 1985. Scaling laws for solute diffusion in equilibrium swollen gels. Polym. Prepr. 26, 72.
Lutchman, D., Dangor, C.M., Perumal, D., 2005. Formulation of rate-modulating pellets for the release of ibuprofen: an extrusion/spheronization process. J. Microencapsulation 22, 643–659.
Manrique, J., Martinez, F., 2007. Solubility of ibuprofen in some ethanol + water cosolvent mixtures at several temperatures. Lat. Am. J. Pharm. 26, 344–354.
Murray, T., Rough, S.L., Wilson, D.I., 2007. The effect of drying technique on tablets formed from extrusion–spheronization granules. Chem. Eng. Res. Des. 85, 996–1004.
Phadnis, N.V., Suryanarayanan, R., 1997. Polymorphism in anhydrous theophylline – implications on the dissolution rate of theophylline tablets. J. Pharm. Sci. 86, 1256–1263.
Poutiainen, S., Honkanen, M., Becker, J., Nachtweide, D., Järvinen, K., Ketolainen, J., 2012. X-ray microtomography analysis of intragranular drug migration during fluidized bed and oven tray drying. J. Pharm. Sci. 101, 1587–1598.
Roblegg, E., Ulbing, S., Zeissmann, S., Zimmer, A., 2010. Development of lipophilic calcium stearate pellets using ibuprofen as model drug. Eur. J. Pharm. Biopharm. 75, 56–62.
Roblegg, E., Jäger, E., Hodzic, A., Koscher, G., Mohr, S., Zimmer, A., Khinast, J., 2011a. Development of sustained-release lipophilic calcium stearate pellets via hot melt extrusion. Eur. J. Pharm. Biopharm. 79, 635–645.
Roblegg, E., Schrank, S., Griesbacher, M., Radl, S., Zimmer, A., Khinast, J., 2011b. Use of the direct compression aid Ludiflash® for the preparation of pellets via wet extrusion/spheronization. Drug Dev. Ind. Pharm. 37, 1231–1243.
Sandler, N., Rantanen, J., Heinämäki, J., Römer, M., Marola, M., Yliruusi, J., 2005. Pellet manufacturing by extrusion–spheronization using process analytical technology. AAPS PharmSciTech 6, E174–E183.
Scherer, G.W., 1990. Theory of drying. J. Am. Ceram. Soc. 73, 3–14.
Schrank, S., Hodzic, A., Zimmer, A., Glasser, B., Khinast, J., Roblegg, E., 2012. Ibuprofen-loaded calcium stearate pellets: drying-induced variations in dosage form properties. AAPS PharmSciTech 13, 686–698.
Schrank, S., Kann, B., Windbergs, M., Glasser, B.J., Zimmer, A., Khinast, J., Roblegg, E., 2013. Microstructure of calcium stearate matrix pellets: a function of the drying process. J. Pharm. Sci. 102, 3987–3997.
Schrank, S., Kann, B., Saurugger, E., Ehmann, H., Werzer, O., Windbergs, M., Glasser, B.J., Zimmer, A., Khinast, J., Roblegg, E., 2014. Impact of drying on solid state modifications and drug distribution in ibuprofen-loaded calcium stearate pellets. Mol. Pharm. 11, 599–609.
Shen, S.-C., Ng, W.K., Chia, L., Dong, Y.-C., Tan, R.B.H., 2010. Stabilized amorphous state of ibuprofen by co-spray drying with mesoporous SBA-15 to enhance dissolution properties. J. Pharm. Sci. 99, 1997–2007.
Siepmann, J., Peppas, N.A., 2001. Modeling of drug release from delivery systems based on hydroxypropyl methylcellulose (HPMC). Adv. Drug Delivery Rev. 48, 139–157.
Sousa, J.J., Sousa, A., Podczeck, F., Newton, J.M., 1996. Influence of process conditions on drug release from pellets. Int. J. Pharm. 144, 159–169.
Warren, J.W., Price, J.C., 1977. Drug migration during drying of tablet granulations II: effect of binder solution viscosity and drying temperature. J. Pharm. Sci. 66, 1409–1412.
Wlosnewski, J.C., Kumpugdee-Vollrath, M., Sriamornsak, P., 2010. Effect of drying technique and disintegrant on physical properties and drug release behavior of microcrystalline cellulose-based pellets prepared by extrusion/spheronization. Chem. Eng. Res. Des. 88, 100–108.
Yano, H., Kleinebudde, P., 2010. Improvement of dissolution behavior for poorly water-soluble drug by application of cyclodextrin in extrusion process: comparison between melt extrusion and wet extrusion. AAPS PharmSciTech 11, 885–893.

5.4 Chemical Imaging of Drug Delivery Systems with Structured Surfaces – a Combined Analytical Approach of Confocal Raman Microscopy and Optical Profilometry

Chemical Imaging of Drug Delivery Systems with Structured Surfaces – a Combined Analytical Approach of Confocal Raman Microscopy and Optical Profilometry

B. Kann, M. Windbergs

AAPS J. **2013**;15:505-510.

DIO: 10.1208/s12248-013-9457-7

The AAPS Journal, Vol. 15, No. 2, April 2013 (© 2013)
DOI: 10.1208/s12248-013-9457-7

Research Article

Chemical Imaging of Drug Delivery Systems with Structured Surfaces–a Combined Analytical Approach of Confocal Raman Microscopy and Optical Profilometry

Birthe Kann[1] and Maike Windbergs[1,2,3,4]

Received 26 November 2012; accepted 10 January 2013; published online 29 January 2013

Abstract. Confocal Raman microscopy is an analytical technique with a steadily increasing impact in the field of pharmaceutics as the instrumental setup allows for nondestructive visualization of component distribution within drug delivery systems. Here, the attention is mainly focused on classic solid carrier systems like tablets, pellets, or extrudates. Due to the opacity of these systems, Raman analysis is restricted either to exterior surfaces or cross sections. As Raman spectra are only recorded from one focal plane at a time, the sample is usually altered to create a smooth and even surface. However, this manipulation can lead to misinterpretation of the analytical results. Here, we present a trendsetting approach to overcome these analytical pitfalls with a combination of confocal Raman microscopy and optical profilometry. By acquiring a topography profile of the sample area of interest prior to Raman spectroscopy, the profile height information allowed to level the focal plane to the sample surface for each spectrum acquisition. We first demonstrated the basic principle of this complementary approach in a case study using a tilted silica wafer. In a second step, we successfully adapted the two techniques to investigate an extrudate and a lyophilisate as two exemplary solid drug carrier systems. Component distribution analysis with the novel analytical approach was neither hampered by the curvature of the cylindrical extrudate nor the highly structured surface of the lyophilisate. Therefore, the combined analytical approach bears a great potential to be implemented in diversified fields of pharmaceutical sciences.

KEY WORDS: chemical imaging; confocal Raman microscopy; drug delivery systems; optical topography.

INTRODUCTION

Raman spectroscopy is a versatile technique for contactless and label-free characterization of diverse samples with a constantly growing impact in pharmaceutical sciences. It facilitates chemically selective analysis without sample destruction and can be used for component distribution analysis, discrimination between different molecular conformations and interaction studies. For pharmaceutical investigations, Raman spectroscopy with a sensor probe recording single Raman spectra is extensively used ranging from bulk material identification and counterfeit detection (1,2) up to sophisticated applications such as PAT (process analytical technology) tools for process monitoring upon manufacturing (3,4). To obtain spatially resolved, three-dimensional chemical information, a Raman spectrometer can be implemented into a confocal microscope. The acquired spectral information is converted into chemically selective spatially resolved false color images. Confocal Raman microscopy is applicable for investigations of diverse drug delivery systems. In this context, the Raman mapping capabilities of the instrument have already been exploited to image the distribution of active pharmaceutical ingredient (API) and excipient(s) within a carrier system (5–7), API release (5–7), as well as interactions of small delivery systems with cells (8,9).

As most customary samples in pharmaceutics feature gradual opacity, the analysis is often restricted to surface structures representing either the outer surface or cross sections. In any case, the majority of these surfaces is structured. However, a confocal setup requires a smooth sample surface as the spectral information is collected from the focal plane. Therefore, different invasive methods of sample preparation such as polishing are often employed prior to Raman analysis to create a smooth sample surface. This can falsify the analytical results due to changes in the original composition, *i.e.*, luting and physical structure of the sample, and should therefore be avoided. In pharmaceutics, the impact of such analytical results is crucial as misleading data can affect further development procedures. It would be highly desirable to establish an analytical approach to combine confocal Raman microscopy with a technique for surface analysis allowing chemically selective investigation of highly structured sample surfaces in their original state.

Among the established techniques for analyzing surface structures are atomic force microscopy and electron microscopy (10,11). However, these techniques exhibit several limitations.

[1] Department of Biopharmaceutics and Pharmaceutical Technology, Saarland University, Campus A4.1, 66123 Saarbruecken, Germany.
[2] Helmholtz-Institute for Pharmaceutical Research Saarland, Campus C2.3, 66123 Saarbruecken, Germany.
[3] PharmBioTec GmbH, Campus C2.2, 66123 Saarbruecken, Germany.
[4] To whom correspondence should be addressed. (e-mail: m.windbergs@mx.uni-saarland.de)

For electron microscopy measurements, the sample has to be sputter coated prior to investigations, thus impeding further analysis with another technique such as Raman spectroscopy. Moreover, the techniques are usually restricted to the investigation of a small sample section, which is often not sufficient for the analysis of common solid carrier systems like extrudates, pellets, or tablets. Atomic force microscopy can be combined with Raman spectroscopy; however, the technique is generally limited to sampling in submicrometer scale. Another microscopic approach is optical profilometry which has already been applied in manifold fields of applications ranging from ink to minerals (12–18). The technique is based on white light scattering after irradiating the sample of interest. The wavelength information of the detected scattered light represents the specific distance between light probe and sample surface which is converted into a topographic profile. Due to its nondestructive nature, optical profilometry suits as a complementary technique for confocal Raman microscopy.

In this study, we present the combined application of optical profilometry with confocal Raman microscopy for all-encompassing chemically selective analysis. In a first attempt, we proved the basic practicability of the combined approach by imaging a tilted silica wafer with a laser-induced mark. In a second step, we adapted the approach for pharmaceutical purposes by analyzing two exemplary drug delivery systems. A cylindrical extrudate consisting of a matrix former in which the drug has been embedded was investigated focusing on component distribution in the core and on the surface. Furthermore, a highly structured lyophilisate loaded with a protein in active and inactive state was analyzed detecting the localization of inactive drug.

MATERIALS AND METHODS

Sample Preparation

Extrudate

A powder mixture consisting of 50% (*w/w*) tripalmitin (Sasol, Witten, Germany) and 50% (*w/w*) theophylline anhydrate (BASF, Ludwigshafen, Germany) was fed into a corotating twin-screw extruder (Mikro 27GL-28D, Leistritz, Nuremberg, Germany) with a feeding rate of 40 $g\,min^{-1}$. The mass was extruded through a die plate with 23 holes (diameter 1 mm, length 2.5 mm) with a screw speed of 30 rpm and a processing temperature of 55°C.

Lyophilisate

Bovine serum albumin (BSA) was purchased from Sigma-Aldrich. Thermally denatured protein was prepared by heating the protein dissolved in water for 90 min at 100°C and verifying the conformation by Raman microscopy. An aqueous solution containing a mixture of native and thermally denatured BSA was freeze-dried in a freeze dryer alpha 2–4 LSC (Christ, Osterode, Germany) for 48 h with a final drying step for 1 h.

Scanning Electron Microscopy

Samples were sputter coated with gold. Scanning electron microscopy measurements were performed by a Zeiss EVO HD15 electron microscope at an accelerating voltage in a range of 3 to 5 kV.

Optical Profilometry

True surface microscopy was performed with a WITec alpha 500/300R+ (WITec GmbH, Ulm, Germany). No sample preparation was needed. The sensor probe can resolve an elevation difference of 3 mm with a step size of 120 nm along the *z*-axis. A silica wafer section of 150×100 μm and a pixel size of 2×2 μm was irradiated with an integration time of 0.1 s. The exterior extrudate surface was rasterized at a step size of 5 μm along the *x* and *y*-axes with an integration time of 0.1 s. The lyophilisate area under investigation was 2,000× 2,000 μm. Every 50 μm in both *x* and *y* direction, a signal was recorded with an integration time of 0.05 s.

Raman Spectroscopy

Raman spectra were recorded with a confocal Raman microscope WITec alpha 500/300R+ (WITec GmbH, Ulm, Germany) using implemented Zeiss objectives (50× NA= 0.55; 50× NA=0.8; 10× NA=0.25). The excitation wavelength of the Nd:YAG laser was 532 nm actuated at 10 mW (lyophilisate), 30 mW (extrudate), or 40 mW (silica wafer). Signals were detected by a back-illuminated CCD camera after passing a 50-μm pinhole. The spectral resolution was 4 cm^{-1}. The wafer image had a pixel resolution of 2×2 μm. Integration time for each Raman spectrum acquisition was 0.2 s. Raman spectra were recorded every 5 μm along the *x* and *y*-axis for the extrudate cross section and exterior surface integrated at 0.1 and 0.5 s, respectively. Two thousand five hundred Raman spectra were collected from the investigated lyophilisate area of 2,000×2,000 μm at an integration time of 0.6 s. No preparation was performed for any sample prior to investigation. The collected Raman spectra were processed and converted into false color images using the software WITec Project Plus (WITec GmbH, Ulm, Germany).

RESULTS AND DISCUSSION

To prove the practicability of the analytical approach combining confocal Raman microscopy with optical topography and to elucidate its potential, we first investigated a silica wafer with a laser-induced mark as a well-defined sample. The wafer itself exhibited a smooth surface and silica is a strong Raman scatterer facilitating the acquisition of Raman spectra. For the proof of concept experiment, we tilted the wafer creating an inclined plane. These surface conditions impaired a comprehensive characterization with a conventional confocal Raman microscope as spectra acquisition was limited to one focal plane at a time (Fig. 1a). Therefore, the analysis of the wafer surface without individual manual focusing for each spectrum was rendered impossible.

Optical topography is based on a white light source and an optical probe. The probe contains a hyperchromatic lens assembly having a distinct linear chromatic error. As white

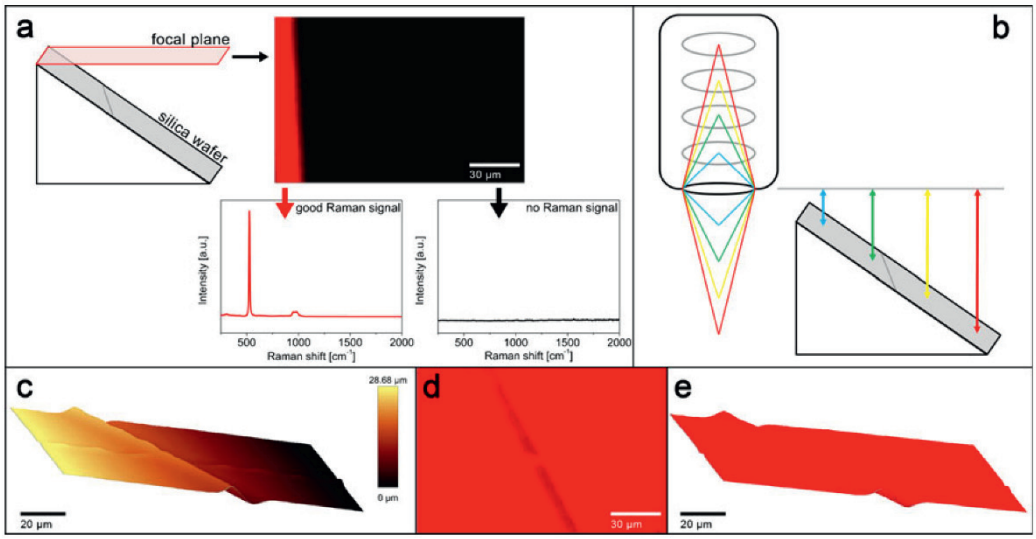

Fig. 1. Combination of Raman microscopy and optical profilometry as complementary analytical techniques. **a** Raman spectra acquisition of a tilted surface with a conventional microscope was limited to the focal plane (visible by the *red area* in the microscopic image). **b** Schematic principle of optical profilometry. White light is focused on the sample surface, and according to the distance between probe and surface, the respective wavelength of the white light is selectively collected by the detector. **c** Surface topography profile of a tilted silica wafer. **d** Two-dimensional false color Raman image of the same tilted silica wafer area. **e** Overlay of topography profile and confocal Raman microscopy analysis data resulting in a three-dimensional chemically selective false color image

light is composed of different colors (different wavelengths), each color has a unique focal distance. By focusing the light onto the sample and collecting the backscattered light through a pinhole, only the color in focus can be detected according to the distance between the probe and the sample surface (Fig. 1b). This information is subsequently converted into topographic height differences. A wafer section of 150× 100 µm was first investigated with the profilometry probe to create the topographic map of the area of interest (Fig. 1c). The subsequent recording of the Raman spectra from the same area was guided by the profilometry information; thus, the microscope focus was individually adjusted according to the sample topography while the sample surface was rasterized for Raman spectra acquisition. Therefore, at every measurement point, the focal plane was positioned at the sample surface which is the key to obtain all-encompassing chemically selective characterization. For component distribution analysis, a confocal microscope is a compulsory feature as confocality is a prerequisite for the mapping capability. The recorded Raman spectral data set was converted into a false color image, where each component is represented by a different color. The false color image is a two-dimensional depiction (Fig. 1d). However, when overlaying the topography profile with the two-dimensional Raman image in a subsequent step, a three-dimensional spatially resolved image was obtained (Fig. 1e).

After this initial proof of concept study, we applied the complementary analytical approach on two different drug delivery systems to evaluate the suitability of the combined techniques for pharmaceutical purposes. In a first step, we investigated lipid-based extrudates, a solid oral dosage form exhibiting a cylindrical morphology. These drug delivery systems were obtained after extrusion of physical powder mixtures and have already been thoroughly characterized in the past (19–21). However, analysis of component distribution with confocal Raman microscopy has thus far been limited to cross sections as the curvature of the cylindrical form impaired analysis of the exterior surface. Nevertheless, the interior component ratio does not automatically represent the exterior distribution of the components due to the manufacturing procedure. In pharmaceutical production, extrudates are often intermediate products mainly processed into pellets. Therefore, a thorough understanding of the initial solid dosage form is of vital importance to evaluate subsequent steps like spheronization. Here, we analyzed extrudates composed of the lipid matrix former tripalmitin and theophylline anhydrate as API regarding their interior and exterior component distribution. As extrudates are opaque systems, the sample was manually cut with a razor blade creating an artificial surface prior to Raman investigations. The light microscopy image in Fig. 2a shows the created smooth surface which was suited for immediate confocal Raman microscopy investigation without further sample preparation. The recorded Raman spectra of the cross section were subsequently converted into false color images. The false color Raman image showing the homogeneous distribution of both components within the created cross sections is visualized in Fig. 2a. For better demonstration of the instrument's mapping capabilities, the individual false color images with the respective Raman spectra of each component tripalmitin and theophylline anhydrate are depicted in Fig. 2b.

Raman mapping of the extrudate cross section is a well-suited technique to portray the component distribution. However, as mentioned before, the interior component distribution does not automatically equal the exterior ratio.

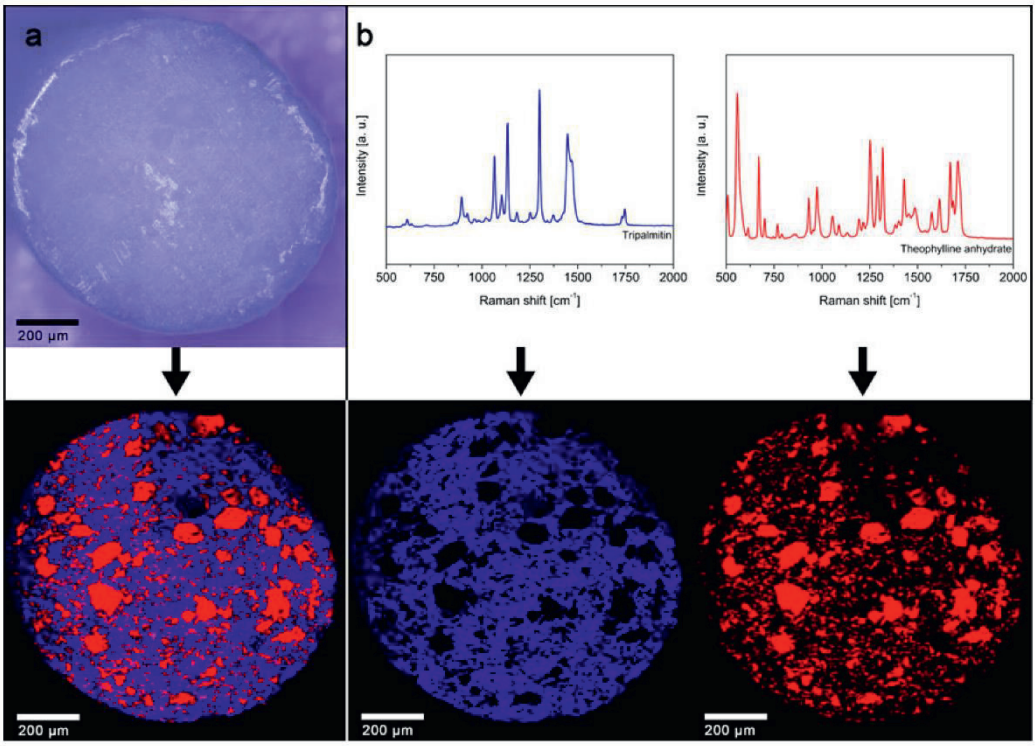

Fig. 2. Component distribution analysis of the interior ratio of an extrudate. **a** Light microscopy image of the investigated extrudate cross section and the resulting false color Raman image. Tripalmitin is represented in blue, whereas theophylline anhydrate is indicated in red. **b** Raman spectra of each component and the respective individual false color Raman images of the two components tripalmitin (*blue*) and theophylline anhydrate (*red*)

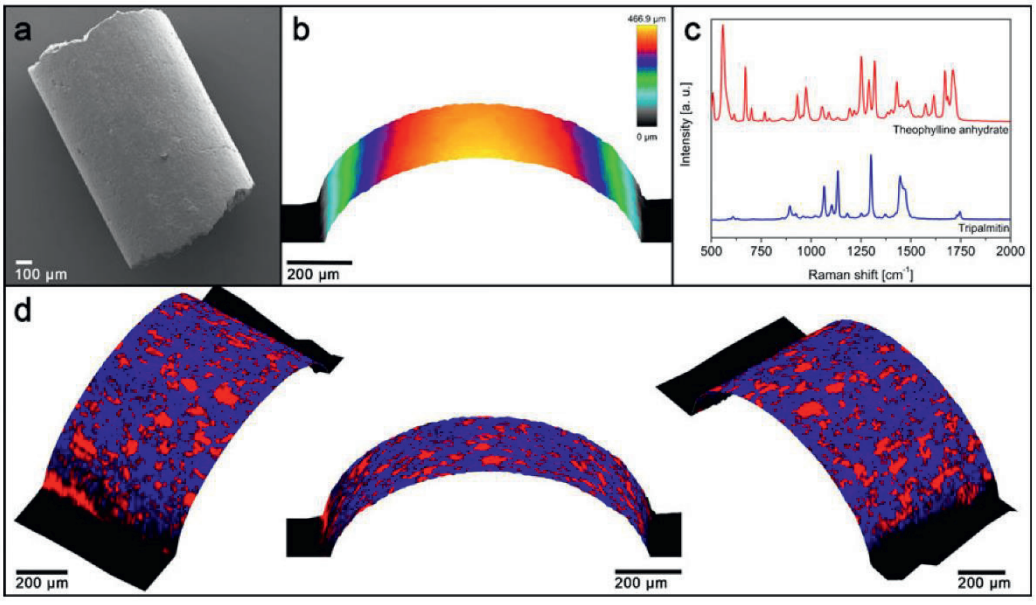

Fig. 3. Component distribution analysis of the exterior extrudate surface. **a** Electron microscopy image of an extrudate. **b** Topography profile of the extrudate showing the curvature of the exterior surface. **c** Single Raman spectra of the individual components tripalmitin (*blue*) and theophylline anhydrate (*red*). **d** Overlay of topography profile with false color Raman image from different angles depicting component distribution on the exterior surface. Tripalmitin is shown in *blue* and theophylline anhydrate in *red*

Therefore, it would be eligible to use mapping as well to visualize the exterior component ratio. The exterior extrudate surface is smooth but exhibits a curvature (Fig. 3a), thus impeding analysis with a conventional confocal Raman microscope. If initially acquiring a topography profile of the curved surface, Raman mapping can be performed in a subsequent step. Figure 3b shows a topography profile of an extrudate section. The symmetric gradient of the color scale nicely demonstrates the curvature and therefore, the precise functioning of the optical sensor probe. The subsequently derived Raman spectral data set was recorded by rasterizing the surface where the topography background information guided the focal point along the curvature of the extrudate. The single Raman spectra for each component are shown in Fig. 3c. To visualize the exterior component ratio, the spectral data set was converted into a chemically selective false color Raman image. By overlaying the topography profile with the Raman image, we obtained not only a chemically selective but also spatially resolved image in three dimensions. Therefore, the analytical results of the extrudate could be examined from different angles (Fig. 3d). In this exemplary case study, the component distribution was homogenous for the cross section image as well as for the topography corrected surface image. Thus, the exterior component ratio did reflect the interior distribution of the extrudate.

As a second example, we fabricated a lyophilisate containing the protein drug BSA in its native and denatured conformation. The lyophilisate formed a white solid cake-like structure with opaque optical properties (22). In contrast to the extrudate which we investigated first, the lyophilisate exhibited a rough and highly structured surface (Fig. 4a). The detailed structure was visualized by electron microscopy in Fig. 4a.

Analytical detection of the protein structural change with Raman microscopy was performed by using the so-called amide I band at 1,500–1,800 cm^{-1} (22–26). The amide I band is generally used to detect changes in the secondary structure of proteins. The Raman signal of this band is mainly derived from the C=O vibrations of the amide groups in the peptide backbone (23,26). A shift of this band in the Raman spectrum is a clear indication for conformational changes (25,26). Thus, the technique is capable to discriminate between therapeutically active and inactive protein structure within the lyophilisate. The embedded BSA in its native and denatured form can be distinguished by its respective Raman spectra as highlighted in Fig. 4b.

Therefore, we created a sample challenging the abilities of the analytical setup. Unlike wafer and extrudate, which showed different morphologies but still exhibited a smooth plane, the lyophilisate had an irregular, fragile surface structure. Furthermore, the component discrimination was mainly based on a marginal spectral difference of one specific peak shift for the lyophilisate, whereas the aforementioned samples were composed of different chemical components showing completely different Raman spectra. In any case, for a versatile application in pharmaceutics, the combined analytical approach of confocal Raman microscopy and optical topography should cope with diverse sample specifications.

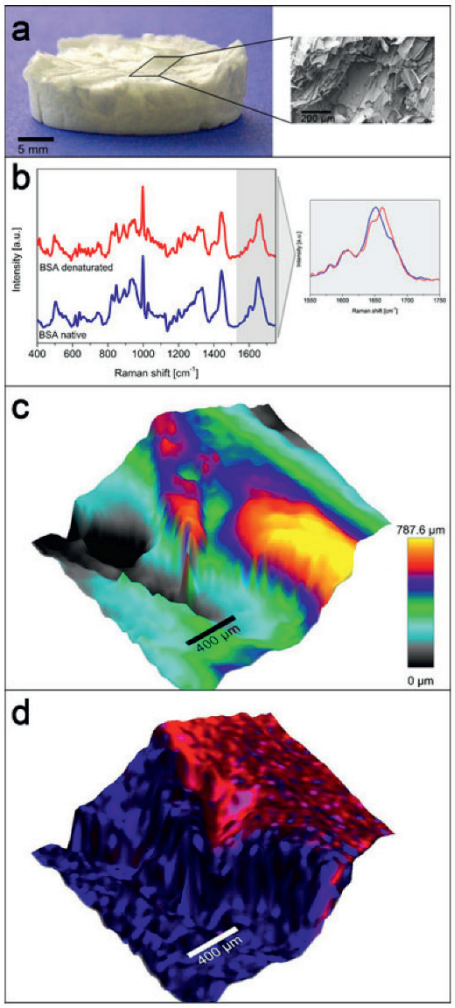

Fig. 4. Investigation of a highly structured lyophilisate section regarding protein conformation location. **a** Lyophilisate and electron microscopy image of an enlarged area visualizing the highly structured surface. **b** Raman spectrum of BSA in its native (*blue*) and denatured (*red*) conformation. The shift of the amide I band between the two conformations is highlighted. **c** Surface topography profile of a lyophilisate section. **d** Overlay of topography profile and respective Raman microscopy analysis data. The resulting three-dimensional chemically selective false color image indicates the native protein in *blue*, whereas *red* represents the denatured protein conformation

Following the analytical order of performing optical topography prior to confocal Raman microscopy analysis, a topography profile of a lyophilisate section of 2,000× 2,000 µm was created as shown in Fig. 4c. The subsequently recorded Raman spectra were then converted into false color images, indicating each BSA conformation in a different color. The native conformation of BSA is represented in blue whereas the denatured conformation is shown in red. In a final step, an overlay of the topographic profile with the Raman image was created by merging the two individual maps (Fig. 4d). For both techniques, the same area with the identical grid for

collection of scattered light was rasterized. Thus, the individual maps were composed of analytical information derived from exactly the same sample spot, enabling the overlay of these complementary data with utmost precision. Ultimately, a three-dimensional characterization of the sample was obtained combining chemical selectivity and surface properties in a spatially resolved image.

CONCLUSION

We successfully introduce the combined analytical approach of confocal Raman microscopy and optical profilometry for investigation of structured surfaces in pharmaceutical science. After proving the concept of the approach, two different drug delivery systems were successfully analyzed regarding their component distribution. The extrudate was built of two components and exhibited a curved surface whereas the challenge for the lyophilisate analysis was based on an unpredictable surface structure and only consisted of one component in two different conformations. Although components and exhibited surface structures varied broadly, precise images regarding spatial resolution and chemical selectivity were obtained. Therefore, the analytical technique is valid for a wide use in pharmaceutical research. The advantage of the non-destructive principle and the informative detailed result outcome bears a high potential for the extensive use of the complementary techniques confocal Raman microscopy and optical profilometry for pharmaceutical investigations.

ACKNOWLEDGMENTS

The authors thank Thomas Dieing for support and valuable discussions.

REFERENCES

1. Been F, Roggo Y, Degardin K, Esseiva P, Margot P. Profiling of counterfeit medicines by vibrational spectroscopy. Forensic Sci Int. 2011;211:83–100.
2. de Veij M, Deneckerea A, Vandenabeele P, de Kaste D, Moens L. Detection of counterfeit Viagra® with Raman spectroscopy. J Pharm Biomed Anal. 2008;46:303–9.
3. Wirges M, Mueller J, Kása Jr P, Regdon Jr G, Pintye-Hódi K, Knop K, Kleinebudde P. From mini to micro scale-feasibility of Raman spectroscopy as a Process Analytical Tool (PAT). Pharmaceutics. 2011;3:723–30.
4. De Waard H, de Beer T, Hinrichs WLJ, Vervaet C, Remon JP, Frijlink HW. Controlled crystallization of the lipophilic drug fenofibrate during freeze-drying: elucidation of the mechanism by in-line Raman spectroscopy. AAPS J. 2012;12:569–75.
5. Windbergs M, Haaser M, McGoverin C, Gordon K, Kleinebudde P, Strachan CJ. Investigating the relationship between drug distribution in solid lipid matrices and dissolution behavior using Raman spectroscopy and mapping. J Pharm Sci. 2010;99:1464–75.
6. Haaser M,Windbergs M, McGoverin CM, Kleinebudde P, Rades T, Gordon KC, Strachan CJ. Analysis of matrix dosage forms during dissolution testing using Raman microscopy. J Pharm Sci. 2011;10:4452–9.
7. Belu A, Mahoney C, Wormuth K. Chemical imaging of drug eluting coatings: combining surface analysis and confocal Raman microscopy. J Control Release. 2008;126:111–21.
8. Matthaeus C, Kale A, Chernenko T, Torchilin V, Diem M. New ways of imaging uptake and intracellular fate of liposomal drug carrier systems inside individual cells, based on Raman microscopy. Mol Pharm. 2008;5:287–93.
9. Chernenko T, Matthaeus C, Milane L, Quintero L, Amiji M, Diem M. Label-free Raman spectral imaging of intracellular delivery and degradation of polymeric nanoparticle systems. ACS Nano. 2009;3:3552–9.
10. Sheparovych R, Motornov M, Minko S. Low adhesive surface that adapt to changing environments. Adv Mater. 2009;21:1840–4.
11. Schrank S, Hodzic A, Zimmer A, Glasser BJ, Khinast J, Roblegg E. Ibuprofen-loaded calcium stearate pellets: drying-induced variations in dosage form properties. AAPS Pharm Sci Technol. 2012;13:686–98.
12. López AJ, Rivas T, Lamas J, Ramil A, Yáñez A. Optimisation of laser removal of biological crusts in granites. Appl Phys A Mater Sci Process. 2010;100:733–9.
13. Truong VK, Lapovok R, Estrin YS, Rundell S, Wang JY, Fluke CJ, *et al.* The influence of nano-scale surface roughness on bacterial adhesion to ultrafine-grained titanium. Biomaterials. 2010;31:3674–83.
14. Azmat NS, Ralston KD, Muster TH, Muddle BC, ColeI S. A high-throughput test methodology for atmospheric corrosion studies. Electrochem Solid-State Lett. 2011;14:C9–C11.
15. Feys J, Vermeir P, Lommens P, Hopkins SC, Granados X, Glowacki BA, *et al.* Ink-jet printing of $YBa_2Cu_3O_7$ superconducting coatings and patterns from aqueous solutions. J Mater Chem. 2012;22:3717–26.
16. Schneider T, Kohl B, Sauter T, Becker T, Krantz K, Schossig M, *et al.* Viability, adhesion and differentiated phenotype of articular chondrocytes in degradable polymers and electro-spun structures thereof. Macromol Symp. 2011;309/310:28–39.
17. Formosa LM, Mallia B, Bull T, Camelleri J. The microstructure and surface morphology of radiopaque tricalcium silicate cement exposed to different curing conditions. Dent Mater. 2012;28:584–95.
18. Manova D, Lutz J, Maendl S. Sputtering effects during plasma immersion ion implantation of metals. Surf Coat Technol. 2010;204:2875–80.
19. Thommes M, Baert L, Rosier J. 800mg Darunavir tablets prepared by hot melt extrusion. Pharm Dev Technol. 2011;16:645–50.
20. Gueres S, Siepmann F, Siepmann J, Kleinebudde P. Drug release from extruded solid lipid matrices: theoretical predictions and independent experiments. Eur J Pharm Biopharm. 2012;80:122–9.
21. Windbergs M, Gueres S, Strachan CJ, Kleinebudde P. Two-step solid lipid extrusion as a process to modify dissolution behavior. AAPS Pharm Sci Technol. 2012;11(1):2–8.
22. Wang W. Lyophilisation and development of solid protein pharmaceuticals. Int J Pharm. 2000;203:1–60.
23. Tantipolphan R, Rades T, Medlicott NJ. Insights into the structure of protein by vibrational spectroscopy. Curr Pharm Anal. 2008;4:53–68.
24. Lippert JL, Tyminski D, Desmeules PJ. Determination of the secondary structure of proteins by laser Raman spectroscopy. J Am Chem Soc. 1976;98:7075–80.
25. Chen MC, Lord RC. Laser-excited Raman spectroscopy of biomolecules. VIII. Conformational study of bovine serum albumin. J Am Chem Soc. 1976;98:990–2.
26. Hédoux A, Willart JF, Paccou L, Guinet Y, Affouard F, Lerbret A, Descamps M. Thermostabilization mechanism of BSA by trehalose. J Phys Chem B. 2009;113:6119–26.

5.5 Solid Dispersions Prepared by Continuous Cogrinding in an Air Jet Mill

Solid Dispersions Prepared by Continuous Cogrinding in an Air Jet Mill

C. Muehlenfeld, B. Kann, M. Windbergs, M. Thommes

J. Pharm. Sci. **2013**,102:4132-4139.

DOI: 10.1002/jps.23731

RESEARCH ARTICLE – *Pharmaceutics, Drug Delivery and Pharmaceutical Technology*

Solid Dispersions Prepared by Continuous Cogrinding in an Air Jet Mill

CHRISTIAN MUEHLENFELD,[1] BIRTHE KANN,[2] MAIKE WINDBERGS,[2,3] MARKUS THOMMES[1]

[1]Institute of Pharmaceutics and Biopharmaceutics, Heinrich-Heine-University, Duesseldorf, 40225, Germany
[2]Department of Biopharmaceutics and Pharmaceutical Technology, Saarland University, Campus A4.1, Saarbruecken, 66123, Germany
[3]Helmholtz Centre for Infection Research (HZI) and Helmholtz-Institute for Pharmaceutical Research Saarland (HIPS), Department of Drug Delivery, Campus A4.1, Saarbruecken, 66123, Germany

Received 3 July 2013; revised 2 August 2013; accepted 26 August 2013

Published online in Wiley Online Library (wileyonlinelibrary.com). DOI 10.1002/jps.23731

ABSTRACT: Embedding a poorly water-soluble drug as a solid dispersion in a hydrophilic carrier by cogrinding is a possible strategy for enhancing the drug dissolution rate. Although general interest in continuous processes for manufacturing drug formulations has increased, many publications still focus on batch processes. The jet mill used in this study is a promising tool for continuous cogrinding. Investigation of different drug-to-carrier ratios (griseofulvin/mannitol) demonstrated that a drug load of 10% is best suited to investigate the enhanced dissolution behavior. To gain deeper insight into the underlying mechanisms, the coground dispersion is compared with different physical mixtures in terms of physicochemical properties and dissolution behavior. Differential scanning calorimetry and X-ray powder diffraction were used to verify the crystalline structure of the coground formulation. On the basis of the Hixson–Crowell model, particle size reduction was ruled out as the main reason for dissolution enhancement. An increase of surface free energies because of grinding is shown with contact angle measurements. Confocal Raman microscopy investigations revealed the drug's bulk dispersity in the coground formulation as an additional factor for the increased dissolution rate. In conclusion, the continuous cogrinding approach is a promising technique to prepare the drug in a rapidly dissolving, yet crystalline, form. © 2013 Wiley Periodicals, Inc. and the American Pharmacists Association J Pharm Sci

Keywords: calorimetry (DSC); solid dispersion; poorly water-soluble drugs; dissolution rate; surface energy; milling; wetting and contact angle; physicochemical properties; Raman spectroscopy; X-ray powder diffractometry

INTRODUCTION

Because of the increasing incidence of poorly water-soluble drug candidates in the drug discovery pipeline, strategies to improve drug solubility and bioavailability are significant topics of interest in pharmaceutical research. Typical physical approaches to improve drug solubility include the use of polymorphs,[1] the conversion of crystalline drugs to their respective amorphous forms,[2] complexation,[3] and solubilization by surfactants (microemulsions and self-microemulsifying drug delivery systems)[4] as well as solid dispersions.[5–7]

Embedding a poorly water-soluble drug in a hydrophilic carrier to form a solid dispersion may increase solubilization and dissolution rate if the drug is uniformly dispersed in its molecular, colloidal, amorphous, or microcrystalline form[5] within a solid carrier. Originally, solid dispersions were prepared by (fusion) melting[7–9] or solvent methods.[10–13] Techniques such as freeze-drying[14] as well as coprecipitation[15] and cogrinding[16–18] have become the focus of more investigations.

In contrast to melting or solvent methods, the cogrinding approach is more versatile. Because fusion melting is a temperature-dependent process, a high temperature is often needed to reach the compound's melting point. Unfortunately, many substances undergo thermal decomposition at these temperature levels. When the processing temperatures of the individual components vary widely, it becomes even more crucial to be mindful of this phenomenon. For solvent methods, avoiding the use of organic solvents is impossible. Therefore, residual solvents are often detectable within the final systems, creating toxicity issues. These limitations do not apply to cogrinding techniques. Despite the increased interest in continuous processes for manufacturing drug formulations, several publications still focus on batch processes in the area of cogrinding.[18–21] The time-consuming nature of such processes combined with small batch sizes is often a hurdle for scale-up and industrial use. Applying a continuous cogrinding process in a jet mill combines the benefits of cogrinding and a higher material throughput.

Cogrinding has been adopted for several poorly water-soluble compounds.[22,23] Modifications of the physical state of the drug, such as creating amorphous drugs in the form of amorphous solid dispersions, have been an active area of research for decades.[18] Drug particles that are highly dispersed in the mixture may also lead to enhanced dissolution behavior because of the reduced agglomeration tendency of the hydrophobic drug particles.[16] On the basis of observations of improved wettability after grinding, it has been reported that applying such intense forces on the particles may increase their surface free energy.[24]

In this study, dissolution enhancement of griseofulvin, a Biopharmaceutics Classification System (BCS) class II drug, was achieved by continuous cogrinding with mannitol, a hydrophilic sugar alcohol. Dissolution and physicochemical properties of a coground mixture were analyzed in comparison with different physical mixtures of the same components. The aim of the study was to produce solid dispersions by using a continuous cogrinding approach, and to investigate the mechanisms responsible

Correspondence to: Markus Thommes (Telephone: +49-211-8114220; Fax: +49-211-8114251; E-mail: markus.thommes@uni-duesseldorf.de, markus.thommes@hhu.de)

Journal of Pharmaceutical Sciences

Table 1. Overview of Formulations Used in This Study

Name	Griseofulvin (Drug)	Mannitol (Carrier)
Coground formulation	Coground	
Physical mixture (PM1)	Unprocessed	Unprocessed
Physical mixture (PM2)	Unprocessed	Ground
Physical mixture (PM3)	Ground	Ground
Physical mixture (PM4)	Ground	Unprocessed

for the enhanced dissolution behavior of the formulation obtained.

MATERIALS AND METHODS

Materials

Micronized griseofulvin served as the model drug (Letco Medical, Decatur, Alabama), and β-mannitol (Pearlitol 160C; Roquette, Lestrem, France) was used as the carrier. All substances were of United States Pharmacopeia (USP) grade and used as received.

Preparation of Coground Formulations

Powder mixtures containing griseofulvin (10%/25%/55%) and mannitol were blended for 15 min in a laboratory-scale blender at 100 rpm (Turbula T2 F; W. A. Bachofen AG, Muttenz, Switzerland) and afterward transferred to the gravimetric powder feeder (KT20, K-Tron; Soder, Lenzard, Switzerland) of the air jet mill (Aeroplex spiral jet mill 50 AS; Hosokawa Alpine AG, Augsburg, Germany). The powder feed rate was set to 4 g/min. The mill consists of a flat, circular grinding chamber with four inclined fluid jets, each of 0.8 mm in diameter, at an angle of 30°. The carrier fluid was compressed air. The injector air pressure was 4.5 bar, and the grinding air pressure was 4 bar. In order to improve the uniformity of the powder feed rate, a vibration tray (DR100; Retsch, Haan, Germany) was mounted between the powder feeder and the air jet mill to reduce fluctuations.

Preparation of Physical Mixtures

Four different physical mixtures were prepared according to Table 1. For physical mixtures containing ground substances, the milling conditions of the coground samples were used. All physical mixtures were prepared by blending 100 g of the mixture in a laboratory-scale blender at 100 rpm (Turbula T2 F, W. A. Bachofen AG). In this manner, the entire amount of drug was gradually combined with an increasing amount of excipient in four steps, each blended for 10 min.

Powder Dissolution Studies

Dissolution tests were performed in a paddle apparatus (DT6; Erweka, Heusenstamm, Germany) under sink conditions in accordance with the USP at 50 rpm using 900 mL water at 37°C as the dissolution medium. Six replicates of each batch were tested and quantified with a UV photometer (Lambda2S; PerkinElmer, Rodgau, Germany) at 295 nm sampling every second.

Differential Scanning Calorimetry

Thermograms were obtained by differential scanning calorimetry (DSC; DSC 1; Mettler Toledo, Giessen, Germany). Accurately weighed samples of 2 –5 mg were investigated at a scanning rate of 10°C/min, covering a temperature range of 0°C–250°C. Each batch was analyzed in duplicate.

Drug Particle Size

Particle size distribution measurements were carried out using a laser diffractometer (Helos/Cuvette; Sympatec GmbH, Clausthal-Zellerfeld, Germany). Powder samples were suspended in a saturated solution of griseofulvin in water and stirred at 500 rpm to strip the excipient from the mixture. A period of sonication (200 s) at a power of 60 W was applied before sizing to ensure sufficient dispersion. Measurements were performed in triplicate.

X-ray Powder Diffraction

X-ray powder diffraction (XRPD) was applied using an X'Pert Pro MPD diffractometer (Panalytical, Almelo, The Netherlands). Measurements were performed with a Cu Kα radiation point source ($\lambda = 1.5406$ Å) at 40 kV and 40 mA. Samples of 300 mg were placed in 13 mm back-loaded holders with a pressure of approximately 20 kN for 10 s exerted by a hydraulic press (Hydraulic Laboratory Press, PerkinElmer, Ueberlingen, Germany). Measurements were taken in the reflection mode from 10° to 50° 2θ.

Hixson–Crowell Model

The Hixson–Crowell model[25] was used to describe the release from the formulations produced. The equation is:

$$m_0^{1/3} - m_R^{1/3} = K_{HC}t \tag{1}$$

where m_0 is the initial amount in the pharmaceutical dosage form, m_R is the remaining amount of drug in the dosage form at time t, and K_{HC} is a constant incorporating the surface–volume relation. Assuming spherical particles and sink conditions, K_{HC} can be substituted, leading to:

$$m_0^{1/3} - m_R^{1/3} = \frac{D(C_S - c)}{3\delta} 4\pi \left(\frac{3}{4\pi\rho}\right)^{2/3} \tag{2}$$

where D is the diffusion coefficient of griseofulvin in water ($8 \pm 1 \times 10^{-10}$ m²/s),[26] C_S is the solubility of griseofulvin in water at 25°C (12.1 ± 0.3 mg/L),[27] δ is the thickness of the diffusion layer (0.02 mm),[28] ρ is the density of griseofulvin (1484 kg/m³), and c is the current concentration in the solution.

The particle size distribution data obtained from the laser diffraction experiments allow the calculation of the initial mass of the drug particles, and the remaining mass after a certain time, t. By extrapolating to the particle size distribution for a defined amount of griseofulvin, it was possible to model a drug dissolution rate based on the decreasing surface of the drug particles during dissolution.

Contact Angle Measurements

The spreading behavior of liquid additives on compacts was investigated using the sessile drop method ($n = 10$). Flat-faced compacts of the different formulations (300 mg, 13 mm diameter) were prepared using a hydraulic press (Hydraulic Laboratory Press, PerkinElmer) and compressed to a compact porosity of 12.5%. Water and diiodomethane (DIM) were used as probe liquids. Contact angles on compacts were measured with a drop shape analyzer (DSA100; Kruess, Hamburg, Germany). A drop

 DOI 10.1002/jps.23731

of 0.75 μL was automatically generated by a micrometer syringe and placed on the test substrate. A video was recorded and the contact angles were analyzed after 1 s.

Surface Free Energy Determinations

The surface free energies of griseofulvin/mannitol compacts were determined from the contact angle data obtained from the sessile drop technique after transposing the equation published by Owens and Wendt (Eq. (3))[29]:

$$\gamma_L(\cos\theta + 1) = 2\sqrt{\gamma_S^D \gamma_L^D} + 2\sqrt{\gamma_S^P \gamma_L^P} \quad (3)$$

where γ_L is the surface tension of the liquid, $\gamma_L{}^P$ and $\gamma_L{}^D$ are the polar and dispersive fractions of the liquid, and $\gamma_S{}^P$ and $\gamma_S{}^D$ are the polar and dispersive fractions of the solid, respectively. To determine the components $\gamma_S{}^P$ and $\gamma_S{}^D$, contact angles of apolar (DIM) and polar (water) liquids were measured to solve the two equations simultaneously, thus obtaining the components and the total surface free energy as the sum of the two components. The liquid probes and their corresponding γ_L, $\gamma_L{}^D$, and $\gamma_L{}^P$ values are taken from the study of Ström et al.[30]

Raman Mapping

Compacts of the different formulations (300 mg, 13 mm diameter) were prepared in the same way as compacts used for contact angle measurements. Raman spectra were recorded with a confocal Raman microscope (WITec alpha 300R+; WITec GmbH, Ulm, Germany) equipped with a Zeiss objective (50× magnification, numerical aperture = 0.8) at an integration time of 0.2 s. The excitation wavelength of the diode laser (Toptica, Munich, Germany) operating at 100 mW was 785 nm. Six individual areas of 50 × 50 μm^2 of each compact surface (as well as an area of 50 × 500 μm^2 recorded at the cross section of the tablet) were investigated with a lateral resolution of 1 μm. The obtained Raman spectral data sets were preprocessed (WITec Project Plus Software) by removing cosmic rays and through background signal reduction. The peaks (1710 and 881 cm^{-1}) were used to identify griseofulvin and mannitol, respectively, during the subsequently performed supervised cluster analysis. The resulting spectral data sets were converted into false color Raman maps displaying griseofulvin in yellow and mannitol in blue. The generated maps were processed with image analysis software (Qwin; Leica, Cambridge, UK), which calculated the projected area of griseofulvin for each Raman map. On the basis of the two-dimensional projection, the equivalent diameter was calculated as the diameter of a circle with the same area as the projected area.

RESULTS AND DISCUSSION

Solid dispersions were prepared from griseofulvin and mannitol via continuous cogrinding. In order to gain deeper insight into the mechanisms that account for enhanced dissolution, the coground dispersion was compared with different physical mixtures of the same components in terms of physicochemical properties and dissolution behavior. The study is divided into three parts. The first part discusses the influence of drug loading within the solid dispersion. In the second part, the dissolution enhancement of the best solid dispersion with its corresponding physical mixtures is compared. The final and third part discusses the enhanced dissolution behavior, and potential reasons for dissolution enhancements are identified.

First, the dissolution behavior of three coground formulations containing 10%, 25%, and 55% drug load was investigated to observe the potential influence of the drug load on release and hence, find the best suited ratio for analyzing the mechanism of the enhanced dissolution behavior.

The griseofulvin load affected the release from the coground formulation (Fig. 1a). Although the coground formulation with 10% drug exhibited a rapid griseofulvin release, the dissolution rate results for higher drug loadings did not reveal such accelerated dissolution behavior. In comparison with the dissolution rate of the plain, micronized drug, the dissolution rate improvement of the coground formulations containing 25% and 55% drug load was still observable. Because the coground formulations represent disordered particulate systems, percolation theory may be applicable[31] to explain the differences between the drug dissolution rates. Because the solubility of griseofulvin is much lower than the solubility of mannitol, a change in the dissolution rate is apparent when the percolation threshold is exceeded. Because the dissolution rate improved most for the 10% coground formulation, this loading was used for further studies.

Four physical mixtures were prepared to reveal the mechanisms behind the dissolution enhancement of the coground formulation. These physical mixtures contained griseofulvin and mannitol with different particle sizes. Their dissolution profiles are compared with the dissolution profile of the 10% coground formulation in Figure 1b. The dissolution rate of the physical mixture (PM1) with unground drug and unground carrier was low, whereas the dissolution rate of coground griseofulvin and mannitol was accelerated by about 10-fold. Compared with the physical mixture containing both ground drug and ground carrier, the dissolution rate from the coground formulation was considerably faster.

One explanation for the higher dissolution rate of solid dispersions is the formation of higher energy, metastable states of the components or a polymorphic transition during fabrication. Figure 2 shows the XRPD patterns of the coground formulation and the corresponding physical mixtures. The diffractograms clearly confirm the crystallinity of the coground formulation. Recently, two new polymorphs of griseofulvin were discovered (forms II and III).[32] The most stable polymorph, form I, was used in this study as confirmed by the X-ray diffraction patterns. The most stable form of mannitol, the β-form, was also used.[33] Each peak can be correlated with the pattern of the unprocessed physical mixture, which does not indicate any loss of crystallinity or polymorphic transition. The reduction in peak intensity could be attributed to the reduced crystallite size.[34] Related to this, a peak broadening was expected, but not observed with any statistical significance because of the low signal-to-noise ratio. According to the Scherrer equation, the limit of quantification for crystallite size is close to our drug particle size (approximately 1 μm).[35] Therefore, this effect was not studied quantitatively. However, it was not the result of amorphous regions. Moreover, it is known that a cocrystal provides a unique X-ray pattern.[36,37] Because all peaks of the X-ray pattern correlate with griseofulvin and mannitol, cocrystal formation is excluded as an underlying reason for the faster drug release.

Besides X-ray diffraction, DSC was used to quantify the amount of higher energy, metastable states of the components.

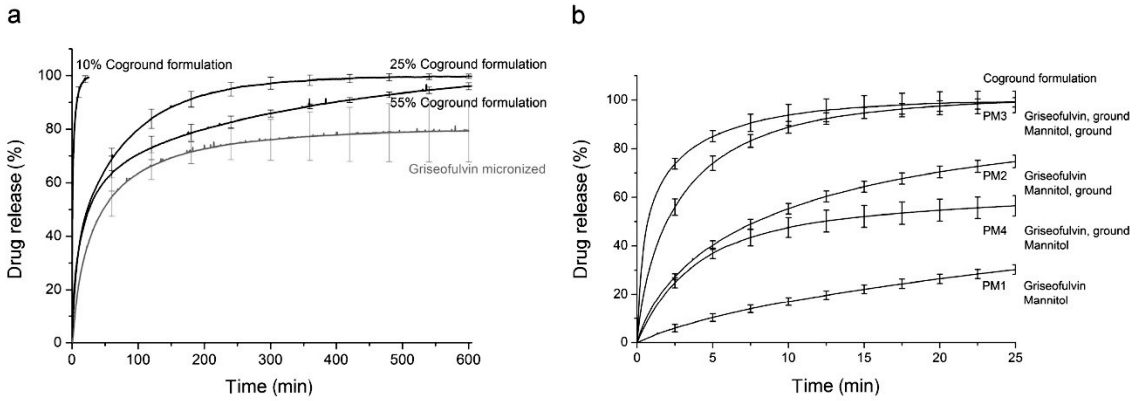

Figure 1. (a) Dissolution rate profile of the coground formulations containing 10%, 25%, and 55% drug load. The dissolution rate of the plain drug is also shown for comparison ($n = 6$, average ± CI, $\alpha = 0.05$). (b) Dissolution rate profiles of 10% coground formulation in comparison with the comparative physical mixtures ($n = 6$, average ± CI, $\alpha = 0.05$).

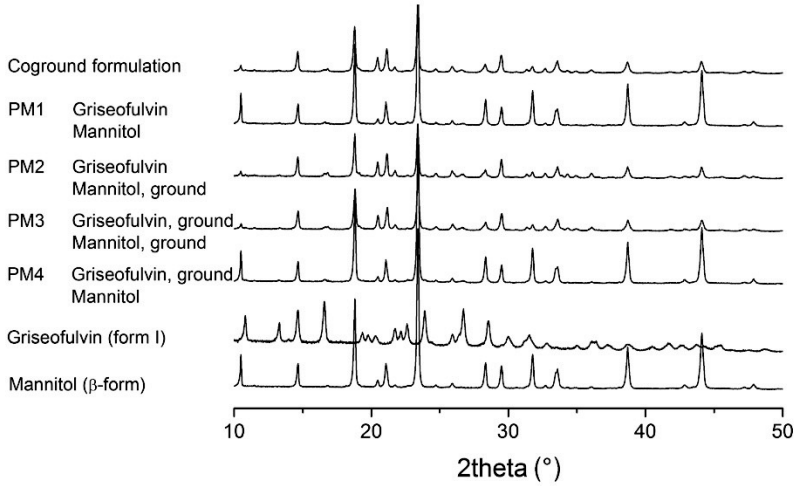

Figure 2. X-ray diffraction patterns of the coground formulation and physical mixtures.

The DSC results in Figure 3a corroborate the X-ray diffraction results, which show that that the two components in the coground formulation exist as separate crystalline phases. All thermograms showed single endothermic peaks with onset temperatures around 167°C and 216°C, corresponding to literature values of pure mannitol[38] and griseofulvin,[39] respectively. The results indicated a slight peak broadening of the griseofulvin endotherm without any change in the heat of fusion of the ground samples, which could be because of the reduction of particle size without a loss of crystallinity of the griseofulvin during milling.[40] Furthermore, the thermograms did not indicate the presence of an amorphous phase because no glass transition was observed. Amorphous griseofulvin exhibits a broad exotherm around the T_G, which is 88°C.[41] Because the peak area of the exotherm is a function of the amorphous purity of the sample, partial amorphization of the coground formulation should lead to an exotherm event at around 110°C. To demonstrate this, mixtures of 5%, 2%, 1%, and 0.5% amorphous griseofulvin in crystalline griseofulvin were prepared, measured, and compared with the thermogram of the coground formulation (Fig. 3b). It can clearly be seen that the mixture of 0.5% amorphous griseofulvin with 99.5% crystalline griseofulvin exhibits a slight exotherm at 125°C, which is within the limit of detection as well as quantitation according to the ICH Q2 guideline.[42] However, the coground formulation prepared via jet milling did not show any exothermic event comparable to this peak. Because the coground formulation consisted of 10% griseofulvin and 90% mannitol, it can be stated that the mixture contained less than 5% amorphous fraction of the drug. Thus, the increased dissolution rate is not related to amorphization of the drug. On the basis of the thermograms, amorphous solid dispersions and the formation of eutectic mixtures are both excluded as possible reasons for the observed drug release enhancements.

Because the enhanced drug dissolution rate is not related to modifications of the physical form of the drug such as polymorph changes, amorphization, or the formation of eutectic mixtures, there are only two main factors that explain the

 DOI 10.1002/jps.23731

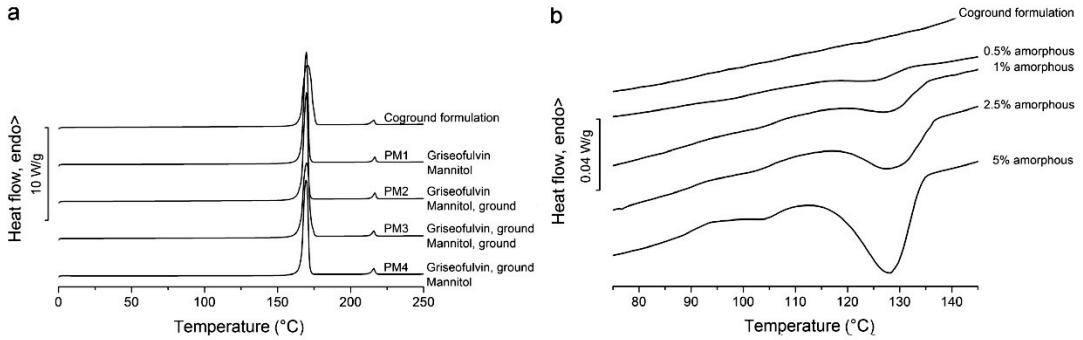

Figure 3. (a) DSC thermograms of cogrund formulation as well as physical mixtures. (b) DSC thermograms of cogrund formulation in comparison with partially amorphous griseofulvin samples (0.5%, 1%, 2%, and 5% amorphous griseofulvin in crystalline griseofulvin).

accelerated dissolution rate of the coground formulation: favored wettability and reduced particle size. The highly water-soluble mannitol powder dissolved quickly (within 1 min), allowing for particle size measurements of the drug suspended only in the medium. Figure 4 depicts the griseofulvin particle size distribution after stripping the mannitol. During cogrinding, drug particles are more reduced in particle size with respect to the pure drug than when grinding the pure drug under the same milling conditions. If the dissolution rate enhancement is mainly caused by the drug particle size, then it should be possible to model the dissolution rate with the Hixson–Crowell cube root law. Figure 5 shows the comparison between the measured dissolution curves (coground drug and physical mixture PM1) and their corresponding Hixson–Crowell calculation. If the dissolution rate is only influenced by the drug particle size, the measured and the calculated dissolution curves would show an approximately equal dissolution rate. As Figure 5 illustrates, the calculated dissolution profile of the physical mixture (PM1) corresponds well with the measured data; however, the drug release of the coground formulation is considerably faster than the corresponding calculation. Therefore, the dissolution rate enhancement because of cogrinding is not only related to drug particle size reduction.

This observation is also substantiated by the dissolution profiles of the different physical mixtures. Differences in the dissolution profiles are not only related to griseofulvin particle size because there is no correlation between the drug particle size and the dissolution rate (Fig. 1b). In fact, unground griseofulvin exhibited a considerably faster dissolution rate in the presence of ground mannitol than was observed for ground griseofulvin in the presence of unground mannitol. The presence of ground mannitol produced a significant increase in the dissolution rate. However, it is unlikely that the increased dissolution rate is because of the increased solubility of griseofulvin in an aqueous solution of mannitol as compared with pure water. Experiments regarding this effect for pure griseofulvin in either water or water containing mannitol showed that griseofulvin does not dissolve any faster in an aqueous mannitol solution than in pure water. However, despite mannitol being a poor solvent for griseofulvin, it was still effective in facilitating wetting of the drug particles.

Hence, a further reason for the enhanced dissolution behavior is the favored wettability. For dissolution-rate-controlled BCS class II drugs such as griseofulvin, this is an important mechanism contributing to the drug dissolution rate.[43] The wettability of the coground formulation, as well as the different physical mixtures, was evaluated with distilled water and DIM (Fig. 6a). In order to ensure comparability, compacts prepared from the different mixtures were compressed to a porosity of 12.5 ± 0.14%. Compacts of the physical mixtures exhibited higher contact angles compared with the coground formulation when applying the sessile drop technique. However, there were

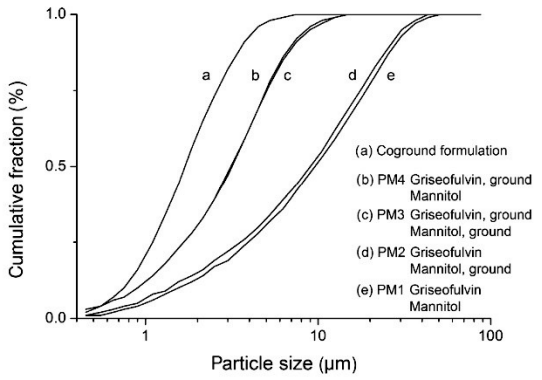

Figure 4. Particle size distribution of the different formulations.

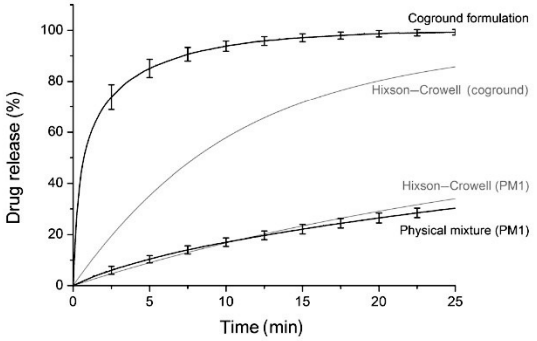

Figure 5. Comparison between Hixson–Crowell calculation and measured dissolution profile of coground formulation and physical mixture (PM1).

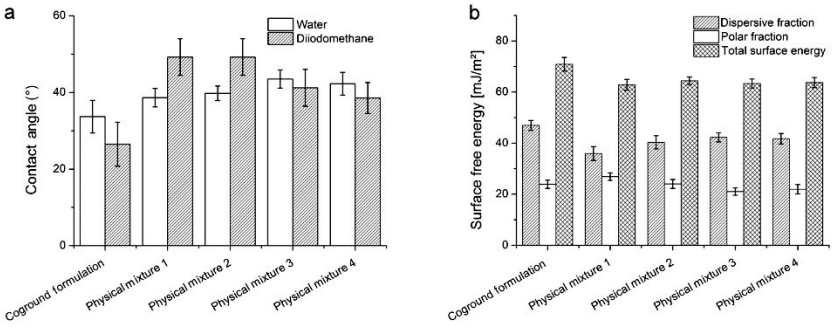

Figure 6. (a) Contact angles of probe liquids on compacts of 12.5% porosity measured by sessile drop method ($n = 10$, average ± CI, $\alpha = 0.05$). (b) Surface energy terms for mixtures containing griseofulvin and mannitol calculated from Owens and Wendt approach (Eq. (3)) ($n = 10$, average ± CI, $\alpha = 0.05$).

no significant differences at a confidence level (CI) of 0.95 in the wetting kinetics exhibited for contact angle measurements made with distilled water. Altogether, in comparison with the different physical mixtures of griseofulvin and mannitol, the coground drug exhibited an improved wetting profile for DIM, indicating a higher surface dispersity that enhanced its dispersive interactions. This effect could be explained by the crystal facet-specific surface energetics of drug and excipient. On the basis of its crystal morphology, the wettability of mannitol is anisotropic because of the variation in the concentration of surface functional groups on the individual facets possessing polar and dispersive interactions of varying magnitude.[44] Thus, grinding may lead to new faces with different surface properties. During grinding, mannitol particles preferentially split along the cleavage plane with the lowest surface energy, which has been assumed to be the crystal face with highest surface area.[45]

The interpretation of contact angle in terms of surface free energy relies on Young's equation.[46] The contact angle values obtained from the sessile drop technique were used to determine the surface free energy according to Owens and Wendt.[29] As shown in Figure 6b, the coground formulation has a higher surface free energy with a significant positive dispersive component along with the polar component. However, the observed differences in surface free energies between the coground drug and the physical mixtures may be an additional factor in the differences in drug dissolution. The higher dispersive forces are mainly responsible for the greater interaction tendency between the surfaces of the coground drug and water or DIM, respectively. However, when comparing the physical mixtures with each other, no significant difference in the total surface free energy was observed.

It is known that finely dispersed drug particles in a mixture can also lead to an enhanced dissolution rate because of a reduced agglomeration tendency; therefore, further investigations focused on bulk dispersity. Confocal Raman microscopy is a chemically selective analytical technique allowing label-free detection of drug and excipient distribution within solid carrier systems.[47] Here, confocal Raman microscopy was applied to evaluate dispersity differences of griseofulvin particles within the different compacts prepared from physical mixtures and the coground formulation. For each of the five compacts, an area of the interior cross section (Fig. 7a) and six randomly distributed areas on the compact surface (Fig. 7b) were investigated. Because no differences between drug dispersity on the exterior and the interior for each compact were observed, only the interior cross-section image of the coground formulation is shown (Fig. 7c). Nevertheless, qualitative differences in drug dispersity between the coground formulation and the different physical mixtures can be perceived (Figs. 7d–7h). The coground formulation displays a more homogeneous distribution of griseofulvin within the mixture, whereas drug particles in the physical mixtures tend to agglomerate to a greater extent. Subsequently performed image analysis of the area containing griseofulvin confirmed this observation. Compared with the size distribution of the drug particles after stripping the mannitol (Fig. 4), drug distribution detected by Raman mapping showed the same trends among the different compacts. However, it must be taken into account that the drug particles detected by Raman mapping within the intact mannitol matrix might be separated into smaller particles during the stripping procedure before analysis with laser diffraction. Thus, the comparison of size distribution trends among different compacts is more appropriate than a direct comparison of absolute size values for drug particles because drug clusters were considered. One reason for the lower drug particle size of the coground drug compared with the physical mixtures containing both ground drug and ground excipient might be the different manufacturing processes. Unlike cogrinding, simple micronization could lead to an agglomeration tendency of micronized powders,[23] probably because of high cohesion forces between these particles.[48] Although a simple blending step after micronization cannot overcome these forces, the cogrinding approach might reduce this effect to a negligible influence resulting in a higher degree of dispersion. Consequently, observations of drug dispersity differences in Raman maps can be used to substantiate the different dissolution behaviors of the formulations presented.

CONCLUSIONS

In this study, the applicability of continuous cogrinding via jet milling and the mechanism behind the dissolution enhancement of a solid dispersion prepared by continuous cogrinding were investigated. Physicochemical properties and dissolution behavior of the solid dispersion were compared with four physical mixtures. In the case of the solid dispersion, it was shown that the increased dissolution rate is not related to a change of

 DOI 10.1002/jps.23731

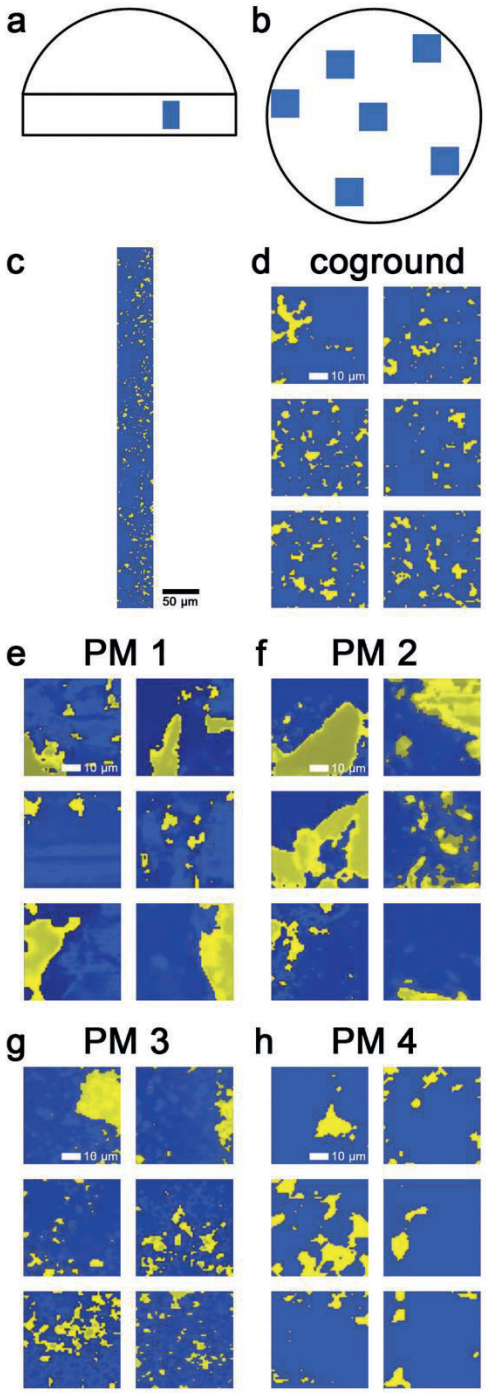

Figure 7. Differences in drug dispersity between the coground formulation and different physical mixtures. Images of coground compact to show exemplarily the interior cross section (a) and six randomly distributed areas on the compact surface (b). Raman maps of griseofulvin (yellow) and mannitol (blue) coground recorded as cross-section image (c) and compact surfaces (d). Raman maps of the different physical mixtures (e–h).

the crystalline form of drug or excipient. Furthermore, a correlation between drug particle size and dissolution rate was observed, but this is not the only aspect to be taken into account. The increase of the surface free energy because of jet milling and the increased bulk dispersity of the drug may be additional factors for the increased dissolution rate. Thus, continuous cogrinding via air jet mill is a suitable technology, with potential for scale-up and industrial applications, to enhance dissolution without changing the crystalline form of the drug.

ACKNOWLEDGMENTS

We gratefully acknowledge Roquette (Roquette, Lestrem, France) for donating materials, Karin Matthee for the DSC measurements, and the assistance of Elizabeth Ely (EIES, Lafayette Indiana) in preparing the manuscript.

REFERENCES

1. Henck JO, Griesser UJ, Burger A. 1997. Polymorphie von Arzneistoffen: Eine wirtschaftliche Herausforderung? Pharmazeutische Industrie 59(2):165–169.
2. Hancock BC, Zografi G. 1997. Characteristics and significance of the amorphous state in pharmaceutical systems. J Pharm Sci 86(1):X1–X12.
3. Loftsson T, Brewster ME. 1996. Pharmaceutical applications of cyclodextrins. 1. Drug solubilization and stabilization. J Pharm Sci 85(10):1017–1025.
4. Kawakami K, Oda N, Miyoshi K, Funaki T, Ida Y. 2006. Solubilization behavior of a poorly soluble drug under combined use of surfactants and cosolvents. Eur J Pharm Sci 28(1–2):7–14.
5. Serajuddin ATM. 1999. Solid dispersion of poorly water-soluble drugs: Early promises, subsequent problems, and recent breakthroughs. J Pharm Sci 88(10):1058–1066.
6. Leuner C, Dressman J. 2000. Improving drug solubility for oral delivery using solid dispersions. Eur J Pharm Biopharm 50(1):47–60.
7. Chiou WL, Riegelman S. 1971. Pharmaceutical applications of solid dispersion systems. J Pharm Sci 60(9):1281–1302.
8. Andrews GP, AbuDiak OA, Jones DS. 2010. Physicochemical characterization of hot melt extruded bicalutamide–polyvinylpyrrolidone solid dispersions. J Pharm Sci 99(3):1322–1335.
9. Sekiguchi K, Obi N. 1961. Studies on absorption of eutectic mixture. I. A comparison of the behavior of eutectic mixture of sulfathiazole and that of ordinary sulfathiazole in man. Chem Pharm Bull 9(11):866–872.
10. Tachibana T, Nakamura A. 1965. A methode for preparing an aqueous colloidal dispersion of organic materials by using water-soluble polymers: Dispersion of β-carotene by polyvinylpyrrolidone. Colloid Polym Sci 203(2)130–133.
11. Gibbs IS, Heald A, Jacobson H, Wadke D, Weliky I. 1976. Physical characterization and activity in vivo of polymorphic forms of 7-chloro-5, 11-dihydrodibenz[b, e][1, 4]oxazepine-5-carboxamide, a potential tricyclic antidepressant. J Pharm Sci 65(9):1380–1385.
12. Weuts I, Kempen D, Decorte A, Verreck G, Peeters J, Brewster M, Van den Mooter G. 2004. Phase behaviour analysis of solid dispersions of loperamide and two structurally related compounds with the polymers PVP-K30 and PVP-VA64. Eur J Pharm Sci 22(5):375–385.
13. Paudel A, Van Humbeeck J, Van den Mooter G. 2010. Theoretical and experimental investigation on the solid solubility and miscibility of naproxen in poly(vinylpyrrolidone). Mol Pharm 7(4): 1133–1148.
14. Betageri GV, Makarla KR. 1995. Enhancement of dissolution of glyburide by solid dispersion and lyophilization techniques. Int J Pharm 126(1–2): 155–160.
15. Dong Z, Chatterji A, Sandhu H, Choi DS, Chokshi H, Shah N. 2008. Evaluation of solid state properties of solid dispersions prepared by hot-melt extrusion and solvent co-precipitation. Int J Pharm 355(1–2):141–149.

DOI 10.1002/jps.23731

16. Sugimoto M, Okagaki T, Narisawa S, Koida Y, Nakajima K. 1998. Improvement of dissolution characteristics and bioavailability of poorly water-soluble drugs by novel cogrinding method using water-soluble polymer. Int J Pharm 160(1):11–19.
17. Vogt M, Kunath K, Dressman JB. 2008. Dissolution improvement of four poorly water soluble drugs by cogrinding with commonly used excipients. Eur J Pharm Biopharm 68(2):330–337.
18. Barzegar-Jalali M, Valizadeh H, Siahi Shadbad M-R, Adibkia K, Mohammadi G, Farahani A, Arash Z, Nokhodchi A. 2010. Cogrinding as an approach to enhance dissolution rate of a poorly water-soluble drug (gliclazide). Powder Technol 197(3):150–158.
19. Io T, Fukami T, Yamamoto T, Suzuki T, Xu J, Tomono K, Ramamoorthy A. 2010. Homogeneous nanoparticles to enhance the efficiency of a hydrophobic drug, antihyperlipidemic probucol, characterized by solid-state NMR. Mol Pharm 7(1):299–305.
20. Friedrich H, Nada A, Bodmeier R. 2005. Solid state and dissolution rate characterization of co-ground mixtures of nifedipine and hydrophilic carriers. Drug Dev Ind Pharm 31(8):719–728.
21. Cirri M, Mura P, Robasco AM, Ginés JM, Moyano JR, Gònzalez-Rodrìguez ML. 2004. Characterization of ibuproxam binary and ternary dispersions with hydrophilic carriers. Drug Dev Ind Pharm 30(1):65–74.
22. Jinno JI, Kamada N, Miyake M, Yamada K, Mukai T, Odomi M, Toguchi H, Liversidge GG, Higaki K, Kimura T. 2006. Effect of particle size reduction on dissolution and oral absorption of a poorly water-soluble drug, cilostazol, in beagle dogs. J Control Release 111(1–2):56–64.
23. Liversidge GG, Cundy KC. 1995. Particle size reduction for improvement of oral bioavailability of hydrophobic drugs: I. Absolute oral bioavailability of nanocrystalline danazol in beagle dogs. Int J Pharm 125(1):91–97.
24. Han X, Ghoroi C, To D, Chen Y, Davé R. 2011. Simultaneous micronization and surface modification for improvement of flow and dissolution of drug particles. Int J Pharm 415(1–2):185–195.
25. Hixson AW, Crowell JH. 1931. Dependence of reaction velocity upon surface and agitation. Ind Eng Chem Res 23(8):923–931.
26. De Smidt JH, Offringa JCA, Crommelin DJA. 1987. Dissolution kinetics of griseofulvin in sodium dodecylsulphate solutions. J Pharm Sci 76(9):711–714.
27. Rao VM, Lin M, Larive CK, Southard MZ. 1997. A mechanistic study of griseofulvin dissolution into surfactant solutions under laminar flow conditions. J Pharm Sci 86(10):1132–1137.
28. Brunner E. 1904. Reaktionsgeschwindigkeit in heterogenen Systemen. Zeitschrift für Physikalische Chemie 47:56–102.
29. Owens DK, Wendt RC. 1969. Estimation of the surface free energy of polymers. J Appl Polym Sci 13(8):1741–1747.
30. Ström G, Fredriksson M, Stenius P. 1987. Contact angles, work of adhesion, and interfacial tensions at a dissolving hydrocarbon surface. J Colloid Interface Sci 119(2):352–361.
31. Leuenberger H, Rohera BD, Haas C. 1987. Percolation theory—A novel approach to solid dosage form design. Int J Pharm 38(1–3):109–115.
32. Mahieu A, Willart JF, Dudognon E, Eddlestone MD, Jones W, Danède F, Descamps M. 2013. On the polymorphism of griseofulvin: Identification of two additional polymorphs. J Pharm Sci 102(2):462–468.
33. Burger A, Henck JO, Hetz S, Rollinger JM, Weissnicht AA, Stöttner H. 2000. Energy/temperature diagram and compression behavior of the polymorphs of D-mannitol. J Pharm Sci 89(4):457–468.
34. Miyamae A, Kema H, Kawabata T, Yasuda T, Otsuka M, Matsuda Y. 1994. X-ray powder diffraction study on the grinding effect of the polymorphs of a novel and orally effective uricosuric agent: FR76505. Drug Dev Ind Pharm 20(18):2881–2897.
35. Jenkins R, Snyder RL. 1996. Diffraction theory. In Introduction to X-ray powder diffractometry, Vol 138 ; Winefordner, JD, Ed. New York: Wiley-Interscience, pp 89–91.
36. McNamara D, Childs SL, Giordano J, Iarriccio A, Cassidy J, Shet MS, Mannion R, O'Donnell Ed, Park A. 2006. Use of a glutaric acid cocrystal to improve oral bioavailability of a low solubility API. Pharm Res 23(8):1888–1897.
37. Yamashita H, Hirakura Y, Yuda M, Teramura T, Terada K. 2013. Detection of cocrystal formation based on binary phase diagrams using thermal analysis. Pharm Res 30(1):70–80.
38. Yu L, Mishra DS, Rigsbee DR. 1998. Determination of the glass properties of D-mannitol using sorbitol as an impurity. J Pharm Sci 87(6):774–777.
39. Townley ER. 1979. Griseofulvin. In Analytical profiles of drug substances, Vol 8; Florey F, Ed. New York: Academic Press, pp 219–249.
40. Willart JF, Carpentier L, Denède F, Descamps M. 2012. Solid-state vitrification of crystalline griseofulvin by mechanical milling. J Pharm Sci 101(4):1570–1577.
41. Trasi N, Byrn S. 2012. Mechanically induced amorphization of drugs: A study of the thermal behavior of cryomilled compounds. AAPS PharmSciTech 13(3):772–784.
42. ICH, I.c.o.H. Q2 (R1). 1995. Validation of analytical procedures: Text and methodology.
43. Löbenberg R, Amidon GL. 2000. Modern bioavailability, bioequivalence and biopharmaceutics classification system. New scientific approaches to international regulatory standards. Eur J Pharm Biopharm 50(1):3–12.
44. Ho R, Hinder SJ, Watts JF, Dilworth SE, Williams DR, Heng JY. 2010. Determination of surface heterogeneity of d-mannitol by sessile drop contact angle and finite concentration inverse gas chromatography. Int J Pharm 387(1–2):79–86.
45. Saxena A, Kendrick J, Grimsey I, Mackin L. 2007. Application of molecular modelling to determine the surface energy of mannitol. Int J Pharm 343(1–2):173–180.
46. Young T. 1805. An essay on the cohesion of fluids. Philos Trans R Soc Lond 95:65–87.
47. Windbergs M, Hasser M, McGoverin CM, Gordon KC, Kleinebudde P, Strachan M. 2010. Investigating the relationship between drug distribution in solid lipid matrices and dissolution behaviour using Raman spectroscopy and mapping. J Pharm Sci 99(3):1464–1475.
48. Kendall K, Stainton C. 2001. Adhesion and aggregation of fine particles. Powder Technol 121(2–3):223–229.

5.6 Submicron Polymeric Particles Prepared by Vibrational Spray-Drying: Semisolid Formulation and Skin Penetration/Permeation Studies

Submicron Polymeric Particles Prepared by Vibrational Spray-Drying: Semisolid Formulation and Skin Penetration/Permeation Studies

T. C. Beber, D. F. Andrade, B. Kann, M. C. Fontana, K. Coradini, M. Windbergs, R. C. R. Beck

Eur. J. Pharm. Biopharm. **2014**;88:602-613.

DOI: 10.1016/j.ejpb.2014.07.008

European Journal of Pharmaceutics and Biopharmaceutics 88 (2014) 602–613

Contents lists available at ScienceDirect

European Journal of Pharmaceutics and Biopharmaceutics

journal homepage: www.elsevier.com/locate/ejpb

Research paper

Submicron polymeric particles prepared by vibrational spray-drying: Semisolid formulation and skin penetration/permeation studies

T.C. Beber [a], D.F. Andrade [a], B. Kann [b], M.C. Fontana [a], K. Coradini [a], M. Windbergs [b,c], R.C.R. Beck [a,*]

[a] Programa de Pós-Graduação em Ciências Farmacêuticas, Faculdade de Farmácia, Universidade Federal do Rio Grande do Sul (UFRGS), Porto Alegre, Brazil
[b] Department of Biopharmaceutics and Pharmaceutical Technology, Saarland University, Saarbruecken, Germany
[c] Helmholtz Centre for Infection Research, Helmholtz-Institute for Pharmaceutical Research Saarland, Department of Drug Delivery, Saabruecken, Germany

ARTICLE INFO

Article history:
Received 12 May 2014
Accepted in revised form 21 July 2014
Available online 29 July 2014

Keywords:
Submicron particles
Vibrational spray-drying
Skin delivery
Dexamethasone
Skin penetration
Skin permeation

ABSTRACT

Topical glucocorticoids (TG) such as dexamethasone (DEX) have been used for decades for the treatment of skin diseases. However, TG present well-documented side effects and their delivery to the skin is often insufficient. Therefore, many efforts have been undergone to improve the amount of drug delivered to the skin and to reduce side effects at the same time. In this work, the feasibility of DEX-submicron polymeric particles (SP) prepared by vibrational spray-drying as an approach to overcome the challenges associated with the topical administration of this drug class was evaluated. DEX was homogeneously dispersed in the SP matrix, according to confocal Raman microscopy analysis. Drug-loaded SP were incorporated into the oil phase of oil-in-water emulsions (creams). The formulation containing polymeric submicron particles (C-SP) showed controlled drug release kinetics and a significant drug accumulation in skin compared to formulations containing non-polymeric particles or free drug. DEX accumulation in the *stratum corneum* was evaluated by tape stripping and a depot effect over time was observed for C-SP, while the formulation containing the free drug showed a decrease over time. Similarly, C-SP presented higher drug retention in epidermis and dermis in skin penetration studies performed on pig skin in Franz diffusion cells, while drug permeation into the receptor compartment was negligible. It was demonstrated, for the first time, the advantageous application of submicron polymeric particles obtained by vibrational spray-drying in semisolid formulations for cutaneous administration to overcome challenges related to the therapy with TG such as DEX.

1. Introduction

Dexamethasone (DEX) is a synthetic glucocorticoid approved by the FDA in 1958 and classified as mild potency (class 4) or low potency (class 7) glucocorticoid according to the British National Formulary or American Classification, respectively [1]. The potency of glucocorticoids is evaluated by a skin vasoconstriction assay known as the blanching test [2]. DEX has been used in the treatment of several dermatological diseases such as psoriasis, atopic dermatitis and acne due to its anti-inflammatory, immunosuppressive, vasoconstrictive and anti-proliferative properties [1,3].

However, topical administration of dexamethasone as well as other topical glucocorticoids (TG) can induce local and systemic side effects. The most common topical side effects are skin reactivity, atrophy, hypopigmentation and telangiectasia [4]. These problems can be aggravated when patients have to use TG for long-term treatment [5].

The main challenges in the cutaneous therapy with glucocorticoids are as follows: to increase their topical bioavailability, to deliver them to the skin as target site – epidermis and/or dermis – and to reduce the dose and frequency of administration for better safety [6,7]. Apart from the development of new molecules, one of the main strategies currently studied to overcome these challenges is the use of drug delivery systems. Liposomes [8], solid lipid nanoparticles [9], nanostructured lipid nanocarriers [7] and polymeric micro- [10] and nanoparticles [11–14] have been investigated, as the type of carrier can have a strong impact on release kinetics and pharmacodynamics of an encapsulated drug.

Abbreviations: SP, dexamethasone-submicron polymeric particles; SNP, dexamethasone-submicron non-polymeric particles; PCL, poly(ε-caprolactone); HPLC, high-performance liquid chromatography; LD, laser diffraction; PDI, polydispersity index; PCS, photon correlation spectroscopy; SEM, scanning electron microscopy; TEM, transmission electron microscopy; SC, *stratum corneum*; VE, viable epidermis; DER, dermis.

* Corresponding author. Av. Ipiranga, 2752, 90610-000 Porto Alegre, RS, Brazil. Tel.: +55 (51) 3308 5411.
E-mail address: ruy.beck@ufrgs.br (R.C.R. Beck).

http://dx.doi.org/10.1016/j.ejpb.2014.07.008
0939-6411/

Despite many published studies about nanoparticles containing DEX in the last decade [15–18], there are few reports about *in vitro* skin penetration/permeation after cutaneous administration of these formulations. Cevc et al. [19] reported highly deformable lipid carriers known as Transfersomes® containing DEX and others TG. They evaluated its biodistribution and pharmacokinetics after cutaneous administration in mice. Specially, administration at high doses led to a systemic absorption of drugs, similar to a subcutaneous injection. On the other hand, the same group described that Transfersomes® with DEX and hydrocortisone were able to deliver the drug to viable skin layers allowing the reduction of the required dose to maintain its efficacy compared to conventional vehicles [20]. More recently, Chandra et al. [21] developed microemulsions prepared with several oils and lecithin as surfactant and isopropyl alcohol as co-surfactant for transdermal delivery of DEX. Formulation based on olive oil showed the best *in vitro* drug permeation, while the microemulsion based on nutmeg oil showed higher *in vivo* anti-inflammatory activity.

In dermatology, polymeric nanoparticles have been used as an interesting and modern approach to improve drug solubility and efficacy, allowing sustainable distribution within the skin besides reducing dose and frequency of administration [13]. However, there is a lack of studies showing the influence of nanoencapsulation of DEX in polymeric nanoparticles on its skin permeation/penetration profile. Marchiori and co-workers [12] prepared hydrogels containing DEX-loaded polymeric nanocapsules intended to treatment of proliferative disorders as psoriasis showing a controlled drug release compared to a hydrogel prepared with the non-encapsulated drug. However, the authors did not perform skin penetration/permeation studies.

Recently, the vibrational atomization spray-drying technology was introduced as an innovative technique for a one step submicron drug particles production. The setup comprises three subunits: (1) an atomization system composed of a piezoelectric actuator driven at an ultrasonic frequency (60 kHz) generating a fine aerosol of droplets with controlled size; (2) a glass dry tower with a laminar air flow promoting fast drying of droplets into dry particles using a gentle heating system; (3) an electrostatic particle collector consisting of a star electrode (cathode) and a cylindrical particle collecting electrode (anode) with an applied high voltage causing the electrostatic deposition of particles on the surface of the cylindrical electrode. In contrast to traditional spray-drying, in which very small particles (<2 μm) are lost during the drying process, this new equipment allows collecting particles in the submicron scale [22,23]. Vibrational atomization spray-drying has been studied to produce polymeric or non-polymeric particles with a range from 300 nm to 5 μm intended for several pharmaceutical applications, including cerebral [24], oral [25], ophthalmic [26] and pulmonary administration [27–29].

In 2013, Durli and co-workers reported the influence of surfactants and solvents on the preparation of non-polymeric submicron particles by vibrational atomization technology using DEX [30]. The type of solvent showed influence on the viscosity of the primary organic solutions, while the nature of surfactant did not show any influence on this parameter. On the other hand, acetone showed the lowest superficial tension among the evaluated organic phases, which is important to facilitate the passage of organic solutions through the membrane and the good formation of the fine droplets during atomization. Regarding the type of surfactant, the addition of ionic surfactants showed higher increase in the process yield (>60%) compared to the addition of non-ionic surfactants, which was explained by the improved electrostatic attraction of particles. The particles obtained in this study showed size around 1 μm. Moreover, the preparation of nanocrystals of DEX and fluorometholone from ethanolic solutions was studied by Baba and Nishida [26] using the Nano Spray Dryer intended to treatment of ophthalmic diseases. The mean particle sizes varied from 833 to 1344 nm depending on the mesh aperture of the atomization membrane.

In this context, the aim of our study was to evaluate the potential of submicron polymeric particles prepared by vibrational atomization spray-drying for local delivery of DEX to the skin. DEX was chosen as a model drug due to its wide use in treatment of skin diseases, its adverse effects and systemic absorption risks. Polymeric submicron particles containing DEX were produced, characterized and incorporated into semisolid creams (oil-in-water emulsions) to study the *in vitro* drug release as well as the drug skin penetration and permeation. To investigate the influence of the particles as well as of the polymer, the semisolid formulation with submicron polymeric particles was compared with semisolid formulations containing non-encapsulated drug or non-polymeric submicron particles, respectively.

2. Materials and methods

2.1. Materials

Dexamethasone (DEX) was kindly donated by Multilab Industry of Pharmaceutical Products Ltda (São Jerônimo, Brazil). Poly(ε-caprolactone) (PCL) (Mw = 80,000) and sodium deoxicholate were acquired from Sigma–Aldrich (São Paulo, Brazil). Caprylic/capric triglyceride and imidazolidinyl urea were supplied from Delaware (Porto Alegre, Brazil). Polysorbate 80 and Salcare® SC 91 (BASF) were acquired from Brasquim (Porto Alegre, Brazil) and Henrifarma (São Paulo, Brazil), respectively. The dialysis membrane was obtained from Millipore (São Paulo, Brazil). HPLC grade acetonitrile was purchased from Tedia (São Paulo, Brazil). All chemicals and solvents were of analytical or pharmaceutical grade and were used as received.

2.2. Preparation of submicron drug particles

Submicron polymeric particles were prepared according to a protocol established in our research group [31]. An organic solution of acetone:water (20:1, v/v) containing 0.1% polycaprolactone (PCL), 0.1% DEX and 0.02% sodium deoxicholate was fed into the Nano Spray Dryer B-90® (Büchi, Switzerland) linked to an Inert Loop B-295 (Büchi, Switzerland) with a spray rate of 100% keeping the oxygen level below 4%. Inlet temperature and air flow were set to 55 °C and 110 L/min, respectively. The Nano Spray Dryer was equipped with a spray mesh of 4.0 mm aperture size and the pump was run in mode number 2. DEX-submicron polymeric particles (SP) were collected from the electrostatic cylinder with a particle scraper as a dry powder. For comparison, a powder consisting of DEX-submicron non-polymeric particles (SNP) was prepared under the same conditions, omitting the PCL.

2.3. Physicochemical characterization of submicron particles

2.3.1. Yield, encapsulation rate and drug content

The process yield (expressed in percentage) was calculated as the ratio of the total weight of recovered powder in the collector and the total dry mass used in the organic solution, while the encapsulation rate was calculated based on the recovery of drug in the powder considering theoretical and experimental values.

The drug content (μg/mL) was assayed by high-performance liquid chromatography (HPLC) according to a previously validated method [32]. The chromatographic system consisted of a Discovery® C18 column (150 mm × 4.6 mm, 5 μm, Supelco Analytical, Sigma–Aldrich, Brazil) and a Shimadzu LC-20A system (LC-20AT pump, SPD-M20A photodiode-array (PDA) detector, CBM-20A

system controller, SIL-20A auto-sampler (Tokyo, Japan). The mobile phase was a mixture of acetonitrile and water (45:55, v/v). The injected volume was 100 μL at an isocratic flow rate of 1.0 mL/min. For analysis, the powder was dispersed in acetonitrile, followed by a dilution in the mobile phase and subsequent filtration through a membrane (0.45 μm, Millipore®). To increase the sensitivity of the method, dexamethasone was detected at 240 nm instead of 254 nm [33]. The method was linear (r = 0.9999) in the range of 0.25–3 μg/mL.

2.3.2. Morphological and particle size analysis

Size and morphology of the submicron particles (shape and surface) were investigated by scanning electron microscopy (SEM) (JEOL JSM-6060, Japan) operating at 10 kV in different magnifications at Centro de Microscopia Eletrônica – UFRGS (Porto Alegre, Brazil). Samples were attached to aluminum stubs and sputter coated with gold. Particle size distribution and mean particle diameter were obtained by analyzing SEM images using the software ImageJ (version 1.44u, National Institutes of Health). Furthermore, the size distribution of particles in the powders was evaluated by laser diffraction (LD) using the dry powder dispersion unit of the Mastersizer 2000® (Malvern, UK). In this case, the refractive index of DEX (n = 1.5) was used to calculate the mean size [14].

2.3.3. Investigation of drug distribution

The DEX distribution within the powder bed of spray-dried particles was investigated by confocal Raman microscopy. Spectral data sets were acquired with a confocal Raman microscope WITec alpha 300R+ (WITec GmbH, Ulm, Germany) through a Zeiss objective (50× magnification, N.A. 0.8) at an integration time of 0.2 s per spectrum. The microscope was operated with a diode laser emitting an excitation wavelength of 785 nm. The laser power was set to 50 mW before the objective. Raman spectra were recorded every 0.5 μm in x and y direction. Due to the surface roughness of the powder bed a topography profile of the investigated area was acquired with a built-in sensor prior to confocal Raman microscopy analysis. Spectral Raman data sets were background corrected and converted into false color images using the software WITec Project Plus (WITec GmbH, Ulm, Germany).

2.4. Preparation of semisolid formulations

Emulsions, here denominated creams due to their consistency, were prepared with mortar and pestle. First, different proportions of medium-chained triglycerides (MCT) and the emulsifier system Salcare® SC 91 were tested to promote adequate dispersion of the submicron particles (data not shown). Salcare® SC 91 is a mixture of sodium acrylates copolymer, mineral oil and PPG-1 trideceth-6. It was chosen due to its ability to form emulsions using a cold process. Prior to preparation of these formulations, a polymer swelling test with a polymeric film (PCL) fully immersed in the pure emulsifier was performed in order to check whether the emulsifier system dissolves PCL and consequently disrupt the original structure of the polymeric particles. This test was carried out over 28 days at 25 ± 2 °C. Each day the polymer film was removed, thoroughly cleaned and weighed. For the preparation of drug-loaded creams, the submicron particles were slowly dispersed in the oil phase. A previously prepared aqueous phase composed of water, citric acid and imidazolidinyl urea (preservative) was slowly added to the oil phase and homogenized using a pestle. According to this procedure creams containing non-encapsulated DEX (free drug) (C-D), creams containing DEX-polymeric submicron particles (C-SP), creams containing DEX-submicron particles (non-polymeric particles) (C-SNP), and blank creams (C-B) were prepared (Table 1). Three independent batches of each formulation were prepared and analyzed.

2.5. Physicochemical characterization of semisolid formulations

2.5.1. Determination of DEX

DEX content in the semisolid formulations was assayed by HPLC. Approximately 1.0 g of each formulation was placed in a 25 mL volumetric flask. Acetonitrile was added and the flask was subjected to 2 min of vortex stirring, 30 min of ultrasonic bath and 1 min of vortex stirring. The resulting dispersion was centrifuged at 2300g for 15 min, followed by a dilution with mobile phase, filtration through a 0.45 μm membrane filter (Millipore®, Billeria – MA, USA) and subsequent injection into the HPLC, according to the parameters described previously. The method was linear (y = 237701x − 2881.1; r = 0.9999) in the range of 0.25–3.0 μg/mL, precise (relative standard deviation of 2.3% for repeatability and 2.8% for intermediate precision) and accurate (103.3%). Specificity was checked and proved, as excipients of the formulations did not alter the DEX assay.

2.5.2. Determination of pH values

The pH values were measured in the dispersions of creams in distilled water (10%, w/v) using a calibrated potentiometer (B474, Micronal, Brazil).

2.5.3. Morphological and particle size distribution analysis

The morphological analysis of semisolid formulations was done by transmission electron microscopy (TEM) (JEM – 1200, Exll, operating at 80 kV, Centro de Microscopia Eletrônica – UFRGS, Porto Alegre, Brazil). Before analysis, appropriate dilutions were prepared in ultrapure water and an aliquot was deposited on carbon support films (grid) and negatively stained with a uranyl acetate solution (2% w/v).

Particle size and particle distribution of creams were analyzed by laser diffraction (LD, Mastersizer 2000®, Malvern, UK) and by photon correlation spectroscopy (PCS) (Zetasizer Nanoseries, Malvern Instruments, Worcestershire, UK). The mean diameter (by volume) was measured ($D_{4,3}$) during LD analysis. For PCS analysis, the z-average diameter was measured after the dilution of an aliquot of cream in purified water (2000×) followed by shaking and filtering through 1.2 mm membrane (Millipore Millex-HP, Billeria MA, USA).

2.5.4. Evaluation of the rheological behavior

Analysis of the rheological properties of formulations was carried out at 25 ± 1 °C using a rotational viscosimeter (LVDV II + Pro model, Brookfield, Middleboro, MA USA) and a spindle SC4-25 with a small sample adaptor. A shear stress (τ) ramp was run up and down from 0.40 to 2.00 rpm, registering 18 points.

Rheograms were obtained by plotting the shear stress (τ) as a function of the shear rate (γ). Resulting data were analyzed with the Rheocalc software (v3. 1-1 version, Brookfield Middleboro, MA, USA). The different flow models Bingham (ideal plastic, $\tau = \tau o + \eta\gamma$), Casson (plastic, $\tau^{0.5} = \tau o^{0.5} + \eta^{0.5}\gamma^{0.5}$), Ostwald (pseudoplastic, $\tau = K\gamma^n$) and Herschel–Bulkley (yield-pseudoplastic, $\tau = \tau o + K\gamma^n$) were used to evaluate the rheograms, where η represents the viscosity (Pa s), K the consistence (Pa sn), γ_o the yield shear stress (Pa), and n is the power law index [34].

2.6. In vitro drug release assay

Vertical automated Franz diffusion cells (MicroettePlus Multi-Group®, Hanson Research Corporation, Chatsworth, CA, USA) were used to study the *in vitro* release of DEX from creams at 37 ± 0.5 °C carried out in triplicate for each formulation. The diffusion area was 1.766 cm^2 and the receptor chamber volume was 7.0 mL. A dialysis membrane (12 kDa, Sigma–Aldrich), pre-hydrated for 8 h, was fixed between donor and receptor compartment. The receptor

Table 1
Qualitative and quantitative composition of semisolid formulations.

Component	C-SP	C-SNP	C-D	C-B
Sodium acrylates copolymer, paraffinum liquidum/PPG-1 trideceth-6 (Salcare® SC 91)	4 g	4 g	4 g	4 g
Caprylic/capric acid triglycerides	2 g	2 g	2 g	2 g
DEX-SP (with polymer)	ad 0.5 mg/g	–	–	–
DEX-SNP (without polymer)	–	ad 0.5 mg/g	–	–
DEX powder (raw material)	–	–	0.05 g	–
Imidazolidinyl urea	0.6 g	0.6 g	0.6 g	0.6 g
Citric acid	0.2 g	0.2 g	0.2 g	0.2 g
Distilled water	ad 100 g	ad 100 g	ad 100 g	ad 100 g

medium composed of phosphate buffer (pH 7.4) and polysorbate 80 (0.02%) was constantly stirred (400 rpm) to ensure sink conditions. Approximately 300 mg of formulation was applied on top of the membrane in the donor compartment. This amount corresponds to an infinite dose able to avoid drug depletion from donor compartment and also suitable to determine the steady state flux values. Half of a milliliter of the receptor medium was taken at predetermined time intervals (2, 4, 8, 12 and 16 h) and replaced by an equal volume of fresh medium. Released DEX was determined by HPLC according to the previously described method. However the receptor medium was used for dilution here instead of the mobile phase. Furthermore, the injection volume was set to 50 μL. The method was linear ($y = 113995x + 2527$; $r = 0.9999$) in the range of 1.0–20.0 μg/mL, precise (relative standard deviation of 1.2% for repeatability and 2.8% for intermediate precision) and specific. For specificity, the components of the medium were tested and none of them did alter the DEX assay. The Higuchi model was used to evaluate the drug release profiles. The software MicroMath® Scientist® (St. Louis, MO, USA) for Windows™ was used to perform this mathematical modeling.

2.7. In vitro skin penetration and permeation assay

Full-thickness skin samples were obtained from the abdominal area of female pigs kindly donated from a local slaughterhouse (Araldi, Nova Roma do Sul, Brazil). Hair from the skin surface was cut and adipose tissue was carefully removed. Pieces of skin were cut into circles (3.0 cm of diameter) and their thickness was measured with a dial thickness gage. Only skin slices with a thickness between 1.8 and 2.2 mm were used. Skin was stored in a freezer (−20 °C) wrapped in aluminum foil. The study was carried out using vertical Franz diffusion cells and receptor medium composed of phosphate buffer and polysorbate 80 (0.02%), under the same conditions described for the *in vitro* drug release studies. Skin slices were mounted in diffusion cells with the dermal side in contact with the receptor medium. Two independent experiments ($n = 3$) were performed for each formulation, resulting in a total of six replicates ($n = 6$).

To analyze the kinetics of skin penetration and permeation of DEX from C-D and C-SP samples were applied for 2, 4, 8, 10 and 12 h on the skin surface. In order to evaluate the influence of the polymer, the same experiment was performed for the formulation containing the non-polymeric submicron particles (C-SNP) after 2 and 12 h of sample application. Approximately 300 mg (infinite dose) of each formulation was applied on the diffusion area (1.766 cm^2) of skin surface.

Stratum corneum (SC), viable epidermis (VE), dermis (DER) and receptor compartment (RC) were analyzed. At the end of each experiment, the total amount of DEX retained in each skin layer was determined by HPLC after appropriated extraction. Formulation excess on the skin surface was removed with cotton. SC was removed by *tape stripping* using 18 tapes (3M tape). After removing the SC, epidermis and dermis were separated by placing the skin in hot water (60 °C) for 45 s. DEX was extracted from each layer in the mobile phase (8 mL for SC and 4 mL for the VE and DER) followed by vortex mixing (2 min), sonication (40 min), vortex mixing (1 min) and centrifugation (15 min at 2300g).

DEX was analyzed by HPLC under the same conditions described in Section 2.6. The method was linear in the range of 0.02–20 μg/mL ($r = 0.9999$). The mean percentage recovery from full skin extraction for the three concentration levels of DEX (0.10, 1.0 and 10.0 μg/mL) were 95.2%, 89.1% and 90.5%, respectively, while relative standard deviations (RSD) were 4.82%, 1.3% and 0.98%. The resulting mean skin recovery (91.1 ± 3.2%) is close or higher than observed by other studies. Paturi and co-workers [35] obtained a recovery of 67.5 ± 4% of DEX from hairless rat skin while Li and co-workers [36] found a recovery range from 89.9% to 96.9% in mouse skin. Moreover, our method was precise (RSD of 2.53% for repeatability and 1.58% for intermediate precision) and accurate (98.43 ± 3.41%).

2.8. Statistical analysis

Results are expressed as mean value ± standard deviation (SD) of a triplicate. Data were evaluated by one-way analysis of variance (ANOVA) for significance at $p \leqslant 0.05$. The Tukey's test was used to compare more than two experimental groups. For the *in vitro* penetration/permeation studies, the results were analyzed in sextuplicate and data were assessed by one-way ANOVA (followed by Tukey's post-tests) as well considering significance at $p \leqslant 0.05$. All analyses were performed using the GraphPad Prism® software version 5.00.

3. Results

All batches of DEX submicron polymeric or non-polymeric particles (SP or SNP, respectively) were characterized for drug content, encapsulation rate, mean size and process yield. Results are shown in Table 2.

Regarding the morphological analysis by SEM, submicron particles have a spherical shape, a rough surface and form agglomerates, regardless of the presence of the polymer (Fig. 1). Polymeric DEX submicron particles showed a mean size of 0.975 μm with a particle size distribution ranged between 0.446 and 2.252 μm, while SNP had a mean size of 0.523 μm. The size was calculated with the support of the software ImageJ for more than 300 particles counted in SEM images with a 5000× magnification (Fig. 1). Fig. 2 shows the particle size distribution of the powders obtained from SEM images.

To analyze the DEX distribution in the spray-dried particle powder bed, confocal Raman microscopy was performed for SP and SNP. Fig. 3A depicts the single Raman spectra of the three components DEX, PCL and deoxycholate contained in the spray-dried particles. As the rough surface of the particle powder hinders accurate spectra acquisition with the confocal microscope, the surface was virtually corrected by recording topography profiles of the

Table 2
Physicochemical characteristics of DEX submicron particles (mean ± SD, $n = 3$).

Powder	Theoretical drug content (mg g^{-1})	Experimental drug content (mg g^{-1})	Encapsulation rate (%)	Yield (%)	Mean size from SEM images (μm)
SP	500.00	467.75 ± 12.77	93.55 ± 2.55	81.01 ± 9.5	0.975 ± 0.29
SNP	833.33	835.53 ± 45.03	100.21 ± 5.41	38.20 ± 1.1	0.523 ± 0.18

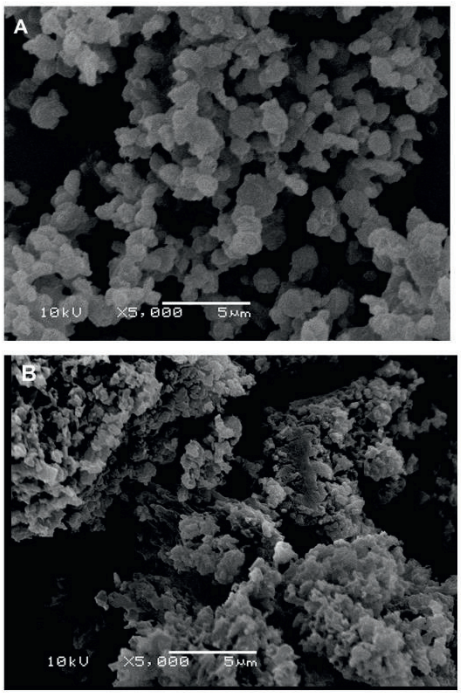

Fig. 1. SEM images of submicron particles. (A) Polymeric particles (SP) and (B) submicron non-polymeric particles (SNP). Image acquisition with a 5000× magnification.

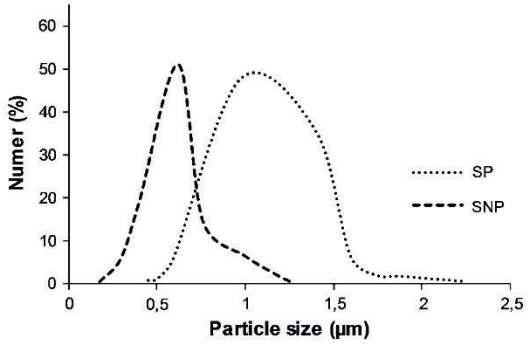

Fig. 2. Particle size distribution of submicron particles (SP and SNP) calculated from SEM images.

respective sample areas prior to Raman analysis [37]. Subsequently, the topography profile could be overlaid with the false color Raman image for a combined three dimensional visualization. Fig. 3B shows the overlay image of the submicron non-polymeric dexamethasone particle (SNP) bed. The small panels on the right hand side depict the Raman images of the two individual

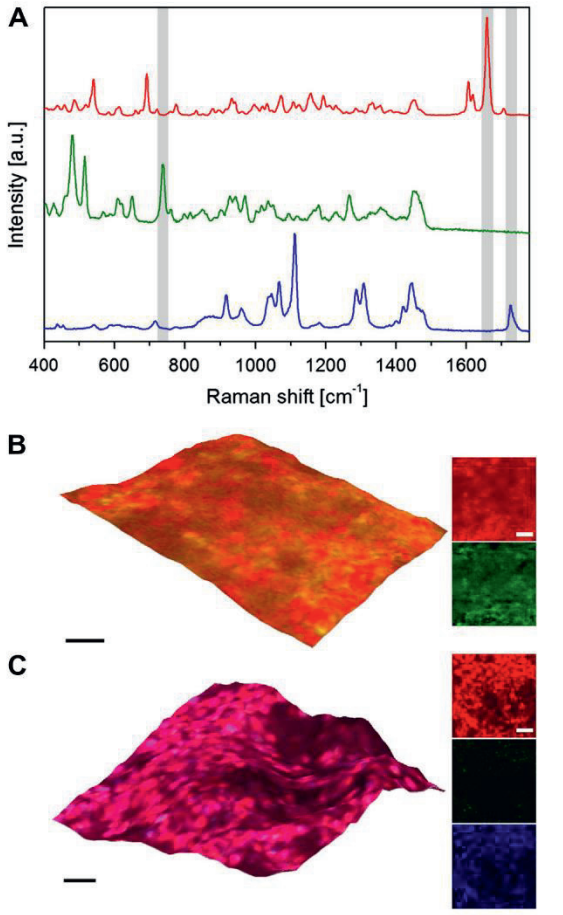

Fig. 3. Drug distribution by confocal Raman microscopy. (A) Single Raman spectra of individual components DEX (red), deoxycholate (green) and PCL (blue). Outstanding peaks for compound identification are highlighted. (B and C) Overlay of topography image with false color Raman image for SNP (B) and SP (C) powders. Colors from three dimensional images are a result of the color combination from Raman images depicting the distribution of individual compounds within the particle powder. Scale bars are sized to 10 μm. (For interpretation of the references to color in this figure legend, the reader is referred to the web version of this article.)

substances DEX (red) and deoxycholate (green). Fig. 3C shows the three dimensional image of the investigated submicron polymeric particle (SP) bed with the respective two dimensional Raman images for the three individual substances DEX, deoxycholate and PCL in the small panels.

To incorporate the produced submicron particles in the oil phase of an emulsion, the emulsifier system was firstly checked for possible negative effects on the structure of PCL. Fig. 4 presents the data of the polymer swelling test, where a thin film of PCL was immersed in the emulsifier system and weighted before

immersion and after 1, 7, 21, and 28 days. No significant variation in the polymer mass over the whole period was observed.

After preparation of semisolid emulsions (creams) their organoleptic and physicochemical characteristics were investigated. Results are summarized in Table 3.

Creams were also analyzed regarding the mean particle size, polydispersity index and granulometric profile by LD and PCS after aqueous redispersion. The data are shown in Table 4 and Fig. 5. In addition, Fig. 6 shows the TEM photomicrographs of formulations C-D and C-SP by SEM.

The rheological data obtained for creams are presented in Fig. 7. The rheograms were compiled by plotting shear stress (Pa × 10) against shear rate (s^{-1}) and they were used to model the non-Newtonian flow profiles.

The regression coefficients (r^2) for the different flow models of each rheogram are presented in Table 5. The Casson flow model fitted best to the data and was chosen to describe the rheological behavior ($r^2 > 0.99$). The parameters plastic viscosity and yield stress for each cream according to this model are presented in Table 6.

The *in vitro* drug release profiles of DEX from all formulations using the vertical Franz diffusion cell are depicted in Fig. 8. The amount of DEX released after 16 h was 61.5 ± 3.4 μg cm^{-2} for the cream containing the free drug (C-D), 52.2 ± 0.95 μg cm^{-2} for the cream containing the submicron particles without polymer (C-SNP) and 43.1 ± 4.6 μg cm^{-2} for the cream containing polymeric submicron particles (C-SP). The released DEX after 16 h was significantly different among all formulations (ANOVA, $p \leqslant 0.05$).

The DEX flux was calculated from the slope of the linear portion of the curve by plotting the amount of DEX released per cm^2 against the square root of time [38,39]. Results are presented in Fig. 9. Creams containing submicron spray-dried particles showed a slower release rate (C-SP: 11.2 ± 2.2 μg cm^2 $h^{-1/2}$ and C-SNP: 14.5 ± 0.8 μg cm^2 $h^{-1/2}$) compared to the cream containing the non-encapsulated (free) drug (C-D: 19.8 ± 0.9 μg cm^2 $h^{-1/2}$) (ANOVA, $p \leqslant 0.05$).

Furthermore, the drug release data were analyzed using the Higuchi square root model (Table 7). C-SP presented the lowest *k* value according to the Higuchi model (11.75 ± 0.24 h^{-1}), followed by C-D (16.56 ± 0.23 h^{-1}) and C-SNP (20.92 ± 0.65 h^{-1}).

In order to determine the drug localization and to quantify the amount of DEX delivered to each skin layer after the applying of creams containing the submicron particles or non-encapsulated drug, *in vitro* skin retention and permeation studies using pig skin as membrane were performed in Franz diffusion cells. DEX was analyzed in the *stratum corneum* (SC) and the subjacent layers, viable epidermis (VE) and dermis (DE), according to the tape stripping and skin extraction techniques, respectively. In addition, the receptor compartment was analyzed to determine the amount of permeated DEX.

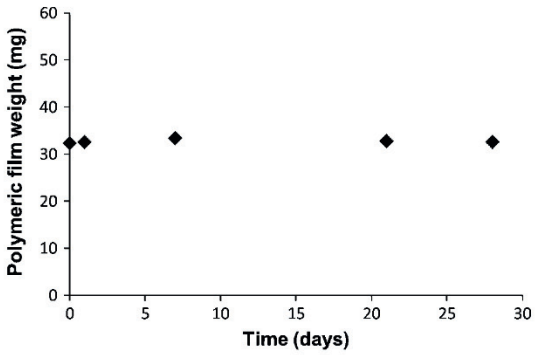

Fig. 4. Polymeric film weight (mg) after immersion in emulsifier system over 28 days at 25 °C.

Table 3
Physicochemical characteristics of creams[a] (mean ± standard deviation, $n = 3$).

Formulation	Appearance	Color	Drug content (mg/g)	pH
C-D	Cream	White	0.502 ± 0.01	7.40 ± 0.10
C-SP	Cream	White	0.496 ± 0.02	7.42 ± 0.04
C-SNP	Cream	White	0.480 ± 0.01	7.39 ± 0.05
C-B	Cream	White	–	7.63 ± 0.06

[a] C-D: creams containing non-encapsulated DEX (free drug); C-SP: creams containing DEX-polymeric submicron particles; C-SNP: creams containing DEX-submicron particles (non-polymeric particles); C-B: blank creams (without dexamethasone or particles).

Table 4
Mean size, SPAN and PDI of creams (mean ± standard deviation, $n = 3$).

Formulation	*D* [4,3][a]	SPAN[a]	Mean size (nm)[b]	PDI[b]
C-D	712 ± 4	1.3 ± 0.06	322 ± 6	0.34 ± 0.16
C-SP	647 ± 17	2.3 ± 0.17	192 ± 4	0.19 ± 0.03
C-SNP	701 ± 21	1.3 ± 0.10	201 ± 5	0.28 ± 0.05
C-B	716 ± 7	1.1 ± 0.05	203 ± 10	0.39 ± 0.06

[a] LD.
[b] PCS.

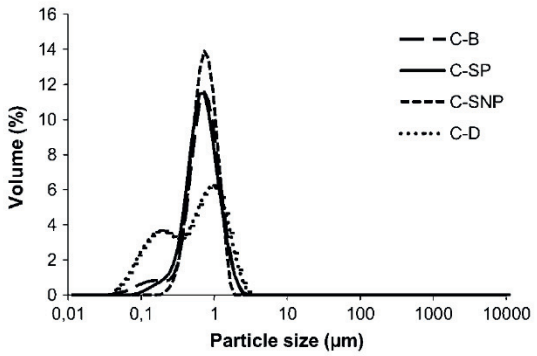

Fig. 5. Granulometric profiles of creams C-B, C-SP, C-SNP and C-D determined by laser diffraction.

Fig. 10 shows the amount of DEX accumulated in the SC after topical application in a penetration kinetic study. After 2 h there was no difference in the amount of DEX retained in SC among all formulations (C-D: 0.90 ± 0.25 μg cm^{-2}; C-SNP 0.89 ± 0.42 μg cm^{-2}; C-SP: 0.42 ± 0.08 μg cm^{-2}) (ANOVA, Tukey's test, $p \leqslant 0.05$). On the other hand, the amount of DEX in the SC was significantly higher after 12 h for C-SP (1.25 ± 0.55 μg cm^{-2}) compared to C-D (0.41 ± 0.09 μg cm^{-2}). The cream prepared with non-polymeric submicron particles (C-SNP) showed 1.09 ± 0.37 μg cm^{-2} of DEX in the SC after this time, which was not significantly different from the formulation C-SP (ANOVA, Tukey's test, $p \leqslant 0.05$). In addition, analyzing the drug accumulation profile over time, a decrease in the amount of DEX penetrated from the formulation containing the non-encapsulated drug (C-D) was observed after some hours. On the other hand, there was an increase in the amount of DEX accumulated in the SC over time for the cream containing the polymeric submicron particles (C-SP).

In the VE layer the amount of DEX after 2 h was not significantly different among the formulations (C-D: 0.175 ± 0.08 μg cm^{-2}; C-SNP: 0.135 ± 0.03 μg cm^{-2}; C-SP: 0.152 ± 0.06 μg cm^{-2}). For

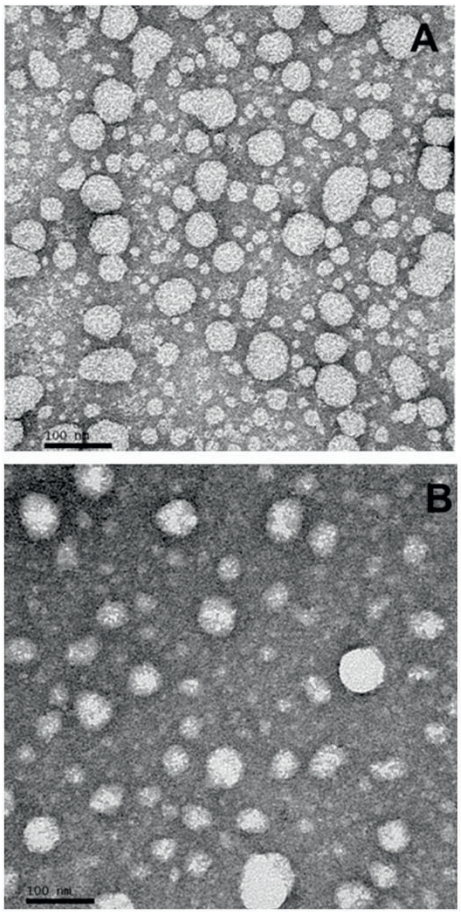

Fig. 6. TEM photomicrographs of creams containing free drug (A) and polymeric submicron particles (B) (size bar corresponds to 100 nm).

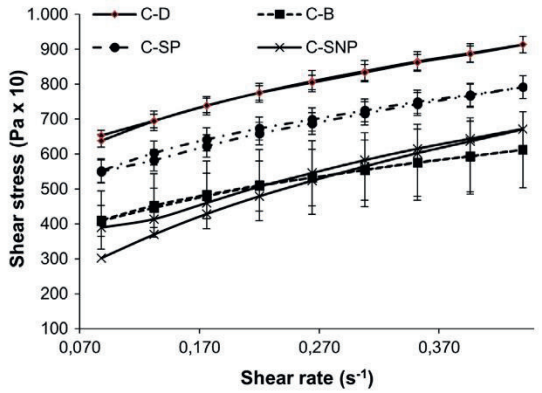

Fig. 7. Rheological profiles of creams. Shear stress (Pa × 10) is plotted against shear rate (s^{-1}) ($n = 3$). (For interpretation of the references to color in this figure legend, the reader is referred to the web version of this article.)

C-D, after 2 and 4 h there was a slight increase of the amount of penetrated DEX, followed by a decrease after 10 and 12 h (Fig. 11). However, a significant increase of DEX penetration over the 12 h of the study was observed after the application of the formulation C-SP. After 12 h, the amount of drug retained in the VE was higher (almost twice) for C-SP (0.54 ± 0.07 μg cm^{-2}) than for C-D (0.265 ± 0.04 μg cm^{-2}) (ANOVA, Tukey's test, $p \leqslant 0.05$). C-SNP showed 0.19 ± 0.07 μg cm^{-2} of dexamethasone penetrated to the viable epidermis, which was lower compared to C-SP (ANOVA, Tukey's test, $p \leqslant 0.05$).

Regarding the dermis layer, when both formulations were compared after 2 h, the amount of DEX was similar between them (C-D: 0.40 ± 0.29 and C-SP: 0.41 ± 0.18 μg cm^{-2}) (ANOVA, Tukey's test, $p > 0.05$). DEX amount penetrated to the dermis layer from the C-SNP was 0.55 ± 0.23, which was similar to the values obtained for the C-D and C-SP formulations. However, there was a gradual increase in the amount of penetrated DEX for C-D and C-SP over time (Fig. 12). So, the amount of penetrated DEX after 12 h was higher for C-SP (2.41 ± 0.33 μg cm^{-2}) compared to C-D (1.80 ± 0.57 μg cm^{-2}) (ANOVA, Tukey's test, $p \leqslant 0.05$). On the other hand, there was no difference between the DEX penetrated into the dermis after 12 h between C-D and C-SNP (1.35 ± 0.23 μg cm^{-2}) (ANOVA, Tukey's test, $p > 0.05$).

The influence of the creams containing free dexamethasone (C-D) or creams containing the submicron polymeric particles (C-SP) on DEX permeation through pig skin after topical application was also assessed *in vitro* using Franz diffusion cells. The amount of DEX was quantified in the receptor compartment of the Franz diffusion cell. Fig. 13 shows that formulations containing spray-dried submicron polymeric particles promote a DEX permeation only after 8 h of application. Nevertheless, there was no statistically significant difference to the formulation containing free dexamethasone after 12 h (C-D: 0.47 ± 0.14 μg cm^{-2}; C-SP: 0.45 ± 0.22 μg cm^{-2}) (ANOVA, Tukey's test, $p > 0.05$). In addition, C-SNP showed a permeation of 0.48 ± 0.15 μg cm^{-2} to the receptor compartment after 12 h, which was also not different from the formulations C-D and C-SP). (ANOVA, Tukey's test, $p > 0.05$).

In addition, the mean flux (J) of permeated drug was calculated from the slope of the linear portion of the curve plotting the cumulative amount of permeated DEX versus time for the formulations C-D and C-SP. As expected from the permeation profiles, there was not any difference between the flux for C-D (0.081 ± 0.01 μg cm^{-2} h^{-1}) and C-SP (0.075 ± 0.04 μg cm^{-2} h^{-1}).

4. Discussion

Our objective in this work was to develop a suitable semisolid formulation (cream) containing a new carrier for topical application in order to control drug release and to deliver the drug to specific skin layers. DEX, a classic glucocorticoid used to treat skin diseases, was chosen as model drug. Thus, polymeric submicron particles containing DEX were prepared by vibrational spray-drying according to a protocol previously optimized by our research group [31]. In order to evaluate the influence of the polymer on the performance of the semisolid formulation, non-polymeric particles (SNP) were also prepared and incorporated in the creams. Polymeric submicron particles (SP) had a mean size of 0.975 ± 0.29 μm while the non-polymeric ones showed a mean size of 0.523 ± 0.18 μm according to SEM image analysis. However, the analysis by laser diffraction demonstrated a mean particle diameter ($D_{3,0}$) of 3.73 ± 0.66 μm for SP, where 90% of these polymeric particles had a size lower than 1.51 ± 0.05 μm, while 50% had a size lower than 0.75 ± 0.05 μm. These slightly different results can be attributed to the different principles of the techniques. The software imageJ allows determining the mean size considering each individual particle (primary particles) from an image. In this work SEM images with a 5000-fold magnification were used and more than 300 particles were counted. This method has been employed

Table 5
Regression coefficients (r^2) for mathematical modeling in shear rate-shear stress curves according to different flow models ($n = 3$).

Formulation	Bingham	Casson	Ostwald	Herschel–Bulckley
C-B	0.988 ± 0.010	0.997 ± 0.010	0.994 ± 0.010	0.997 ± 0.001
C-D	0.983 ± 0.003	0.994 ± 0.003	0.988 ± 0.006	0.984 ± 0.011
C-SP	0.986 ± 0.001	0.996 ± 0.001	0.990 ± 0.001	0.993 ± 0.001
C-SNP	0.989 ± 0.001	0.995 ± 0.001	0.986 ± 0.001	0.994 ± 0.001

Table 6
Plastic viscosity and yield stress of the creams according to the Casson model.

Formulation	Viscosity (mPa s)	Yield stress (N/m^2)
C-B	17,562 ± 691	46.3 ± 2.0^a
C-D	16,108 ± 3501	29.2 ± 3.3^b
C-SP	16,284 ± 877	39.0 ± 3.1^c
C-SNP	17,420 ± 223	28.9 ± 0.05^b

Means in column with the same letter are not statistically different (ANOVA, Tukey's test, $p \leqslant 0.05$).

Table 7
Rate constant (k), correlation coefficients (r) and MSC determined for DEX release from creams using the Higuchi's square root model.

Higuchi model	C-D	C-SNP	C-SP
k (h^{-1})	16.56 ± 0.23^a	20.92 ± 0.65^b	11.75 ± 0.24^c
r	0.979 ± 0.000	0.969 ± 0.007	0.974 ± 0.003
MSC	2.648 ± 0.020	2.415 ± 0.169	2.523 ± 0.108

Means with the same letter are not statistically different (ANOVA, Tukey's test, $p \leqslant 0.05$).

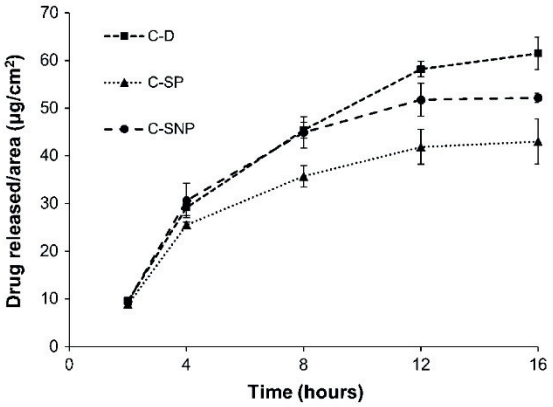

Fig. 8. *In vitro* DEX release profile from the semisolid formulations using vertical Franz diffusion cells ($n = 3$).

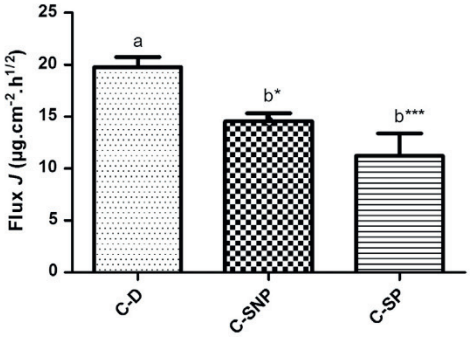

Fig. 9. Flux (µg cm^2 $h^{-1/2}$) of DEX from creams calculated from *in vitro* drug release experiments ($n = 3$). Means with the same letter are not statistically different (ANOVA, Tukey's test, $^*p \leqslant 0.05$ and $^{***}p \leqslant 0.01$).

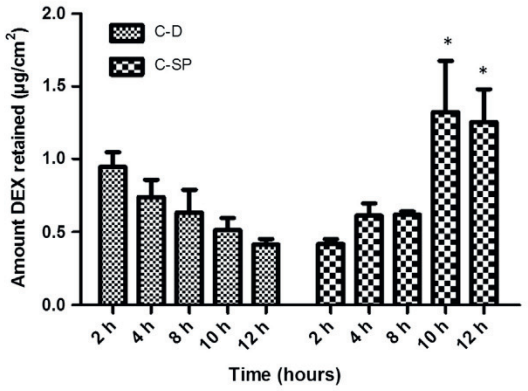

Fig. 10. Amount of DEX penetrated in the *stratum corneum* (SC) after 2, 4, 8, 10 and 12 h. The values are expressed as mean ± standard deviation ($n = 6$) (ANOVA, Tukey's test, $^*p \leqslant 0.05$).

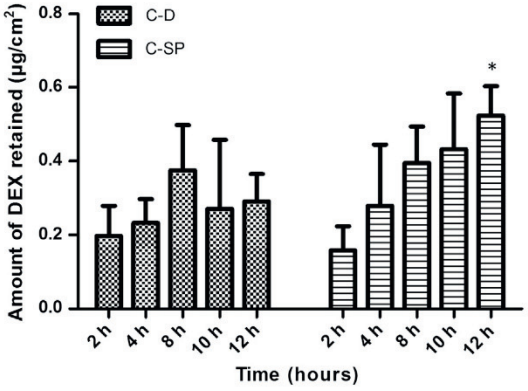

Fig. 11. Amount of DEX penetrated in the viable epidermis (VE) after 2, 4, 8, 10 and 12 h. The values reported are expressed as mean ± standard deviation ($n = 6$) (ANOVA, Tukey's test, $^*p \leqslant 0.05$).

for size analysis of powders, including those obtained by vibrational spray-drying [24,28,40,41]. On the other hand, laser diffraction analysis is based on light scattering of several particles, leading to the measurement of single particles as well as particle agglomerates, which can increase the final mean size.

Regarding the DEX encapsulation rate, both submicron particles showed values higher than 90%. The production of the powders prepared with PCL was done at higher process yield (>80%), with

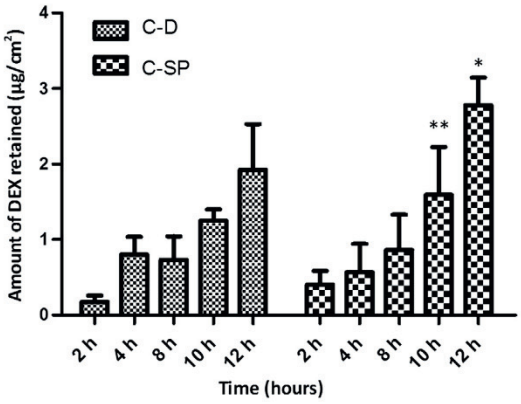

Fig. 12. Percutaneous penetration of DEX into the dermis (DE) after 2, 4, 8, 10 and 12 h. The values reported are expressed as mean ± standard deviation ($n = 6$). $^{*}p \leq 0.05$ and $^{**}p \leq 0.01$.

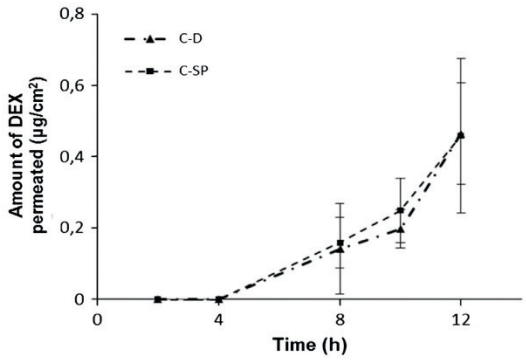

Fig. 13. Mean cumulative amount of DEX permeated from semisolid formulations (creams) versus time. The values reported are expressed as mean ± standard deviation ($n = 6$).

a very low loss of powder. This result confirms another notable advantage of vibrational spray-drying over the conventional spray-drying approach (two-fluid nozzle or rotatory atomizer), besides the feasibility of working with very low amount of samples. In the present work, batches were produced to obtain 100 mg of powder/batch. When powders of SNP were produced, the yield decreased by 50% probably due to the production of low density particles leading to their losing through the air stream and during the collect.

To evaluate the feasibility of using confocal Raman microscopy for the analysis of DEX distribution within the spray-dried powder, single Raman spectra were recorded for the three incorporated substances DEX, PCL and deoxycholate. For each substance one outstanding peak was identified in the single Raman spectra (Fig. 3A). Thus, the components can be discriminated in the spectral data set, making confocal Raman microscopy a suitable technique to investigate drug distribution. For both SP and SNP powders each substance was detected in each acquired spectrum of the spectral data set. Therefore, the small image panels in Fig. 3B and C show uniform colors each representing one compound. Overlaying these individual Raman images results in a false color image in the mixed color of the individual panels. Thus, the three dimensional image combination of topography and Raman results for the SNP powder is colored orange (red + green), whereas the overlay for SP powder is of pink color (red + green + blue). In fact, we could show that DEX is homogenously distributed within the particle powder bed in both cases. Furthermore, the use of PCL for particle preparation does not influence the drug distribution, which is a valuable information for subsequent release studies from these carrier systems.

After preparation of the carriers in the submicron scale, their incorporation in an adequate vehicle intended for topical use was an essential step. To assure the intact and homogeneous distribution of the particles in the topical skin formulation, a method for their dispersion in a semisolid vehicle was developed. In this study, we proposed the use of emulsions as semisolid formulation to incorporate the developed drug delivery system for dermatological administration. The main semisolid vehicles reported for incorporation of nanoparticles such as solid lipid nanoparticles, nanospheres and nanocapsules for dermatological formulations are hydrogels, since they enable easy incorporation of these colloids structures and, theoretically, less risk of stability problems [42]. So, to the best of our knowledge, there is little information about the incorporation of nanocarriers into emulsions. Creams are water in oil (w/o) or oil in water (o/w) emulsions and are one of the most used semisolid formulations for dermatological and cosmetic purposes due to their versatility to disperse or dissolve both hydrophilic and lipophilic components and drugs [43]. Moreover, creams are well accepted by patients because they are soft, easily spreadable and have esthetic properties. Furthermore, they are the most appropriate vehicles to treat acute and subacute dermatitis [44].

The classic method to disperse two immiscible phases is emulsification under very hard heating (70–85 °C for each phase), which may cause chemical degradation of the drug and PCL. Here, an emulsifier system to produce o/w emulsions using a cold preparation process was chosen to avoid the exposition of drug and polymer to high temperatures. The components of the oil phase were carefully selected to prepare the creams. Powders and the free (non-encapsulated) drug were successfully dispersed into the oil phase. The risk of dissolving the PCL by the emulsifier and thus altering the properties of the spray-dried particles was investigated using a polymer swelling test. This method was firstly proposed by Guterres and co-workers [45]. According to the polymer swelling experiment, the emulsifier system used to prepare the creams in our work did not dissolve the PCL film within 28 days, suggesting the physical stability of submicron particles after their incorporation in the creams. In addition, it has been previously described that the mixture of caprylic/capric acid triglycerides does not dissolve the PCL [45]. MCT, the main lipid component used in the oily phase of emulsion associated to oil mineral from the emulsifier system facilitated the very easily dispersion of DEX, a lipophilic drug. In addition, it has been reported that MCT is considered as a non skin penetrating oil without influence as penetration enhancer [46], whereas non-ionic surfactants (as PPG1-trideceth-6), may have a small effect in the ability to enhance the skin drug penetration [47].

Therefore, we incorporate the produced submicron polymeric particles in creams, which could be also named emulgel because the emulsifier system is composed of oil, a surfactant and a polymer. Emulgels have recently been considered an emergent technology for topical drug delivery preparations. This term is used for emulsions containing the dispersant phase gelled by a polymer with improved rheology and release properties [48,49].

Regarding the organoleptic characteristics, all semisolid formulations had a white color as well as a homogeneous appearance being esthetically acceptable for potential patients. The formulations had a pH value close to neutral which could be explained by the anionic character of the emulsifier system. The decrease in the pH values observed for C-D, C-SNP and C-SP compared to C-B could be attributed to the presence of DEX.

Laser diffraction analysis showed that the semisolid formulations had very similar granulometric profiles. It was not possible to detect only the size profile concerning the submicron particles in the creams. This means that it is difficult to determine the particle size of the nanocarrier in these emulsions, as their oil droplets are sized in the same scale. These results corroborate with results from Jenning and co-workers [50] who described the same limitation to characterize o/w emulsions containing solid lipid nanoparticles due to the coexistence of nanoparticles and droplets in the same nanoscopic range. Nevertheless, it was possible to observe that C-D showed a bimodal profile while C-SP and C-SNP presented a unimodal profile. Furthermore, the particle mean size of C-SP showed that the incorporation of the powder in the oil phase promoted an adequate dispersion, since the raw material (powder) had a higher mean particle size (>3.7 μm) than the cream (>0.61 μm) when analyzed by the same technique. PCS analysis has been used to verify the presence of intact nanoparticles after aqueous redispersion of carbomer hydrogels [51]. In our study, the mean size determined by PCS after the aqueous redispersion of creams were lower than those obtained by LD due to the use of a membrane filter with a 1.2 μm pore size, allowing only the passage of small particles. In other words, similar mean particle sizes were observed for all formulations (C-D, C-SP and C-SNP) due to the overlapping of particle size distribution of droplets and particles. Only the blank formulation (C-B) had a different and higher mean size (>320 nm). In addition, morphological analyses were performed by TEM for C-B and C-SP (Fig. 6). In both samples it was observed droplets of very small size.

Rheology analysis is a very important tool to characterize semisolid formulations. Rheological properties of creams as well as other vehicles may influence skin application, the manufacturing process, flow packaging [52], the stability of the formulation [53], controlled drug release [54] as well as skin permeation/penetration [55]. In our study, all formulations showed non-Newtonian behavior as their viscosities changed as a function of shear rate (data not shown). Mathematical modeling was used to better understanding of the rheological behavior of creams using the shear rate-shear stress data. The Casson model showed the best fit, since the regression coefficients were higher than 0.99. According to the Casson model a semisolid formulation does not flow immediately when a shear stress is applied to it, therefore, presenting a plastic behavior [56]. Plastic and pseudoplastic flows are described in the literature to be ideal for formulations intended for topical application [34]. The addition of submicron particles and free drug (raw-material) decreased the viscosity of formulations in comparison to the blank cream (C-B). However, according to the rheograms (Fig. 7), the flow type was not modified for any formulation. This is in accordance with the results reported by Alves and co-workers [57] showing that the addition of nanocapsules, nanospheres or nanoemulsions does not change the flow properties of hydrogels. In addition, C-D and C-SP lower values necessary for formulations to start flowing (lower yield stress) compared to C-SNP, which suggests its easier skin application.

After the physicochemical and rheological evaluation, the *in vitro* DEX release from all creams was investigated. Analysis of drug release from a topical formulation is important to ensure drug diffusion from the vehicle, affecting its availability to the skin surface. Moreover, the other objective at this point was to evaluate whether the submicron particles produced by vibrational spray-drying could promote a controlled drug release from creams. So, according to the *in vitro* drug release profiles, C-D presented the highest amount of released DEX, as expected, since in this formulation the drug was incorporated as raw material (non-encapsulated form). In contrast, creams containing polymeric submicron particles (C-SP) exhibited a controlled DEX release profile during 16 h, which amount of drug released was lower than that obtained for C-SNP. This result shows the positive influence of the presence of the polymer in the submicron particles to control the drug release from the semisolid formulations. Additionally, drug fluxes were in the following order C-D > C-SNP > C-SP confirming the influence of the polymer on the drug released control (Fig. 9).

After investigating the *in vitro* controlled DEX release, skin penetration/permeation studies were carried out. At this time, it is important to keep in mind that one of the most important skin functions is its barrier property against transepidermal water loss and environmental penetration of microorganisms and chemicals [58]. However this is also a limiting factor to transport drugs intended for either topical (local) or transdermal (systemic) therapies [59]. The epidermis, representing the uppermost layer, is responsible for this property due its sophisticated process of differentiation and architecture. It is divided into *stratum corneum* (SC) and viable epidermis (VE).

SC is the horny layer and consists of highly keratinized dead cells (corneocytes) embedded in a lipid matrix [60]. It is known as a brick and mortar organization represented by the corneocytes and intercellular lipids, respectively. Tight junctions and desmosomes are also responsible for cohesion and intercellular adhesion [61]. Due to its complex composition, SC is the rate limiting barrier to percutaneous absorption of drugs [62]. For topical treatment of dermatological diseases with glucocorticoids (TG), it is necessary to overcome this barrier in order to reach their sites of action, the viable epidermis and/or dermis. The mechanism of action of TG includes their binding in human receptor found in skin keratinocytes and fibroblasts [3,63]. Some strategies used to increase the skin delivery of topical glucocorticoids include new vehicles such as metered dose aerosol sprays with hydrofluoroalkane [64] and foams [65], chemical enhancers [66], iontophoresis [35] as well as micro- and nanoparticles [11,20,51,67,68].

To prove our initial hypothesis to increase DEX delivery to viable skin, DEX must firstly be released from submicron particles and from the semisolid formulation, as discussed above, followed by its penetration and diffusion through the SC to the viable epidermis and dermis, being available to bind to glucocorticoid receptors [1,69]. So, the distribution of DEX-associated to submicron particles into skin layers after the application of creams was investigated using Franz diffusion cells and pig skin as biological membrane. Pig skin has great similarity with human skin due to its anatomical and physiological characteristics. It is considered the best choice among animal membranes for *in vitro* skin permeation/penetration studies [70,71].

Regarding the results from this experiment, the formulation containing free drug (C-D) presented a significant decrease of DEX penetration in the SC as a function of time. The time was the determining factor in the reduction of the drug amount, when comparing the different time points after application (ANOVA, $p \leqslant 0.05$). However, the cream containing the submicron polymeric particles (C-SP) led to a significant increase of drug retained in the SC throughout time, especially after 10 h of application (ANOVA, $p \leqslant 0.05$). Although C-SP retained higher amount of drug in the SC, there was no significant difference compared to the C-SNP. Anyway, these results demonstrated a very pronounced depot effect when the vehicle with submicron particles was applied on the skin.

After stripping the SC off, the underlying epidermis was separated from dermis by heat method. After 12 h, C-SP delivered a higher DEX amount (approximately 50% higher) to the VE compared to the amount delivered by the C-D. These results indicate that the drug depot in the SC previously discussed provides a local skin reservoir to the VE, the main target site of TG treatment. Moreover, C-SP showed higher DEX amounts retained in the VE after 12 h compared to C-SNP, indicating that the presence of the polymer in the submicron particles was significant to increase

the localization of drug into the VE. Other authors aimed to increase the accumulation of topical corticoids in the epidermis using nanoparticles. In 2004, Cevc and co-workers [20] compared the skin distribution of DEX-loaded very deformable vesicles and a commercial cream containing the free drug. The nanoencapsulation increased the amount of DEX retained in the VE (from 15% to 30% in relation to cream containing its free form). Şenyiğit and co-workers [72] also found significant higher amounts of drug in the epidermis and dermis for clobetasol-17-propionate encapsulated in lecithin/chitosan nanoparticles compared to a chitosan gel and a commercial cream containing the free drug at the same concentration. However, our study is the first report about the increased delivery of dexamethasone to VE using polymeric submicron particles.

A similar DEX accumulation profile in the dermis occurred as observed in the VE. Time had a significant influence in the amount of drug reaching the dermis after 10 h, regardless of the formulation. In addition, after 10 and 12 h the drug showed a higher penetration into the dermis from the formulation containing the polymeric submicron particles compared to the formulation containing the free drug.

Although the penetration of the spray-dried polymeric submicron particles in the skin layers was not investigated in the present study, we could suggest that the higher DEX penetration to the viable skin layers as well as the lack of difference on the receptor compartment from the formulation containing the submicron polymeric particles could be a result of their penetration into the hair follicles. There are several reports showing that solid micro- and nanoparticles can penetrate and accumulate into hair follicles [73–76]. Patzelt and co-workers [77] prepared PLGA and silica particles ranged from 122 to 1000 nm and evaluated their penetration in pig ear skin. They observed that particles with medium size penetrated deeper in the hair follicles.

Finally, the receptor compartment (RC) was analyzed for DEX content to evaluate the risk of its systemic absorption after topical application. Up to 4 h DEX was not detected in the RC, regardless of the formulation. Only after 8 h it was possible to quantify DEX in this medium. After 12 h of the experiment, the permeated amount of dexamethasone was similar and very low for all formulations. Additionally, the calculated flux values to the receptor medium were also not different between the formulations C-D and C-SP. The low content of the drug found in the RC indicates that the formulations have low risk of systemic absorption and besides the targeting to the viable epidermis and dermis, the developed formulation containing submicron polymeric particles does not increase the risk of systemic absorption compared to those containing the free drug and submicron non-polymeric particles.

5. Conclusions

The present work demonstrates for the first time the production of semisolid formulations containing polymeric submicron spray-dried particles produced by vibrational atomization as potential topical skin drug delivery systems. An o/w emulsion was prepared using the emulgel technology which allows a very good dispersion of the particles. Adequate rheological properties of the formulations for application and patient compliance were accomplished. The presence of PCL in the particles was the main factor controlling drug release from the formulation. The developed semisolid formulation containing the submicron polymeric particles exhibited a depot effect in the SC and improved the drug accumulation in the viable skin layers (epidermis and dermis) without increasing the risk of systemic absorption. The recent and the modern technology to produce submicron polymeric particles by vibrational spray-drying combined with the novel approach to develop a pharmaceutical vehicle with appropriate physicochemical characteristics is proposed in this study as a promising new strategy to target DEX in viable skin layers with a potential to reduce its dose.

Acknowledgments

TCB, MCF, KC and DFA thank CAPES/Brazil for their scholarship. The authors thank FAPERGS, PROBRAL-CAPES, CNPq/Brazil, INCT_if and German Academic Exchange Service (DAAD) for the financial support. The authors thank Faculdade de Farmácia and Centro de Microscopia of UFRGS for the infrastructure support.

References

[1] S. Wiedersberg, C.S. Leopold, R.H. Guy, Bioavailability and bioequivalence of topical glucocorticoids, Eur. J. Pharm. Biopharm. 68 (3) (2008) 453–466.
[2] P. Smit, H.A.M. Neumann, H.B. Thio, The skin-blanching assay, J. Eur. Acad. Dermatol. Venereol. 26 (10) (2012) 1197–1202.
[3] T. Rhen, J.A. Cidlowski, Antiinflammatory action of glucocorticoids—new mechanisms for old drugs, N. Engl. J. Med. 353 (16) (2005) 1711–1723.
[4] H. Schäcke, W.D. Döcke, K. Asadullah, Mechanisms involved in the side effects of glucocorticoids, Pharmacol. Ther. 96 (1) (2002) 23–43.
[5] U.R. Hengge, T. Ruzicka, R.A. Schwartz, M.J. Cork, Adverse effects of topical glucocorticosteroids, J. Am. Acad. Dermatol. 54 (1) (2006) 1–15.
[6] T. Senyigit, O. Ozer, Corticosteroids for skin delivery: challenges and new formulation opportunities, in: Glucocorticoids – New Recognition of Our Familiar Friend, InTech, 2012, pp. 595–612.
[7] M. Schäfer-Korting, W. Mehnert, H.C. Korting, Lipid nanoparticles for improved topical application of drugs for skin diseases, Adv. Drug Deliv. Rev. 59 (6) (2007) 427–443.
[8] M. Elsayed, O.Y. Abdallah, V.F. Naggar, N.M. Khalafallah, Lipid vesicles for skin delivery of drugs: reviewing three decades of research, Int. J. Pharm. 332 (1) (2007) 1–16.
[9] C.S. Maia, W. Mehnert, M. Schäfer-Korting, Solid lipid nanoparticles as drug carriers for topical glucocorticoids, Int. J. Pharm. 196 (2) (2000) 165–167.
[10] A.R. Pohlmann, F.N. Fonseca, K. Paese, C.B. Detoni, K. Coradini, R.C. Beck, S.S. Guterres, Poly(ε-caprolactone) microcapsules and nanocapsules in drug delivery, Expert Opin. Drug Deliv. 10 (5) (2013) 623–638.
[11] F.K. Santos, M. Helena Oyafuso, C. Priscila Kiill, M. Palmira Daflon-Gremiao, M. Chorilli, Nanotechnology-based drug delivery systems for treatment of hyperproliferative skin diseases – a review, Curr. Nanosci. 9 (1) (2013) 159–167.
[12] M.L. Marchiori, G. Lubini, G. Dalla Nora, R.B. Friedrich, M.C. Fontana, A.F. Ourique, M.O. Bastos, L.A. Rigo, C.B. Silva, S.B. Tedesco, R.C.R. Beck, Hydrogel containing dexamethasone-loaded nanocapsules for cutaneous administration: preparation, characterization, and in vitro drug release study, Drug Dev. Ind. Pharm. 36 (8) (2010) 962–971.
[13] A. Kumari, S.K. Yadav, S.C. Yadav, Biodegradable polymeric nanoparticles based drug delivery systems, Colloids Surf. B: Biointerfaces 75 (1) (2010) 1–18.
[14] C. Gómez-Gaete, E. Fattal, L. Silva, M. Besnard, N. Tsapis, Dexamethasone acetate encapsulation into Trojan particles, J. Control. Release 128 (1) (2008) 41–49.
[15] R.C.R. Beck, A.R. Pohlmann, C. Hoffmeister, M.R. Gallas, E. Collnot, U.F. Schaefer, S.S. Guterres, C.M. Lehr, Dexamethasone-loaded nanoparticle-coated microparticles: correlation between in vitro drug release and drug transport across Caco-2 cell monolayers, Eur. J. Pharm. Biopharm. 67 (1) (2007) 18–30.
[16] L. Gan, S. Han, J. Shen, J. Zhu, C. Zhu, X. Zhang, Y. Gan, Self-assembled liquid crystalline nanoparticles as a novel ophthalmic delivery system for dexamethasone: improving preocular retention and ocular bioavailability, Int. J. Pharm. 396 (1) (2010) 179–187.
[17] X. Luo, C. Matranga, S. Tan, N. Alba, X.T. Cui, Carbon nanotube nanoreservior for controlled release of anti-inflammatory dexamethasone, Biomaterials 32 (26) (2011) 6316–6323.
[18] J. Urbańska, A. Karewicz, M. Nowakowska, Polymeric delivery systems for dexamethasone, Life Sci. 96 (1) (2014) 1–6.
[19] G. Cevc, G. Blume, A. Schätzlein, Transfersomes-mediated transepidermal delivery improves the regio-specificity and biological activity of corticosteroids in vivo, J. Control. Release 45 (3) (1997) 211–226.
[20] G. Cevc, G. Blume, Hydrocortisone and dexamethasone in very deformable drug carriers have increased biological potency, prolonged effect, and reduced therapeutic dosage, Biochim. Biophys. Acta Biomembr. 1663 (1) (2004) 61–73.
[21] A. Chandra, P.K. Sharma, R. Irchhiaya, Microemulsion-based hydrogel formulation for transdermal delivery of dexamethasone, Asian J. Pharm. 3 (1) (2009).
[22] D. Heng, S.H. Lee, W.K. Ng, R.B. Tan, The nano spray dryer B-90, Expert Opin. Drug Deliv. 8 (7) (2011) 965–972.
[23] K. Schmid, C. Arpagaus, W. Friess, Evaluation of the nano spray dryer B-90 for pharmaceutical applications, Pharm. Dev. Technol. 16 (4) (2011) 287–294.
[24] N. Bege, T. Renette, T. Endres, M. Beck-Broichsitter, D. Hänggi, T. Kissel, In situ forming nimodipine depot system based on microparticles for the treatment of posthemorrhagic cerebral vasospasm, Eur. J. Pharm. Biopharm. 84 (1) (2013) 99–105.

[25] V. Martena, R. Censi, E. Hoti, L. Malaj, P. Di Martino, A new nanospray drying method for the preparation of nicergoline pure nanoparticles, J. Nanopart. Res. 14 (6) (2012) 1–10.
[26] K. Baba, K. Nishida, Steroid nanocrystals prepared using the nano spray dryer B-90, Pharmaceutics 5 (1) (2013) 107–114.
[27] K. Bürki, I. Jeon, C. Arpagaus, G. Betz, New insights into respirable protein powder preparation using a nano spray dryer, Int. J. Pharm. 408 (1) (2011) 248–256.
[28] M. Beck-Broichsitter, C. Schweiger, T. Schmehl, T. Gessler, W. Seeger, T. Kissel, Characterization of novel spray-dried polymeric particles for controlled pulmonary drug delivery, J. Control. Release 158 (2) (2012) 329–335.
[29] A. Schoubben, P. Blasi, M.L. Marenzoni, L. Barberini, S. Giovagnoli, C. Cirotto, M. Ricci, Capreomycin supergenerics for pulmonary tuberculosis treatment: preparation, in vitro, and in vivo characterization, Eur. J. Pharm. Biopharm. 83 (2013) (2013) 388–395.
[30] T.L. Durli, F.A. Dimer, M.C. Fontana, A.R. Pohlmann, R.C.R. Beck, S.S. Guterres, Innovative approach to produce submicron drug particles by vibrational atomization spray drying: influence of the type of solvent and surfactant, Drug Dev. Ind. Pharm. (2013) 1–10.
[31] M.C.T. Fontana, L. Durli, A.R. Pohlmann, S.S. Guterres, R.C.R. Beck, Polymeric controlled release inhalable powder produced by vibrational spray-drying: one-step preparation and in vitro lung deposition, Powder Technol. 258 (2014) 49–59.
[32] R.B. Friedrich, M.C. Fontana, M.O. Bastos, A.R. Pohlmann, S.S. Guterres, R.C.R. Beck, Drying polymeric drug-loaded nanocapsules: the wet granulation process as a promising approach, J. Nanosci. Nanotechnol. 10 (1) (2010) 616–621.
[33] R.B. Friedrich, M.O. Bastos, M.C. Fontana, A.F. Ourique, R.C.R. Beck, Tablets containing drug-loaded polymeric nanocapsules: an innovative platform, J. Nanosci. Nanotechnol. 10 (9) (2010) 5885–5888.
[34] M.P. Alves, R.P. Raffin, S.B. Fagan, Rheological Behavior of Semisolid Formulations Containing Nanostructured Systems, in: Nanocosmetics and Nanomedicines, Springer, Berlin, Heidelberg, 2011, pp. 37–45.
[35] J. Paturi, H.D. Kim, B. Chakraborty, P.M. Friden, A.K. Banga, Transdermal and intradermal iontophoretic delivery of dexamethasone sodium phosphate: quantification of the drug localized in skin, J. Drug Target. 18 (2) (2010) 134–140.
[36] L. Li, P. Ma, J. Wei, K. Qian, L. Tao, LC-ESI-MS method for the determination of dexamethasone acetate in skin of nude mouse, J. Chromatogr. B 933 (2013) 44–49.
[37] B. Kann, M. Windbergs, Chemical imaging of drug delivery systems with structured surfaces – a combined analytical approach of confocal Raman microscopy and optical profilometry, AAPS J. 15 (2) (2013) 505–510.
[38] C.K. Brown, H.D. Friedel, A.R. Barker, L.F. Buhse, S. Keitel, T.L. Cecil, J. Kraemer, M. Morris, C. Reppas, M.P. Stickelmeyer, C. Yomota, V.P. Shah, FIP/AAPS joint workshop report: dissolution/in vitro release testing of novel/special dosage forms, AAPS PharmSciTech. 12 (2) (2011) 782–794.
[39] G.L. Flynn, V.P. Shah, S.N. Tenjarla, M. Corbo, D. DeMagistris, T.G. Feldman, J.L. Zatz, Assessment of value and applications of in vitro testing of topical dermatological drug products, Pharm. Res. 16 (9) (1999) 1325–1330.
[40] X. Li, N. Anton, C. Arpagaus, F. Belleteix, T.F. Vandamme, Nanoparticles by spray drying using innovative new technology: the Büchi nano spray dryer B-90, J. Control. Release 147 (2) (2010) 304–310.
[41] S.H. Lee, D. Heng, W.K. Ng, H.K. Chan, R.B. Tan, Nano spray drying: a novel method for preparing protein nanoparticles for protein therapy, Int. J. Pharm. 403 (1) (2011) 192–200.
[42] F.S. Poletto, R.C. Beck, S.S. Guterres, A.R. Pohlmann, Polymeric nanocapsules: concepts and applications, in: Nanocosmetics and Nanomedicines, Springer, Berlin, Heidelberg, 2011, pp. 49–68.
[43] C.T. Ueda, V.P. Shah, K. Derdzinski, G. Ewing, G. Flynn, H. Maibach, A. Yacobi, Topical and transdermal drug products, Pharmacop. Forum 35 (3) (2009) 750–764.
[44] V.S. Beltrani, F.A. Barsanti, L. Bielory, Effects of glucocorticosteroids on the skin and eye, Immunol. Allergy Clin. North Am. 25 (3) (2005) 557–580.
[45] S.S. Guterres, V. Weiss, L.D.L. Freitas, A.R. Pohlmann, Influence of benzyl benzoate as oil core on the physicochemical properties of spray-dried powders from polymeric nanocapsules containing indomethacin, Drug Deliv. 7 (4) (2000) 195–199.
[46] M. Mélot, P.D. Pudney, A.M. Williamson, P.J. Caspers, A. Van Der Pol, G.J. Puppels, Studying the effectiveness of penetration enhancers to deliver retinol through the stratum corneum by in vivo confocal Raman spectroscopy, J. Control. Release 138 (1) (2009) 32–39.
[47] A.C. Williams, B.W. Barry, Penetration enhancers, Adv. Drug Deliv. Rev. 64 (2012) 128–137.
[48] V. Singla, S. Saini, B. Joshi, A.C. Rana, Emulgel: a new platform for topical drug delivery, Int. J. Pharm. Biol. Sci. 3 (1) (2012).
[49] A. Alexander, A. Khichariya, S. Gupta, R.J. Patel, T.K. Giri, D.K. Tripathi, Recent expansions in an emergent novel drug delivery technology: emulgel, J. Control. Release 171 (2) (2013) 122–132.
[50] V. Jenning, M. Schäfer-Korting, S. Gohla, Vitamin A-loaded solid lipid nanoparticles for topical use: drug release properties, J. Control. Release 66 (2) (2000) 115–126.
[51] M.C. Fontana, J.F.P. Rezer, K. Coradini, D.B.R. Leal, R.C.R. Beck, Improved efficacy in the treatment of contact dermatitis in rats by a dermatological nanomedicine containing clobetasol propionate, Eur. J. Pharm. Biopharm. 79 (2) (2011) 241–249.
[52] A.R. Gennaro, Rheology, in: Remington: The Science and Practice of Pharmacy, Ed. Lippincott Williams & Wilkins, Philadelphia, 2000.
[53] T. Tadros, Application of rheology for assessment and prediction of the long-term physical stability of emulsions, Adv. Colloid Interface Sci. 108 (2004) 227–258.
[54] C.H. Lee, V. Moturi, Y. Lee, Thixotropic property in pharmaceutical formulations, J. Control. Release 136 (2) (2009) 88–98.
[55] K. Welin-Berger, J.A. Neelissen, B. Bergenståhl, The effect of rheological behaviour of a topical anaesthetic formulation on the release and permeation rates of the active compound, Eur. J. Pharm. Sci. 13 (3) (2001) 309–318.
[56] M.T. Islam, N. Rodríguez-Hornedo, S. Ciotti, C. Ackermann, Rheological characterization of topical carbomer gels neutralized to different pH, Pharm. Res. 21 (7) (2004) 1192–1199.
[57] P.M. Alves, A.R. Pohlmann, S.S. Guterres, Semisolid topical formulations containing nimesulide-loaded nanocapsules, nanospheres or nanoemulsion: development and rheological characterization, Pharmazie 60 (12) (2005) 900–904.
[58] P.M. Elias, J.S. Wakefield, Skin barrier function, in: Nutrition for Healthy Skin, Springer, Berlin, Heidelberg, 2011, pp. 35–48.
[59] D. Karadzovska, J.D. Brooks, N.A. Monteiro-Riviere, J.E. Riviere, Predicting skin permeability from complex vehicles, Adv. Colloid Interface Sci. 65 (2) (2013) 265–277.
[60] J.M. Jungersted, L.I. Hellgren, G.B. Jemec, T. Agner, Lipids and skin barrier function – a clinical perspective, Contact Derm. 58 (5) (2008) 255–262.
[61] K.A. Walters, M.S. Roberts, The structure and function of skin, in: K.A. Walters (Ed.), Dermatological and Transdermal Formulations, first ed., vol. 119, Marcel Dekker, Inc., New York, 2002, pp. 1–39.
[62] C.R. Harding, The stratum corneum: structure and function in health and disease, Dermatol. Ther. 17 (2004) 6–15.
[63] A. Ahluwalia, Topical glucocorticoids and the skin-mechanisms of action: an update, Mediat. Inflamm. 7 (3) (1998) 183–193.
[64] M.L. Reid, F. Benaouda, R. Khengar, S.A. Jones, M.B. Brown, Topical corticosteroid delivery into human skin using hydrofluoroalkane metered dose aerosol sprays, Int. J. Pharm. 452 (1) (2013) 157–165.
[65] L. Stein, Clinical studies of a new vehicle formulation for topical corticosteroids in the treatment of psoriasis, J. Am. Acad. Dermatol. 53 (1) (2005) S39–S49.
[66] T. Şenyiğit, C. Padula, Ö. Özer, P. Santi, Different approaches for improving skin accumulation of topical corticosteroids, Int. J. Pharm. 380 (1) (2009) 155–160.
[67] R.H. Neubert, Potentials of new nanocarriers for dermal and transdermal drug delivery, Eur. J. Pharm. Sci. 77 (1) (2011) 1–2.
[68] L.B. Jensen, E. Magnussson, L. Gunnarsson, C. Vermehren, H.M. Nielsen, K. Petersson, Corticosteroid solubility and lipid polarity control release from solid lipid nanoparticles, Int. J. Pharm. 390 (1) (2010) 53–60.
[69] A. Henning, D. Neumann, K.H. Kostka, C.M. Lehr, U.F. Schaefer, Influence of human skin specimens consisting of different skin layers on the result of in vitro permeation experiments, Skin Pharmacol. Physiol. 21 (2) (2008) 81–88.
[70] S.P. Huong, J.D. Fourneron, J.P. Reynier, V. Andrieu, Use of various models for in vitro percutaneous absorption studies of ultraviolet filters, Skin Pharmacol. Physiol. 15 (3) (2009) 253–261.
[71] B. Godin, E. Touitou, Transdermal skin delivery: predictions for humans from in vivo, ex vivo and animal models, Adv. Drug Deliv. Rev. 59 (11) (2007) 1152–1161.
[72] T. Şenyiğit, F. Sonvico, S. Barbieri, Ö. Özer, P. Santi, P. Colombo, Lecithin/chitosan nanoparticles of clobetasol-17-propionate capable of accumulation in pig skin, J. Control. Release 142 (3) (2010) 368–373.
[73] J. Lademann, H. Richter, M.C. Meinke, B. Lange-Asschenfeldt, C. Antoniou, W.C. Mak, R. Renneberg, W. Sterry, A. Patzelt, Drug delivery with topically applied nanoparticles: science fiction or reality, Skin Pharmacol. Physiol. 26 (4–6) (2013) 227–233.
[74] F. Knorr, J. Lademann, A. Patzelt, W. Sterry, U. Blume-Peytavi, A. Vogt, Follicular transport route – research progress and future perspectives, Eur. J. Pharm. Biopharm. 71 (2) (2009) 173–180.
[75] T.W. Prow, J.E. Grice, L.L. Lin, R. Faye, M. Butler, Becker, E.M.T. Wurm, C. Yoong, T.A. Robertson, H.P. Soyer, M.S. Roberts, Nanoparticles and microparticles for skin drug delivery, Adv. Drug Deliv. Rev. 63 (6) (2011) 470–491.
[76] A.S. Raber, A. Mittal, J. Schäfer, U. Bakowsky, J. Reichrath, T. Vogt, U.F. Schaefer, S. Hansen, C.M. Lehr, Quantification of nanoparticle uptake into hair follicles in pig ear and human Forearm, J. Control. Release 179 (2014) 25–32.
[77] A. Patzelt, H. Richter, F. Knorr, U. Schäfer, C.M. Lehr, L. Dähne, W. Sterry, J. Lademann, Selective follicular targeting by modification of the particle sizes, J. Control. Release 150 (1) (2011) 45–48.

5.7 Characterization and Evaluation of a Modified PVPA Barrier in Comparison to Caco-2 Cell Monolayers for Combined Dissolution and Permeation Testing

Characterization and Evaluation of a Modified PVPA Barrier in Comparison to Caco-2 Cell Monolayers for Combined Dissolution and Permeation Testing

S. P. Gantzsch*, B. Kann*, M. Ofer-Glaessgen, P. Loos, H. Berchtold, S. Balbach, T. Eichinger, C.-M. Lehr, U. F. Schaefer, M. Windbergs

J. Controlled Release. **2014**;175:79-86.

* both authors contributed equally and are listed in alphabetical order

DOI: 10.1016/j.conrel.2013.12.009

Journal of Controlled Release 175 (2014) 79–86

Contents lists available at ScienceDirect

Journal of Controlled Release

journal homepage: www.elsevier.com/locate/jconrel

Characterization and evaluation of a modified PVPA barrier in comparison to Caco-2 cell monolayers for combined dissolution and permeation testing

Sandra P. Gantzsch [a,1], Birthe Kann [a,1], Monika Ofer-Glaessgen [b], Petra Loos [b], Harald Berchtold [b], Stefan Balbach [b], Thomas Eichinger [b], Claus-Michael Lehr [a,c], Ulrich F. Schaefer [a,*], Maike Windbergs [a,c,**]

[a] Saarland University, Department of Biopharmaceutics and Pharmaceutical Technology, Campus A4.1, 66123 Saarbruecken, Germany
[b] Sanofi-Aventis Deutschland GmbH, Lead Generation to Candidate Realization, Industriepark Hoechst, 65926 Frankfurt/Main, Germany
[c] Helmholtz Centre for Infection Research and Helmholtz Institute for Pharmaceutical Research Saarland, Department of Drug Delivery, Campus A4.1, 66123 Saarbruecken, Germany

ARTICLE INFO

Article history:
Received 6 August 2013
Accepted 4 December 2013
Available online 19 December 2013

Keywords:
Artificial membrane
Permeability
Controlled release
Solid oral dosage forms
Confocal Raman microscopy
Three dimensional imaging

ABSTRACT

Aim of this study was to implement a modified phospholipid vesicle-based permeation assay (PVPA) barrier as alternative to Caco-2 cell monolayers in a combined dissolution and permeation system for testing of solid dosage forms. Commercially available Transwell® inserts were coated with egg phospholipids (Lipoid E 80) and characterized by confocal Raman microscopy. The modified PVPA barrier was then evaluated in permeation studies with solutions of different drugs as well as in combined dissolution and permeation studies utilizing an immediate and an extended release tablet formulation.

Raman cross section images demonstrated complete filling of the membrane pores with lipids and the formation of a continuous lipid layer of increasing thickness on top of the membrane during the stepwise coating procedure. Furthermore, it could be shown that this lipid coating remains intact for at least 18 h under dynamic flow conditions, significantly exceeding the viability of Caco-2 cell monolayers.

Permeability data for both drug solutions as well as for a fast and slow release tablet formulation were in excellent correlation with those data obtained for Caco-2 cell monolayers. Especially under the dynamic flow conditions prevailing in such a setup, the modified PVPA barrier is more robust and easier to handle than epithelial cell monolayers and can be prepared rather easily at a fraction of costs and time. The modified PVPA barrier may therefore represent a valuable alternative to Caco-2 cell monolayers in such context.

1. Introduction

As drug application via the gastrointestinal route is still the prevalent therapeutic pathway into the human body, solid oral dosage forms, like e.g. tablets, play a major role as drug delivery systems. After application, the drug is generally released from its delivery system and subsequently permeates across the intestinal mucosa. Thus, a drug's bioavailability depends on both, the release process and the permeation.

Consequently, for the development of novel oral therapeutics appropriate methods to analyze drug release and permeation are required. For measuring drug release, the pharmacopoeia describes different dissolution testing apparatuses depending on the delivery system. As dissolution testing provides information about drug release only, different devices have been developed for combined dissolution and permeation studies (d/p-systems) to investigate correlations and potential dependencies of drug dissolution and subsequent permeation [1–4]. To simulate the intestinal mucosa forming the permeation barrier in the human body, Caco-2 cell monolayers are often the first choice, as they mimic the biological properties of the intestinal epithelia cells quite well [1–6].

However, as cultivated cells are living systems, reproducibility and stability of these models vary. For instance, lacking barrier integrity has been detected by decreasing transepithelial electrical resistance (TEER) values over time [7], thus impeding long term studies with extended release formulations. Furthermore, long cultivation times and

* Correspondence to: U.F. Schaefer, Saarland University, Department of Biopharmaceutics and Pharmaceutical Technology, Campus A4.1, 66123 Saarbruecken, Germany. Tel.: +49 681 302 2019; fax: +49 681 302 4677.
** Correspondence to: M. Windbergs, Saarland University, Department of Biopharmaceutics and Pharmaceutical Technology, Campus A4.1, 66123 Saarbruecken, Germany. Tel.: +49 681 302 4763; fax: +49 681 302 4677.
E-mail addresses: s.gantzsch@mx.uni-saarland.de (S.P. Gantzsch), birthe.kann@mx.uni-saarland.de (B. Kann), Monika.Ofer-Glaessgen@sanofi.com (M. Ofer-Glaessgen), Petra.Loos@sanofi.com (P. Loos), Harald.Berchtold@sanofi.com (H. Berchtold), Stefan.Balbach@sanofi.com (S. Balbach), Thomas.Eichinger@sanofi.com (T. Eichinger), lehr@mx.uni-saarland.de (C.-M. Lehr), ufs@mx.uni-saarland.de (U.F. Schaefer), m.windbergs@mx.uni-saarland.de (M. Windbergs).
[1] Both authors contributed equally and are listed in alphabetical order.

0168-3659/$ – see front matter © 2013 Elsevier B.V. All rights reserved.
http://dx.doi.org/10.1016/j.jconrel.2013.12.009

high expenses have to be taken into account curbing the attractiveness for high throughput screening.

Lipid-based membrane models have the potential to overcome some drawbacks of cell culture systems, as there are no cultivation times while reproducibility and stability are improved. Such alternative systems were first described by Kansy et al. [8] as so called parallel artificial membrane permeability assays (PAMPA). These systems generally consist of a porous polymer membrane covered with a lipid dispersed in organic solvents [9–11], as a blank membrane lacks appropriate diffusion resistance. Recently, efforts have been made to modify PAMPA models circumventing the use of organic solvents as they often interact with the supportive membrane. By deposition of an aqueous phospholipid dispersion on an artificial membrane, Flaten et al. described an alternative organic solvent-free model named phospholipid vesicle-based permeation assay (PVPA) for passive drug permeability evaluation [12,13].

Prior to implementing the lipid-coated system into a combined dissolution and permeation device, physical properties and permeation behavior of the coating have to be compared against the established Caco-2 cell monolayers, as only a sufficient robustness of the coating renders the model valid for drug permeation studies.

For in-depth analysis, Flaten et al. [13] successfully applied confocal fluorescence microscopy to visualize the phospholipids deposited on the membrane. In this context, confocal Raman microscopy offers an analytical alternative for component visualization. In contrast to fluorescence microscopy generally necessitating labeling of the components for detection, confocal Raman microscopy is a label-free, inherently chemically selective technique. It has already been successfully adopted in pharmaceutical research for diversified applications spanning from drug distribution investigations [14,15] to drug release in solid dosage forms and implants [15,16].

In this study, a PVPA-based permeation model was thoroughly characterized by confocal Raman microscopy to gain a deeper understanding of membrane coating assembly and coating integrity. In a subsequent step, permeation experiments with drug solutions as well as combined dissolution and permeation studies were performed utilizing the PVPA-based model as well as established Caco-2 cell monolayers to evaluate the suitability of the PVPA-based model in direct comparison to cultivated cells. To investigate the discriminative power of both systems, an immediate as well as an extended release tablet formulation of the same drug was utilized.

2. Materials and methods

2.1. Materials

Commercially available cell culture inserts were purchased from Corning Incorporated (Transwell® type 3460, Corning, NY, USA). The polyester membrane (polyethylene terephthalate, thickness 10 μm) of the inserts was equipped with randomly distributed pores (mean diameter 0.4 μm). Lipoid E 80 composed of egg phospholipids with 80% phosphatidylcholine and di-oleoylphosphatidylcholine was generously provided by Lipoid GmbH (Ludwigshafen, Germany). Atenolol, rhodamine 123 and sodium fluorescein (Sigma-Aldrich, Steinheim, Germany), domperidone and domperidone maleate (Transo-Pharm, Siek, Germany), furosemide and propranolol HCl (Synopharm GmbH & Co KG, Barsbuettel, Germany) and talinolol (extracted from Cordanum tablets, AWD.pharma, Radebeul, Germany) served as model drugs. All reagents for high-performance liquid chromatography (HPLC) quantification were obtained from Sigma-Aldrich (Steinheim, Germany) in HPLC gradient grade. High purity water was prepared by a Millipore Milli-Q Synthesis system (Merck Millipore, Darmstadt, Germany). All other chemicals and reagents used in this study were of analytical grade.

Propranolol tablets (10 mg) as an immediate and an extended release formulation were prepared according to Motz et al. [17]. Krebs Ringer Buffer (KRB) adjusted to pH 7.4 was used in the following composition: 142.03 mM NaCl, 10.0 mM HEPES, 4.00 mM D-Glucose, 3.00 mM KCl, 1.41 mM $CaCl_2$, 2.56 mM $MgCl_2$ and 0.44 mM K_2HPO_4. Phosphate buffered saline (PBS) had the following composition: 129 mM NaCl, 2.5 mM KCl, 7.07 mM $Na_2HPO_4 * 7\ H_2O$, 1.3 mM KH_2PO_4, pH 7.4.

2.2. Methods

2.2.1. Preparation of the modified phospholipid vesicle-based permeation assay (PVPA) barrier

Membrane coating was performed according to a modified version of the protocol of Flaten et al. [12]. Liposomes for the coating made out of Lipoid E 80 were prepared by using the film method. PBS was used for rehydration of the phospholipid film. Membrane coating was achieved in five centrifugation steps (centrifuge Universal 32R, Hettich, Tuttlingen, Germany) at 600g for four minutes at 20 °C with subsequent drying at 37 °C in an oven. For each step, 100 μl liposomal dispersion were added onto the apical side of the membrane. Before drying, the PBS buffer excess was evacuated.

2.2.2. Preparation of a parallel artificial membrane permeability assay (PAMPA)

Di-oleoylphoshatidylcholine dissolved in n-dodecane (4% w/v) was spread on the polymer membrane according to the protocol of Kansy et al. [8] and characterized immediately after fabrication.

2.2.3. Cell culture

Caco-2 cells (clone C2BBe1) were purchased from American Tissue Culture Collection (ATCC, Manassas, VA, USA). Cells were cultured and seeded on permeable supports (Transwell®) following an internal protocol [17]. Passages 61–70 within 21–25 days after seeding were used for experiments. Only Transwells® showing TEER values above 300 Ω^*cm^2 were used.

2.2.4. Confocal Raman microscopy

Confocal Raman microscopy was performed with a WITec alpha 300R+ (WITec GmbH, Ulm, Germany) using objectives with a 50 fold magnification (Zeiss 50 × N.A. = 0.8; Olympus 50 × N.A. = 0.35). Raman spectra were acquired at an excitation wavelength of 532 nm (10 mW, Nd:YAG laser) or 785 nm (50 mW, diode laser) without any further sample preparation. The spectral resolution was 4 cm^{-1}. All three dimensions (x-, y- and z-axis) were exploited for imaging. In a subsequent step, the recorded spectra were converted into false color images (WITec Project Plus). Pixel assigned to polyester membrane spectra are represented in red, whereas pixel assigned to Lipoid E 80 spectra are depicted in blue color. For virtual cross sections focusing on pore morphology, spectra were recorded every 0.5 μm along x- and z-axis with an integration time of 0.3 s. Stacked images have a resolution of 0.2 μm per pixel in x- and y-direction and a distance of 0.5 μm between focal planes. Each spectrum was integrated for 0.15 s. For analysis of the coating procedure, Raman spectra were acquired every 100 μm along x- and y-axis across the entire membrane area with an integration time of 4 s. Virtual cross sections of coating thickness have a resolution of 5 μm^2 per pixel (100 μm^2 for entire cross section images, respectively). Each spectrum was integrated for 0.7 s.

2.2.5. Optical topography

Surface topography profiles were obtained by optical profilometry (WITec alpha 300R+ with a built-in chromatic sensor) with an integration time of 0.02 s. No further sample preparation was necessary. In combination with confocal Raman microscopy, optical profilometry is able to supplement compensational altitude analysis, thus ensuring the acquisition of Raman spectra at the very surface of a structured sample surface [18,19]. Optical profile images for coating procedure analysis

and respective Raman images have the same geometric dimension and a concordant image point resolution (100 μm × 100 μm).

2.2.6. Combined dissolution and permeation testing

Experiments were performed in an automated apparatus (d/p-system) [4,7,17]. Prior to mounting in the flow through permeation cell (FTPC), inserts with Caco-2 cells or with lipid coating were pre-incubated with KRB for 30 min and the flow rate was adjusted to 1.0 ml/min in the permeation module. For permeability experiments with solutions, only the FTPC was used and sampling took place automatically at the basolateral side. The used drug concentrations are summarized in Table 1. For simultaneous dissolution and permeation studies, two propranolol tablets were inserted in the flow through dissolution cell for each experiment. The flow rate was adjusted to 6.5 ml/min in this module and it was in-line connected to the FTPC. As dissolution and permeation medium, KRB was used and the experiments were performed in a water bath at 37 °C. At certain time points, sampling took place at the apical (A) and basolateral (B) compartment of the FTPC by the SIA system, which consisted of a FIAlab 3500 running on FIAlab software for Windows® version 5.9.192 (FIAlab Instruments, Bellevue, USA). TEER values were monitored online with a computer-controlled EVOM (World Precision Instruments, Berlin, Germany) using LabVIEW software (Version 2009, National Instruments Germany GmbH, Munich, Germany) [7].

2.2.7. Permeation experiments under classical conditions using drug solutions

Experiments were performed in a classical transport experimental setup with 1.5 ml KRB in the receiver (basolateral) compartment and 0.5 ml drug solution in the donor (apical) compartment. Throughout experiments, inserts were shaken (orbital shaker, IKA®-Werke GmbH and Co KG, Staufen, Germany) at 150 rpm in an incubator (37 °C). Samples (100 μl) were taken at defined time points from the receiver compartment over 3 h for Caco-2 cells and over 24 h for the modified PVPA barrier. The sample volume was replaced with fresh KRB.

2.2.8. Quantification of drug substances

Using solutions as well as tablets, the concentration of substance in the basolateral compartment at each sampling time point was determined via HPLC or fluorescence measurement in a plate reader after automatic bottling by the SIA system. Further details of the quantification methods are summarized in the supplementary part.

Using tablets, the concentration of propranolol in the apical compartment was determined online by fluorimetric detection with the FIAlab fluorescence detector PMT-FL. Scan rate was adjusted to 4 Hz and integration time was set to 80 ms.

2.2.9. Determination of apparent permeability (P_{app})

The apparent permeability (P_{app}) across the modified PVPA barrier and the Caco-2 cell monolayer, respectively, was determined using solutions of each substance and calculated according to the following equation (Eq. 1) derived from Fick's law for steady state and sink conditions.

$$P_{app} = \frac{dQ}{dt} \times \frac{1}{A \times c_0} \quad (1)$$

From the linear part of the diagram (increasing mass in the basolateral part versus time), the ratio dQ/dt was calculated. Furthermore, A [cm^2] is the permeation area of the membrane and c_0 [μg/ml] is the donor concentration at t = 0 h.

3. Results and discussion

3.1. Characterization of the modified PVPA barrier assembly, integrity of the lipid coating and its stability against media

The permeation model system is based on a porous polyester membrane fixed in a commercially available cell culture insert forming a supportive layer. The apical membrane surface is coated with a phospholipid layer in a multiple step deposition procedure (Fig. 1a). Raman spectra of the two components allow chemically selective analysis due to spectral differences (Fig. 1b), while coating and membrane material would be otherwise indistinguishable. Confocal Raman microscopy operates non-destructive and label-free, keeping the sample in its pristine state throughout in-depth investigation of spatial phospholipid deposition, the fabrication process and robustness against media. Furthermore, the entire lipid-coated permeation area of the model can be visualized in a lateral overview as well as in virtual cross-section images due to the beneficial combination of motorized scan stage and confocal setup of the microscope.

As drug molecules will primarily pass the membrane through the pores during permeation experiments, investigations in this context were focused on pore shape throughout the membrane as well as lipid-filling status.

At first, Raman spectra were acquired along the xz–axes of the blank membrane framing a vertical plane which was virtually cutting through the pore. By converting the normalized Raman spectra into a false color image assigning polyester membrane spectra to red image pixel, a two dimensional virtual cross section of each pore was obtained (Fig. 2a). All pores show similar morphology and boundaries are straight, sharp and distinct. Investigated pores were randomly chosen and equally distributed across the permeation area derived from a minimum of three individual cell culture inserts. Due to manual setting of the focal plane for the image, the pore might potentially not be struck in its exact center. To safeguard preceding results, Raman spectra were acquired from the same lateral area but in different focal planes. Resulting individual images depicting the round shape of the pore diameter were assembled on top of each other in consecutive order forming an image stack showing the three dimensional pore shape (Fig. 2b). Thus, results obtained

Table 1
Overview of properties, concentrations of the drugs and of P_{app} values. Data presented as mean ± SD (n ≥ 3). Molecular weight (MW) and xlogP3 value are presented according to PubChem database [20]. Substances marked with [1] are p-glycoprotein substrates.

Substance	Concentration [μM]	MW [g/mol]	xlogP3	P_{app} Caco-2 cells [$*10^{-6}$ cm/s]	P_{app} modified PVPA barrier [$*10^{-6}$ cm/s]	Permeability classification according to BCS [21,22]
Atenolol	5	266.3	0.2	0.44 ± 0.20	0.52 ± 0.13	Low
Furosemide[1]	1209.5	330.7	2	0.18 ± 0.02	1.41 ± 0.64	Low
Sodium fluorescein	14	376.3	3.4 (without Na)	0.34 ± 0.08	0.16 ± 0.07	Low
Rhodamine 123[1]	15	380.8	2.5	1.60 ± 0.23	1.61 ± 0.43	Low
Propranolol HCl	385.7	259.3	3	25.00 ± 5.20 [17]	13.30 ± 2.40	High
Talinolol[1]	27.5	363.5	2.6	1.50 ± 0.42	3.72 ± 0.56	High
Domperidone[1]	23.5	425.9	3.9	6.08 ± 0.52	5.18 ± 0.77	High
Domperidone maleate[1]	23.5	542.0	–	8.11 ± 2.19	8.60 ± 1.30	High

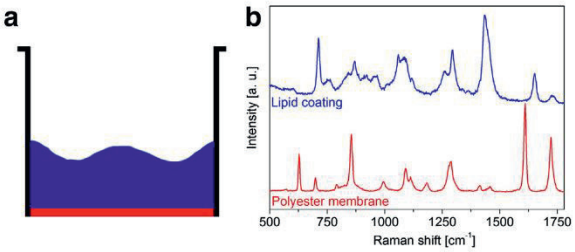

Fig. 1. a) Scheme of the modified PVPA barrier with the supportive membrane (red) and the applied lipid coating on the apical side (blue). b) Raman spectra of lipid coating (blue) and polyester membrane (red) material. (For interpretation of the references to color in this figure legend, the reader is referred to the web version of this article.)

from the virtual cross sections of the cone shaped pore morphology were confirmed.

Next, pores after coating were investigated, when their inlets were no longer visible. Fig. 2c displays the spatially resolved image stack of a lipid filled pore as generated for the uncoated membrane. For a better spatial understanding, separate images of membrane pore and its lipid filling are depicted additionally, proving the distinct analytical discrimination within the two component system. Pore boundaries are sharp and lipid can precisely be distinguished from the membrane. The complete filling was found for all investigated pores from arbitrarily chosen positions across the membrane area and a minimum of three individual coated membranes.

Moreover, the formation of the lipid layer by iterated coating was thoroughly investigated. As the coating surface crisscrosses numerous focal planes, it actually exceeds the analytical capabilities of the confocal microscope. To overcome this limitation, optical profilometry was introduced as a complementary technique. The surface height information derived from the topography profiles (Suppl. Fig. A) served as a reference for subsequent guided Raman spectra acquisition of the same area for distinct chemical discrimination. Resulting Raman images of the coated membrane after each individual coating step provide visualization of the increasing coverage of the membrane with phospholipid (Fig. 3a). After the first coating step, two concentric circles of lipid could be observed, one in the center and another one at the outer boundaries of the membrane. With the second step, the lipid-covered membrane area increased until a full coating was obtained at the end of the third coating step, implying that the remaining two steps solely add lipid to stabilize the coating.

Due to the surface patterns, it can be expected that coating thickness varies across the membrane diameter. Thus, a profound analysis was performed with virtual Raman cross sections. First, Raman spectra were acquired across the diameter of the membrane along the xz–axes and converted into chemically selective false color images (Fig. 3b). For a detailed analysis, five randomly chosen equally distributed areas across the diameter of the membrane were imaged in more detail after each coating step (Suppl. Fig. B). The cross sections after the first coating step show blank membrane as well as parts with a thin lipid coating. After the second step, the coating spreads over the membrane in a thin layer until a consistent layer is achieved after the third step. The wavelike pattern already begins to arise and becomes more prominent after the remaining two coating steps. Thus, the results gained from the cross-section investigation (Fig. 3b and Suppl. Fig. B) correlate well with the lateral xy–images of the lipid distribution (Fig. 3a).

In comparison, Fig. 3c depicts a PAMPA system consisting of a lipid dissolved in organic solvent on top of the porous membrane. The liquid state of the system implicates a rather smooth surface, but due to surface tension the liquid also forms a conical shape on the membrane. Even though this PAMPA system can be fabricated in a convenient one-step procedure, the solvent is prone to interact with the polymer membrane. In addition, the liquid state of this system is not resistant against dynamic flow conditions as required for the combined dissolution and permeation testing system introduced in this study.

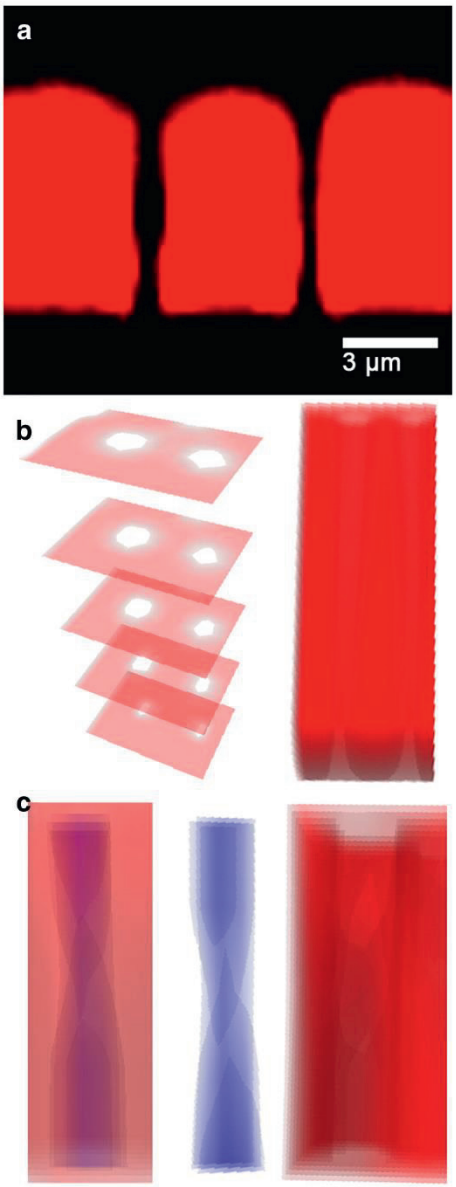

Fig. 2. Pore morphology characterization of blank (a, b) and coated (c) membrane. a) False color image of pore morphology derived from virtual Raman cross sectioning of the blank membrane. b) Images derived from vertically adjacent focal planes were stacked visualizing the entire pore morphology. c) Three dimensional image stack showing the entire pore filled with lipid. For depicting chemically selective identification of the two components and a better spatial understanding, the image stack was split into individual images for lipid filling (blue) and membrane (red). (For interpretation of the references to color in this figure legend, the reader is referred to the web version of this article.)

In addition to investigating the modified PVPA barrier system and its fabrication, the performance of such a system under dynamic flow conditions was tested. As these lipid-based permeation models serve as the barrier during drug permeation experiments, the lipid coating has to withstand liquid media. To address this issue, coating integrity was

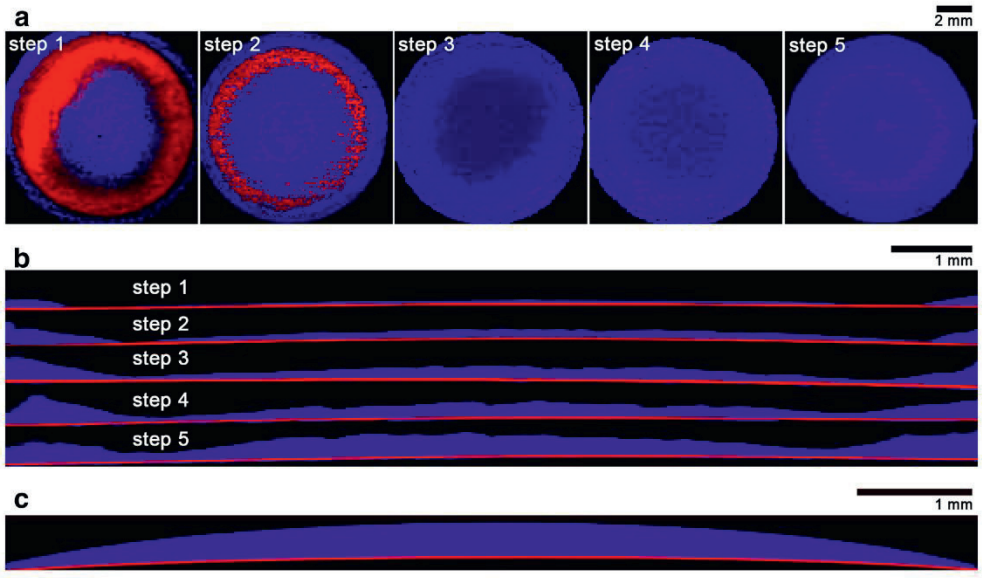

Fig. 3. Raman images showing gradual lipid assembly (blue) on the supportive membrane (red) after each coating step. a) Lateral topography images overlaid with respective Raman data visualizing the entire permeation area. b) Virtual cross section images of the entire membrane diameter depicting coating structure. c) Virtual cross section image of a PAMPA system illustrating the membrane in red and the lipid dissolved in organic solvent in blue. Due to image size the free aspect ratio of the cross section images was deregulated for better visualization. (For interpretation of the references to color in this figure legend, the reader is referred to the web version of this article.)

proven after defined exposure times (6 h and 18 h) to KRB medium under experimental dynamic flow conditions. After drying, the membranes were investigated with confocal Raman microscopy. Following analysis of coating assembly, virtual cross sections across the entire diameter of the diffusion area were acquired and converted into chemically selective false color images (Fig. 4). Neither cross section images after 6 h nor after 18 h exposure time revealed any uncovered membrane areas. Therefore, permeation experiments up to 18 h can be conducted with the modified PVPA barrier under dynamic flow conditions in the combined dissolution and permeation system without integrity deficiency of the membrane coating.

3.2. Monitoring barrier integrity by transepithelial electrical resistance (TEER)

To investigate and compare barrier integrity for the established Caco-2 cell monolayers and modified PVPA barrier, both barriers were mounted in the flow through permeation cell (FTPC) and TEER values were monitored online throughout the entire experiment. During the first 0.5 h of the experiment TEER values increased until the equilibrium to flow conditions was achieved. TEER values for Caco-2 cell monolayers remained above 300 Ω^*cm^2 for about 3 h, followed by decreasing TEER values indicating an integrity breakdown of the cellular barrier. For the modified PVPA barrier, TEER values reached a constant plateau roughly 1.5 h after inserting in the FTPC. In contrast to Caco-2 cells, TEER values remained over 600 Ω^*cm^2 for 18 h, thus confirming long term coating stability under dynamic flow conditions.

3.3. Permeation experiments under dynamic flow conditions using drug solutions

Permeation experiments were first conducted with different drugs in aqueous solution and the P_{app} values were compared with those for Caco-2 cell monolayers, grown on the same membrane and used in the same apparatus according to the same protocol. Permeation experiments with either type of barrier were performed in the FTPC for 3 h or 18 h, respectively, ensuring constant drug concentrations at the apical side of the permeation barrier. The individual P_{app} values are provided in Table 1. The modified PVPA barrier provided comparable permeability data and ranking of the drug substances compared to Caco-2 cell monolayers. Hence, both models can equally well distinguish between highly, medially and poorly permeable substances.

To evaluate the modified PVPA barrier against existing PVPA models, experiments in a classical permeation experiment without dynamic flow conditions were conducted with drug solutions in comparison to established Caco-2 cell monolayers. Fig. 5a depicts log P_{app} data for the PVPA barrier developed by Flaten et al. [12] and the modified PVPA barrier as well as for Caco-2 cells. The individual data points are similarly distributed along the line of identity. Thus, the modified PVPA barrier exhibited suitable performance for drug permeation experiments.

Fig. 4. Raman cross section images of the entire membrane diameter depicting lipid coating (blue) on the supportive membrane (red) prior to (0 h), after 6 h and 18 h of investigating coating resistance against media under dynamic flow conditions. Due to image size the free aspect ratio was deregulated for better visualization. (For interpretation of the references to color in this figure legend, the reader is referred to the web version of this article.)

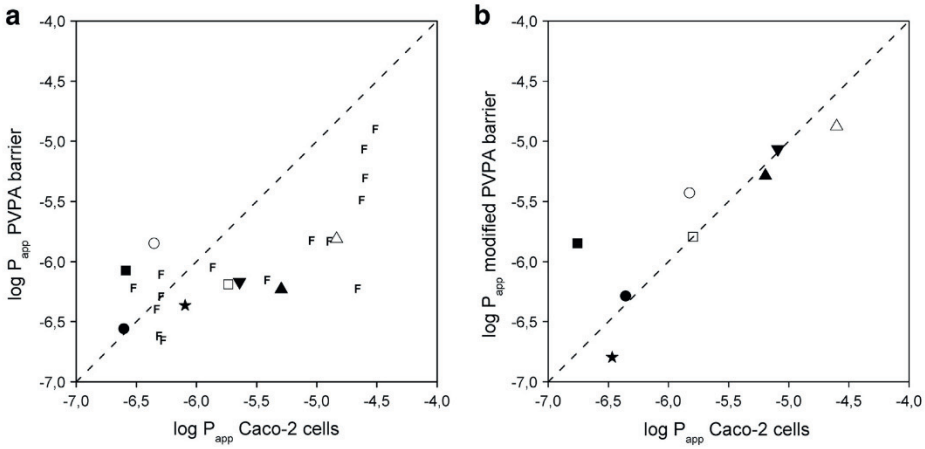

Fig. 5. Correlation between Caco-2 cells and PVPA barriers. Permeability data determined under classical conditions (a) and dynamic flow conditions (b) for atenolol (●), domperidone (▲), domperidone maleate (▼), sodium fluorescein (*), furosemide (■), propranolol (△), rhodamine 123 (□) and talinolol (○). Data taken from Flaten et al. [12] are marked with F. Dashed lines represent lines of identity.

Subsequently, permeation data were acquired for the modified PVPA barrier and the Caco-2 cells under dynamic flow conditions. As for the classical setup, the individual data points are uniformly distributed along the line of identity (Fig. 5b).

Besides passive diffusion, being the only transport mechanism for the artificial membrane model, Caco-2 cells also exhibit influx and efflux transporters influencing permeation. To address the influence of p-glycoprotein (p-gp) efflux on transport rates in permeation testing in the combined dissolution and permeation testing setup, the inhibition ratio of Caco-2 cell monolayers with and without incubation with TPGS (0.01%) as a well-known p-gp inhibitor was investigated. In the classical setup with no dynamic flow, the inhibition ratios (Suppl. Eq. 2) were in the range of 1.62–3.11 for Caco-2 cells (Suppl. Table A). With the dynamic flow setup, the inhibition ratios (Suppl. Eq. 2) in the range of 0.94–1.54 for Caco-2 cells were even smaller (Suppl. Table A), which is in good agreement with results acquired in the classic Transwell® setup [23]. As these values are very low, the influence of efflux on the overall absorptive transport in Caco-2 cells (apical to basolateral side) is neglectable. Therefore, Caco-2 cells (passive and efflux transport) and lipid-coated membranes (only passive transport) do not show significantly different overall transport rates for p–gp substrates (Table 1). Even though transport proteins are missing in the non-cellular model, it represents a suitable model for permeation studies as passive diffusion is the main route for drug uptake *in vivo* [24] and the good correlation to Caco-2 cells under dynamic flow conditions confirm the specific application of the presented modified PVPA barrier.

3.4. Combined dissolution and permeation testing with tablets

A main advantage of the combined dissolution and permeation system is the possibility to analyze intact solid oral dosage forms. Immediate (IR) and extended release (ER) propranolol tablets were tested with respect to dissolution and permeation in the combined setup.

The release profiles of the IR and ER tablet acquired behind the dissolution module at the apical compartment A (Fig. 6) are different according to the standard f2-test [25] and independent from the permeation barrier.

Surprisingly however, the permeation profiles of the two release kinetics show no statistically significant difference (Fig. 7). This was, however, observed with both Caco-2 cell monolayers and with the modified PVPA barrier. Thus, the differences as observed in the dissolution

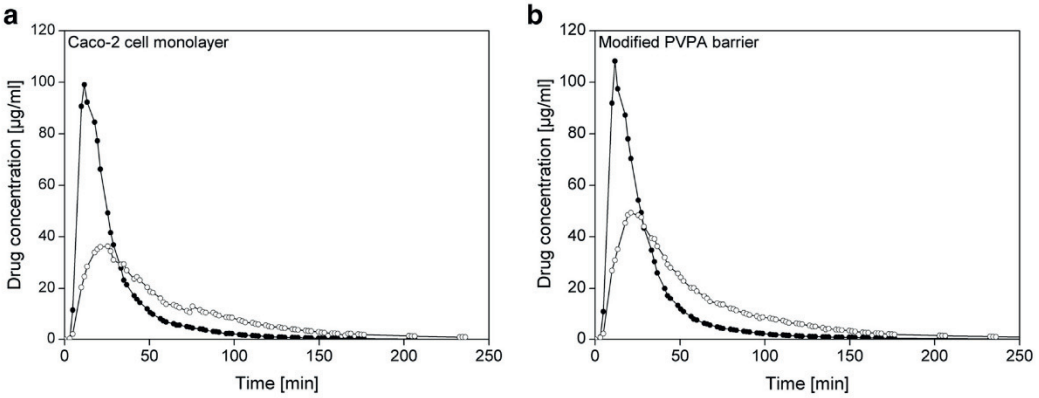

Fig. 6. Concentration time trends at the apical compartment A for tablets with immediate (●) and extended (○) drug release. Data are derived with inserted Caco-2 cell monolayer (a) or modified PVPA barrier (b). For the sake of clarity, data are presented as mean ($n \geq 3$) without SD.

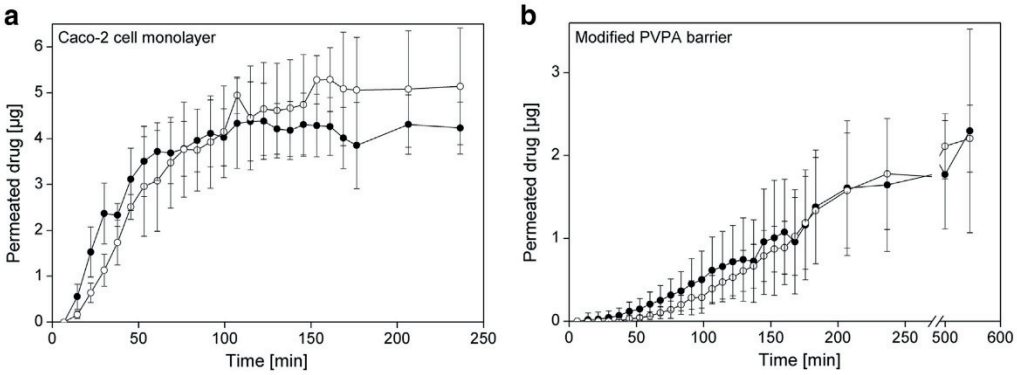

Fig. 7. Permeated amount calculated from the concentration assessed at the basolateral compartment B for Caco-2 cell monolayers (a) and modified PVPA barrier (b). Closed symbols (●) represent immediate release tablets and open symbols (○) represent extended release tablets. Cumulative data are presented as mean ± SD ($n \geq 3$).

profiles are obviously not strong enough to affect the permeation data. This finding underscores not only the equivalence of the two barrier systems in such a setup. Moreover, these data also demonstrate the advantage of combined dissolution and permeation testing in general, pointing to the fact that the observed differences in the dissolution profiles might not necessarily lead to differences in drug bioavailability.

The release profiles of the two tablet formulations were obviously independent of and therefore not affected by the chosen surrogate barrier. In contrast, the permeation process observed with the Caco-2 cell monolayers was faster and led to somewhat higher end concentrations in the basolateral compartment than was observed with the modified PVPA barrier. However, these differences can be well explained: Firstly, Caco-2 cell monolayers have a thickness of about 5 to 10 µm, whereas the thickness of the lipid coating goes up to about 83 µm (Suppl. Fig. B). Therefore, the longer diffusion way from the apical to the basolateral side may be expected to result in a slower permeation rate. Secondly, the lipid coating may also act as a depot, which is filled up at the beginning and is emptied, although the drug concentration at the apical side was almost zero. Thirdly, previous experiments with drug solutions of propranolol had already shown about 2-fold higher P_{app} values for the modified PVPA barrier as compared to cell-based barriers (Table 1). As lower P_{app} values indicate less permeability, this explains the lower permeated amount than observed with the Caco-2 cells. Nevertheless, the results confirm the suitability of the modified PVPA barrier for tablet testing in a combined dissolution and permeation system, taking advantage of its essential feature to test intact solid oral dosage forms without the necessity to disintegrate the formulation prior to the experiment [26].

4. Conclusion

A modified PVPA barrier was successfully implemented into a combined dissolution and permeation system, allowing the testing of intact solid oral dosage forms. By elucidating the potential pathway for drugs through the membrane, pore morphology and its complete lipid filling was visualized in three dimensions using confocal Raman microscopy in addition to the morphology of the entire coating formed after repeated lipid deposition on the membrane. Moreover, its mechanical stability and suitability as permeation barrier in a combined dissolution and permeation system was successfully demonstrated under dynamic flow conditions. Permeation experiments with solutions of different drugs, as well as direct comparison of an immediate versus an extended release tablet of the same drug (propranolol) were in very good correlation with data obtained from analogous experiments with Caco-2 cell monolayers. Due to the high stability of the modified PVPA barrier over time, the experimental time frame to investigate dissolution and permeation simultaneously can be extended beyond the limit for Caco-2 cell monolayers. This offers the possibility to investigate extended release formulations over a relevant period of time. In addition, the modified PVPA barrier can be prepared much faster and easier than growing epithelial cells, but using the same standardized supports (e.g. Transwell®). While the potential influence of cellular transporter systems and metabolizing enzymes can of course not be taken into account with such a simplified membrane model, this approach provides first biopharmaceutically relevant information from tablet formulations rather quickly and reproducibly.

Supplementary data to this article can be found online at http://dx.doi.org/10.1016/j.jconrel.2013.12.009.

Acknowledgement

Heike Stumpf and Petra Koenig are acknowledged for cultivation of Caco-2 cells. Thanks to Peter Meiers for the discussion regarding drug quantification via HPLC and to José David Gómez-Mantilla for the help with the f2 test.

References

[1] M.J. Ginski, R. Taneja, J.E. Polli, Prediction of dissolution–absorption relationships from a continuous dissolution/caco-2 system, AAPS PharmSci. 1 (1999) 1–12.
[2] M. Kataoka, Y. Masaoka, Y. Yamazaki, T. Sakane, H. Sezaki, S. Yamashita, In vitro system to evaluate oral absorption of poorly water-soluble drugs: simultaneous analysis on dissolution and permeation of drugs, Pharm. Res. 20 (2003) 1674–1680.
[3] M. Kobayashi, N. Sada, M. Sugawara, K. Iseki, K. Miyazaki, Development of a new system for prediction of drug absorption that takes into account drug dissolution and pH change in the gastro-intestinal tract, Int. J. Pharm. 221 (2001) 87–94.
[4] S.A. Motz, J. Klimundová, U.F. Schaefer, S. Balbach, T. Eichinger, P. Solich, C.M. Lehr, Automated measurement of permeation and dissolution of propranolol HCl tablets using sequential injection analysis, Anal. Chim. Acta. 581 (2007) 174–180.
[5] P. Stenberg, K. Luthman, P. Artursson, Virtual screening of intestinal drug permeability, J. Control. Release 65 (2000) 231–243.
[6] Y. Sambuy, I. Angelis, G. Ranaldi, M.L. Scarino, A. Stammati, F. Zucco, The Caco-2 cell line as a model of the intestinal barrier: influence of cell and culture-related factors on Caco-2 cell functional characteristics, Cell Biol. Toxicol. 21 (2005) 1–26.
[7] M. Muendoerfer, U.F. Schaefer, P. Koenig, J.S. Walk, P. Loos, S. Balbach, T. Eichinger, C.M. Lehr, Online monitoring of transepithelial electrical resistance (TEER) in an apparatus for combined dissolution and permeation testing, Int. J. Pharm. 392 (2010) 134–140.
[8] M. Kansy, F. Senner, K. Gubernator, Physicochemical high throughput screening: parallel artificial membrane permeation assay in the description of passive absorption processes, J. Med. Chem. 41 (1998) 1007–1010.
[9] A. Avdeef, The rise of PAMPA, Expert Opin. Drug Metab. Toxicol. 1 (2005) 325–342.
[10] B. Faller, Artificial membrane assays to assess permeability, Curr. Drug Metab. 9 (2008) 886–892.
[11] S.T. Buckley, S.M. Fischer, G. Fricker, M. Brandl, In vitro models to evaluate the permeability of poorly soluble drug entities: challenges and perspectives, Eur. J. Pharm. Sci. 45 (2012) 235–250.
[12] G.E. Flaten, A.B. Dhanikula, K. Luthman, M. Brandl, Drug permeability across a phospholipid vesicle based barrier: a novel approach for studying passive diffusion, Eur. J. Pharm. Sci. 27 (2006) 80–90.

[13] G.E. Flaten, H. Bunjes, K. Luthman, M. Brandl, Drug permeability across a phospholipid vesicle-based barrier-2. Characterization of barrier structure, storage stability and stability towards pH changes, Eur. J. Pharm. Sci. 28 (2006) 336–343.
[14] M. Windbergs, M. Haaser, C.M. McGoverin, K.C. Gordon, P. Kleinebudde, C.J. Strachan, Investigating the relationship between drug distribution in solid lipid matrices and dissolution behaviour using Raman spectroscopy and mapping, J. Pharm. Sci. 99 (2010) 1464–1475.
[15] M. Haaser, M. Windbergs, C.M. McGoverin, P. Kleinebudde, T. Rades, K.C. Gordon, C.J. Strachan, Analysis of matrix dosage forms during dissolution testing using Raman microscopy, J. Pharm. Sci. 100 (2011) 4452–4459.
[16] A. Belu, C. Mahoney, K. Wormuth, Chemical imaging of drug eluting coatings: combining surface analysis and confocal Raman microscopy, J. Control. Release 126 (2008) 111–121.
[17] S.A. Motz, U.F. Schaefer, S. Balbach, T. Eichinger, C.M. Lehr, Permeability assessment for solid oral drug formulations based on Caco-2 monolayer in combination with a flow through dissolution cell, Eur. J. Pharm. Biopharm. 66 (2007) 286–295.
[18] L. Franzen, C. Mathes, S. Hansen, M. Windbergs, Advanced chemical imaging and comparison of human and porcine hair follicles for drug delivery by confocal Raman microscopy, J. Biomed. Opt. 18 (2013) 061210.
[19] B. Kann, M. Windbergs, Chemical imaging of drug delivery systems with structured surfaces—a combined analytical approach of confocal Raman microscopy and optical profilometry, AAPS J. 15 (2013) 505–510.
[20] National Center for Biotechnology Information, PubChem Compound Database, Jan. 05, 2013, (http://pubchem.ncbi.nlm.nih.gov/).
[21] C.Y. Wu, L.Z. Benet, Predicting drug disposition via application of BCS: transport/absorption/elimination interplay and development of a biopharmaceutics drug disposition classification system, Pharm. Res. 22 (2005) 11–23.
[22] B.A. Chavan, K.K. Mali, R.J. Dias, L.D. Kate, Solid state characterization of multicomponent inclusion complex of domperidone with β-cyclodextrin, polyvinyl pyrrolidone and citric acid, Der Pharmacia Lettre 3 (2011) 281–290.
[23] E.M. Collnot, C. Baldes, U.F. Schaefer, K.J. Edgar, M.F. Wempe, C.M. Lehr, Vitamin E TPGS P-glycoprotein inhibition mechanism: influence on conformational flexibility, intracellular ATP Levels, and role of time and site of access, Mol. Pharm. 7 (2010) 642–651.
[24] A.K. Mandagere, T.N. Thompson, K.K. Hwang, Graphical model for estimating oral bioavailability of drugs in humans and other species from their Caco-2 permeability and in vitro liver enzyme metabolic stability rates, J. Med. Chem. 45 (2002) 304–311.
[25] J.W. Moore, H.H. Flanner, Mathematical comparison of dissolution profiles, Pharm. Technol. 20 (1996) 64–74.
[26] J. Kanzer, I. Tho, G.E. Flaten, M. Magerlein, P. Holig, G. Fricker, M. Brandl, In-vitro permeability screening of melt extrudate formulations containing poorly water-soluble drug compounds using the phospholipid vesicle-based barrier, J. Pharm. Pharmacol. 62 (2010) 1591–1598.

SUPPLEMENTARY DATA

Quantification of drug substances

HPLC quantification was performed with a Dionex system (Thermo Fisher GmbH, Idstein, Germany) consisting of a Dionex ISO-3100A pump, a Dionex WPS-3000 TSL autosampler, a Dionex VWD-3400 variable wavelength detector, a Dionex TCC-3000 column compartment and a Dionex SRD-3200 solvent rack. The system runs on Chromeleon software version 6.80 SP2. Calibration was done with external standards.

Quantification of atenolol was performed with a RP-18 select B (LiChrospher® 60, Merck), 5 µm, 12.5 cm column. The mobile phase was composed of 90 % (v/v) acid water, 5 % (v/v) methanol and 5 % (v/v) acetonitrile. The oven temperature was 40 °C and the flow rate was set to 1.2 ml/min. Detection was performed with a fluorescence detector (L-2480, Merck Hitachi) (λ_{exc}= 231 nm, λ_{em}= 307 nm), linearity (R>0.999) was given between 4 ng/ml and 1 µg/ml. The retention time was 5.2 ± 0.1 min.

Domperidone and domperidone maleate were quantified with a RP-18e (LiChrospher® 100, Merck), 5 µm, 12.5 cm column. The mobile phase consisted of 50 % (v/v) methanol and 50 % (v/v) phosphate buffer pH 2.3. The oven temperature was 40 °C and the flow rate was 1.0 ml/min. Detection was performed with UV at 285 nm, linearity (R>0.9989) was given between 20 ng/ml and 1000 ng/ml. The retention time was 2.6 ± 0.1 min.

Quantification of furosemide was performed with a RP-18 select B (LiChrospher® 60, Merck), 5 µm, 12.5 cm column. The mobile phase was composed of 60 % (v/v) water, 30 % (v/v) acetonitrile, 10 % (v/v) methanol, 0.033 % (v/v) triethylamine and 0.044 % (v/v) phosphoric acid. The oven temperature was 40 °C and the flow rate was 1.2 ml/min. Detection was performed with UV at 235 nm, linearity (R>0.999) was given between 25 ng/ml and 4000 ng/ml. The retention time was 3.0 ± 0.1 min.

Propranolol was quantified with a RP-18 (LiChrospher® 100, Merck), 5 µm, 12.5 cm column. The mobile phase was composed 45 % (v/v) water, 22 % (v/v) acetonitrile, 33 % (v/v) methanol, 0.033 % (v/v) triethylamine and 0.044 % (v/v) phosphoric acid. The oven temperature was 40 °C and the flow rate was set to 1.2 ml/min. Detection was performed with UV at 215 nm, linearity (R>0.999) was given between 30 ng/ml and 100 µg/ml. The retention time was 3.0 ± 0.2 min.

Quantification of talinolol was performed with a RP-18 select B (LiChrospher® 60, Merck), 5 µm, 12.5 cm column. The mobile phase consisted of 77 % (v/v) triethylammoniumphosphate (0.025 M/l) and 23 % (v/v) acetonitrile. The oven temperature was 40 °C and the flow rate was 1.2 ml/min. Detection was performed with a fluorescence detector (L-2480, Merck Hitachi) (λ_{exc}= 252 nm, λ_{em}= 332 nm), linearity (R>0.999) was given between 3 ng/ml and 1000 ng/ml. Retention time was 5.7 ± 0.1 min.

Quantification of sodium fluorescein was performed using a fluorescence plate reader (TECAN infinite M200, Tecan GmbH, Crailsheim, Germany; λ_{exc}= 485 nm, λ_{em}= 530 nm). Linearity (R>0.999) was given between 5 ng/ml and 1000 ng/ml.

Quantification of rhodamine 123 was performed using a fluorescence plate reader (TECAN infinite M200, Tecan GmbH, Crailsheim, Germany; λ_{exc}= 480 nm, λ_{em}= 530 nm). Linearity (R>0.999) was given between 4 ng/ml and 200 ng/ml.

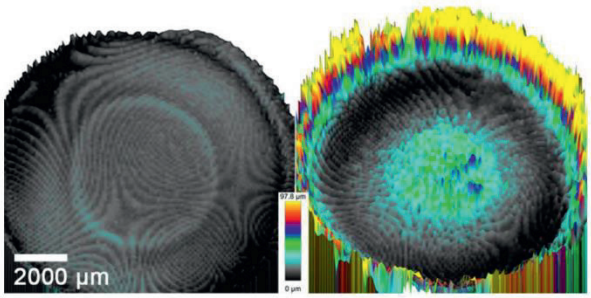

Suppl. Figure A. Exemplary topography profile of a membrane in blank state (left) and after the third coating step (right) serving as template for subsequent guided Raman spectra acquisition.

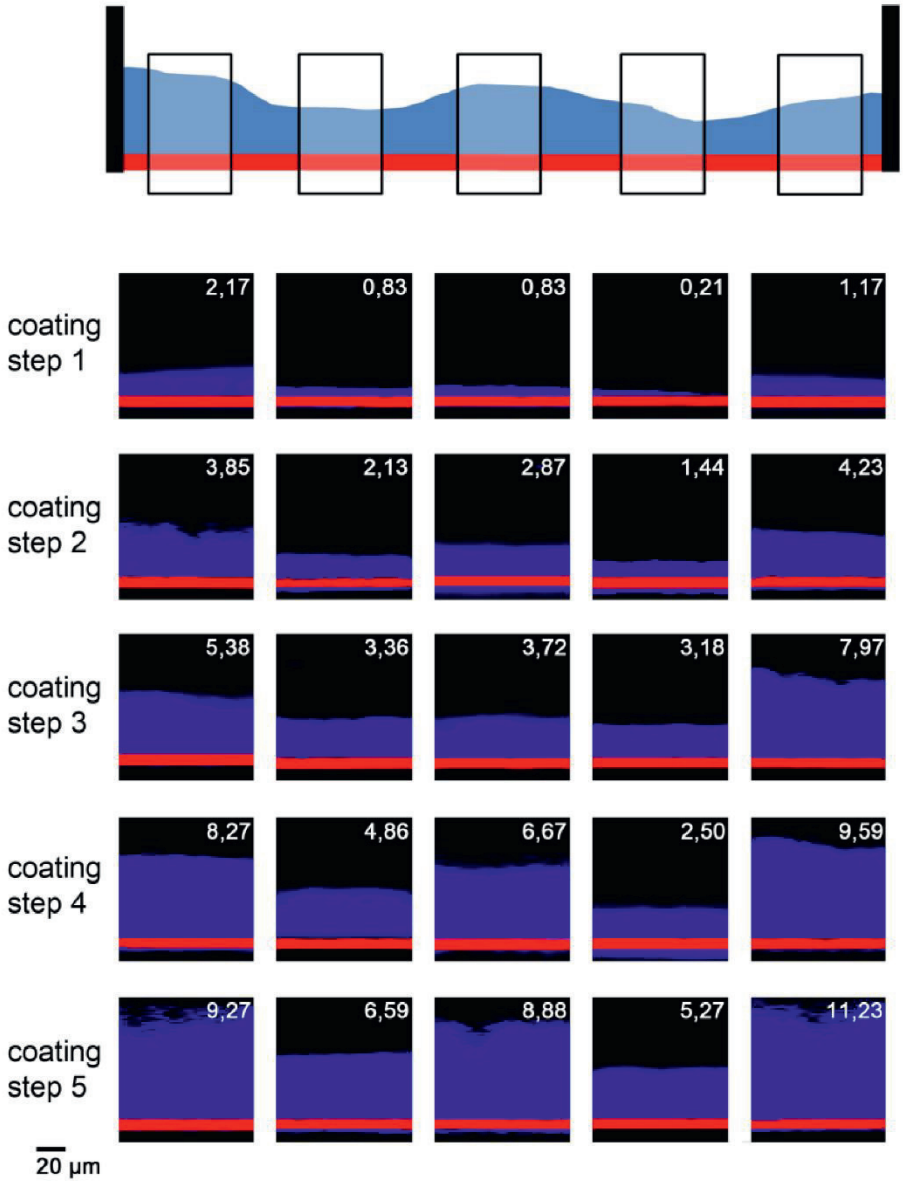

Suppl. Figure B. Schematic close up of the **modified PVPA barrier** with five highlighted areas for detailed coating pattern evaluation. Investigated areas are equally distributed across the membrane diameter. For each coating step, the resulting Raman images of the highlighted areas are displayed. Coating thickness is given as factor of supportive membrane thickness (10 µm).

Influence of p-glycoprotein inhibition

To evaluate the influence of p-glycoprotein (p-gp) classical static as well as dynamic transport experiments were performed with the five p-gp substrates using Caco-2 cell monolayers. Classical static experiments were performed in a 12-well cell culture plate adding 0.5 ml drug solutions at the apical side and 1.5 ml KRB at the basolateral side. Dynamic transport experiments were performed in the FTPC. For inhibition studies of p-gp 0.01 % TPGS 1000 (d-alpha tocopheryl polyethylene glycol 1000 succinate, Sigma-Aldrich, Steinheim, Germany) was added to the solutions.

For the rating of the inhibitory effect on the permeation an inhibition ratio was calculated according to the following equation (eq. 2)

$$inhibition\ ratio = \frac{P_{app\ (with\ inhibitor)}}{P_{app\ (without\ inhibitor)}} \qquad \text{(eq. 2)}$$

The mean P_{app} values were taken from the transport experiments in absorptive direction (A→B).

Suppl. Table A. Comparison of inhibition ratio with 0.01 % TPGS (66 µM).

Substance	Classical static setup	Dynamic setup
Furosemide	1.62	0.94
Rhodamine 123	1.71	Not tested
Domperidone	1.65	1.43
Domperidone maleate	3.11	1.54
Talinolol	2.04	1.34

5.8 Label-free In Vitro Visualization of Particle Uptake into Human Oral Buccal Epithelial Cells by Confocal Raman Microscopy

Label-free In Vitro Visualization of Particle Uptake into Human Oral Buccal Epithelial Cells by Confocal Raman Microscopy

B. Kann, B. J. Teubl, E. Roblegg, M. Windbergs

Analyst. **2014**;139:5069-5074.

DIO: 10.1039/c4an00371c

Analyst

COMMUNICATION

View Article Online
View Journal | View Issue

Cite this: *Analyst*, 2014, **139**, 5069

Received 21st February 2014
Accepted 6th August 2014

DOI: 10.1039/c4an00371c

www.rsc.org/analyst

Label-free *in vitro* visualization of particle uptake into human oral buccal epithelial cells by confocal Raman microscopy†

B. Kann,[a] B. J. Teubl,[ab] E. Roblegg[bc] and M. Windbergs*[ade]

In this study, we present confocal Raman microscopy for chemically selective analysis of a human buccal epithelial cell layer with a focus on label-free visualization of particle uptake into the cells. We demonstrate the suitability and benefit of this analytical technique in comparison to confocal fluorescence microscopy for three dimensional imaging of *in vitro* cell models.

The uptake of small particles into the human body has become of major interest in various areas of research. This trend is not only due to the increasing attempt to develop novel nano-sized particulate therapeutics for targeted medical application of drugs. In addition, particles in the nano- and micrometer size range are to an increasing degree incorporated in various consumer products like tooth paste and cosmetics, and are also used as food additives.[1–7] Thus, profound scientific knowledge about the fate of such particles in the human body is mandatory to estimate absorption and potential toxicological effects.

In this context, titanium dioxide (TiO_2), a white, inorganic, crystalline compound plays an important role, as this substance is frequently used as white pigment in paint and plastic, sunscreen, tablets, chewing gum and as food additive.[1,8] Due to the prevalent use of TiO_2, the Organization for Economic Co-operation and Development (OECD) listed TiO_2 as priority nanomaterial to analyze the fate upon contact with the human body.[9]

Most products containing TiO_2 are regularly or spuriously taken up *via* the oral route. Consequently, the buccal mucosa is the first site of contact, where these particles may be absorbed into the human body. Thus, studying the interaction of TiO_2 particles with this biological barrier is of high relevance.

Excised porcine buccal mucosa is a common system for *in vitro* studies simulating the human mucosa quite accurately.[10,11] However, due to limited tissue access, a cell culture-based model using a human oral epithelial cell line has successfully been established as an alternative *in vitro* system.[12–14] Furthermore, the suitability to study nanoparticle uptake into this buccal *in vitro* model has been demonstrated.[14] However, adequate analysis of such systems is challenging.

In this context, the combination of spectroscopic and microscopic techniques is a valuable analytical approach to investigate cells or tissue on the subcellular level as well as to analyze cellular internalization of particulate systems. In this field, fluorescence microscopy is currently the most applied spectroscopic technique. For selective fluorescence detection, the structure of interest is labeled with a selective marker molecule prior to investigation. However, these marker molecules are often prone to photobleaching, limiting the time span for fluorescence microscopy analysis. Furthermore, due to linkage of the marker substance to a compound of the particulate system or a cellular structure, the physicochemical properties of the sample molecule might be altered. Thus, the observed analytical results may not represent the native situation of the sample.

Recently, confocal Raman microscopy has gained increasing impact as an alternative analytical method for biomedical imaging[15–18] and specific cellular investigations[19,20] including uptake studies of diverse particulate systems.[21–26] For confocal Raman microscopy, the sample is irradiated with laser light. The frequency shift between incident and scattered light due to the interaction of photons and sample molecules is detected. Thus, non-destructive component identification within a sample can be performed by detecting the individual Raman scattering patterns serving as a molecular fingerprint.

[a]*Saarland University, Department of Biopharmaceutics and Pharmaceutical Technology, Campus A4.1, 66123 Saarbruecken, Germany. E-mail: m.windbergs@mx.uni-saarland.de*

[b]*University of Graz, Institute of Pharmaceutical Sciences, Department of Pharmaceutical Technology, Humboldtstrasse 46, 8010 Graz, Austria*

[c]*Research Center Pharmaceutical Engineering GmbH, Inffeldgasse 13, 8010 Graz, Austria*

[d]*Helmholtz Centre for Infection Research and Helmholtz-Institute for Pharmaceutical Research Saarland, Department of Drug Delivery, Campus A4.1, 66123 Saarbruecken, Germany*

[e]*PharmBioTec GmbH, Department of Drug Delivery, Campus C2.2, 66123 Saarbruecken, Germany*

† Electronic supplementary information (ESI) available. See DOI: 10.1039/c4an00371c

Consequently, the technique operates label-free and chemically selective, thus providing a promising and complimentary alternative to confocal fluorescence microscopy.

In this study, we present a non-destructive analysis of TiO_2 particles interacting with oral buccal epithelium by confocal Raman microscopy. First, we image an oral buccal epithelial cell layer discriminating cell nucleus from cell body based on the chemically selective Raman spectra of the different cellular structures. Raman microscopy images are compared to fluorescence microscopy images. In subsequent experiments, the uptake of well-characterized TiO_2 particles into oral buccal cells is visualized by confocal Raman microscopy exploiting all three spatial dimensions. Lateral images are acquired for particle localization within the cell layer, whereas vertical cross section images prove particle internalization.

For profound, label-free analysis of TiO_2 particle internalization into buccal epithelial cells by confocal Raman microscopy, a sophisticated spectroscopic investigation of the cells is initially required. Here, scattering patterns of diverse molecular structures deriving from the individual chemical composition of different cellular compartments are identified, which will later allow not only for potential internalization studies but also for TiO_2 localization within the cells. This analytical capability can be of high importance as the potential invasion of TiO_2 into cellular compartments such as the nucleus might be a concern regarding genotoxicity.

For this study, oral epithelial TR146 cells (Imperial Cancer Research Technology, London, UK) were grown in DMEM with supplements of 10% FBS, 200 μM L-glutamine, 100 IU ml^{-1} penicillin and 100 μg ml^{-1} streptomycin maintaining standard culture conditions. Sub-cultivation was performed weekly with 0.25% trypsin–EDTA. Passages 9–20 were used for experiments.

Single Raman spectra recorded from cell nucleus (blue) and cell body (red) of the buccal epithelial cells are depicted in Fig. 1A. Despite the different origin within the cell, both spectra show a dominant peak between 2800–3020 cm^{-1}. This peak represents the prominent CH-stretch vibrations,[19] which are consistent in the respective Raman spectra throughout cellular investigations, as these molecular bonds are dominant in biological samples. The spectral region between 500–1800 cm^{-1} is generally termed as the fingerprint region, as it comprises outstanding peaks, which allow the recognition of different molecular structures. Fig. 1B depicts the Raman spectra of cell body (red) and nucleus (blue) acquired in the fingerprint region. The cell nucleus representing a major compartment is a DNA rich region, where especially phosphate groups of the DNA backbone contribute to a strong scattering activity. The respective outstanding peaks at 785, 1095 and 1575 cm^{-1} are highlighted in Fig. 1B. They derive from ring breathing modes of pyrimidine bases as well as from the symmetric stretching modes of phosphate esters in DNA[19,27] allowing spectral discrimination of the nucleus from the remaining cell body based on Raman analysis. As the focus of this study is to investigate the internalization of titanium dioxide nanoparticles and their localization to the cell nucleus, compartments other than nucleus and cytoplasm are neglected.

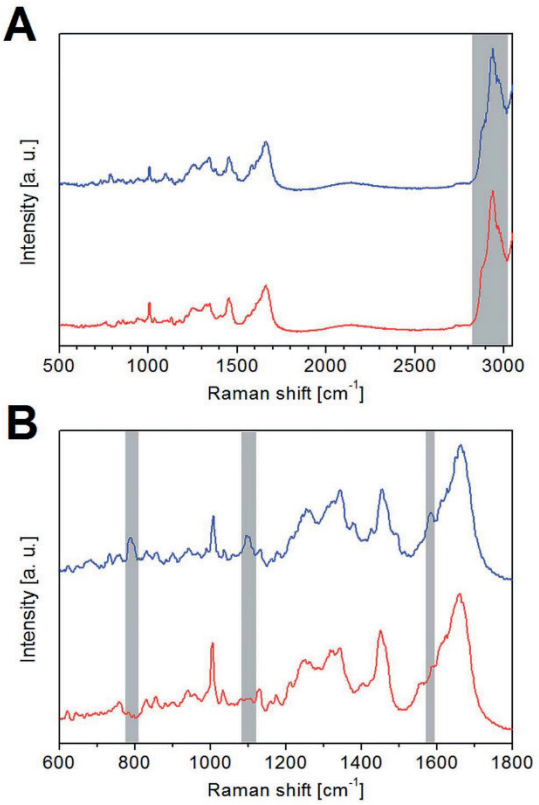

Fig. 1 Raman spectra from cell nucleus (blue) and cell body (red). (A) Overview spectra covering the entire spectral bandwidth. (B) Spectra from the fingerprint region with highlighted areas for outstanding DNA specific peaks in the nucleus spectrum.

However, literature shows that confocal Raman microscopy is suited to visualize multiple other cellular compartments.[19,20,28]

For general and quick evaluation of cultured cells with respect to morphology and confluence levels, light microscopy is the standard visualization technique used in daily cell culture lab work (Fig. 2A). However, this visual examination is only based on personal subjective observations, and therefore not suited for specified investigations.

To evaluate the potential of confocal Raman microscopy as a suitable complimentary analytical technique for cellular visualization, we performed an equally structured study with confocal fluorescence microscopy representing the current state-of-the-art technique in this field. Here, specific marker substances are used to label and consequently visualize the cellular structures of interest. Fig. 2B shows fluorescence microscopy images of a buccal epithelial cell layer (TR146) used in this study. Images were acquired with a LSM510 Meta confocal laser scanning microscope (Zeiss, Germany) through a Zeiss objective (63× magnification) with 405/BP 420–480 for the blue channel and BP 525/50 nm band pass detection for the green channel. For visual discrimination, nuclei of living cells

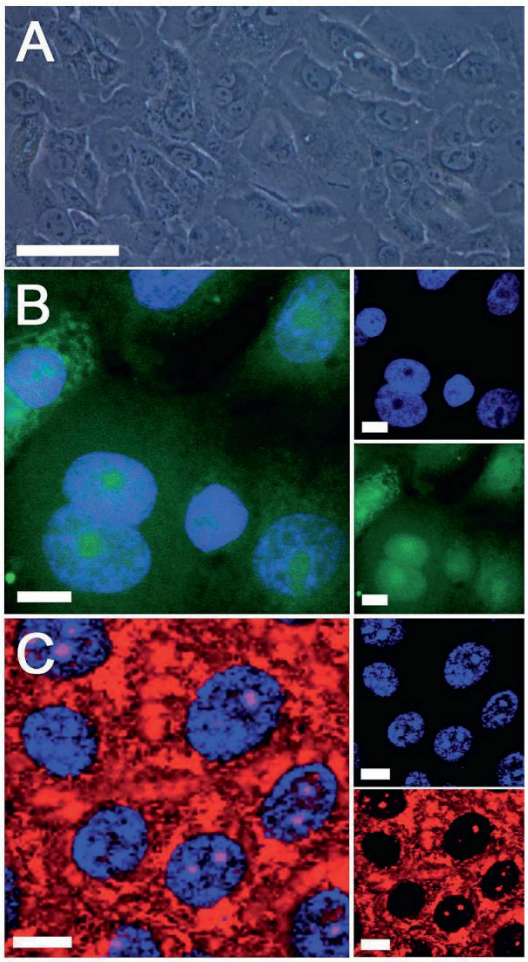

Fig. 2 Microscopic images of a buccal epithelial cell layer. (A) Light microscopy image. (B) Confocal fluorescence microscopy images showing nuclei in blue and cell bodies in green. The large panel depicts the merged image and the small panels the channel separated images. (C) Confocal Raman microscopy images visualizing nuclei in blue and cell bodies in red. The large panel shows the combined image, whereas the small panels depict the split images for each Raman signal. Scale bars are sized to 10 μm.

were stained with Hoechst 33342 (Invitrogen, Austria; 1 μg ml^{-1}), whereas the cytoplasm was stained using Calcein AM (Invitrogen, Austria; 2.5 μg ml^{-1}). Both structures are displayed in a merged fluorescence image (Fig. 2B, large panel) as well as in separate images (Fig. 2B, small panels), one showing cell nuclei (blue) the other depicting cell bodies (green). Although confocal fluorescence microscopy is successfully applied for cellular investigations, it bears several limitations. Linking marker substances to cellular structures and external particles might alter the native behavior upon interaction[29] and thus, lead to misinterpretation of analytical results. In addition, improper linkage entails loose marker molecules diffusing uncontrolled in the sample falsifying any analysis. Furthermore, the number of structures which can be visualized simultaneously is dependent on the microscopic setup, as each marker has to be irradiated by its specific absorption wavelength. Moreover, the time span for fluorescence microscopy analysis is in many cases limited, as the marker molecules are often prone to photobleaching. This results in a decrease of signal intensity or even a loss of signal as the capability of light emission of the marker molecule is destroyed over time.

In contrast, confocal Raman microscopy is a suitable complimentary technique offering the advantageous combination of label-free, chemically selective and spatially resolved analysis. Thus potential limitations of fluorescence microscopy can be overcome, as the technique solely probes molecular vibrations of inherent chemical structures of the sample which do not change in their intensity with time. According to fluorescence microscopy analysis, we imaged a TR146 cell layer by confocal Raman microscopy (alpha 300R+, WITec GmbH, Ulm, Germany) at an excitation wavelength of 532 nm (Nd:YAG laser operated at 30 mW before the objective). Raman spectra were collected through a Zeiss objective (63× magnification, NA = 1.0) at an integration time of 0.5 s. Image resolution was 0.5 μm × 0.5 μm.

The acquired spectral data set was background corrected and cosmic spikes were removed (software WITec Project Plus, WITec GmbH, Germany). Subsequently, the spectral data set was clustered. Here, each spectrum of the data set was sorted into one cluster according to the highlighted peaks of DNA and CH-vibrations in Fig. 1. Each cluster was allotted to a different colour and converted into a false colour Raman image (Fig. 2C). Image pixels assigned to Raman spectra of the cellular body are shown in red colour, whereas spectra acquired from the cell nuclei are depicted in blue image pixels. Based on the results of the cluster analysis, each component (nuclei and cell body) is depicted in a single Raman image (Fig. 2C, small panels), which can be overlaid for a combined visualization (Fig. 2C, large panel). Thus, despite the different procedures to generate microscopic images, the presentation of analytical results does not differ between confocal fluorescence and Raman microscopy proving the latter as a valuable technique for cellular investigations.

After successful label-free visualization of the model buccal epithelium, we performed confocal Raman microscopy to study the internalization of NM100 TiO_2 particles (TIONA) by buccal TR146 cells. Prior to uptake studies, TiO_2 particles dispersed in HBSS (10 μg ml^{-1}) were characterized. Hydrodynamic size, polydispersity index (PdI) and aggregation index (AI) were measured by photon correlation spectroscopy (Malvern ZetasizerNano ZSP, Malvern Instruments, UK) at a detection angle of 173°. The zeta potential was determined by laser Doppler velocimetry (scattering angle of 17°) coupled with photon correlation spectroscopy (Zetasizer SP, Malvern Instruments, Malvern, UK). The dispersed particles show a mean hydrodynamic size of 416.2 ± 50.65 nm and a zeta potential of −6.61 ± 2.27 mV, respectively. Furthermore, a PdI of 0.158 ± 0.059 and an aggregation index of −0.179 were measured. Consequently, as the PdI value is low, the TiO_2 particles form a stable suspension. Particles tend to form small

aggregates as the hydrodynamic size deviates from the nominated particle size of 125 nm. However, aggregates are uniform with smooth outer surface indicated by the low AI. These findings are in good agreement with electron microscopy studies performed on the TiO_2/HBSS dispersion (10 μg ml^{-1}) dried on a silicon wafer and sputter coated with gold. Images were taken with a Zeiss EVO HD15 electron microscope (Zeiss, Germany) at an accelerating voltage of 5 kV. Fig. 3A shows single TiO_2 particles as well as small aggregates within the size range nominated by PdI values.

Titanium dioxide exists in three polymorphs namely anatase, rutile, and brookite.[8,30] The NM100 TiO_2 (TIONA) particles are claimed to be anatase. To confirm this, we acquired a Raman spectrum of the raw material (ESI†). The identified Raman peaks at 146, 198, 398, 519, and 642 cm^{-1} are in good agreement with the peak positions for the Raman active modes of TiO_2 anatase crystals found in literature 144, 197, 639 cm^{-1} (all E_g), 399 cm^{-1} (B_{1g}) and 515 cm^{-1} (B_{1g} and A_{1g})[30–32] considering a resolution of 4 cm^{-1} of our spectrometer. Thus, the polymorphic form of TIONA particles used in our study is anatase.

The diverse spectral patterns of different cellular compartments facilitate not only the visualization of cells in detail by confocal Raman microscopy, but also revealing potential compartment specific internalization of particles in the cell. As tracing of particle uptake is based on spectral discrimination of the individual components, we first compared the single Raman spectra of the buccal cells and the TiO_2 model particles. Fig. 3B depicts the respective Raman spectra. The TiO_2 spectrum shows three outstanding peaks at 398, 519 and 642 cm^{-1} in the lower wavenumber region, whereas prominent peaks from cellular spectra are visible at higher wavenumbers (500–1800 cm^{-1}). Thus, spectral discrimination and consequently particle tracing is feasible by using the peak at 642 cm^{-1} for TiO_2 (Fig. 3B).

For particle uptake studies, TR146 cell layers were incubated with NM 100 TiO_2 (TIONA) particle suspension (10 μg ml^{-1} in HBSS) prior to Raman analysis. After 4 hours, residual particles were removed in three washing steps. Subsequently, samples were fixed and placed on the scan stage of the confocal microscope for Raman spectra acquisition. At first, Raman spectra from the lateral plane (*xy*) were recorded. The spectral data sets were background subtracted. Subsequently, cluster analysis was performed using the peaks at 642 cm^{-1} as well as the peaks at 785, 1095 and 1575 cm^{-1} to differentiate TiO_2 and cell nucleus from the cell body spectra. The resulting lateral image in Fig. 4A shows the location of TiO_2 particle agglomerates (yellow) on the cells. However, lateral images do not differentiate surface attached and internalized particles as they were only recorded

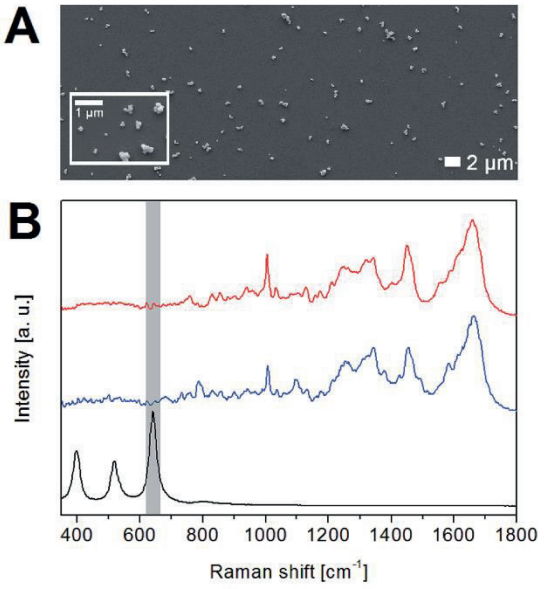

Fig. 3 (A) Electron microscopy image of TiO_2 particles. (B) Raman spectra of cellular compartments (red: cell body; blue: nucleus) and TiO_2 particles (black). The highlighted peak represents the peak used for TiO_2 identification.

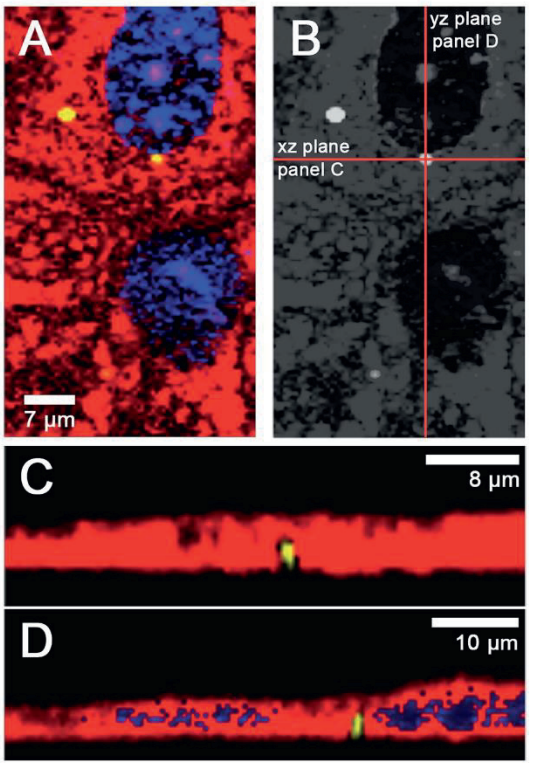

Fig. 4 Particle internalization study by confocal Raman microscopy. (A) Lateral false colour image showing the position of agglomerated TiO_2 particles (yellow) on the cell layer (nuclei in blue, cell body in red). (B) Decolourized panel A with red lines representing vertical planes for Raman microscopy analysis to discriminate between particle adhesion and internalization. (C) and (D) Raman microscopy cross section images showing internalized TiO_2 particles from the *xz*-plane (C) as well as from the *yz*-plane (D).

in one horizontal focal plane. Therefore, to prove internalization, additional cross section images are required.

Confocal Raman microscopy allows spectral acquisition in vertical as well as in horizontal planes. Thus, cross section images of cells can be acquired by virtually cutting through the cell. In Fig. 4B, the location of virtual planes exemplarily cutting the cell layer in vertical directions for Raman analysis is marked. Due to the non-destructive working principle of the analytical technique, the sample is investigated in its fixed state. As neither particles nor cellular compartments are labelled, interactions of TR146 cells with model TiO_2 particles are not altered and analytical results represent the actual native condition of the system. The acquired Raman spectra from vertical planes in *xz*- as well as in *yz*-direction, encompassing the localized TiO_2 particle, were converted into false colour Raman images. Both cross section images prove the cellular internalized TiO_2 as visualized in Fig. 4C (*xz*) and Fig. 4D (*yz*). Thus, oral buccal epithelia cells take up TiO_2 particles within 4 hours. With virtual cross sectioning, it can be differentiated between adhesion and internalization, not only with regards to the entire cell, but also within endogeneous cell compartments.

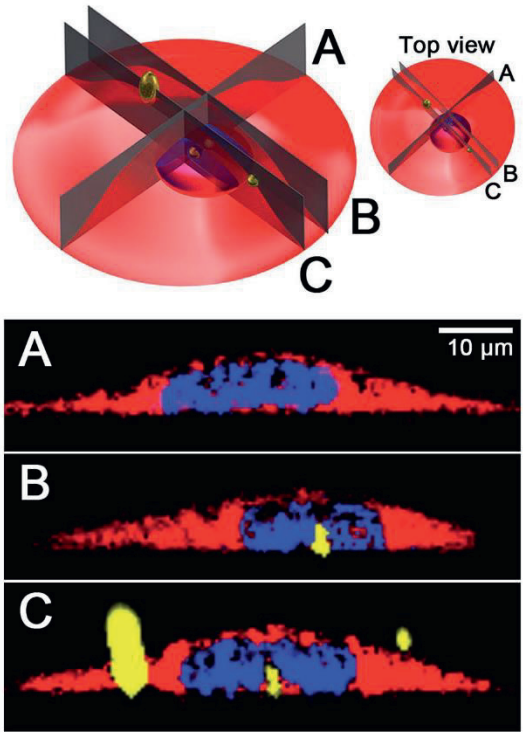

Fig. 5 Three dimensional sketch of a cell showing different particle engulfment states. Virtual vertical planes locating the area for confocal Raman microscopy are indicated. (A) Raman image showing a vertical plane set off target. (B) Raman image depicting a nucleus engulfed particle. (C) False colour cross section image visualizing multiple locations of particles on the cell. Cell bodies are shown in red, nuclei in blue and TiO_2 in yellow.

Therefore, label-free imaging in vertical planes with confocal Raman microscopy is beneficial for non-destructive observation of compartment specific particle internalization. Especially, particle invasion into the cell nucleus is of high interest, as this effect could potentially initiate genotoxic effects *in vivo*.

In this study, multiple areas of at least three incubated different cell layers were investigated. In all analyzed samples, various locations of internalized TiO_2 within cells were determined, even the enclosure of TIONA particles into the nucleus as a distinct cellular compartment was detected. Here, the gain of non-destructive cross section Raman imaging becomes evident. A three dimensional cell sketch depicting particles in different engulfment states is shown in Fig. 5, revealing that the selection of the right analysis plane is of high importance. The individual virtual section planes *A*, *B* and *C* represent different positions to localize particles as shown in their respective Raman images in the lower panel A, B and C. Fig. 5A solely depicts cell body and nucleus, whereas in the appropriate vertical plane particles can be localized within the nucleus due to spectral discrimination (Fig. 5B). Even cell adhesive and nucleus ingested particles can simultaneously be displayed in one image (Fig. 5C). However, to state and prove possible effects such as genotoxic consequences of the TiO_2 invasion into the nucleus, a subsequent, profound analysis on the molecular level and *in vivo* studies have to follow.

Conclusions

In this study, we successfully performed confocal Raman microscopy to image buccal epithelial cells on a subcellular level by discriminating between spectral differences of cell body and nucleus. The false colour Raman images were compared with fluorescence microscopy images. Coinciding analytical results prove confocal Raman microscopy to be a suitable complimentary label-free technique.

Furthermore, the internalization of TiO_2 particles into oral buccal epithelial cells was visualized in lateral images as well as in virtual cross section images. Here, analysis benefits from the chemically selective operating principle of confocal Raman microscopy as the samples are not altered for investigation. Based on non-destructive cross sectional imaging, differentiation between particle adhesion and internalization is enabled. Additionally, particle invasion into the cell nucleus was visualized. Thus, confocal Raman spectroscopy shows a high potential as a valuable method to follow selective particle uptake into endogenous cell compartments as the nucleus.

Overall, further studies of epithelial cell culture models and particle interaction can benefit from three dimensional confocal Raman microscopy analyses, circumventing the necessity of laborious sample preparation without losing analytical accuracy.

Acknowledgements

The authors thank C. Stiers for creating schematic graphs of the cell, B. Bauer for helping with the cell culture experiments and

and M. Absenger for the support in acquisition of confocal fluorescence microscopy images.

Notes and references

1 M. C. Lomer, R. P. Thompson, J. Commisso, C. L. Keen and J. J. Powell, *Analyst*, 2000, **125**, 2339–2343.
2 M. C. Lomer, C. Hutchinson, S. Volkert, S. M. Greenfield, A. Catterall, R. P. Thompson and J. J. Powell, *Br. J. Nutr.*, 2004, **92**, 947–955.
3 ICTA, *Petition to the United States Food and Drug Administration*, 2006.
4 A. T. Harris and R. Bali, *J. Nanopart. Res.*, 2008, **10**, 691–695.
5 F. Gottschalk, T. Sonderer, R. W. Scholz and B. Nowack, *Environ. Sci. Technol.*, 2009, **43**, 9216–9222.
6 D. P. K. Lankveld, A. G. Oomen, P. Krystek, A. Neigh, A. Troost de Jong, C. W. Noorlander, J. C. H. Van Eijkeren, R. E. Geertsma and W. H. De Jong, *Biomaterials*, 2010, **31**, 8350–8361.
7 J. J. Powell, N. Faria, E. Thomas-McKay and L. C. Pele, *J. Autoimmun.*, 2010, **34**, J226–J233.
8 E. Fröhlich, B. J. Teubl and E. Roblegg, *Bionanomater. Dent. Appl.*, 2013, **14**, 25–35.
9 OECD, in *Chemicals Testing Monographs No. 29*, 2011.
10 C. A. Lesch, C. A. Squier, A. Cruchley, D. M. Williams and P. Speight, *J. Dent. Res.*, 1989, **68**, 1345–1349.
11 H. Zhang and J. R. Robinson, in *Oral Mucosal Drug Delivery*, ed. M. J. Rathbone, Marcel Dekker, New York, 1996, pp. 51–63.
12 J. Jacobsen, B. Vandeurs, M. Pedersen and M. R. Rassing, *Int. J. Pharm.*, 1995, **125**, 165–184.
13 E. Roblegg, E. Frohlich, C. Meindl, B. Teubl, M. Zaversky and A. Zimmer, *Nanotoxicology*, 2012, **6**, 399–413.
14 B. J. Teubl, M. Absenger, E. Fröhlich, G. Leitinger, A. Zimmer and E. Roblegg, *Eur. J. Pharm. Biopharm.*, 2013, **84**, 386–393.
15 A. Nijssen, T. C. B. Schut, F. Heule, P. J. Caspers, D. P. Hayes, M. H. A. Neumann and G. J. Puppels, *J. Invest. Dermatol.*, 2002, **119**, 64–69.
16 N. J. Crane, T. S. Brown, K. N. Evans, J. S. Hawksworth, S. Hussey, D. K. Tadaki and E. A. Elster, *Wound Repair Regen.*, 2010, **18**, 409–416.
17 B. Brozek-Pluska, J. Musial, R. Kordek, E. Bailo, T. Dieing and H. Abramczyk, *Analyst*, 2012, **137**, 3773–3780.
18 L. Mavarani, D. Petersen, S. F. El-Mashtoly, A. Mosig, A. Tannapfel, C. Koetting and K. Gerwert, *Analyst*, 2013, **138**, 4035–4039.
19 C. Matthaus, T. Chernenko, J. A. Newmark, C. M. Warner and M. Diem, *Biophys. J.*, 2007, **93**, 668–673.
20 K. Meister, D. A. Schmidt, E. Brundermann and M. Havenith, *Analyst*, 2010, **135**, 1370–1374.
21 A. A. van Apeldoorn, H. J. van Manen, J. M. Bezemer, J. D. de Bruijn, C. A. van Blitterswijk and C. Otto, *J. Am. Chem. Soc.*, 2004, **126**, 13226–13227.
22 C. Matthaeus, A. Kale, T. Chernenko, V. Torchilin and M. Diem, *Mol. Pharmaceutics*, 2008, **5**, 287–293.
23 T. Chernenko, C. Matthaus, L. Milane, L. Quintero, M. Amiji and M. Diem, *ACS Nano*, 2009, **3**, 3552–3559.
24 K. Meister, J. Niesel, U. Schatzschneider, N. Metzler-Nolte, D. A. Schmidt and M. Havenith, *Angew. Chem., Int. Ed.*, 2010, **49**, 3310–3312.
25 T. Chernenko, R. R. Sawant, M. Miljkovic, L. Quintero, M. Diem and V. Torchilin, *Mol. Pharmaceutics*, 2012, **9**, 930–936.
26 C. Matthäus, S. Schubert, M. Schmitt, C. Krafft, B. Dietzek, U. S. Schubert and J. Popp, *ChemPhysChem*, 2013, **14**, 155–161.
27 M. Diem, C. Matthäus, T. Chernenko, M. J. Romeo, M. Milkovic, B. Bird, J. Schubert, K. Papamarkakis and N. Laver, in *Infrared and Raman Spectroscopy Imaging*, ed. R. Salzer and H. W. Siesler, Wiley-VCH, Weinheim, 1st edn, 2009, ch. 5, pp. 173–201.
28 C. Krafft, T. Knetschke, R. H. W. Funk and R. Salzer, *Anal. Chem.*, 2006, **78**, 4424–4429.
29 K. T. Thurn, T. Paunesku, A. Wu, E. M. B. Brown, B. Lai, S. Vogt, J. Maser, M. Aslam, V. Dravid, R. Bergan and G. E. Woloschak, *Small*, 2009, **5**, 1318–1325.
30 T. Ohsaka, F. Izumi and Y. Fujiki, *J. Raman Spectrosc.*, 1978, **7**, 321–324.
31 V. Swamy, A. Kuznetsov, L. S. Dubrovinsky, R. A. Caruso, D. G. Shchukin and B. C. Muddle, *Phys. Rev. B: Condens. Matter Mater. Phys.*, 2005, **71**, 184302.
32 J. Surmacki, P. Wronski, M. Szadkowska-Nicze and H. Abramczyk, *Chem. Phys. Lett.*, 2013, **566**, 54–59.

Electronic Supplementary Material (ESI) for Analyst.

Supplemental material

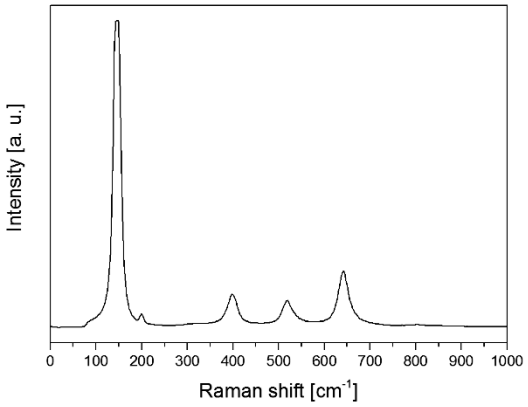

Suppl. Figure. Raman spectrum of titanium dioxide NM100 (TIONA) raw material.

5.9 Intracellular Delivery of Poorly Soluble Polyphenols - Elucidating the Interplay of Self-Assembling Nanocarriers and Human Chondrocytes

Intracellular Delivery of Poorly Soluble Polyphenols - Elucidating the Interplay of Self-Assembling Nanocarriers and Human Chondrocytes

B. Kann, C. Spengler, K. Coradini, L. A. Rigo, M. L. Bennink, K. Jacobs, H. L. Offerhaus, R. C. R. Beck, M. Windbergs

Anal. Chem. **2016**;88:7014-7022.

DOI: 10.1021/acs.analchem.6b00199

analytical chemistry

Article

pubs.acs.org/ac

Intracellular Delivery of Poorly Soluble Polyphenols: Elucidating the Interplay of Self-Assembling Nanocarriers and Human Chondrocytes

Birthe Kann,[†,‡] Christian Spengler,[§] Karine Coradini,[∥] Lucas A. Rigo,[∥] Martin L. Bennink,[⊥] Karin Jacobs,[§] Herman L. Offerhaus,[‡] Ruy C. R. Beck,[∥] and Maike Windbergs*[,†,#,▽]

[†]Saarland University, Department of Biopharmaceutics and Pharmaceutical Technology, Campus A4.1, 66123 Saarbruecken, Germany

[‡]University of Twente, Optical Sciences Group, MESA+ Institute for Nanotechnology, P.O. Box 217, 7500 AE Enschede, The Netherlands

[§]Saarland University, Experimental Physics, Campus E2.9, 66123 Saarbruecken, Germany

[∥]Programa de Pós-Graduação em Ciências Farmacêuticas, Faculdade de Farmácia, Federal University of Rio Grande do Sul (UFRGS), 90610-000, Porto Alegre, Rio Grande do Sul, Brazil

[⊥]University of Twente, Nanobiophysics Group, MESA+ Institute for Nanotechnology, P.O. Box 217, 7500 AE Enschede, The Netherlands

[#]Helmholtz Centre for Infection Research and Helmholtz Institute for Pharmaceutical Research Saarland, Department of Drug Delivery, Campus E 8.1, 66123 Saarbruecken, Germany

[▽]PharmBioTec GmbH, Department of Drug Delivery, Science Park 1, 66123 Saarbruecken, Germany

ABSTRACT: Increased molecular understanding of multifactorial diseases paves the way for novel therapeutic approaches requiring sophisticated carriers for intracellular delivery of actives. We designed and characterized self-assembling lipid-core nanocapsules for coencapsulation of two poorly soluble natural polyphenols curcumin and resveratrol. The polyphenols were identified as high-potential therapeutic candidates intervening in the intracellular inflammation cascade of chondrocytes during the progress of osteoarthritis. To elucidate the interplay between chondrocytes and nanocapsules and their therapeutic effect, we pursued a complementary analytical approach combining label-free visualization with biological assays. Primary human chondrocytes did not show any adverse effects upon nanocapsule application and coherent anti-Stokes Raman scattering images visualized their intracellular uptake. Further, by systematically blocking different uptake mechanisms, an energy independent uptake into the cells could be identified. Additionally, we tested the therapeutic effect of the polyphenol-loaded carriers on inflamed chondrocytes. Treatment with nanocapsules resulted in a major reduction of nitric oxide levels, a well-known apoptosis trigger during the course of osteoarthritis. For a more profound examination of this protective effect on joint cells, we pursued studies with atomic force microscopy investigations. Significant changes in the cell cytoskeleton as well as prominent dents in the cell membrane upon induced apoptosis were revealed. Interestingly, these effects could not be detected for chondrocytes which were pretreated with the nanocapsules. Overall, besides presenting a sophisticated carrier system for joint application, these results highlight the necessity of establishing combinatorial analytical approaches to elucidate cellular uptake, the interplay of codelivered drugs and their therapeutic effect on the subcellular level.

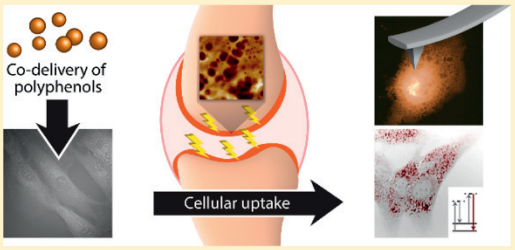

Because of a continuously growing understanding of origination and course of complex diseases on a molecular level, there is a high demand for sophisticated carrier systems allowing for intracellular delivery of active pharmaceutical ingredients (API) and thus treatment of such diseases on a subcellular level.

One example in this context is osteoarthritis, a multifactorial degenerative joint disease with a severe impact on life quality especially for the elderly population.[1] During the course of the disease, the chondrocytes within the cartilage tissue are inflamed, subsequently resulting in a breakdown of the connective tissue in the affected joint.[2−5] Despite this knowledge, osteoarthritis is generally treated symptomatically using nonsteroidal, anti-inflammatory drugs limited to temporary effects without complete curing.[6,7] Recently, natural polyphenols gained considerable interest as therapeutic alternatives due to their anti-inflammatory, antioxidant, and chemo preventive potential.[3,8−10] It was shown that curcumin (diferuloylmethane) and resveratrol (*trans*-3,4′-trihydroxystilbene) have a protective effect on chondrocytes by modulating

Received: January 16, 2016
Accepted: June 22, 2016
Published: June 22, 2016

DOI: 10.1021/acs.analchem.6b00199
Anal. Chem. 2016, 88, 7014−7022

the intracellular inflammation cascade.[6,11−13] Interestingly, this effect could even synergistically be increased by combining different polyphenols.[6,12] However, because of their low water solubility, the polyphenols were dissolved in organic solvents before application to cultivated chondrocytes.[6,11,14,15] Such organic solvents do not only artificially increase the solubility of the polyphenols but also increase the permeability of the chondrocytes. Thereby, the extent of intracellular uptake of the actives is artificially facilitated and increased which is not reflecting the *in vivo* situation in a human joint. To overcome these issues, we designed a delivery system for codelivery of resveratrol and curcumin based on self-assembling lipid-core nanocapsules (LNC) consisting of an oily core surrounded by a biocompatible and biodegradable shell of polycaprolactone (PCL).[16,17] These capsules provide protection and solubility enhancement for the lipophilic actives as well as a controlled release pattern.[18−20] Furthermore, a first study in a rat model of osteoarthritis showed promising results for LNC loaded with the polyphenols as a novel therapeutic approach.[21]

However, for in-depth understanding of such a novel approach for codelivery of two polyphenols, sophisticated analytics are required to elucidate cellular uptake and response. In terms of visualizing biological structures, research benefits from progress in microscopic techniques, especially in confocal laser scanning fluorescence microscopy for cell imaging. However, the technique requires biomarkers and these can cause misinterpretation of analytical results.[22,23] In addition to visualization, the analysis of cellular biomechanics upon drug application is important as inflammatory processes in osteoarthritic chondrocytes entail changes in their cell biomechanics and consequently their membrane structure.

In this study, we performed a multidisciplinary approach to bridge the aforementioned scientific gaps. We encapsulated resveratrol and curcumin in lipid-core nanocapsules and investigated their interactions with human primary chondrocytes. Further analysis focused on their therapeutic effects on the chondrocytes treated with a chemical NO-donor to induce apoptosis, thereby mimicking the conditions of diseased cells in osteoarthritic joints. To gain new insights, noninvasive and label-free coherent anti-Stokes Raman scattering (CARS) microscopy was used for visualization of interactions with chondrocytes and intracellular location of the capsules after uptake. Further, the cellular uptake process was elucidated by selective blocking of individual endocytosis pathways and subsequent CARS analysis. In addition, the therapeutic effect of the nanocapsules on chondrocytes was analyzed by a combination of bioassays and atomic force microscopy (AFM) to probe cellular nanobiomechanics and membrane structure as well as to investigate changes upon diseased state and therapeutic effects of the nanocapsules on human chondrocytes.

EXPERIMENTAL SECTION

Materials. Curcumin, poly(ε-caprolactone), sorbitan monostearate, 5-(*N*-ethyl-*N*-isopropyl) amiloride (ENIA), monensin sodium, chlorpromazine HCl, nystatin, sodium nitroprusside dehydrate (SNP), and methylthiazolyldiphenyl-tetrazolium bromide (MTT) as well as analytical solvents were purchased from Sigma-Aldrich. Grape seed oil was obtained from Delaware (Porto Alegre, Brazil). Resveratrol was supplied by Pharma Nostra (Anápolis, Brazil), and polysorbate 80 was acquired from Henrifarma (São Paulo, Brazil). All chemicals and solvents were of pharmaceutical or HPLC grade and were used as received.

Preparation of Lipid-Core Nanocapsules. The protocol for LNC preparation was established by Jornada et al.[20] In brief, 27 mL of acetone including dissolved PCL (0.1 g), grape seed oil (165 μL) and sorbitan monostearate (0.0385 g) were injected into the aqueous phase (water 54 mL) containing polysorbate 80 (0.077g) under magnetic stirring at room temperature. Curcumin and/or resveratrol (5 or 2.5 mg) were part of the organic phase. Subsequently, acetone was eliminated under reduced pressure and the suspension was concentrated to a final volume of 10 mL. LNC containing 0.5 mg/mL of resveratrol (R-LNC) and curcumin (C-LNC) individually and in combination (Co-LNC) as well as polyphenol free nanocapsules were prepared. To investigate a possible dose dependent effect, LNC with 0.25 mg/mL of curcumin and resveratrol were fabricated additionally. For cell culture experiments a 50-fold dilution of LNC suspensions was used.

Characterization of Lipid-Core Nanocapsules. Physicochemical characteristics were acquired by photon correlation spectroscopy at a scattering angle of 173 °C for hydrodynamic size and polydispersity index (PdI) measurements and coupled with laser Doppler velocimetry to determine the zeta potential (Zetasizer Nano ZSP/SP, Malvern instruments, Malvern, U.K.). LNC suspensions were diluted in Milli-Q water (1/50) prior to measurements. The pH-value was directly determined from the LNC suspension using a calibrated potentiometer (VB-10, Denver Instrument Company, Colorado). Morphological characteristics were visualized by transmission electron microscopy (TEM) (JEM 2010, Tokyo, Japan). LNC suspensions, diluted in ultrapure water (200-fold) were placed on a specimen grid and counterstained with phosphotungstic acid hydrate (1% w/v). The microscope was operated at 200 kV. The *in vitro* release of resveratrol and curcumin from LNC was carried out by the dialysis bag method according to Coradini et al.[24] with minor modifications. A volume of 0.8 mL of the samples (Co-LNC, R-LNC, and C-LNC) were placed into a dialysis bag with a 10 kDa molecular weight cutoff and suspended into 80 mL of release medium (water/Tween 80/ethanol (80:2:20 v/v)). The samples ($n = 3$) were maintained at 37 °C under gentle agitation. At predetermined time intervals, 1 mL of release medium was withdrawn and replaced with fresh medium. The samples were diluted with mobile phase, filtered through a 0.45 μm membrane, and analyzed by the previously described HPLC method.[24]

Cell Culture Experiments. Human primary chondrocytes were purchased from PromoCell (Heidelberg, Germany) and cultured in chondrocyte growth medium (PromoCell) which was supplemented with 10% (v/v) fetal calf serum in an atmosphere of 5% CO_2 at 37 °C. During routinely performed subcultivation cells were seeded at a density of 20 000 cells/cm^2. Passages 9−11 were used for experiments.

CARS Microscopy. Chondrocytes were cultured in imaging dishes with a cover class insert in tissue culture quality. Preincubation with uptake inhibitors (5 μg/mL chlorpromazine, monensin, nystatin, ENIA) was done for 1 h prior to adding polyphenol-loaded LNC. To investigate energy dependent uptake, cells were moved to the refrigerator at 4 °C for LNC incubation. After 7 h in total the medium was replaced and dishes were moved onto the stage of the custom built CARS microscope, which is described in detail elsewhere.[25] The picosecond pulsed laser, which is coupled to the setup,

DOI: 10.1021/acs.analchem.6b00199
Anal. Chem. 2016, 88, 7014−7022

Table 1. Physicochemical Characteristics of Lipid-Core Nanocapsules in Aqueous Suspension and after 24 h Incubation in Cell Culture Medium (Mean Value ± SD, n = 3)

	in aqueous suspension			after 24 h in cell culture medium		
formulation	size (nm)	PdI	zeta potential (mV)	size (nm)	PdI	zeta potential (mV)
unloaded LNC	201.90 ± 1.95	0.077 ± 0.004	−22.43 ± 0.60	222.27 ± 1.67	0.159 ± 0.025	−4.40 ± 0.85
R-LNC	211.73 ± 1.65	0.093 ± 0.028	−21.73 ± 0.35	217.10 ± 1.65	0.140 ± 0.008	−5.73 ± 1.13
C-LNC	205.70 ± 1.04	0.077 ± 0.030	−22.17 ± 0.23	218.93 ± 1.81	0.168 ± 0.020	−4.81 ± 0.94
Co-LNC (1 mg/mL)	199.73 ± 0.93	0.115 ± 0.017	−20.97 ± 0.55	204.27 ± 0.67	0.154 ± 0.016	−3.56 ± 0.21
Co-LNC (0.5 mg/mL)	201.67 ± 1.80	0.067 ± 0.008	−22.50 ± 0.36	208.53 ± 2.82	0.143 ± 0.001	−4.49 ± 0.73

operated at a fundamental wavelength of 1032 nm (aeroPULSE-10, NKT Photonics, Birkerød, Denmark). An Olympus 60× water immersion objective was used to record the images.

Nitric Oxide Release. Chondrocytes were seeded in 96 well plates (10 000 cell per well, p10/11). Incubation times for LNC and 2 mM SNP (297.95 g/mol; 11.88 mg in 20 mL of medium) were 24 h. Cells were preincubated with LNC before exchanging for SNP solution. The Griess Reagent System (Promega Corporation, Madison, WI) was used according to provided instructions. For each assay a nitrite standard reference curve (0.1 M−0 M) was prepared in triplicate. The absorption of the formed purple colored azo compound was measured at 535 nm (Infinite M200Pro, Tecan GmbH, Crailsheim, Germany). Statistical analysis was performed using the student's t-test ($p < 0.05$).

Cell Viability Testing. Cell viability was investigated by the MTT assay (n = 8). Cells cultured in 96 well plates (10 000 cells/well) were washed with HBSS buffer prior to incubation with SNP for 24 h at 37 °C. As a positive control, 1% Triton X in medium was used. Cells were washed with HBSS and 100 μL of medium with 10% MTT reagent was added to each well. After 4 h of incubation on the shaker at 37 °C, the medium was exchanged for DMSO. After 30 min, the absorption of the formed formazan was measured at 550 nm (duration 5 s; amplitude 3 nm; Infinite M200Pro).

Atomic Force Microscopy. Chondrocytes were cultured in Petri dishes (10 000 cells/dish) with a growth area of 8.7 cm^2. The incubation time for Co-LNC and 2 mM SNP was 24 h each, where SNP was only applied after removing the medium containing nanocapsules. Subsequently, cells were fixed in 3% formaldehyde and air-dried just before AFM investigations. AFM images were recorded in air on a Dimension Fastscan Bio (Bruker-Nano, Santa Barbara, CA) operated in a dynamic force interaction control mode (Peak Force QNM) with Nanoscope 9 software. Silicon nitride tips were used (spring constants of 0.06 N/m, SNL-D tips from Bruker-Nano) as cantilevers with loading forces of approximately 1 nN. The lateral resolution of the depicted (50 μm)^2 AFM images is 48.8 nm/pixel. In the case of the (5 μm)^2 scans, the lateral resolution is 9.8 nm/pixel. Cross sectioning and bearing analyses of the images were carried out using Nanoscope Analysis software.

■ RESULTS AND DISCUSSION

The first step of this study involved a physicochemical and morphological analysis of the lipid-core nanocapsules loaded with the two polyphenols as well as their drug release kinetics. Jornada et al.[20] already proved that the granulometry profile of such lipid-core nanocapsules fabricated by interfacial deposition of PCL correlates with the concentration of raw materials in the aqueous and in the organic phase, respectively. Lipid-core nanocapsules were either loaded with curcumin or with resveratrol (C-LNC, R-LNC, 0.5 mg polyphenol/mL) as well as with both polyphenols in combination (Co-LNC, 0.5 mg of each polyphenol/mL). For direct comparison between the effect of curcumin and resveratrol and their combination in terms of dose dependency and synergistic effects, an additional Co-LNC batch containing a total polyphenol dose of 0.5 mg/mL was included in the experiments. These Co-LNC (0.25 mg of each polyphenol/mL), which are introduced here for the first time, have a hydrodynamic diameter of 201.67 nm ±1.80 nm with a low size distribution (PdI 0.067 ± 0.008), a zeta potential of −22.50 mV ± 0.36 mV, and a pH value of 6.18 ± 0.21 in aqueous suspension. These physicochemical parameters are in good agreement with published data of C-LNC, R-LNC, and Co-LNC (0.5 mg/mL each), which have been investigated during the optimization of the LNC formulation for the encapsulation of the poorly water-soluble polyphenols.[24]

As hydrodynamic diameter, size distribution and zeta potential are important for evaluating the colloidal stability of LNC under cell culture conditions, these physicochemical characterization data for all generated nanocapsules in aqueous suspension are summarized in Table 1. As the comparison of unloaded capsules and capsules loaded with the different polyphenols proves, the fabrication process is well controlled and generates highly reproducible and physically stable nanocapsules. Drug loadings for lipid-core nanocapsules encapsulating resveratrol and/or curcumin are close to the theoretical value (R-LNC 0.49 mg/mL ± 0.01 mg/mL; C-LNC 0.49 mg/mL ± 0.02 mg/mL; Co-LNC 0.50 mg/mL ± 0.01 mg/mL (resveratrol); and 0.50 mg/mL ± 0.01 mg/mL (curcumin) as already published.[21,24,26] Consequently, the encapsulation efficiency is almost 100% for these formulations (R-LNC 98.00%; C-LNC 97.33%; Co-LNC 100.00% (resveratrol) and 99.33% (curcumin)). For this study, the physical stability of the lipid-core nanocapsules in cell culture medium is important to account for potential interactions with biomolecules in cell culture medium simulating the situation in the human body. The results of the physicochemical characterization of LNC after 24 h incubation in the medium at 37 °C are summarized in Table 1. All different LNC formulations are sized around 210 nm maintaining their narrow size range (PdI < 0.17) and a negative zeta potential. Low standard deviations suggest a homogeneous fraction of LNC despite different loadings. In comparison to LNC in aqueous suspension, the zeta potential decreases. The high values in aqueous suspension are potentially based on steric hindrances due to the presence of polysorbate 80 forming a micellar structure around the capsules.[27] In the presence of cell culture medium containing fetal calf serum among other nutritional supplements, this steric hindrance is most likely decreasing resulting in lower zeta potential values. Nevertheless, PdI values and standard deviations for investigated physicochemical characteristics remain as low as values obtained from LNC in aqueous

DOI: 10.1021/acs.analchem.6b00199
Anal. Chem. 2016, 88, 7014−7022

suspension. Thus, lipid-core nanocapsules retain their physicochemical characteristics in biorelevant media without agglomeration tendency which is frequently found for other nanocarriers.[28]

An expected round shape of the nanocapsules is confirmed by transmission electron microscopy images (Figure 1).

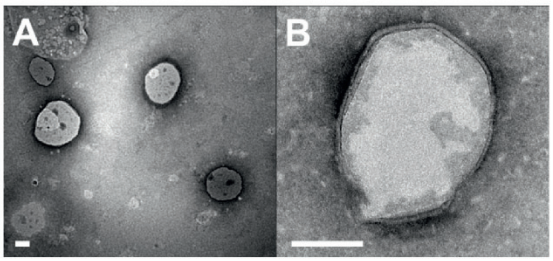

Figure 1. Representative transmission electron microscopy images showing LNC at a low magnification (10 000-fold) (A) and a close-up view showing the PCL wall (50 000-fold) (B). Scale bars denote 100 nm.

Additionally, the hydrodynamic size determined by photon correlation spectroscopy is in good agreement with the mean particle size observed during TEM analysis. The PCL wall of the nanocapsules surrounding the lipid core is homogeneous and has an estimated thickness of 8 nm.

Further, the release kinetics of the polyphenols from the nanocapsules were analyzed. The release of resveratrol (solid circle symbol) shows a steep slope which turns into a plateau phase after about 24 h, whereas curcumin (open circle symbol) release is much slower resulting in a continuous slope as depicted in Figure 2. Interestingly, neither coencapsulation of resveratrol and curcumin in the same capsules (dotted line versus straight line), nor the overall loading of the nanocapsules (0.5 mg/mL versus 1 mg/mL) does significantly change these kinetics.[24] However, a relationship between polyphenol solubility in grape seed oil, the main component of the capsule

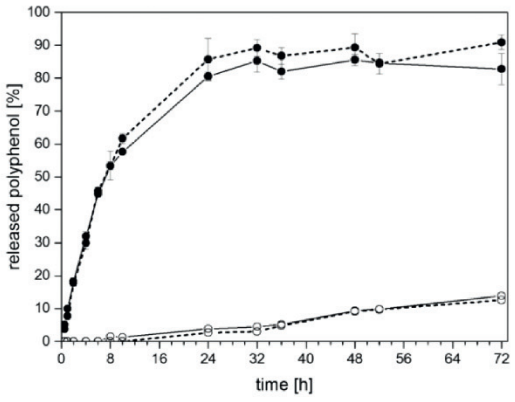

Figure 2. Drug release profiles of curcumin (○) and resveratrol (●) from lipid-core nanocapsules. Straight lines represent the capsules with one polyphenol, whereas dotted lines show the capsules loaded with both polyphenols (mean value ± SD, n = 3). For clarity reasons standard deviations for curcumin release which were ≤±2.64% are not shown.

core, and their different release kinetics was recently indicated. The solubility of resveratrol in grape seed oil was found to be 90 μg/mL and the solubility for curcumin in grape seed oil was determined as 475 μg/mL.[26] These solubility findings coincide well with the respective drug release, as a lower resveratrol solubility goes along with a faster release from the lipid-core nanocapsule, whereas the opposite is found for curcumin. The combination of synergistic actives like resveratrol and curcumin with different release kinetics bears a great potential for one single therapeutic system providing a fast initial therapeutic onset (resveratrol) in combination with prolonged treatment (curcumin) in one single application system.

However, physicochemical characterization of the polyphenol-loaded capsules as well as their *in vitro* release kinetics do not provide any information about the absorption into cells or the interplay of the two drugs. Osteoarthritis represents a potential therapeutic target for curcumin and resveratrol. The human joint as an application site for osteoarthritis treatment comprises a complex assembly of articular cartilage with chondrocytes as the predominant cell type. During the course of osteoarthritis, chondrocytes are severely inflamed, finally resulting into apoptosis and cartilage degeneration. It has already successfully been shown that resveratrol and curcumin have a positive effect on inflamed chondrocytes.[6,11,14,15] By encapsulating curcumin and resveratrol in lipid-core nanocapsules, we can improve their solubility circumventing the use of toxic organic solvents and at the same time avoiding precipitation. Thus, LNC facilitate the application of a higher dose delivery combined with a controlled drug release over longer therapy intervals. Further, the protective effect of nanocapsules on the polyphenols is highly beneficial.[24] In a first study, the therapeutic effect of LNC on complete Freund's adjuvant-induced arthritis in rats was tested.[21] Results were very promising especially for the formulation containing both polyphenols. Nevertheless, by using intraperitoneal injection, the administration site is far from the therapeutic target in the hind paw of the rat. Further, no experimental data were generated elucidating how the polyphenols reach the inflamed joint and their local uptake mechanism. For these investigations sophisticated analytics are necessary combining biological assays with high-end visualization techniques. In this context, we focus on cellular delivery of LNC using human chondrocytes to investigate the interplay of carrier, polyphenols, and cellular response by a multifactorial analytical approach.

The postulated pharmacological target for polyphenols in order to treat osteoarthritis is the intracellular inflammation cascade in which these substances are supposed to intervene.[6,11−13] Therefore, investigating the uptake of LNC into chondrocytes is of high interest including the potential to gain a deeper insight into their specific uptake mechanism.

For this purpose, we utilized coherent anti-Stokes Raman scattering (CARS) microscopy. This analytical method facilitates instantaneous visualization of the sample by solely detecting light scattering from an excited endogenous molecular structure The protein band at 2928 cm^{-1} is representative for the cell body. It was chosen to investigate cellular engulfment of LNC. The lipid core of the nanocapsules is the dominant structure of the carrier with the best scattering properties, thus the band for lipids located at 2845 cm^{-1} was set for LNC detection. The signal at both bands is accompanied by a nonresonant background that reveals the surrounding structure. Although cells naturally contain lipids themselves,

DOI: 10.1021/acs.analchem.6b00199
Anal. Chem. 2016, 88, 7014−7022

the local density of grape seed oil in the core provides a sufficient contrast for chemically selective imaging. In Figure 3,

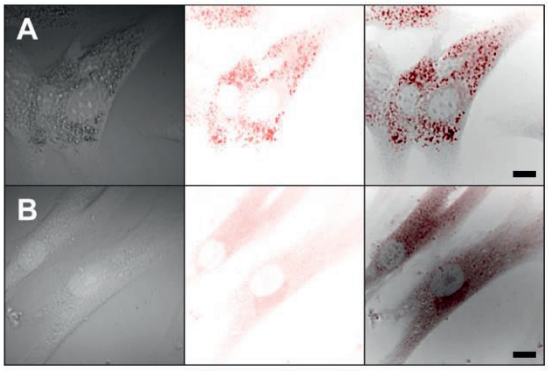

Figure 3. Coherent anti-Stokes Raman scattering microscopy images of chondrocytes engulfing lipid-core nanocapsules (A) and negative control chondrocytes (B). Left panels depict images generated by exciting the protein band. Center panels show false color background-free images of lipid location. Right panels show the overlay of left and center panels. Scale bars denote 10 μm.

the left panels depict plain cell bodies visualized by recording the protein band excitation, whereas the center panels were created by probing the lipid vibrations at 2548 cm^{-1} and using the common part of both images to remove the nonresonant background. For improved visualization and a clear differentiation in an overlap image (right panels), a MatLab algorithm was employed to create false color image based on the spectral data indication the background-free lipids in red color. The right panels depict an overlay of left and center panels.

Chondrocytes incubated with LNC are shown in Figure 3A. Cell bodies (left panel) show dark spots representing areas where molecular vibrations from proteins could not be sufficiently excited compared to the other cell parts. However, when comparing these dark spots with the false color lipid image (center panel), they colocalize with the prominent red spots. In these positions, the nanocapsules are located and their lipid signal exceeds the intensity of the protein signal. Thus, in the presence of LNC, scattering of the proteins is barely detectable. The overlay image (right panel) underlies this spectroscopic signal contrast. A very light red hue is visible almost across the entire cell body. This observation is a logic consequence of the omnipresence of intracellular lipids especially in the cell walls. This hue is also present in the negative control chondrocytes visualized in Figure 3B. Nevertheless, the density of the grape seed oil in the nanocapsule core triggers an increased signal and its intensity is converted into a more intense color in the image, making the detection of LNC feasible even among other cellular lipids. Different incubation times were tested (6, 10, 24, and 72 h) to determine the maximum uptake. However, no obvious differences were detected, neither based on the duration of the incubation interval nor based on the different nanocapsule formulations (data not shown). Thus, all images presented here involve an exposure of chondrocytes to Co-LNC (1 mg/mL) for 6 h, as the major focus of the study is on the codelivery of both polyphenols.

There are different ways for a nanocarrier to enter a cell, mainly involving phagocytosis and nonphagocytic pathways.[17,29,30] Only a few specialized cells including macrophages and dendritic cells are able to perform phagocytosis, whereas nonphagocytic pathways occur ubiquitously.[30,31] These are categorized as micropinocytosis, clathrin-mediated endocytosis, caveolae-mediated endocytosis, and clathrin- as well as caveolae-independent endocytosis.[17,30] As chondrocytes do not belong to the group of specialized cells, most likely they do not engulf lipid-core nanocapsules by phagocytosis. Therefore, different uptake inhibitors were chosen based on the endocytic pathways for a more detailed investigation of the uptake mechanism of LNC into chondrocytes. Monensin was chosen to block clathrin- and caveolae-independent endocytosis.[32] In addition, chlorpromazine and nystatin were used to investigate if LNC uptake was driven by clathrin-mediated or caveolin-mediated endocytosis, respectively.[22,33] To examine micropinocytosis, amiloride (ENIA) was taken.[33] Chondrocytes were incubated with the respective inhibitors for 1 h before cells were exposed to LNC. CARS images were recorded to visualize potential uptake. Figure 4 depicts the CARS images with each row A–D showing experiments with another uptake

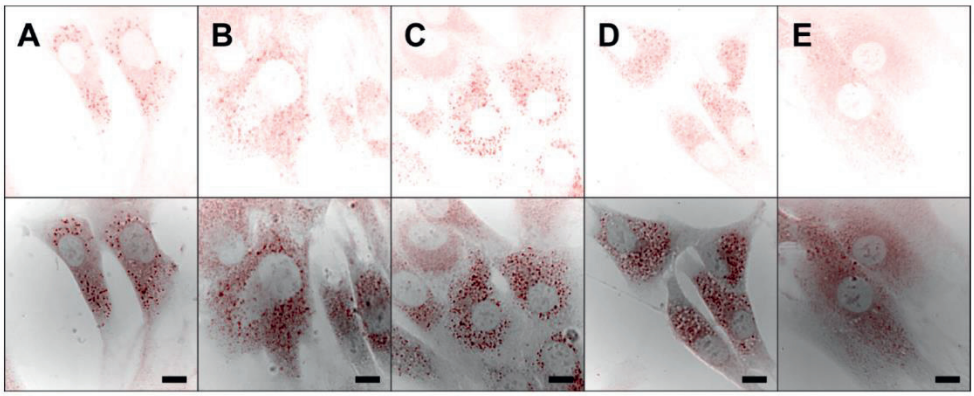

Figure 4. Coherent anti-Stokes Raman scattering microscopy images of chondrocytes exposed to lipid-core nanocapsules after preincubation with monensin (A), chlorpromazine (B), nystatin (C), ENIA (D), or at 4 °C (E). Upper panels depict CARS images generated by exciting lipid molecules. Lower panels show the overlay of cell body image and left panel. Scale bars denote 10 μm.

DOI: 10.1021/acs.analchem.6b00199
Anal. Chem. 2016, 88, 7014–7022

inhibitor. To discover possible effects of the inhibitors, the images were taken at fixed excitation intensities, scaled to the same size and are displayed at the same intensity scale. For all inhibitors, the upper panel depicts background-free CARS images acquired using the lipid frequency. Images in the lower panel show the overlay image of recorded lipid and protein band (Images after exciting the protein band are not depicted individually). There are no obvious differences in the uptake behavior of chondrocytes under the influence of the different inhibitors. All cells show a typical cell morphology, and LNC are visible in the cell body. LNC are located in the cytosol but could not be found in the nucleus. All images are comparable to the positive control but not to the negative control (Figure 3B). Therefore, monensin (Figure 4A), chlorpromazine (Figure 4B), nystatin (Figure 4C), and ENIA (Figure 4D), which are known to block nonendocytic pathways, do not hinder nanocasule engulfment by chondrocytes. Even switching to a higher concentration than 5 μg/mL did not lead to an uptake inhibition. Contrarily, apart from no effect for nystatin and monensin, higher concentrations had direct toxic effects on the cells (chlorpromazine, ENIA) preventing further examination (data not shown). Cytochalasin D which blocks macropincytosis and phagocytosis also had a toxic effect on chondrocytes even in lower contentrations. Because of morphological changes visible by light microscopy, this inhibitor was excluded from the studies. However, if cells were provided with fresh medium, they recovered which is in accordance with literature.[33] Phagocytosis is unlikely to be the engulfment mechanism due to the cell type, and the investigation of micropinocytosis was performed with amiloride. In order to examine if cellular uptake was driven by physical proximity of LNC and cell membrane, chondrocytes exposed to LNC were kept at 4 °C for the entire incubation period prior to CARS microscopy analysis to minimize energy-dependent processes like endocytosis.[22] The recorded images are depicted in Figure 4E in the same panel structure. Unlike images from inhibitor studies, CARS images in Figure 4E look similar to images of the negative control chondrocytes (Figure 3B). In both cases, the lipid-derived images consist of a red hue lacking deeply colored areas. Consequently, the local accumulation of lipid molecules represented by LNC are missing. Therefore, only lipids originating from the cell are detected and converted into images with a colored hue. The overlay image in the bottom panel visualizes the localization of the red hue over most parts of the cell body.

Thus, the uptake of LNC by human chondrocytes is most likely driven by the physical proximity of nanocapsules and cell membrane. No evidence was found that an inhibitor successfully blocked an endocytic uptake route.

As a next experimental step, the pharmacological effect of the nanocapsules is analyzed. For this a suitable readout is required. In this context, nitric oxide (NO) is a stimulus to cause apoptosis in chondrocytes and consequently progression of osteoarthritis, which has been found in high levels in osteoarthritic cartilage.[34] Sodium nitroprusside (SNP) is a NO generator which can be added to cell culture medium to investigate NO induced apoptosis mechanisms.[35−37] The increase of cellular reactive oxygen species (ROS), which are involved in many physiological cell functions, is triggered by exogenous nitrite oxide.[37,38] However, ROS becomes cytotoxic once its level exceeds a threshold marked by the cell's antioxidant ability.[37,39] To determine this threshold, we performed an MTT assay after incubating chondrocytes with SNP at different concentrations for 24 h. After 24 h, only 19.52% ± 0.04% (n = 8) of the cells were viable when exposed to 2 mM SNP, while the viability remained high for incubation experiments with 1.5 mM and 1 mM SNP (93.05% ± 0.04% and 108.33% ± 0.04%, respectively; n = 8). Thus, 2 mM SNP was used in the subsequent experiments to investigate if polyphenol loaded LNC have a protective effect against SNP induced oxidative stress. The results are depicted in Figure 5.

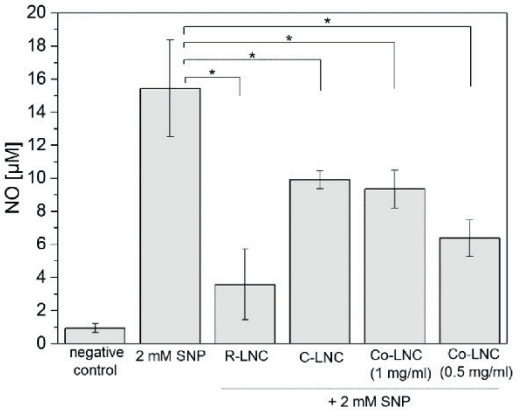

Figure 5. Nitric oxide (NO) levels expressed by chondrocytes under the influence of sodium nitroprusside (SNP) and a preincubation with different lipid-core nanocapsules ($n \geq 3$). Calculations are based on a standard calibration curve (n = 3). Statistical significance ($p < 0.05$) is indicated by *.

Chondrocytes express nitrite oxide (NO), as the molecule is a physiological messenger. Under the influence of 2 mM SNP, the NO level significantly increases. Similar to cell viability measurements, the level of NO depends on the SNP concentration. Incubation with 1 mM SNP resulted in 8.8 μM ± 1.5 μM of nitric oxide, whereas application of 1.5 mM SNP resulted in a readout of 11.2 μM ± 0.6 μM NO (n = 10). After preincubation with LNC, the amount of expressed NO significantly decreases ($p < 0.05$). The lowest value was found for R-LNC followed by Co-LNC (0.5 mg/mL), Co-LNC (1 mg/mL), and C-LNC. The contrary findings for R-LNC and C-LNC are very plausible as they correlate with the drug release profiles (Figure 2). Resveratrol shows the fastest release and is thus immediately available to scavenge ROS, consequently protecting chondrocytes, which is represented by the expression of low nitric oxide values (Figure 5, R-LNC). In contrast, a highly protective effect of curcumin is hardly expectable as only 3.9% ± 0.3% of the polyphenol are released after 24 h. Consequently, the expression of NO levels is rather high (Figure 5, C-LNC). Interestingly, the effect of coencapsulated polyphenols is in-between the results for R-LNC and C-LNC, respectively. Although the release profiles of the individual polyphenols from the combined formulation are coinciding with their counterparts R-LNC and C-LNC, resveratrol does not perform accordingly as the NO values at least for Co-LNC containing 0.5 mg/mL of resveratrol would be expected to be similar to R-LNC results. A study by Liang et al.[40] showed that resveratrol applied in solution prevented the SNP induced production of reactive oxygen species in rabbit chondrocytes as the polyphenol scavenged ROS. The authors proposed a signaling pathway which is invaded by resveratrol

DOI: 10.1021/acs.analchem.6b00199
Anal. Chem. 2016, 88, 7014−7022

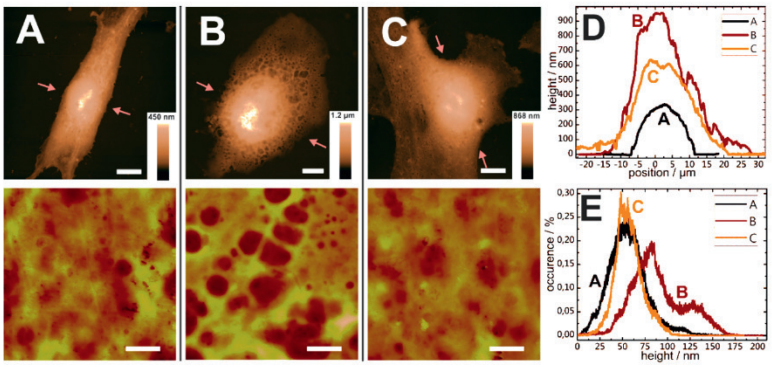

Figure 6. Atomic force microscopy analysis of chondrocytes as control (A), exposed to 2 mM SNP (B), and preincubation with Co-LNC prior to SNP exposure (C). Panels in the upper row show the entire cell bodies acquired in tapping mode (scale bars are 10 μm). Panels in the lower row show a close up of the cell surfaces with a *z*-scale of 200 nm (scale bars are 1 μm). Panel D shows cross sections of all cells through their highest point (indicated by the small arrows in parts A–C, upper panels). Panel E displays the results of bearing analysis from all closeup scans.

before ROS reaches the mitochondria. Curcumin was not included in this study. However, multiple studies employing curcumin and/or resveratrol are published where IL-1β was used to trigger inflammation in chondrocytes.[6,13,15,41,42]

Csaki et al.[6] studied synergistic effects of dissolved curcumin and resveratrol on chondrocytes upon exposure to IL-1β. The authors proposed that both polyphenols intervene in the same intracellular reaction cascade; however, curcumin interferes earlier than resveratrol. Implying a similar situation for the SNP induced mechanism, our findings lead to the following conclusions: Delivery of polyphenols by LNC and different release profiles seem to influence the protective effects of the two polyphenols and hinder a synergistic effect when codelivered in this case. Thus, the detected NO levels for nanocapsules comprising both polyphenols are higher than results for R-LNC but lower than results for C-LNC. Furthermore, the polyphenol loading of Co-LNC seems to have an impact as well. Detected NO values for Co-LNC encapsulating 0.5 mg/mL are lower than for an encapsulated polyphenol concentration of 1 mg/mL. Less curcumin is available in Co-LNC (0.5 mg/mL) to interfere with resveratrol effects, strengthening the protective effect resveratrol against SNP induced apoptotic effects by nitric oxide. While physicochemical characteristics did not show any influence on uptake behavior between capsules carrying various polyphenol loads as determined by CARS microscopy analysis, we gain a different insight from the NO-assay. Thus, this analysis is an illustrative example for the importance of research approaches using different complementary techniques to gain a "big picture" rather than relying on one single analysis. Even though the NO-assay provides interesting insight into the mechanism and interaction of the two polyphenols, the results are not suited for evaluating the overall "therapeutic effect" of the LNC codelivering the two polyphenols as the comparison with other analytical techniques shows. Further, a generally neglected factor is posed by changes of cell membrane and cytoskeleton of the cells upon induced inflammation and application of drugs.

In this context, AFM has lately been employed to detect physical differences between healthy and diseased cells, as cellular ultrastructures tend to alter in diseased or cancerous cells.[43−45] The high spatial resolution of this technique enables the investigation of cell membrane properties.[46] AFM provides an attractive addition to conventional visualization and molecular biological assays in order to gain further information on cellular surface topography. Here, we use AFM to study the apoptotic effect of SNP and the preventive abilities of Co-LNC on cell morphology and membrane nanostructure of human chondrocytes.

AFM analysis was performed with chondrocytes without any treatment (control), after treatment with 2 mM SNP as well as after preincubation with Co-LNC prior to SNP exposure. Representative AFM images of the entire cell body as well as close-ups of the cell surface are displayed in Figure 6A–C. The control chondrocyte shows an elongated cell body with a rather homogeneous height forming lamellopodia in order to get into contact with other cells (Figure 6A). In contrast, the chondrocyte treated with 2 mM SNP presents a rather round, contracted shape with a structured surface, which is generally expected upon cell exposure with toxic substances and apoptosis (Figure 6B). These results are corroborated by results from MTT analysis showing that cell viability severely drops to 19.52% ± 0.04 after incubation with 2 mM SNP. A cell which was pretreated with Co-LNC prior to SNP exposure is shown in Figure 6C. Interestingly, in comparison to Figure 6A,B, the cell rather shows similarity to the untreated cell and defects due to SNP exposure (as seen in Figure 6B) are neglectable. Besides morphology analysis, height profiles of the cells were acquired. For all chondrocytes, the nucleus represents the highest area of the cell body, as displayed in Figure 6D. The differences in morphology revealed in Figures 6A–C are reflected in the height profiles. The control chondrocyte has a height of about 300 nm, whereas the cell treated with SNP is more than 3 times higher. When pretreated with Co-LNC prior to SNP, the cell height only increases to approximately 600 nm. Thus, the effect of SNP on cell height and morphology is significantly attenuated by polyphenol loaded LNC. To study changes in the cell membrane in more detail, close-up AFM images were recorded (Figure 6A–C, lower panel). Again, the images taken from control chondrocytes and cells pretreated with LNC depict a similar membrane structure. On the contrary, the cell membrane of SNP exposed chondrocytes exposes dents and bumps. Again, AFM analysis shows the protective effect of polyphenol-loaded LNC against SNP exposure. Nanocapsules delivering resveratrol and curcumin into the cell are likely to have a protective impact on chondrocytes against SNP. To

DOI: 10.1021/acs.analchem.6b00199
Anal. Chem. 2016, 88, 7014–7022

quantify the differences in surface morphology, a subsequent bearing analysis was performed (Figure 6E). The control chondrocyte and the Co-LNC pretreated cell show very similar height distributions with a maximum at approximately 50 nm. The SNP treated cell without protective pretreatment shows a different height distribution with two maxima at 75 and 140 nm, respectively. This reflects the visualized surface pattern well, as the two maxima can directly be correlated to the pitted surface structure.

Overall, the results of the AFM study are in good agreement with confocal fluorescence microscopy investigations by Liang et al. showing a remodeling of the cell's cytoskeleton upon exposure to SNP.[40] F-actin filaments shortened, microtubule structures were disrupted and thus the cell shrunk, which is observable in the AFM image in Figure 6B. A preincubation with resveratrol prevented these extreme effects on the cell, which can be substantiated by our findings. In this context, AFM investigations expanded the insight into the interplay between cells and carrier by visualizing cellular reactions and the advantage of combining different analytical procedures to create a more comprehensive picture in spite of a snapshot becomes evident. Overall, the nanocapsules have a positive effect on cellular nanobiomechanics reflected in the cell membrane morphology preventing damage leading to cell death by an externally applied nitric oxide donor.

■ CONCLUSIONS

In summary, we have successfully combined biological assays with sophisticated nondestructive, label-free microscopic techniques (CARS and AFM) for the an all-encompassing investigation of the therapeutic effects of advanced nanocapsules loaded with two polyphenols against induced osteoarthritic states of human chondrocytes. CARS microscopy images depict a clear uptake of the well-characterized lipid-core nanocapsules into the cellular cytosol. However, no distinct endocytotic pathway could be determined and cellular uptake was found to be energy dependent. The extent of these effects was found to be determined by the drug release kinetics from the capsules as well as by their drug loadings. Findings from these assays were underlined by AFM studies visualizing a protective effect on cell morphology and membrane surface as a result of chondrocytes treatment with the polyphenol-loaded nanocapsules. Thus, besides presenting a sophisticated carrier system for joint application, these results highlight the necessity and potential of establishing combinatorial analytical approaches to elucidate cellular uptake, the interplay of codelivered drugs, and their therapeutic effect on the subcellular level to gain a "big picture" for in-depth understanding of novel therapeutic approaches.

■ AUTHOR INFORMATION

Corresponding Author

*E-mail: m.windbergs@mx.uni-saarland.de. Fax: +49 681 98806 1009.

Author Contributions

The manuscript was written through contributions of all authors. All authors have given approval to the final version of the manuscript.

Notes

The authors declare no competing financial interest.

■ ACKNOWLEDGMENTS

The authors thank Petra Koenig for support with cell culture and the Medical Cell BioPhysics Group at the University of Twente for sharing their lab facilities. The German Academic Exchange Service (DAAD) and Coordenação de Aperfeiçoamento de Pessoal de Nível Superior (CAPES) as well as the Collaborative Research Centre 1027 (DFG Sonderforschungsbereich 1027) are acknowledged for financial support.

■ REFERENCES

(1) van der Kraan, P. M.; van den Berg, W. B. *Ageing Res. Rev.* **2008**, *7*, 106−113.
(2) Goldring, M. B. *Arthritis Rheum.* **2000**, *43*, 1916−1926.
(3) Im, H. J.; Li, X.; Chen, D.; Yan, D.; Kim, J.; Ellman, M. B.; Stein, G. S.; Cole, B.; Kc, R.; Cs-Szabo, G.; van Wijnen, A. J. *J. Cell. Physiol.* **2012**, *227*, 3488−3497.
(4) Malemud, C. J.; Islam, N.; Haqqi, T. M. *Cells Tissues Organs* **2003**, *174*, 34−48.
(5) van der Kraan, P. M.; Buma, P.; van Kuppevelt, T.; van den Berg, W. B. *Osteoarthritis Cartilage* **2002**, *10*, 631−637.
(6) Csaki, C.; Mobasheri, A.; Shakibaei, M. *Arthritis Res. Ther.* **2009**, *11*, R165.
(7) Jin, H.; Liang, Q.; Chen, T.; Wang, X. *PLoS One* **2014**, *9*, e91611.
(8) Wadsworth, T. L.; Koop, D. R. *Biochem. Pharmacol.* **1999**, *57*, 941−949.
(9) Bisht, K.; Wagner, K. H.; Bulmer, A. C. *Toxicology* **2010**, *278*, 88−100.
(10) Shen, C. L.; Smith, B. J.; Lo, D. F.; Chyu, M. C.; Dunn, D. M.; Chen, C. H.; Kwun, I. S. *J. Nutr. Biochem.* **2012**, *23*, 1367−1377.
(11) Shakibaei, M.; Schulze-Tanzil, G.; John, T.; Mobasheri, A. *Ann. Anat.* **2005**, *187*, 487−497.
(12) Shakibaei, M.; Mobasheri, A.; Buhrmann, C. *Genes Nutr.* **2011**, *6*, 171−179.
(13) Csaki, C.; Keshishzadeh, N.; Fischer, K.; Shakibaei, M. *Biochem. Pharmacol.* **2008**, *75*, 677−687.
(14) Shakibaei, M.; Csaki, C.; Nebrich, S.; Mobasheri, A. *Biochem. Pharmacol.* **2008**, *76*, 1426−1439.
(15) Shakibaei, M.; John, T.; Schulze-Tanzil, G.; Lehmann, I.; Mobasheri, A. *Biochem. Pharmacol.* **2007**, *73*, 1434−1445.
(16) Sinha, V. R.; Bansal, K.; Kaushik, R.; Kumria, R.; Trehan, A. *Int. J. Pharm.* **2004**, *278*, 1−23.
(17) Hillaireau, H.; Couvreur, P. *Cell. Mol. Life Sci.* **2009**, *66*, 2873−2896.
(18) Ourique, A. F.; Pohlmann, A. R.; Guterres, S. S.; Beck, R. C. *Int. J. Pharm.* **2008**, *352*, 1−4.
(19) Fontana, M. C.; Coradini, K.; Guterres, S. S.; Pohlmann, A. R.; Beck, R. C. *J. Biomed. Nanotechnol.* **2009**, *5*, 254−263.
(20) Jornada, D. S.; Fiel, L. A.; Bueno, K.; Gerent, J. F.; Petzhold, C. L.; Beck, R. C. R.; Guterres, S. S.; Pohlmann, A. R. *Soft Matter* **2012**, *8*, 6646−6655.
(21) Coradini, K.; Friedrich, R. B.; Fonseca, F. N.; Vencato, M. S.; Andrade, D. F.; Oliveira, C. M.; Battistel, A. P.; Guterres, S. S.; da Rocha, M. I.; Pohlmann, A. R.; Beck, R. C. *Eur. J. Pharm. Sci.* **2015**, *78*, 163−170.
(22) Herd, H.; Daum, N.; Jones, A. T.; Huwer, H.; Ghandehari, H.; Lehr, C. M. *ACS Nano* **2013**, *7*, 1961−1973.
(23) Torchilin, V. P. *Adv. Drug Delivery Rev.* **2005**, *57*, 95−109.
(24) Coradini, K.; Lima, F. O.; Oliveira, C. M.; Chaves, P. S.; Athayde, M. L.; Carvalho, L. M.; Beck, R. C. R. *Eur. J. Pharm. Biopharm.* **2014**, *88*, 178−185.
(25) Garbacik, E. T.; Herek, J. L.; Otto, C.; Offerhaus, H. L. *J. Raman Spectrosc.* **2012**, *43*, 651−655.
(26) Friedrich, R. B.; Kann, B.; Coradini, K.; Offerhaus, H. L.; Beck, R. C. R.; Windbergs, M. *Eur. J. Pharm. Sci.* **2015**, *78*, 204−213.
(27) Sabuncu, A. C.; Kalluri, B. S.; Qian, S.; Stacey, M. W.; Beskok, A. *Colloids Surf., B* **2010**, *78*, 36−43.
(28) Allouni, Z. E.; Cimpan, M. R.; Hol, P. J.; Skodvin, T.; Gjerdet, N. R. *Colloids Surf., B* **2009**, *68*, 83−87.

DOI: 10.1021/acs.analchem.6b00199
Anal. Chem. 2016, 88, 7014−7022

(29) Conner, S. D.; Schmid, S. L. *Nature* **2003**, *422*, 37−44.
(30) Zaki, N. M.; Tirelli, N. *Expert Opin. Drug Delivery* **2010**, *7*, 895−913.
(31) Aderem, A.; Underhill, D. M. *Annu. Rev. Immunol.* **1999**, *17*, 593−623.
(32) Pohlmann, R.; Kruger, S.; Hasilik, A.; Von Figura, K. *Biochem. J.* **1984**, *217*, 649−658.
(33) Nakase, I.; Niwa, M.; Takeuchi, T.; Sonomura, K.; Kawabata, N.; Koike, Y.; Takehashi, M.; Tanaka, S.; Ueda, K.; Simpson, J. C.; Jones, A. T.; Sugiura, Y.; Futaki, S. *Mol. Ther.* **2004**, *10*, 1011−1022.
(34) Diaz-Gallego, L.; Prieto, J. G.; Coronel, P.; Gamazo, L. E.; Gimeno, M.; Alvarez, A. I. *J. Orthop. Res.* **2005**, *23*, 1370−1376.
(35) Blanco, F. J.; Ochs, R. L.; Schwarz, H.; Lotz, M. *Am. J. Pathol.* **1995**, *146*, 75−85.
(36) Tonomura, H.; Takahashi, K. A.; Mazda, O.; Arai, Y.; Inoue, A.; Terauchi, R.; Shin-Ya, M.; Kishida, T.; Imanishi, J.; Kubo, T. *Osteoarthritis Cartilage* **2006**, *14*, 545−553.
(37) Wu, G. J.; Chen, T. G.; Chang, H. C.; Chiu, W. T.; Chang, C. C.; Chen, R. M. *J. Cell. Biochem.* **2007**, *101*, 1520−1531.
(38) Lo, Y. Y.; Conquer, J. A.; Grinstein, S.; Cruz, T. F. *J. Cell. Biochem.* **1998**, *69*, 19−29.
(39) Stoop, R.; Buma, P.; van der Kraan, P. M.; Hollander, A. P.; Billinghurst, R. C.; Poole, A. R.; van den Berg, W. B. *Arthritis Rheum.* **2000**, *43*, 2121−2131.
(40) Liang, Q.; Wang, X.-p.; Chen, T.-s. *Apoptosis* **2014**, *19*, 1354−1363.
(41) Mathy-Hartert, M.; Jacquemond-Collet, I.; Priem, F.; Sanchez, C.; Lambert, C.; Henrotin, Y. *Inflammation Res.* **2009**, *58*, 899−908.
(42) Lei, M.; Wang, J.-g.; Xiao, D.-m.; Fan, M.; Wang, D.-p.; Xiong, J.-y.; Chen, Y.; Ding, Y.; Liu, S.-l. *Eur. J. Pharmacol.* **2012**, *674*, 73−79.
(43) Cross, S. E.; Jin, Y. S.; Tondre, J.; Wong, R.; Rao, J.; Gimzewski, J. K. *Nanotechnology* **2008**, *19*, 384003.
(44) Iyer, S.; Gaikwad, R. M.; Subba-Rao, V.; Woodworth, C. D.; Sokolov, I. *Nat. Nanotechnol.* **2009**, *4*, 389−393.
(45) Lee, G. Y.; Lim, C. T. *Trends Biotechnol.* **2007**, *25*, 111−118.
(46) Lesniewska, E.; Emmanuel Milhiet, P.; Giocondi, M.-C.; Le Grimellec, C. In *Methods in Cell Biology*, Bhanu, P. J., Hörber, J. K. H., Eds.; Academic Press: New York, 2002; pp 51−65.

DOI: 10.1021/acs.analchem.6b00199
Anal. Chem. 2016, 88, 7014−7022

6 References

[1] C.V. Raman, K.S. Krishnan, A new type of secondary radiation, Nature, 121 (1928) 501-502.

[2] H.J. van Manen, Y.M. Kraan, D. Roos, C. Otto, Single-cell Raman and fluorescence microscopy reveal the association of lipid bodies with phagosomes in leukocytes, Proc. Natl. Acad. Sci. U.S.A., 102 (2005) 10159-10164.

[3] G.P.S. Smith, C.M. McGoverin, S.J. Fraser, K.C. Gordon, Raman imaging of drug delivery systems, Adv. Drug Deliv. Rev., 89 (2015) 21-41.

[4] B. Kann, M. Windbergs, Chemical Imaging - Einblick in das Unsichtbare durch molekulare Fingerabdrücke, TechnoPharm, 3 (2013) 146-149.

[5] M. Miljkovic, T. Chernenko, M.J. Romeo, B. Bird, C. Matthaus, M. Diem, Label-free imaging of human cells: algorithms for image reconstruction of Raman hyperspectral datasets, Analyst, 135 (2010) 2002-2013.

[6] D. Clark, M. Henson, F. LaPlant, S. Sasic, L. Zhang, Pharmaceutical applications of chemical mapping and imaging, in: Applications of Vibrational Spectroscopy in Pharmaceutical Research and Development, Wiley, 2007, pp. 309-335.

[7] T.F. Haefele, K. Paulus, Confocal Raman Microscopy in Pharmaceutical Development, in: T. Dieing, O. Hollricher, J. Toporski (Eds.) Confocal Raman Microscopy, Springer, 2011, pp. 165-202.

[8] D. Pappas, B.W. Smith, J.D. Winefordner, Raman imaging for two-dimensional chemical analysis, Appl. Spectrosc. Rev., 35 (2000) 1-23.

[9] K.C. Gordon, C.M. McGoverin, Raman mapping of pharmaceuticals, Int. J. Pharm., 417 (2011) 151-162.

[10] P. Lasch, Spectral pre-processing for biomedical vibrational spectroscopy and microspectroscopic imaging, Chemom. Intell. Lab. Syst., 117 (2012) 100-114.

[11] M. Hedegaard, C. Matthäus, S. Hassing, C. Krafft, M. Diem, J. Popp, Spectral unmixing and clustering algorithms for assessment of single cells by Raman microscopic imaging, Theor. Chem. Accounts, 130 (2011) 1249-1260.

[12] S. Šašić, Raman mapping of low-content API pharmaceutical formulations. I. Mapping of alprazolam in Alprazolam/Xanax tablets, Pharm. Res., 24 (2007) 58-65.

[13] E. Ploetz, S. Laimgruber, S. Berner, W. Zinth, P. Gilch, Femtosecond stimulated Raman microscopy, Appl. Phys. B: Lasers Opt., 87 (2007) 389-393.

[14] G.J. Puppels, F.F.M. De Mul, C. Otto, J. Greve, M. Robert-Nicoud, D.J. Arndt-Jovin, T.M. Jovin, Studying single living cells and chromosomes by confocal Raman microspectroscopy, Nature, 347 (1990) 301-303.

[15] M.D. Duncan, J. Reintjes, T.J. Manuccia, Scanning coherent anti-Stokes Raman microscope, Opt. Lett., 7 (1982) 350-352.

[16] M. Haaser, M. Windbergs, C.M. McGoverin, P. Kleinebudde, T. Rades, K.C. Gordon, C.J. Strachan, Analysis of matrix dosage forms during dissolution testing using raman microscopy, J. Pharm. Sci., 100 (2011) 4452-4459.

[17] M. Windbergs, M. Haaser, C.M. McGoverin, K.C. Gordon, P. Kleinebudde, C.J. Strachan, Investigating the relationship between drug distribution in solid lipid matrices and dissolution behaviour using Raman spectroscopy and mapping, J. Pharm. Sci., 99 (2010) 1464-1475.

[18] A.L. Fussell, P. Kleinebudde, J. Herek, C.J. Strachan, H.L. Offerhaus, Coherent anti-Stokes Raman Scattering (CARS) Microscopy Visualizes Pharmaceutical Tablets During Dissolution, J. Visualized Exp., (2014) e51847.

[19] M. Jurna, M. Windbergs, C.J. Strachan, L. Hartsuiker, C. Otto, P. Kleinebudde, J.L. Herek, H.L. Offerhaus, Coherent anti-stokes raman scattering microscopy to monitor drug dissolution in different oral pharmaceutical tablets, J. Innovative Optt Health Sci., 2 (2009) 37-43.

[20] M. Windbergs, M. Jurna, H.L. Offerhaus, J.L. Herek, P. Kleinebudde, C.J. Strachan, Chemical imaging of oral solid dosage forms and changes upon dissolution using coherent anti-stokes raman scattering microscopy, Anal. Chem., 81 (2009) 2085-2091.

[21] K. Udipi, M. Chen, P. Cheng, K. Jiang, D. Judd, A. Caceres, R.J. Melder, J.N. Wilcox, Development of a novel biocompatible polymer system for extended drug release in a next-generation drug-eluting stent, J. Biomed. Mater. Res., Part A, 85 (2008) 1064-1071.
[22] A. Belu, C. Mahoney, K. Wormuth, Chemical imaging of drug eluting coatings: Combining surface analysis and confocal Raman microscopy, J. Controlled Release, 126 (2008) 111-121.
[23] J. Dong, J.D. Foley, C.D. Frethem, R.A. Hoerr, M.J. Matuszewski, J.E. Puskas, G. Haugstad, Multimodal dynamic imaging of therapeutic biomedical coatings in aqueous medium, Langmuir, 25 (2009) 5442-5445.
[24] K.B. Biggs, K.M. Balss, C.A. Maryanoff, Pore networks and polymer rearrangement on a drug-eluting stent as revealed by correlated confocal Raman and atomic force microscopy, Langmuir, 28 (2012) 8238-8243.
[25] E. Kang, H. Wang, I.K. Kwon, J. Robinson, K. Park, J.-X. Cheng, In Situ Visualization of Paclitaxel Distribution and Release by Coherent Anti-Stokes Raman Scattering Microscopy, Anal. Chem., 78 (2006) 8036-8043.
[26] S. Šašić, An in-depth analysis of Raman and near-infrared chemical images of common pharmaceutical tablets, Appl. Spectrosc., 61 (2007) 239-250.
[27] A. Kuriyama, Y. Ozaki, Assessment of Active Pharmaceutical Ingredient Particle Size in Tablets by Raman Chemical Imaging Validated using Polystyrene Microsphere Size Standards, AAPS PharmSciTech, 15 (2014) 375-387.
[28] M.J. Henson, L. Zhang, Drug characterization in low dosage pharmaceutical tablets using raman microscopic mapping, Appl. Spectrosc., 60 (2006) 1247-1255.
[29] N. Chieng, S. Rehder, D. Saville, T. Rades, J. Aaltonen, Quantitative solid-state analysis of three solid forms of ranitidine hydrochloride in ternary mixtures using Raman spectroscopy and X-ray powder diffraction, J. Pharm. Biomed. Anal., 49 (2009) 18-25.
[30] A. Heinz, C.J. Strachan, K.C. Gordon, T. Rades, Analysis of solid-state transformations of pharmaceutical compounds using vibrational spectroscopy, J. Pharm. Pharmacol., 61 (2009) 971-988.
[31] K. Kachrimanis, D.E. Braun, U.J. Griesser, Quantitative analysis of paracetamol polymorphs in powder mixtures by FT-Raman spectroscopy and PLS regression, J. Pharm. Biomed. Anal., 43 (2007) 407-412.
[32] E. Räsänen, N. Sandler, Near infrared spectroscopy in the development of solid dosage forms, J. Pharm. Pharmacol., 59 (2007) 147-159.
[33] H. Wikström, P.J. Marsac, L.S. Taylor, In-line monitoring of hydrate formation during wet granulation using Raman spectroscopy, J. Pharm. Sci., 94 (2005) 209-219.
[34] H. Qu, M. Louhi-Kultanen, J. Rantanen, J. Kallas, Solvent-mediated phase transformation kinetics of an anhydrate/hydrate system, Cryst. Growth Des., 6 (2006) 2053-2060.
[35] T.R.M. De Beer, C. Bodson, B. Dejaegher, B. Walczak, P. Vercruysse, A. Burggraeve, A. Lemos, L. Delattre, Y.V. Heyden, J.P. Remon, C. Vervaet, W.R.G. Baeyens, Raman spectroscopy as a process analytical technology (PAT) tool for the in-line monitoring and understanding of a powder blending process, J. Pharm. Biomed. Anal., 48 (2008) 772-779.
[36] D.S. Hausman, R.T. Cambron, A. Sakr, Application of Raman spectroscopy for on-line monitoring of low dose blend uniformity, Int. J. Pharm., 298 (2005) 80-90.
[37] T.R.M. De Beer, W.R.G. Baeyens, J. Ouyang, C. Vervaet, J.P. Remon, Raman spectroscopy as a process analytical technology tool for the understanding and the quantitative in-line monitoring of the homogenization process of a pharmaceutical suspension, Analyst, 131 (2006) 1137-1144.
[38] A.S. El Hagrasy, S.Y. Chang, D. Desal, S. Kiang, Raman spectroscopy for the determination of coating uniformity of tablets: Assessment of product quality and coating pan mixing efficiency during scale-up, J. Pharm. Innov., 1 (2006) 37-42.
[39] S. Romero-Torres, J.D. Pérez-Ramos, K.R. Morris, E.R. Grant, Raman spectroscopic measurement of tablet-to-tablet coating variability, J. Pharm. Biomed. Anal., 38 (2005) 270-274.

[40] S. Romero-Torres, J.D. Pérez-Ramos, K.R. Morris, E.R. Grant, Raman spectroscopy for tablet coating thickness quantification and coating characterization in the presence of strong fluorescent interference, J. Pharm. Biomed. Anal., 41 (2006) 811-819.
[41] J. Mueller, K. Knop, J. Thies, C. Uerpmann, P. Kleinebudde, Feasibility of Raman spectroscopy as PAT tool in active coating Raman spectroscopy as PAT tool in active coating, Drug Dev. Ind. Pharm., 36 (2010) 234-243.
[42] M. Wirges, A. Funke, P. Serno, K. Knop, P. Kleinebudde, Monitoring of an active coating process for two-layer tablets-model development strategies, J. Pharm. Sci., 102 (2013) 556-564.
[43] L. Saerens, L. Dierickx, B. Lenain, C. Vervaet, J.P. Remon, T.D. Beer, Raman spectroscopy for the in-line polymer-drug quantification and solid state characterization during a pharmaceutical hot-melt extrusion process, Eur. J. Pharm. Biopharm., 77 (2011) 158-163.
[44] L. Saerens, C. Vervaet, J.P. Remon, T. De Beer, Visualization and process understanding of material behavior in the extrusion barrel during a hot-melt extrusion process using raman spectroscopy, Anal. Chem., 85 (2013) 5420-5429.
[45] L. Saerens, D. Ghanam, C. Raemdonck, K. Francois, J. Manz, R. Krüger, S. Krüger, C. Vervaet, J.P. Remon, T. De Beer, In-line solid state prediction during pharmaceutical hot-melt extrusion in a 12 mm twin screw extruder using Raman spectroscopy, Eur. J. Pharm. Biopharm., 87 (2014) 606-615.
[46] L. Saerens, N. Segher, C. Vervaet, J.P. Remon, T. De Beer, Validation of an in-line Raman spectroscopic method for continuous active pharmaceutical ingredient quantification during pharmaceutical hot-melt extrusion, Anal. Chim. Acta, 806 (2014) 180-187.
[47] A. Hédoux, Y. Guinet, M. Descamps, The contribution of Raman spectroscopy to the analysis of phase transformations in pharmaceutical compounds, Int. J. Pharm., 417 (2011) 17-31.
[48] A. Hédoux, L. Paccou, S. Achir, Y. Guinet, Mechanism of protein stabilization by trehalose during freeze-drying analyzed by in situ micro-raman spectroscopy, J. Pharm. Sci., 102 (2013) 2484-2494.
[49] U. Roessl, S. Leitgeb, S. Pieters, T. De Beer, B. Nidetzky, In situ protein secondary structure determination in ice: Raman spectroscopy-based process analytical tool for frozen storage of biopharmaceuticals, J. Pharm. Sci., 103 (2014) 2287-2295.
[50] S. Verrier, I. Notingher, J.M. Polak, L.L. Hench, In situ monitoring of cell death using Raman microspectroscopy, Biopolymers, 74 (2004) 157-162.
[51] S.O. Konorov, H.G. Schulze, J.M. Piret, M.W. Blades, R.F. Turner, Label-free determination of the cell cycle phase in human embryonic stem cells by Raman microspectroscopy, Anal. Chem., 85 (2013) 8996-9002.
[52] C. Krafft, T. Knetschke, A. Siegner, R.H.W. Funk, R. Salzer, Mapping of single cells by near infrared Raman microspectroscopy, Vibrational Spectroscopy, 32 (2003) 75-83.
[53] N. Uzunbajakava, A. Lenferink, Y. Kraan, B. Willekens, G. Vrensen, J. Greve, C. Otto, Nonresonant Raman imaging of protein distribution in single human cells, Biopolymers, 72 (2003) 1-9.
[54] C. Krafft, T. Knetschke, R.H.W. Funk, R. Salzer, Identification of organelles and vesicles in single cells by Raman microspectroscopic mapping, Vib. Spectrosc., 38 (2005) 85-93.
[55] C. Krafft, T. Knetschke, R.H.W. Funk, R. Salzer, Studies on stress-induced changes at the subcellular level by Raman microspectroscopic mapping, Anal. Chem., 78 (2006) 4424-4429.
[56] C. Matthaeus, T. Chernenko, J.A. Newmark, C.M. Warner, M. Diem, Label-free detection of mitochondrial distribution in cells by nonresonant Raman microspectroscopy, Biophys. J., 93 (2007) 668-673.
[57] K. Meister, D.A. Schmidt, E. Brundermann, M. Havenith, Confocal Raman microspectroscopy as an analytical tool to assess the mitochondrial status in human spermatozoa, Analyst, 135 (2010) 1370-1374.
[58] M. Derenzini, L. Montanaro, D. Treré, What the nucleolus says to a tumour pathologist, Histopathology, 54 (2009) 753-762.

[59] H.G. Schulze, S.O. Konorov, J.M. Piret, M.W. Blades, R.F. Turner, Label-free imaging of mammalian cell nucleoli by Raman microspectroscopy, Analyst, 138 (2013) 3416-3423.
[60] V.V. Pully, A.T.M. Lenferink, C. Otto, Time-lapse Raman imaging of single live lymphocytes, J. Raman Spectrosc., 42 (2011) 167-173.
[61] K.E. Uhrich, S.M. Cannizzaro, R.S. Langer, K.M. Shakesheff, Polymeric Systems for Controlled Drug Release, Chem. Rev., 99 (1999) 3181-3198.
[62] A.A. van Apeldoorn, H.J. van Manen, J.M. Bezemer, J.D. de Bruijn, C.A. van Blitterswijk, C. Otto, Raman imaging of PLGA microsphere degradation inside macrophages, J. Am. Chem. Soc., 126 (2004) 13226-13227.
[63] T. Chernenko, C. Matthäus, L. Milane, L. Quintero, M. Amiji, M. Diem, Label-free raman spectral imaging of intracellular delivery and degradation of polymeric nanoparticle systems, ACS Nano, 3 (2009) 3552-3559.
[64] C. Matthäus, S. Schubert, M. Schmitt, C. Krafft, B. Dietzek, U.S. Schubert, J. Popp, Resonance Raman spectral imaging of intracellular uptake of β-carotene loaded poly(D, L -lactide-co-glycolide) nanoparticles, ChemPhysChem, 14 (2013) 155-161.
[65] C. Matthäus, A. Kale, T. Chernenko, V. Torchilin, M. Diem, New ways of imaging uptake and intracellular fate of liposomal drug carrier systems inside individual cells, based on raman microscopy, Mol. Pharmaceutics, 5 (2008) 287-293.
[66] T. Chernenko, R.R. Sawant, M. Miljkovic, L. Quintero, M. Diem, V. Torchilin, Raman microscopy for noninvasive imaging of pharmaceutical nanocarriers: Intracellular distribution of cationic liposomes of different composition, Mol. Pharmaceutics, 9 (2012) 930-936.
[67] J. Ye, S.A. Fox, M. Cudic, E.M. Rezler, J.L. Lauer, G.B. Fields, A.C. Terentis, Determination of penetratin secondary structure in live cells with Raman microscopy, J. Am. Chem. Soc., 132 (2010) 980-988.
[68] H.J. van Manen, A. Lenferink, C. Otto, Noninvasive imaging of protein metabolic labeling in single human cells using stable isotopes and Raman microscopy, Anal. Chem., 80 (2008) 9576-9582.
[69] C. Matthaus, C. Krafft, B. Dietzek, B.R. Brehm, S. Lorkowski, J. Popp, Noninvasive imaging of intracellular lipid metabolism in macrophages by Raman microscopy in combination with stable isotopic labeling, Anal. Chem., 84 (2012) 8549-8556.
[70] H. Yamakoshi, K. Dodo, A. Palonpon, J. Ando, K. Fujita, S. Kawata, M. Sodeoka, Alkyne-tag Raman imaging for visualization of mobile small molecules in live cells, J. Am. Chem. Soc., 134 (2012) 20681-20689.
[71] L. Wei, F. Hu, Y. Shen, Z. Chen, Y. Yu, C.C. Lin, M.C. Wang, W. Min, Live-cell imaging of alkyne-tagged small biomolecules by stimulated Raman scattering, Nat. Methods, 11 (2014) 410-412.
[72] H. Yamakoshi, K. Dodo, M. Okada, J. Ando, A. Palonpon, K. Fujita, S. Kawata, M. Sodeoka, Imaging of EdU, an alkyne-tagged cell proliferation probe, by Raman microscopy, J. Am. Chem. Soc., 133 (2011) 6102-6105.
[73] S.F. El-Mashtoly, D. Petersen, H.K. Yosef, A. Mosig, A. Reinacher-Schick, C. Kotting, K. Gerwert, Label-free imaging of drug distribution and metabolism in colon cancer cells by Raman microscopy, Analyst, 139 (2014) 1155-1161.
[74] R. Yuste, Fluorescence microscopy today, Nat. Methods, 2 (2005) 902-904.
[75] T.E. Meyerrose, D.A. De Ugarte, A.A. Hofling, P.E. Herrbrich, T.D. Cordonnier, L.D. Shultz, J.C. Eagon, L. Wirthlin, M.S. Sands, M.A. Hedrick, J.A. Nolta, In vivo distribution of human adipose-derived mesenchymal stem cells in novel xenotransplantation models, Stem Cells, 25 (2007) 220-227.
[76] J. Tolar, A.J. Nauta, M.J. Osborn, A.P. Mortari, R.T. McElmurry, S. Bell, L. Xia, N. Zhou, M. Riddle, T.M. Schroeder, J.J. Westendorf, R.S. McIvor, P.C.W. Hogendoorn, K. Szuhai, L. Oseth, B. Hirsch, S.R. Yant, M.A. Kay, A. Peister, D.J. Prockop, W.E. Fibbe, B.R. Blazar, Sarcoma derived from cultured mesenchymal stem cells, Stem Cells, 25 (2007) 371-379.
[77] H. Mao, R. Cai, N. Kawazoe, G. Chen, Long-term stem cell labeling by collagen-functionalized single-walled carbon nanotubes, Nanoscale, 6 (2014) 1552-1559.

[78] C.A. Puckett, J.K. Barton, Fluorescein redirects a ruthenium-octaarginine conjugate to the nucleus, J. Am. Chem. Soc., 131 (2009) 8738-8739.
[79] K. Meister, J. Niesel, U. Schatzschneider, N. Metzler-Nolte, D.A. Schmidt, M. Havenith, Label-Free Imaging of Metal-Carbonyl Complexes in Live Cells by Raman Microspectroscopy, Angew. Chem., Int. Ed., 49 (2010) 3310-3312.
[80] S. Pahlow, S. Meisel, D. Cialla-May, K. Weber, P. Rösch, J. Popp, Isolation and identification of bacteria by means of Raman spectroscopy, Adv. Drug Del. Rev., 89 (2015) 105-120.
[81] J. Kneipp, H. Kneipp, M. McLaughlin, D. Brown, K. Kneipp, In vivo molecular probing of cellular compartments with gold nanoparticles and nanoaggregates, Nano Lett., 6 (2006) 2225-2231.
[82] K. Kneipp, A.S. Haka, H. Kneipp, K. Badizadegan, N. Yoshizawa, C. Boone, K.E. Shafer-Peltier, J.T. Motz, R.R. Dasari, M.S. Feld, Surface-enhanced raman spectroscopy in single living cells using gold nanoparticles, Appl. Spectrosc., 56 (2002) 150-154.
[83] A. Sujith, T. Itoh, H. Abe, A.A. Anas, K. Yoshida, V. Biju, M. Ishikawa, Surface enhanced Raman scattering analyses of individual silver nanoaggregates on living single yeast cell wall, Appl. Phys. Lett., 92 (2008).
[84] J. Xie, Q. Zhang, J.Y. Lee, D.I.C. Wang, The synthesis of SERS-active gold nanoflower tags for in vivo applications, ACS Nano, 2 (2008) 2473-2480.
[85] J. Fang, S. Du, S. Lebedkin, Z. Li, R. Kruk, M. Kappes, H. Hahn, Gold mesostructures with tailored surface topography and their self-assembly arrays for surface-enhanced Raman spectroscopy, Nano Lett., 10 (2010) 5006-5013.
[86] Z. Wang, J. Zhang, J.M. Ekman, P.J.A. Kenis, Y. Lu, DNA-mediated control of metal nanoparticle shape: One-pot synthesis and cellular uptake of highly stable and functional gold nanoflowers, Nano Lett., 10 (2010) 1886-1891.
[87] A.M. Fales, H. Yuan, T. Vo-Dinh, Silica-coated gold nanostars for combined surface-enhanced Raman scattering (SERS) detection and singlet-oxygen generation: A potential nanoplatform for theranostics, Langmuir, 27 (2011) 12186-12190.
[88] A.M. Fales, H. Yuan, T. Vo-Dinh, Cell-penetrating peptide enhanced intracellular Raman imaging and photodynamic therapy, Mol. Pharmaceutics, 10 (2013) 2291-2298.
[89] Q. Li, Y. Jiang, R. Han, X. Zhong, S. Liu, Z.Y. Li, Y. Sha, D. Xu, High surface-enhanced Raman scattering performance of individual gold nanoflowers and their application in live cell imaging, Small, 9 (2013) 927-932.
[90] H. Yuan, A.M. Fales, C.G. Khoury, J. Liu, T. Vo-Dinh, Spectral characterization and intracellular detection of Surface-Enhanced Raman Scattering (SERS)-encoded plasmonic gold nanostars, J. Raman Spectrosc., 44 (2013) 234-239.
[91] L. Xiao, S. Harihar, D.R. Welch, A. Zhou, Imaging of epidermal growth factor receptor on single breast cancer cells using surface-enhanced Raman spectroscopy, Anal. Chim. Acta, 843 (2014) 73-82.
[92] Q. Liu, L. Wei, J. Wang, F. Peng, D. Luo, R. Cui, Y. Niu, X. Qin, Y. Liu, H. Sun, J. Yang, Y. Li, Cell imaging by graphene oxide based on surface enhanced Raman scattering, Nanoscale, 4 (2012) 7084-7089.
[93] Z. Liu, Z. Guo, H. Zhong, X. Qin, M. Wan, B. Yang, Graphene oxide based surface-enhanced Raman scattering probes for cancer cell imaging, Phys. Chem. Chem. Phys., 15 (2013) 2961-2966.
[94] S. Krimm, J. Bandekar, Vibrational spectroscopy and conformation of peptides, polypeptides, and proteins, Adv. Protein Chem., 38 (1986) 181-364.
[95] W.E. Huang, K. Stoecker, R. Griffiths, L. Newbold, H. Daims, A.S. Whiteley, M. Wagner, Raman-FISH: Combining stable-isotope Raman spectroscopy and fluorescence in situ hybridization for the single cell analysis of identity and function, Environ. Microbiol., 9 (2007) 1878-1889.
[96] A.J. McQuillan, The discovery of surface-enhanced Raman scattering, Notes Rec. R. Soc., 63 (2009) 105-109.
[97] M.K. Gregas, F. Yan, J. Scaffidi, H.N. Wang, T. Vo-Dinh, Characterization of nanoprobe uptake in single cells: spatial and temporal tracking via SERS labeling and modulation of surface charge, Nanomedicine, 7 (2011) 115-122.

[98] P. Verderio, L. Pandolfi, S. Mazzucchelli, M.R. Marinozzi, R. Vanna, F. Gramatica, F. Corsi, M. Colombo, C. Morasso, D. Prosperi, Antiproliferative effect of ASC-J9 delivered by PLGA nanoparticles against estrogen-dependent breast cancer cells, Mol. Pharmaceutics, 11 (2014) 2864-2875.
[99] M.D. Sonntag, E.A. Pozzi, N. Jiang, M.C. Hersam, R.P. Van Duyne, Recent Advances in Tip-Enhanced Raman Spectroscopy, J. Phys. Chem. Lett., 5 (2014) 3125-3130.
[100] N.A. Brazhe, E.Y. Parshina, V.V. Khabatova, A.A. Semenova, A.R. Brazhe, A.I. Yusipovich, A.S. Sarycheva, A.A. Churin, E.A. Goodilin, G.V. Maksimov, O.V. Sosnovtseva, Tuning SERS for living erythrocytes: Focus on nanoparticle size and plasmon resonance position, J. Raman Spectrosc., 44 (2013) 686-694.
[101] K.V. Kong, Z. Lam, W.D. Goh, W.K. Leong, M. Olivo, Metal carbonyl-gold nanoparticle conjugates for live-cell SERS imaging, Angew. Chem., Int. Ed., 51 (2012) 9796-9799.
[102] S. Lee, H. Chon, J. Lee, J. Ko, B.H. Chung, D.W. Lim, J. Choo, Rapid and sensitive phenotypic marker detection on breast cancer cells using surface-enhanced Raman scattering (SERS) imaging, Biosens. Bioelectron., 51 (2014) 238-243.
[103] Š. Bálint, S. Rao, M.M. Sánchez, V. Huntošová, P. Miškovský, D. Petrov, Diffusion and cellular uptake of drugs in live cells studied with surface-enhanced Raman scattering probes, J. Biomed. Opt., 15 (2010) 027005.
[104] S. Schrank, B. Kann, E. Saurugger, M. Hainschitz, M. Windbergs, B.J. Glasser, J. Khinast, E. Roblegg, The effect of the drying temperature on the properties of wet-extruded calcium stearate pellets: pellet microstructure, drug distribution, solid state and drug dissolution, Int. J. Pharm., 478 (2015) 779-787.
[105] M.C. Chen, R.C. Lord, Laser-excited Raman spectroscopy of biomolecules. VIII. Conformational study of bovine serum albumin, J. Am. Chem. Soc., 98 (1976) 990-992.
[106] A. Hédoux, J.F. Willart, L. Paccou, Y. Guinet, F. Affouard, A. Lerbret, M. Descamps, Thermostabilization mechanism of bovine serum albumin by trehalose, J. Phys. Chem. B, 113 (2009) 6119-6126.
[107] J.L. Lippert, D. Tyminski, P.J. Desmeules, Determination of the secondary structure of proteins by laser Raman spectroscopy, J. Am. Chem. Soc., 98 (1976) 7075-7080.
[108] W. Wang, Lyophilization and development of solid protein pharmaceuticals, Int. J. Pharm., 203 (2000) 1-60.
[109] R. Tantipolphan, T. Rades, N.J. Medlicott, Insights into the structure of protein by vibrational spectroscopy, Curr. Pharm. Anal., 4 (2008) 53-68.
[110] S.T. Buckley, S.M. Fischer, G. Fricker, M. Brandl, In vitro models to evaluate the permeability of poorly soluble drug entities: Challenges and perspectives, Eur. J. Pharm. Sci., 45 (2012) 235-250.
[111] P. Stenberg, K. Luthman, P. Artursson, Virtual screening of intestinal drug permeability, J. Controlled Release, 65 (2000) 231-243.
[112] Y. Sambuy, I. Angelis, G. Ranaldi, M.L. Scarino, A. Stammati, F. Zucco, The Caco-2 cell line as a model of the intestinal barrier: influence of cell and culture-related factors on Caco-2 cell functional characteristics, Cell Biol. Toxicol., 21 (2005) 1-26.
[113] R. Hayeshi, C. Hilgendorf, P. Artursson, P. Augustijns, B. Brodin, P. Dehertogh, K. Fisher, L. Fossati, E. Hovenkamp, T. Korjamo, C. Masungi, N. Maubon, R. Mols, A. Müllertz, J. Mönkkönen, C. O'Driscoll, H.M. Oppers-Tiemissen, E.G.E. Ragnarsson, M. Rooseboom, A.L. Ungell, Comparison of drug transporter gene expression and functionality in Caco-2 cells from 10 different laboratories, Eur. J. Pharm. Sci., 35 (2008) 383-396.
[114] M. Kansy, F. Senner, K. Gubernator, Physicochemical high throughput screening: Parallel artificial membrane permeation assay in the description of passive absorption processes, J. Med. Chem., 41 (1998) 1007-1010.
[115] K. Sugano, H. Hamada, M. Machida, H. Ushio, K. Saitoh, K. Terada, Optimized conditions of bio-mimetic artificial membrane permeation assay, Int. J. Pharm., 228 (2001) 181-188.
[116] F. Wohnsland, B. Faller, High-throughput permeability pH profile and high-throughput alkane/water log P with artificial membranes, J. Med. Chem., 44 (2001) 923-930.

[117] L. Di, E.H. Kerns, K. Fan, O.J. McConnell, G.T. Carter, High throughput artificial membrane permeability assay for blood-brain barrier, Eur. J. Med. Chem., 38 (2003) 223-232.
[118] J.A. Ruell, O. Tsinman, A. Avdeef, Acid-base cosolvent method for determining aqueous permeability of amiodarone, itraconazole, tamoxifen, terfenadine and other very insoluble molecules, Chem. Pharm. Bull., 52 (2004) 561-565.
[119] A. Avdeef, O. Tsinman, PAMPA - A drug absorption in vitro model: 13. Chemical selectivity due to membrane hydrogen bonding: In combo comparisons of HDM-, DOPC-, and DS-PAMPA models, Eur. J. Pharm. Sci., 28 (2006) 43-50.
[120] G.E. Flaten, H. Bunjes, K. Luthman, M. Brandl, Drug permeability across a phospholipid vesicle-based barrier - 2. Characterization of barrier structure, storage stability and stability towards pH changes, Eur. J. Pharm. Sci., 28 (2006) 336-343.
[121] G.E. Flaten, A.B. Dhanikula, K. Luthman, M. Brandl, Drug permeability across a phospholipid vesicle based barrier: A novel approach for studying passive diffusion, Eur. J. Pharm. Sci., 27 (2006) 80-90.
[122] M.J. Ginski, R. Taneja, J.E. Polli, Prediction of dissolution-absorption relationships from a continuous dissolution/caco-2 system, AAPS PharmSci, 1 (1999) 1-12.
[123] M. Kobayashi, N. Sada, M. Sugawara, K. Iseki, K. Miyazaki, Development of a new system for prediction of drug absorption that takes into account drug dissolution and pH change in the gastro-intestinal tract, Int. J. Pharm., 221 (2001) 87-94.
[124] M. Kataoka, Y. Masaoka, Y. Yamazaki, T. Sakane, H. Sezaki, S. Yamashita, In Vitro System to Evaluate Oral Absorption of Poorly Water-Soluble Drugs: Simultaneous Analysis on Dissolution and Permeation of Drugs, Pharm. Res., 20 (2003) 1674-1680.
[125] S.A. Motz, J. Klimundová, U.F. Schaefer, S. Balbach, T. Eichinger, P. Solich, C.M. Lehr, Automated measurement of permeation and dissolution of propranolol HCl tablets using sequential injection analysis, Anal. Chim. Acta, 581 (2007) 174-180.
[126] D.S. Jornada, L.A. Fiel, K. Bueno, J.F. Gerent, C.L. Petzhold, R.C.R. Beck, S.S. Guterres, A.R. Pohlmann, Lipid-core nanocapsules: Mechanism of self-assembly, control of size and loading capacity, Soft Matter, 8 (2012) 6646-6655.
[127] K. Coradini, F.O. Lima, C.M. Oliveira, P.S. Chaves, M.L. Athayde, L.M. Carvalho, R.C.R. Beck, Co-encapsulation of resveratrol and curcumin in lipid-core nanocapsules improves their in vitro antioxidant effects, Eur. J. Pharm. Biopharm., 88 (2014) 178-185.
[128] R.B. Friedrich, B. Kann, K. Coradini, H.L. Offerhaus, R.C.R. Beck, M. Windbergs, Skin penetration behavior of lipid-core nanocapsules for simultaneous delivery of resveratrol and curcumin, Eur. J. Pharm. Sci., 78 (2015) 204-213.

7 Acknowledgments

I was very fortunate to be involved in many national and international research cooperations and my contributions to all these projects are now concluding in this thesis. It probably requires as many pages again to give a proper thanks to all the people who became companions over the last years. Nevertheless, I would like to mention a few people in person.

As there is no graduation without a professor, who believes in you and your work, I would like to thank you, Claus-Michael, for welcoming me in your research group. You provided a great environment combining excellent working conditions and social activities which made it enjoyable to come to the institute every day.

Maike, I can count myself very lucky to have had such a great person and enthusiastic researcher by my side. You have been one of the biggest constants over the last years and really put my best forward. I am still amazed that we can check all the points from your first email off today. Chapeau!

Lutz, the “E” for effort really made us and Sir Raman a good team and big fans of toques and warm coats.

I am grateful to the German Academic Exchange Service (DAAD) that I was awarded with a grant (Kurzstipendium für Doktoranden) which enabled me to perform some of my PhD work at the University of Twente in the Netherlands. Herman Offerhaus and the entire Optical Sciences Group led by Jennifer Herek made my stay very successful and enjoyable. Especially one person showed me that physics has more to offer than sharing the first letter with pharmaceutics.

I would not have come this far without the unreserved support and encouragement of my parents and family from both sides of the ocean over the years. They all contributed their share to this thesis as well. A simple thank you is not enough.

Last but not least, I would like to thank my graduation committee for their willingness to accompany me throughout this final stretch of my PhD time.

Thank you all!